

Functional nanoelectronic devices

Single-electron transport, memristivity, and thermoelectricity in nanoscale films using self-assembly and graphene



Hippolyte P.A.G. Astier

Supervisor: Prof. C.J.B. Ford

Cavendish Laboratory, Department of Physics
University of Cambridge

This dissertation is submitted for the degree of
Doctor of Philosophy

Fitzwilliam College, Cambridge

January 2019

This thesis is dedicated to H el ene Doucet, Gustave Louat, C ecile Astier, Christophe Astier,
and Cyprien Astier.

Declaration

I hereby declare that except where specific reference is made to the work of others, the contents of this dissertation are original and have not been submitted in whole or in part for consideration for any other degree or qualification in this, or any other university. This dissertation is my own work and contains nothing which is the outcome of work done in collaboration with others, except as specified in the text and Acknowledgements. This dissertation contains fewer than 65,000 words including appendices, bibliography, footnotes, tables and equations and has fewer than 150 figures.

Hippolyte P.A.G. Astier
January 2019

Acknowledgements

First and foremost I would like to thank my supervisor Chris Ford. I feel very lucky to have had such a fantastic supervisor for my PhD, and I am infinitely grateful. I hope we continue working together when I leave.

Secondly I would like to thank Prof. Neil Greenham and Prof. Tim Albrecht for accepting to be my examiners, especially given the time constraints. I hope they have enjoyed reading my thesis and examining me. My viva was a very interesting discussion, and will be very useful in my future research.

I would also like to thank the people who have worked with me in Cambridge, in particular Dean Kos and Jan Girovsky, with whom it has been an absolute pleasure to work. Several people are to thank for the work that I have done during my time in Cambridge, and I would like to express my gratitude to Ateeq Nasir, Melanie Tribble, Lissa Eyre, Ben Robinson, Alex Robson, Xintai Wang, Luke O'Driscoll, Martin Bryce, Hatef Sadeghi, Michael Jay, Colin Lambert, James Xiao, Heather Goodwin, Akshay Rao, Wenting Guo, Shanglong Ning, Vijay Narayan, James Aldous, Domenico De Fazio, Ugo Sassi, Andrea Ferrari, Marcus Böhm, Jan Mertens, Giuliana Di Martino, Jeremy Baumberg, Dave Ritchie, Crispin Barnes, Richard Langford, J.J. Rickard, Eric Tapley, Justin Llandro, Joel Fruhman, Adrian Ionescu, Luka Skoric, Philip Leung, Dave Ellis, Jonathan Griffiths, Jan Mol, Xinya Bian, Andrew Briggs, Ouyang Chun, Yutaka Majima, Yannick Dappe, Nicolas Clément, Li Yang.

My time at Cambridge has been an eventful few years, and I am immensely grateful to all the people who made it so special. I would like to dedicate a very special word of gratitude to David Arvidsson-Shukur, whose indefectible enthusiasm, ambition, silliness and friendship I couldn't have done without, for nearly the past ten years, and hope never have to.

What a fantastic population has inhabited my laboratory. Firstly I would like to thank my academic twin sister, Ankita Anirban, I will miss our alternatively hopeful and blasé artisan-coffee-fueled conversations. Hugo Lepage, a saint of friendliness, supportivity, discernment, and humour, I am so happy you joined us. Bruno Loureiro, and soulmate Giuseppe Papallo, I send you gourmet love. Aleksander Lasek, I am incredibly delighted you could come back to us, not least because you owe me five pounds. A few more people I would like to thank for

my time at the Cavendish are Marianne Haroche, Simona Pace, Vivek Chidambaram, Ollie Batey, Carmen Palacios Berraquero, Ugo Siciliani De Cumis, Adam Klimont.

Few people are lucky enough to find several families in their lives, but the fortuitous French invasion of Fitzwilliam College et environs led to nothing short of a *mifa de ouf*, and I want to thank Hugo Poplimont, Fabio Lima, Guillaume Baverez, Romain Alves, and Victor Allard; I couldn't have done this without you, I was happy beyond words to live with you, literally or virtually, and I give you the biggest of *mercis*.

The Boot, the Dracula, and the Ariane, network of transcendental splendour, for which my love is infinite, I want to thank you all, wonderful Noémie Lachance, Daniel Chiritoiu, Boruo Bono Xu, Eleni Courea, Bram van der Velden, Elisabetta Garletti, Dario Palumbo, Sophie Morrison, Martin Schlegel, Susie Ní Chróinín, David Ginsborg, Enrico Ghiorzi, George Dicken, Yasmin Alishenas. We've lived so many adventures together that I never thought a PhD could contain, and I feel so lucky to have you as my friends.

One of the biggest events in my PhD was to join the NanoDTC's community. It has changed my course, and life, so significantly I cannot thank the people involved enough. I would like to thank the organisers of the programme, Kim Cole and Karishma Jain, I am impressed by how smoothly everything works in this enormous and tentacular community, and I am very grateful. I want to thank the cohort of 2017 whom I was lucky enough to go to Grenoble with; this was such a fantastic trip and I am so happy I spent it with you, Ryan Greenhalgh, Bluebell Drummond, Tom Parton, Greg Chant, Roger Rubio, Kevin Lim, Joshua Tuffnell, Jedrek Morzy, Theo Lundberg, Takashi Lawson, Katarzyna Sokol. It was also excellent to spend time with other members of this community on other occasions, and I would like to thank Andreas Wagner, Lauren McKenzie-Sell, and Anna Gunnarsdóttir.

I would like to thank my friends at CYL, for the comradely adventures and support: Rox Middleton, Finlay Knops-McKim, Helena Blair, Caitlin de Jode, Dan Kerry.

What is a toast without a word for absent friends, who, all things considered, were thankfully not too absent. I would like to thank my Durham friends with whom the distance was only geographical: Tom Sargeant, Ben Beswick, Eléonore Gaudin, William Hammersley, Clive Knipe, Azin Khan, Oliver White, Oliver Goodman, Rob Law, Damien Jacobée, Daan Arroo, Hein Smit, Joseph Packham, Daniel Rowbottom, Catherine Able-Thomas, Amy Paynter.

A few years ago I was in a town called Heidelberg, where I met some people I am so happy were still in my life during my time at Cambridge. These *Freunde* are Alexander 'Palace' Archer, Bart Andrews, Rebecca Breitman, Sophie Baker, Tom Webster.

Even earlier, I was in France, and the few, hopefully happy few, with whom the friendship has survived the distance and the number of years I would like to express my love to. I would

like to thank Rémi Vaissié, Magda Hennebo, Marwan Debbiche, Romain Meslier, Marie Fonteneau, Léonard Tapié, Emma Gillet. Thank you for being with me all along.

A special word of gratitude goes to Maja Dackland whom I am very lucky to have as a friend. Other friends scattered across the world or in Cambridge I would like to express my gratitude to are Rodrigo García-Velasco, Brandon Jackson, Love Hedman, Natalie Donback, Carles Morante, Matheus Nunes, Katarzyna Doniec, Katren Rogers, Lorenz Fenk, Lina Xing, Lorenzo Maniscalco, François Rostand, Stéphanie Childress, Jérémy Vey, Kamélia Pidik, Lucie J.F., Humbert de Miribel, Davide Stefani, Jan Overbeck.

There are a few more people without whom I would probably never have set foot in my laboratory. I would like to thank my collègue teacher Mme Bringué, my first English teacher. I would like to particularly thank two of my lycée teachers, Mme Robb and M Lartigue. Sans vous ce travail n'aurait pas été possible, et je serais quelqu'un de bien différent.

What would I be without my family? I am so lucky to have such supportive relatives, and I would like to use this page to reiterate my gratitude to mon parrain Sylvain; je te remercie pour ton soutien et tes sages enseignements. Merci à ma marraine Nathalie Mesny; je suis très heureux d'avoir pu te voir autant ces dernières années, merci pour ton soutien. I would like to say a word of gratitude to Camille Doucet and Christophe Louat; I am beyond blessed that I have been able to see you so often in the past few years and witness (happy!) turning points in your lives and mine! I hope my desires of adventure do not keep me away from you and little Gustave and Marcel too much. Hello and thank you to my cousins, whom it was lovely to see occasionally over the past few years. Cyrielle Bruneau, thank you for your impromptu visits to Cambridge. Je voudrais remercier Marlène Odinot tout particulièrement; merci pour tout, je pense à toi.

Merci à mes parents Christophe et Cécile, et mon frère Cyprien. Il est bien plus simple d'expliquer le fonctionnement d'un système d'électronique quantique que de trouver les mots pour vous dire à quel point je vous suis reconnaissant. Je vous dois tout.

Abstract

This dissertation reports on several experimental projects studying electronic transport in thin-film electronic devices. Self-assembly methods and graphene were used to realise devices contacting films of self-assembled PbS quantum dots. The devices have exhibited single-electron tunneling with a high yield. The electrical properties of the junctions are studied individually and collectively using statistical tools to extract correlations between device geometries and electrical data. The dissertation includes discussion of the theory of relevant electronic transport including numerical simulations. Several initiated projects deriving from this work are introduced. A second device reported in this thesis is a memristive switch. Contacting thin films of Al_2O_3 with graphene delivered junctions which exhibit memristive behaviour with an ultrahigh on-off conductance ratio. The conduction state of the junctions is correlated with morphological changes in the devices, whereby conductive filament formation in the junction is found to lead to electrically-controllable and reversible gas encapsulation in bubbles in the structure. The device is measured electrically and topographically, and the correlation between the two aspects is studied. A discussion of memristive conduction is included with numerical simulations. A third section reports on a project studying thermoelectricity in self-assembled molecular junctions, as they show potential for improved thermoelectric efficiency for energy harvesting; this is discussed in the dissertation. Strategies to benchmark the studies are presented with relevant devices fabricated and measured. These include the development of a measurement protocol to study thermoelectricity in devices, studies of electrical coupling between various molecular structures and graphene electrodes, molecular-structure dependence of electrical and thermal conductance of junctions. Preliminary results and on-going work are discussed.

Table of contents

List of figures	xvii
List of tables	xxv
Nomenclature	xxvii
1 Introduction	1
1.1 Thesis outline	1
1.2 Nanoscale electronics	1
1.2.1 Landauer formalism	2
1.2.2 Brief overview of molecular-scale electronic research	4
1.2.3 Graphene nanoelectronics	6
2 Single-electron tunnelling in self-assembled monolayers of quantum dots	11
2.1 Introduction	11
2.2 Background	12
2.2.1 Nanocrystals and quantum dots	12
2.2.2 Electronic structure of semiconductor nanocrystals	13
2.2.3 Single-electron tunnelling devices	16
2.3 Theory	17
2.3.1 Single-electron tunnelling	17
2.3.2 Negative differential resistance	24
2.4 Experimental procedures	26
2.4.1 Device design and fabrication	26
2.4.2 Electrical characterisation	32
2.4.3 Imaging	33
2.4.4 Quartz crystal microbalance	34
2.5 Results	36
2.5.1 Verification of monolayer formation	36

2.5.2	<i>I-V</i> profiles	39
2.5.3	Statistical analysis	47
2.5.4	Discussion	53
2.6	Further devices	55
2.6.1	Self-assembly variations	55
2.6.2	Top-gated devices	57
2.6.3	Single-quantum-dot junctions	61
2.6.4	Conclusion	62
3	Memristive switching devices for electrically controllable nano and micro actuation	65
3.1	Introduction	65
3.1.1	History and development of memristivity	66
3.1.2	Memristive mechanism	68
3.1.3	Actuation at the nanoscale	69
3.2	Theory	71
3.2.1	Transport in memristors	71
3.2.2	Plasmonic detection with nanoparticles on a mirror	75
3.3	Experimental procedures	76
3.3.1	Device design and fabrication	76
3.3.2	Electrical characterisation	78
3.3.3	Optical set-up	79
3.3.4	Imaging	82
3.4	Results	82
3.4.1	Memristive behaviour	82
3.4.2	Actuation through bubble inflation	83
3.4.3	Filament profile	86
3.4.4	Plasmonics	87
3.5	Discussion	89
3.5.1	Comparison of transport with standard memristor	89
3.5.2	Bubble control	90
3.6	Conclusion	90
4	Thermoelectricity in molecular self-assembled monolayers	93
4.1	Introduction	93
4.2	Thermoelectricity	94
4.2.1	First principles	94

4.2.2	Thermoelectric efficiency	96
4.2.3	Thermoelectricity and density of states	97
4.2.4	Thermoelectricity in a weakly coupled junction	100
4.2.5	Thermoelectric materials	102
4.2.6	Thermoelectric devices	104
4.3	Experimental procedures	106
4.3.1	Molecules	106
4.3.2	Device design and fabrication	109
4.3.3	Electrical characterisation	115
4.3.4	Thermoelectric measurement	119
4.4	Preliminary results	122
4.4.1	<i>I-V</i> characterisation	122
4.4.2	Thermopower	131
4.5	Discussion	132
4.6	Conclusion	134
5	Conclusion	135
	References	137

List of figures

1.1	Schematic of a Landauer junction. Two leads, source and drain, are on each side of a junction with quantised energy levels.	2
2.1	Band structure of bulk lead sulphide, PbS, as calculated by S.E. Kohn <i>et al.</i> [1], adapted from Ref. [2]. E_i ($i = \{0, 1, 2, 3\}$) are the band gaps of the structure, E_0 being the primary and a direct band gap.	15
2.2	Size-dependence of PbS electronic structure. a , calculated density of states at $T = 4.2K$ for PbS clusters of 8, 32, 56, 88 atoms, and bulk PbS; adapted from [3]. b , band-gap energy as a function of QD size, as obtained from various experimental measurements and theoretical models [4–8], adapted from [8].	16
2.3	Diagram of a Coulomb blockade configuration. The central island is a dot with a discrete energy spectrum. Two energy scales operate in parallel to determine the transport, i.e. the charging energy, and, in the quantum case, the discretised density of states in the dot. These determine an energy difference ΔE , which represents the energy needed to change the charge occupancy in the dot. a , system at zero bias. b , system at non-zero source-drain voltage, such that an energy level is available for tunnelling which results in a single-electron tunnelling current.	17
2.4	Schematic of the charge occupancy of a quantum dot as a function of external charge. a , charging energy $U(N)$ for different values of N of the dot as a function of external charge Q_G . b , net charge q of a dot as a function of external charge. Adapted from [9].	19

- 2.5 Schematic of a Coulomb diamond. The central plot shows differential conductance as a function of source-drain voltage V_{SD} and gate voltage V_G , where the gate tunes the electrochemical potential inside the dot without affecting the leads. The peaks in conductance draw diamond-like structure in the V_{SD} - V_G space. Schematics 1-4 illustrate the transition points in the Coulomb diamond from an energy point of view, where the horizontal axis is position and vertical axis is energy. Cyan arrows show the allowed electron transfers. The distances between these peaks are revealing of the energy structure and capacitance of the dot. The annotated energy differences can be expressed as $\Delta E = \mu_d(N+1) - \mu_d(N) = \epsilon_{N+1} - \epsilon_N + e^2/C$, $\Delta E_{ex} = \epsilon_{N+1} - \epsilon_N$, whilst the gradients of the lines in the planes reveal the individual capacitances between the terminals, i.e. $\alpha_S = -C_G/C_D$, $\alpha_D = C_G/C_S$ 21
- 2.6 Simulations of transport in metal-dot-graphene junctions. **a**, in a weakly coupled dot, the energy levels scan the graphene's DOS where, in an appropriate alignment of the levels with the Dirac cone leads to NDR. **b**, simulation in a similar system where the dot is more strongly coupled to the electrodes, leading to Lorentzian broadening, which efface the current blockade and the minimum in the graphene's DOS. 26
- 2.7 Junction structure. **a**, photograph of a die. **b**, micrograph of junctions with left: OL device design, right: EBL device design. **c**, coloured SEM image of OL junctions where blue is SLG, pink is QD-coated Au, and yellow is bare Au. **d**, coloured SEM image of an EBL-design junction with similar colour code. **e**, electrical diagram of a junction as connected to a current source. The RC junctions represent the tunnelling barriers on each side of the QD. **f**, SEM image of a Au surface functionalised with the QD SAM. 27

- 2.8 Mask design for device fabrication. Orange/brown: pattern for evaporated Au, blue: OL pattern for SLG patterning, magenta: OL layer for selective SA, cyan: EBL pattern for SLG patterning. **a**, mask design for a single die of devices, including 39 junctions. One batch of such dice consists of an array of 6×6 dice. One die is approximately $3 \times 3 \text{ mm}^2$. At its edges, squares of thick Au are bonding pads connected to micron-sized junction in the central region of the die. **b**, detail of the die's central region. QD-decorated junctions appear as vertical Au fingers on the picture; the selective assembly determined by the OL layer (in magenta) exposes them the SA whilst protecting the fingers appearing horizontal here which are used for grounding. The SLG pattern coats the tips of all junctions, draping over the QD-decorated electrodes and in direct contact with the grounding electrodes. The overlap between the SLG layer and the QD-decorated electrodes determines the junction area. In this pattern variability in the junction size was deliberately introduced, and the junction size was of the order of the standard error on OL alignment, so as to obtain a statistical range of junction areas, including sub-micron features. **c-d**, detail of the design for EBL-defined junctions. The graphene is first etched according to the OL design, and a second step tailors trenches in the graphene to reduce the area of overlap between the graphene and the QD-decorated electrode down to areas of order $100\text{-}1000 \text{ nm}^2$. Design by JM Fruhman. 28
- 2.9 Junction structure. **a-c**, SA steps. **d**, impression of the SA structure at the single-QD scale. $\sim 5 \text{ nm}$ -diameter QDs are attached to Au through the SAM of C6S2 linkers. The QDs have OA ligands. A sheet of CVD graphene is draped over the QD SAM. **e**, schematic of a junction. The Au finger is coated with the QD SAM and a layer of SLG coats their tips. 30
- 2.10 QD size measurement from TEM imaging. **a**, QD diameter extracted from TEM imaging, binned. **b**, TEM image from dropcast QDs. Crystal facets can be seen on some of the QDs. 33
- 2.11 Quartz crystal microbalance QCM set-up. **a**, schematic of a QCM sample with front and side views. **b**, electrical set-up driving the QCM. This includes the QCM's circuit which is connected to an ammeter and a voltmeter. The I - V phase is measured by a phase detector and rectified through frequency by an integrator connected to a voltage-controlled oscillator (VCO). The relevant quantity, the resonant frequency, can be extracted via a frequency counter. 36

2.12	SAM verification using mechanical cleaning. a-b , height profile cross-section of QD SAM. a , height profile, the line shows cross-section used for height profile analysis shown in b . c-d , height profile cross-section on control substrate without SAM, examined in a similar way.	38
2.13	AFM imaging of QD SAM formed on template-stripped Au. a , imaging of template-stripping-prepared Au substrate. b , imaging of the QD SAM. . . .	39
2.14	<i>I-V</i> measurements displaying Coulomb staircases, from OL junctions (a , e , and details of these measurement) and EBL junctions (f , h , i and details); the areas are displayed in graphs. These measurements are selected representative measurements of each junction, their behaviour varying only in a minor way over successive measurements. Taken from [10].	40
2.15	<i>I-V</i> curve of junction exhibiting Coulomb staircase at 62 K.	42
2.16	Schematic of the system. a , schematic of a single-QD system as contacted in the junction. b , corresponding energy structure. The C6S2 SAM and the OA ligands form tunnelling barriers on each side of the junction. The two leads are Au and SLG.	42
2.17	Junctions exhibiting smooth non-Ohmic <i>I-V</i> profiles. a-e , <i>I-V</i> measurements and Landauer fits. Blue line: experimental data. Red dotted line: Landauer model fit. f , measurement shown in a in form $ V^2/I $ versus voltage V	44
2.18	Hysteresis in staircases in <i>I-V</i> characteristics. a , <i>I-V</i> curve of junction exhibiting Coulomb staircase. b-c details of subsequent measurements of the same junction. b , two measurements whilst varying the voltage in the same direction show similar characteristics with slightly shifted steps. c , voltage bias sweeps in opposite directions show displaced current steps and different transitions. Figure taken from [10].	46
2.19	Waterfall plots of <i>I-V</i> curves of junctions exhibiting NDR. Subsequent measurements of the same junction are shifted vertically for clarity. Junction IDs are as follows: a : 290014; b : 260030; c : 290033.	48
2.20	Categories of junction characteristics and comparison of conductance. a , representative ShC. b , example of SmC. c-e , histograms displaying G_0/A , the conductance per unit area (whereby the area used is the junction's area), for different populations of junctions. c , comparison of the three main categories StC, ShC, and SmC in OL devices. d , comparison of SmC for OL and EBL devices with control C6S2 SAM devices made with OL and EBL. e , comparison between OL and EBL devices for StC and ShC junctions. . . .	51

- 2.21 Logistic regression of StC yield as a function of junction geometry. **a**, logistic regression against junction area for OL devices. Top (bottom): histograms of occurrence of StC (SmC and ShC) as a function of junction area. Centre: logistic regression. Orange line: regression, spring green region: confidence interval. Adapted from [10]. **b**, logistic regression for OL and EBL junctions against junction area, where solid (dashed) lines are the average and confidence interval of the regression for OL (EBL) junction. Crosses show individual events (1 for StC, 0 for SmC or ShC). **c**, logistic regression against perimeter of the SLG open edge; vertical noise has been added to crosses so as to make their densities more apparent. 52
- 2.22 Scatter plot of step fit parameters with junction geometry and I - V characteristics. **a**, Scatter plot of step height against junction area. The different populations are made explicit by a colour code and a shift separating the batches of OL devices. For all batches two populations have been distinguished with the colour code due to their different conductance regime (high and low) and apparent inclusion in different trends in the scatter plot. The EBL batch has a further division consisting of OL-sized junctions included in the EBL pattern. **b**, scatter plot of conductance at 0 V, G_0 , against step height I_h extracted from the step fits. Circles (triangles): first steps occurring at positive (negative) voltage polarity. The size of the marker is proportional to our appreciation of the clarity of the step, i.e. presence of noise, or background conduction. 53
- 2.23 AFM-UFM imaging of different regions of a device. The height profile for all surfaces is on the same scale for comparison. The colour shading gives a measure of the rigidity of the underlying surface. 55
- 2.24 Mask used for first design of device with top gate. **a**, mask design made by J.M. Fruhman including dielectric layer (light blue) and top Au gate (green). **b**, micrograph of a device. 58
- 2.25 Top-gated device. **a**, false-colour micrograph of a device, where pink is QD SAM-coated Au electrodes, gold is Au fingers, blue is SLG, and green is top gate contacts. **b**, schematic of the device's structure. On top of the standard device, a layer of parylene is deposited and serves as the dielectric. A layer of Au contacts is deposited on top of the parylene and is used as top gates. 59
- 2.26 Imaging of nanogap devices used for single-QD studies. **a**, SEM image of a metallic nanogap device taken by O. Chun. **b**, AFM image of a SLG nanogap device decorated with PbS QDs. 61

3.1	Sketch of the memristive reaction in an oxide film. a , initial state of an oxide-based memristor: an insulating oxide film is placed between two electrodes. b , oxygen ion migration and oxygen-depleted filament formation as a voltage bias is applied across the film. c , memristor in <i>on</i> state, a conductive filament fully bridges across the film. d , reversal of the transition: a voltage bias in the opposite direction reintegrates oxygen into the reduced filaments, allowing a transition back into the insulating state. Adapted from Ref. [11].	70
3.2	My simulations of a memristive system. a-d , evolution of the system of several AC periods. These were produced using the following parameters: $R_{\text{OFF}}/R_{\text{ON}} = 100$, $\omega = 5.03\text{ Hz}$, $v_0 = 1\text{ V}$, $d = 10\text{ nm}$, $\mu_i = 10^4\text{ nm}^2\text{ s}^{-1}\text{ V}^{-1}$. e-f , frequency dependence of the system. Only changing the AC frequency, different regimes, labelled 1, 2, and 3, can be seen in relation to the critical frequency ω_M , found here to be 3.96 Hz —where Eq. 3.12 gives 4 Hz . e shows a low frequency regime, at $\omega = 628\text{ mHz}$, where the maximum on-off ratio $R_{\text{OFF}}/R_{\text{ON}}$ ratio is reached. f , effective on-off ratio $\epsilon R_{\text{OFF}}/R_{\text{ON}}$ as a function of frequency.	74
3.3	Memristive device structure. a , sketch of the device structure. b , SEM image of the device; the scale bar is $200\mu\text{m}$. c , false-colour detail of b , where yellow is Au, green is the Al_2O_3 film, and blue is SLG. Adapted from D. Kos and H.P.A.G. Astier <i>et al.</i> [12].	76
3.4	Dark-field optical set-up. The illumination is deviated from the detector so as to collect isotropic luminescence from the NPs.	79
3.5	Micrographs of a junction. a , bright-field micrograph. b , dark-field micrograph.	81
3.6	Electrical measurement of the junctions. a , I - V cycles in a given junction. b , conductance cycles. c , sketch of device structure, side view (left) and top view (right). d-f , dark-field image of the junction as voltage is applied; scale bar: $5\mu\text{m}$. Adapted from Ref. [12].	82
3.7	Profile of bubbles. a , AFM image of a large bubble. b , height cross section of imaged bubble. c , high-angle SEM image of a bubble (scale bar $1\mu\text{m}$). d , pressure fits from AFM-imaged bubbles. Adapted from [12]. e , estimate of the degree of conversion of oxygen transfer from film to bubble for bubbles measured as a function of their height.	84
3.8	Electroforming in the device structure. a , Schematic of the device topography in its inflated form. b , Conduction state stability as a function of time. Adapted from [12].	86

3.9	Evolution of the NPs' luminescence spectra during actuation. a-b , dark-field micrograph of junction with NP colour switching. c , corresponding luminescence spectrum of indicated NPs. d-e , NP spectrum (d) and corresponding junction current (e) as voltage is increased. f-g , NP spectrum (f) as voltage is swept in cycles (g). Taken from [12].	88
4.1	Sketch of basic thermoelectric cells. a , Seebeck cell: heat supplied by the environment generates current in the circuit via the thermoelectric effect. b , Peltier cell: supplying current to the cell creates a temperature difference between the two surfaces.	95
4.2	Thermocurrent in a molecular junction. a , energy schematic of a single-level junction where the source and drain are at different temperatures, T_S and T_D respectively. The single level ϵ_d in the junction filters the conduction to a restricted energy interval. The finite temperature results in vacant states in the electrodes and a temperature difference can lead to transfer of electrons into the electrode having more vacant states in this interval. b , Landauer model simulation of the current at zero voltage resulting from a temperature difference; the energy level is set at -100 meV and temperature in the drain was varied from 293 K to 393 K while the source temperature was kept at 293 K.	102
4.3	Optical lithography mask design for device with pore/valley junctions. a , central region. b , detail of valleys. Brown: bottom electrodes, orange: connection to bonding pads, blue: self-assembly region, cyan: top electrode (graphene), green: insulator with pores, pink, top gate contacts.	110
4.4	Device design with pores. a , AFM image taken of etched pore with photoresist from OL. b , schematic of device with pore design.	114
4.5	Electrical characterisation set-up. a , schematic of the mixed AC/DC set-up. b , electrical diagram of the I - V converter. c , electrical diagram of the AC/DC mixer, described in Section 4.3.3.	116
4.6	Electrical set-up to measure the thermoelectric effect via the 2ω method. a , schematic of the whole set-up. b , electrical diagram of the V - I converter.	119
4.7	Electrical characterisation of devices from batch 1. a , extraction of the decay coefficient for CnS from averaging measurements. b , extraction of the decay coefficient for OPEs.	122
4.8	I - V measurements of batch 1 devices contacting C12S. a , junctions exhibiting a non-Ohmic profile. b , junctions exhibiting a breakdown behaviour where the conductance undergoes an irreversible shift during a measurement.	123

4.9	Batch 4 CnS devices. a , micrograph of a device with an SLG:Au top electrode. b , CnS length dependence of current density for devices with an SLG:Au top electrode. c , CnS length dependence of current density for devices with an SLG top electrode.	125
4.10	Extraction of the decay factor for the devices of batch 5 as listed in Table 4.1, taken from 132 measured junctions. a , histograms of current at a fixed voltage for C8S junctions. b , similarly for C10S. c , similarly for C12S junctions. d , extraction of the decay coefficient as a function of CnS . The colour code in the histograms corresponds to the populations used to extract the average current for the junctions: combined blue and gold include the whole data, gold is a subset of the data used for the analysis omitting outliers in blue.	126
4.11	Conductance data for BOC8S junctions. a-f , conductance data over successive measurements for junctions with 100% BOC8S. g-h , conductance data for junctions with 20% BOC8S. An arrow indicates the order of the measurements, in all the junctions displayed, the conductance increases over successive measurements.	128
4.12	I - V data for BOC8S junctions. The junctions, figure indices, and colours match those shown in Fig. 4.11. a-f , I - V data over successive measurements for junctions with 100% BOC8S. g-h , I - V data for junctions with 20% BOC8S. Arrows indicates the order of the measurements, in all the junctions displayed, the conductance increases over successive measurements.	129
4.13	Conductance profile of two (a , b) BOC8S junctions over many successive voltage cycles. A continuous conductance increase is seen over successive measurements.	130
4.14	Test of the 2ω measurement set-up. An AC voltage was set across the SLG electrode at two different frequencies, and the AC voltage across the junction was measured at the first and second harmonics.	131

List of tables

1.1	Inventory of most important molecules and molecular structures used and discussed in this dissertation, with formula and shorthand.	10
2.1	Parameters of Landauer model shown in Fig. 2.6.	26
2.2	Parameters of Landauer model fits on non-Ohmic smooth curves displayed in Fig. 2.17.	43
2.3	Database structure. Four tables constitute the database compiling the data. These have database fields to enable a statistical analysis.	50
2.4	Devices with SA variations. Capping ligands with asterisk (*) are obtained through ligand exchange following the SA on the anchor SAM; being dithiolates they are likely to cross-link QDs within the superlattice.	56
3.1	Values used for pressure calculations.	84
4.1	Principal benchmarking devices fabricated and measured.	115

Nomenclature

Acronyms / Abbreviations

AC	Alternating current
AFM	Atomic force microscope
ALD	Atomic layer deposition
BNC	Bayonet Neill–Concelman (connector)
CnS_2	<i>n</i> -anedithiol
CnS	<i>n</i> -anethiol
DC	Direct current
DOS	Density of states
DUV	Deep ultraviolet
EBL	Electron-beam lithography
EDX	Energy-dispersive X-ray spectroscopy
HOMO	Highest occupied molecular orbital
IPA	Isopropyl alcohol
IR	Infrared
LCC	Leadless chip carrier
LUMO	Lowest unoccupied molecular orbital
MCBJ	Mechanically controlled break junction

NC	Nanocrystal
OL	Optical lithography
PEDOT	Poly(3,4-ethylenedioxythiophene)
PLO	Phase-locked oscillator
PMMA	Poly(methyl methacrylate)
PSS	Polystyrene sulfonate
QCM	Quartz crystal microbalance
QD	Quantum dot
QI	Quantum interference
RF	Radio frequency
RIE	Reactive ion etching
RMS	Root mean square
RTS	Random telegraph signal
SAM	Self-assembled monolayer
SA	Self-assembly
SEM	Scanning electron microscope
ShC	Short circuit
SLG	Single-layer graphene
SmC	<i>Smooth</i> curve
SMU	Source measure unit
StC	<i>Step</i> curve
STM	Scanning tunnelling microscope
TEG	Thermoelectric generator
TEM	Transmission electron microscope

TE Thermoelectricity; thermoelectric

UFM Ultrasonic force microscope

UV Ultraviolet

VCO Voltage-controlled oscillator

XPS X-ray photoelectron spectroscopy

Chapter 1

Introduction

1.1 Thesis outline

In this thesis, I present experimental projects where nanoscale or nanoscale structures are contacted in thin-film devices using graphene as an electrode, to investigate different types of electrical transport that address technological applications beyond standard electrical component properties as a result of the confinement of the structures. I have separated three projects according to the type of transport investigated. Chapter 2 reports on devices which contact quantum dots electrically to yield a type of current operated by single electrons flowing through the structure at a time. Chapter 3 describes a project where by contacting 10 nm-thin films of Al_2O_3 , we built devices which combined electrical properties of a memristive switch and electrically controllable actuation at the nano and micro scale. In Chapter 4, I describe experiments to develop thermoelectric generator devices relying on films of self-assembled molecules as their thermoelectric material. For clarity, this thesis is structured in such a way as to distinguish these projects and introduce them individually, with the relevant literature background, theory concepts, and experimental reports. As a consequence of this, this introductory chapter will be kept concise, giving a brief overview of relevant concepts in nanoscale electronics which will be treated more in depth in the individual chapters in the context of each type of device. The projects presented being collaborative, the contributions from collaborators are made explicit in each of the chapters.

1.2 Nanoscale electronics

The term nanoelectronics refers to the use of nanotechnology for building electrical components, or the study of electronic properties in nano-size systems. The field of study has

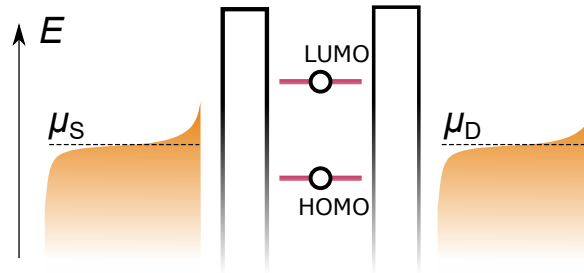


Fig. 1.1 Schematic of a Landauer junction. Two leads, source and drain, are on each side of a junction with quantised energy levels.

been developed in parallel to a continuous decrease in electrical component size in technology, needed to improve the performance of electronic devices. Below a certain size, electronic confinement leads to the prominence of quantum-mechanical effects that make their properties different from bulk components. This has motivated the investigation of these components on a fundamental level, as well as leading to new technologies only made possible by these properties. Three main structures of nanoscale dimensions are investigated in this thesis, namely nanocrystals, thin oxide films, and molecules.

1.2.1 Landauer formalism

Nanocrystals are crystals which are of nanometric dimensions in all three dimensions. As will be explored in Sec. 2.2.1, this spatial confinement leads to changes in its energy structure. While their bulk counterpart has continuous ranges of electronic states which charge carriers can occupy, nanocrystals see their electronic spectrum discretised in a way that likens them to molecules and their electronic orbitals. In a special disposition where they are placed between two electrodes, a source and a drain, in addition to this discretisation of their energy spectrum, Coulomb repulsion can lead the current to be filtered to single electrons flowing through them at a time in what is known as single-electron tunnelling. Interestingly, a similar type of transport can be obtained in molecules if, in a similar set-up where they are placed between two electrodes, their coupling to these electrodes is weak enough. The resulting electrical properties of such a junction then reflects the energy structure of the nanocrystal or the molecule and their energy levels which become conduction channels.

A simple model to describe the electrical transport in these junctions is the Landauer formalism. If one considers the electrodes in the electrodes as two ideal Fermi electron gases, electrons will occupy a continuum of states in their energy spectrum, according to the Fermi-Dirac distribution:

$$f_{\text{FD}}(E) = \frac{1}{1 + \exp\left(\frac{E-\mu}{k_{\text{B}}T}\right)}, \quad (1.1)$$

where E is energy, μ is the chemical potential in the electrode, k_B is the Boltzmann constant, and T is temperature. If a voltage V is applied across this junction, the chemical potential in these leads will be adjusted as follows.

$$\mu_S = E_F + qV/2, \quad (1.2)$$

$$\mu_D = E_F - qV/2, \quad (1.3)$$

where the subscripts S and D stand for source and drain, E_F is the Fermi energy, and q is the charge of the carrier considered. The electrical behaviour of this junction can then be inferred from the electronic structure of the contacted nano-object, its density of states $D(E)$, and the strength of its electrical coupling to the electrodes Γ_S and Γ_D , through the so-called transmission function

$$\mathcal{T}(E) = 2\pi D(E) \frac{\Gamma_S \Gamma_D}{\Gamma_S + \Gamma_D}. \quad (1.4)$$

The resulting current $I(V)$ can then be calculated as

$$I(V) = \frac{2q}{h} \int_{-\infty}^{\infty} dE \mathcal{T}(E) [f_S(E, V) - f_D(E, V)], \quad (1.5)$$

where h is the Planck constant. This formula is known as the Landauer, or Landauer-Büttiker, formula [13, 14]. The most simple system to consider is that of a junction with a single energy level. The coupling of the structure to the electrodes leads to a Lorentzian broadening, or lifetime broadening, which can be related to the uncertainty principle relating time and energy. The density of states for this single-level is given as

$$D(E) = \frac{1}{\pi} \frac{\Gamma}{(E - E_F)^2 + (\Gamma/2)^2}, \quad (1.6)$$

where $\Gamma = \Gamma_S + \Gamma_L$ is the coupling to the electrode [13]. In practice, transport in many molecules can be simplified by taking the two orbitals that are nearest to the Fermi energy: the highest unoccupied molecular orbital (HOMO) below the Fermi energy, and the lowest unoccupied molecular orbital (LUMO) above the Fermi energy. Depending on the structure of the molecule, one or the other can be closer to the Fermi energy, and therefore dominate the transport at low voltage. More accurate transmission functions can be simulated using various techniques, which is a focus of study for theorists in the field. This model illustrates that it is possible to probe a nano-object electrically such as to obtain a reading of its electronic structure.

The formalism can be adapted for many variations, depending on the system, e.g. for non-metallic electrodes by adapting the density of states in the leads to the relevant one for

the material, for temperature gradients across the junctions, by adjusting the temperatures in the Fermi-Dirac distributions in the leads, or for asymmetric coupling to the electrode by tying the junction's density of states to the voltage in one of the leads. All of these variations appear in subsequent chapters in this thesis to illustrate different systems. We will see in this thesis that these variations often bring properties that can be valuable for various applications. For example, semiconductor electrodes in this set-up can produce an electrical behaviour known as negative differential resistance (Sec. 2.3.2); asymmetry in the coupling to the leads can lead the junction to behave as a diode (Sec. 2.5.2). Finally, a temperature gradient across a junction can lead to thermoelectric current (Sec. 4.2.4).

1.2.2 Brief overview of molecular-scale electronic research

Experimentally, the research efforts to probe nanostructures, such as nanocrystals and molecules, electrically, can be divided into two approaches, that of single-nanomaterial electronics and that of ensemble systems. Both of these approaches can be divided further into experiments studying transport through conductive-tip measurements (scanning tunnelling microscopes, atomic force microscopy), and devices which contact the structures as fixed electrical components. The first account of a molecule contacted by scanning tunnelling microscope (STM) has been attributed to Joachim *et al.* in 1995 [15]. Since then, conductive-tip measurements of single molecules have become an active field of study internationally [16–19]. In the case of quantum dots, similar set-ups have been used to probe their electrical transport [20–22]. In the case of molecules, a standard measurement consists in functionalising a surface with target molecules, and use an actuated tip to probe it. By putting the tip in contact with the conductive substrate, and slowly retracting it whilst running a current, which is monitored, from the tip to the substrate. The resulting current profile as a function of the separation from the substrate, sometimes referred to as $I(s)$, gives a reading of the molecule's conductance. When the tip is in contact with the substrate a high conductance plateau is seen, as it is retracted, if the molecule bridges a contact between the two, a current plateau will be seen before the tip loses contact with the whole structure. The intermediate plateau is then a reading of the junction bridged by the molecule. Interestingly, in the device approach, an analogous concept exists, in mechanically controllable break junctions. In these junctions, a bow-tie metallic structure can be caused to break by mechanically pulling the two ends apart. If the structure is exposed to molecules able to attach, a similar $I(s)$ reading will be seen. This type of devices has also been explored by several groups around the world [23–26]. Another type of device using for single-molecule or single-nanomaterial studies is that of nanogaps, i.e. structures where two electrodes are separated by a nano-size gap which a molecule or nanomaterial can bridge. Several strategies exist to produce these, although

the difficulty to do so and the typically low yield of devices makes a transition to commercial technology difficult to envisage as yet. Examples of these are metallic nanogaps produced through Au plating used to contact nanocrystals [27], nanogaps formed by electromigration [28], or electroburned graphene nanogaps [29]. The single-object approach allows for a direct reading of the properties of the nano-object as can be seen in the citations.

The other approach, on the other hand, is concerned with ensembles of molecules or nanomaterials. It typically consists in coating a surface with a film, usually through self-assembly, and contacting this film electrically. In the case of molecules, the research can focus on several-layer thick, usually polymeric, films of molecules, or self-assembled monolayers (SAMs) of molecules, which is the approach of interest in this thesis. In the case of quantum dots, these two approaches also exist, and we are more concerned with self-assembled monolayers of nanocrystals, or nanocrystal superlattices as will be detailed in Chapter 2. In ensemble electronics too the same two schools of study exist with conductive tip experiments, and devices. In the case of conductive tips, several systems have been developed to probe areas of SAMs electrically. These can be Au tip experiments [30] or using an EGaIn tip [31, 32]. The device approach typically relies on depositing an electrode above the film to realise usually micron size junctions. Several architectures have been developed, but the effective contact of such structures with a high yield is still a challenge in the community despite recent improvements [33]. SAM devices are considered to be the more scalable approach of molecular and nanomaterial devices, and the one more transferable to everyday technology, motivating the development of many fabrication protocols [34–36]. This type of devices being very relevant to Chapters 2 and 4, they will be discussed more in depth.

Interestingly, in both the single-object and ensemble approaches, analysis of the data often demands a statistical approach. Indeed, in the single-object paradigm, the current measured across a junction of a similar structure may give variable results. This variation can be due to environmental effects, the structure being sensitive to its electrostatic environment, or different natures of chemical bonds, or physisorption, attaching it to the leads [13]. As a result, to characterise a junction, one must usually repeat the measurement thousands of times and analyse the results statistically to extract the underlying electronic structure. In the case of ensemble junctions, variations also occur, although they can be attributed to other factors. These can be the result of impurities between the top contact (tip or fixed electrode), or defects in the film, leading to different qualities of contact and random variations [37, 38]. Additionally, pinholes in the film occasionally lead to short circuits between the substrate and the top contact. It is therefore useful to conduct repeated measurements, and resort to statistical analysis to average out the random variations, and exclude unwanted outliers in the results. The variations in chemical bonds between the molecules or nanostructures and their

substrates are often assumed to be averaged out in large-area junctions contacting thousands of molecules [39]. While this statistical analysis is useful in conductive-tip experiments in both approaches for analysing transport properties, it is also used to verify the suitability of devices to contact films. In devices especially, short circuits are common, due to the sensitivity of the fabrication, and differentiating transport through a film and a short circuit is not a trivial task. An appropriate way to verify that the film is indeed contacted is to contact films of different elements and compare the results statistically. This aspect will be discussed at length in Chapter 4. In the case of single-object devices, statistical analysis is also used to rate the yield, or rate of success, of a fabrication method, where the successful formation of gap can be assessed and the successful integration of a structure within this gap can be measured [27].

1.2.3 Graphene nanoelectronics

Since its discovery in 2004 [40], the one atom-thick two-dimensional carbon material graphene has become a very active field of interdisciplinary research. Several exceptional properties explain this, the first of which is its being the first truly two-dimensional crystal discovered, which is sufficiently isolated in its transverse dimension to behave as such [41]. Graphene is also an excellent conductor; its electronic properties were studied and gathered in an extensive review [42]. Measurements and estimations of its rigidity also established it as the strongest known material [43]. Its thermal properties make it an excellent heat conductor in plane [44]. Other characteristics for applications that can be of interest are its transparency and flexibility. Chemical Vapour Deposition (CVD) allows for the growth of large areas of graphene, which one can pattern, making scalable device fabrication possible. Efforts have been made to utilise these exceptional properties in technology, and several devices have been demonstrated, such as optical detectors or phototransistors [45], photovoltaics [46], memory devices [47], flexible display technology [48], amongst other. Recently it was proposed in electronic systems as an electrode, which is the application we are interested in.

Both for low-scale electronics and optoelectronic applications, vertical device architectures suffer from limitations in their electrode. In optoelectronic applications, there is a need for top electrodes which are transparent and conductive. A commonly used material is indium tin oxide (ITO); however it is costly, has poor transparency in the blue and infra-red and is chemically unstable with acids and bases [49, 50]. In vertical low-scale electronics, as described in Sec. 1.2.2, contacting thin films with a top electrodes to form a high-yield device is challenging. Several methods for such junction fabrication have been reported. Metal evaporation was found to give rather low yield due to filamentary shorting (evaporation in-between molecules) and to actually damage the molecules [51]. Another solution has

been to use conductive polymer films between molecular junctions and a top electrode; this increases the yield but the interface between these layers is not well understood and is believed to change the conduction properties of the junction [35].

An ideal electrode for electronic and optoelectronic applications needs to allow for the optical and electronic investigation or stimulation of an active medium, without corrupting it. Electronically, this requires linear conduction properties and low scattering. Optically, this means transparency on a broad frequency range. Graphene is a semi-metal, i.e. a semiconductor with null band gap energy $E_g = 0$. As a result it behaves as a conductor whilst offering possibilities of doping [52]. It has remarkably high electron mobility, $200,000\text{ cm}^2/\text{Vs}$ in suspended graphene [53], $25,000\text{ cm}^2/\text{Vs}$ on a SiO_2 substrate (which induces scattering with charge impurities and phonons) [54]. Jo *et al.* demonstrated a broad-range GaN light-emitting diode (LED) using graphene as a top electrode, using the fact that it is transparent for most of the visible spectrum [50]. The combined use of PbS colloidal nanocrystals and a graphene bottom electrode was shown to enable the construction of photodetectors [45] with a gain of 10^8 electrons per photon; this is five orders of a magnitude higher than previous quantum-dot based photodetectors which are limited by the low carrier mobility of quantum-dot films [55]. The photonic excitation of the PbS quantum dots creates electron-hole pairs which, by gating the graphene, allow holes to tunnel into the graphene electrode whilst electrons are trapped in the nanocrystals and emphasise this gating effect.

Such fabrication requires technical knowledge of graphene as an architectural element in a device; this implies knowledge of its topography in various configurations and assembly processes. A suspended configuration was used to experimentally determine the elasticity of graphene [43]. Small cavities covered by free-standing graphene were indented with atomic force microscopy and a force-to-indentation relation served to determine the elastic stiffness of the membrane and find a Young modulus of 1.0 TPa , confirming graphene as the strongest material known. Such membranes were studied extensively by McEuen's group in which such cavities were used as mechanical resonators [56] and a *balloon* [57] of which the inflation can be precisely tuned by adjusting the pressure gradient across the membranes. It also demonstrates the impermeability of graphene to particle transfer; it offers a protection to enclosed elements. This protection principle was explored in a different arrangement by Yuk *et al.* [58] who worked on drop-casting clusters and nanoparticles onto graphene sheets and covering them with a second graphene sheet (and repetition of the process for more layers). They distinguished different arrangements this principle can lead to: *sandwiches* where the particle monolayer would be dense enough to not let graphene protrude between the elements, and *veils* where the upper graphene sheets cover individual particles completely and assemble on the lower graphene sheet via a van der Waals interaction. It was found

that in the latter case the resulting *bumps* in the upper graphene layer were of a triangular shape, as a geometric result of the hexagonal lattice structure of graphene. Bringing Au particles in such structures to evaporation conditions, it was observed that *sandwich* structures allowed migration and aggregation of the particles whereas *veils* protected and constrained particles which in majority kept their original configuration. This architecture could be interesting for optoelectronic experiments as it should offer great stability of the particles which can be optically active and work, for example, similarly to the photodetector described above. Other recent work has been dedicated to the topography of graphene suspended on nanoparticles. Vejpravova *et al.* [59] have investigated the relationship between the amount of wrinkling of the graphene layer and its Raman spectrum and have found the latter to be an accurate way to quantify the former. Osváth *et al.* have used and related different imaging techniques, atomic force microscopy, scanning tunnelling microscopy and spectroscopy to study graphene supported on gold nanoparticles [60].

After these early developments—selected in the context of this thesis, and by no means exhaustive or most representative—towards the integration of graphene into complex structures for devices, in recent years graphene has become a playing field as a new electrode for nanoelectronics. In the case of molecular electronics, a structure proposed by Wang *et al.* [35] contacts SAMs of alkanethiols (C_nS) of various lengths with a multilayer graphene top electrode to demonstrate a molecular device with a yield of 90%, which may have been the highest demonstrated for a SAM device at the time of publication in 2011. In 2018, Li *et al.* [61] reported on a device which similarly contacted a SAM of biphenyl-4,4'-dithiol, where interestingly, the contacting efficiency ranged between 10 and 100% of the molecules encapsulated, compared with the typical 10^{-4} often cited in the literature [39]. In 2016, single-layer graphene (SLG) was shown to be an appropriate substrate for alkylamine SAMs [62], which suggests that some of the common structures in the field relying e.g. on thiol-terminated molecules forming SAMs on Au, are transferable to an SLG substrate. In 2018, Bouvron *et al.* demonstrated a structure where cobalt phthalocyanine molecules assembled on a back-gated graphene substrate could be gated through the graphene while contacted by an STM tip, in what may constitute the first step towards a vertical molecular transistor [63]. SLG electrodes were also used to sandwich superlattices of CdSe nanocrystals to demonstrate a type of conduction mainly operated by the nanocrystals' ligands [64]. In the single-object approach, graphene was also used to fabricate nanogaps through electroburning. Using graphene patterned in a bow-tie shape, running a high current through it causes the bow-tie's constriction to heat up and burn a nano-size gap at this constriction [65]. This was used to investigate thermoelectricity in single-molecule junctions [29]. Additionally, in 2018, mechanically controlled graphene break junctions were used to investigate quantum

interference in transport [66]. In the past two years, single-molecule measurements with an actuated tip have also been adapted for graphene electrodes, tip and substrate [17, 67]. In the past few years, the number of publications involving graphene in the field of molecular-scale transport has multiplied, which should in turn establish it as a standard material in the field.

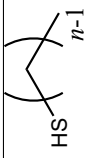

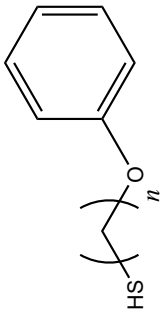
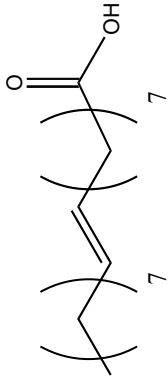
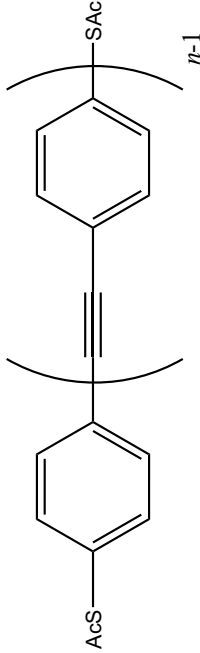
Name	Formula	Shorthand	Structure
Alkanethiol	$\text{CH}_3\text{-(CH}_2\text{)}_{n-1}\text{-SH}$	C_nS	
Alkanedithiol	$\text{HS-(CH}_2\text{)}_n\text{-SH}$	C_nS_2	
	$\text{C}_6\text{H}_5\text{-O-(CH}_2\text{)}_n\text{-SH}$	BOC_nS	
Oleic acid	$\text{CH}_3\text{-(CH}_2\text{)}_7\text{CH=CH(CH}_2\text{)}_7\text{-COOH}$	OA	
Oligo(phenylene-ethynylene)dithiol	$\text{HS-C}_6\text{H}_4\text{-(C}\equiv\text{C-C}_6\text{H}_4\text{-C}\equiv\text{C)}_{n-1}\text{-SH}$	OPE_n	

Table 1.1 Inventory of most important molecules and molecular structures used and discussed in this dissertation, with formula and shorthand.

Chapter 2

Single-electron tunnelling in self-assembled monolayers of quantum dots

2.1 Introduction

Single-electron tunnelling is a form of electrical conduction where the current is filtered down to single charge carriers travelling through a structure at a time. It can be obtained in particular systems where a charge island, a quantum dot, is placed between a source and a drain and current is run through in conditions where the quantum dot's charging energy is not compensated by thermal fluctuations. This type of transport has been predicted to deliver a new generation of electronic devices relying on single-electron signals, with applications in e.g. sensitive detection or memory. However, challenges in developing devices reliably delivering this kind of transport with a high yield has kept it from transition from research topic to commercial technology. In this chapter we study this type of transport and its theoretical formalism. We report on a device which contacts self-assembled monolayers of quantum dots in large-area junctions using graphene to obtain single-electron transport. We discuss these devices' different properties. Further devices derived from this project are presented with a discussion of possible extensions of the system.

Contributions

The standard device presented in this chapter was initially designed by J.M. Fruhman with C.J.B. Ford's help. A first batch was fabricated by him, and I shadowed and assisted the fabrication of following batches of devices. These devices were measured electrically by

myself, J.M. Fruhman, L.F.L. Eyre, and L. Skoric. I measured devices on the set-up with temperature control. The work on self-assembly characterisation was done by myself with help from X. Wang and B.J. Robinson. The colloidal quantum dots were grown by B. Ehrler; he and M. Boehm helped with self-assembly. Single-layer graphene (SLG) growth and transfer were done by U. Sassi and assistance on graphene processing was provided by him, D. De Fazio and A.C. Ferrari. Some of the AFM imaging of quantum-dot self-assembled monolayers was done by me with help from X. Wang. The data analysis was planned by me, J.M. Fruhman and C.J.B. Ford, where I wrote all MATLAB tools for compiling and analysing the junctions' characteristics, with input from J.M. Fruhman, C.J.B. Ford, and P. Leung. The data interpretation was by me, J.M. Fruhman and C.J.B. Ford. A scientific publication is in preparation [10]. The simulations presented in this chapter are made by myself, which includes a discussion of negative differential resistance being studied at the time of writing. In the top-gated devices presented at the end of the chapter, a first attempt was fabricated by J.M. Fruhman and measured by me, L.F.L. Eyre and J.M. Fruhman, and a second attempt was made by myself where I fabricated the device with assistance from specified collaborators for individual processes and measured it. The work on nanogap devices comes from collaborations I set up, in which the collaborators, Y. Majima and J.A. Mol sent me devices, and I developed self-assembly processes for our structures.

2.2 Background

2.2.1 Nanocrystals and quantum dots

In the broad sense a nanoparticle is a solid-state system of nanometric size in all three dimensions. Its small size confines electrons and quasiparticles in a restricted, effectively zero-dimensional (0D) space. This makes their atomic and electronic structure very different from their bulk counterpart, i.e. the same chemical assembly at larger volume in all three dimensions. At such small scales their electronic, optical and magnetic properties become highly dependent on the size of these particles or the extent of this confinement [68].

The use of nanoparticle colloids dates from ancient times [68]: colloidal glass dyes were reported in late Roman artefacts in the 4th century AD [69]. Nanoparticles were found as a constituent of a paint used for pottery and murals by Mayans in the 7th century AD, the Mayan blue [70]. Their physical understanding and indeed study, however, came only centuries later. It is often quoted that M. Faraday worked with metal colloids and understood the nature of colloids as solutions of fine particles [71]. G. Mie and R. Gans proposed in the early 20th century a theoretical explanation of optical properties and particle-size dependence

of Au and Ag colloids based on absorption experiments [72–74]. In 1937, H. Fröhlich suggested that at that size and at sufficiently low temperature, the electronic properties of such particles would differ from the bulk counterpart of the same material by a *sharpening* of the electronic spectrum [75, 68]. Particularly relevant to this dissertation, in the 1950s it became possible to deposit nanometric droplets of Au on films and observe charging effects [76]. Subsequent developments in microfabrication and nanofabrication has made it possible to integrate nanocrystals into devices and reveal a great potential for a variety of applications such as solar-energy harvesting [77], diodes [78], bio-detection and labelling [79]. Of particular interest to us is the integration of nanocrystals as 0D islands into electronic circuits [80].

A few words about terminology, in order to prevent possible confusion: in the experimental part of this thesis, the terms *nanocrystal* and *quantum dot* may be used interchangeably. These, however, are not equivalent in all contexts. ‘Nanocrystal’ typically refers to a nanosize crystal, chemically and crystallographically speaking, whereas ‘quantum dot’ refers to an object which physically, electronically and optically, behaves in a way that approximates it to a system constrained in all three dimensions. In our project, the latter is the utility of the former. For example, the ‘nanocrystal structure’ would more readily refer to the crystal structure and element content of the object, whereas the ‘quantum-dot structure’ is more likely to refer to the electronic structure of the object. Objects other than a nanocrystal can behave as quantum dots, e.g. certain molecules or atoms in particular arrangements. The following section explains the correlation between the nanocrystal structure and the quantum-dot properties.

2.2.2 Electronic structure of semiconductor nanocrystals

The electronic properties of the lattice of a bulk crystal are appropriately described by its band structure, the dispersion relation of its reciprocal lattice. Such a band structure, that of lead sulphide, PbS, is shown in Fig. 2.1. One classifies these crystals according to the location of the Fermi energy with respect to these bands and the energy difference between the edges of these bands. The Fermi energy determines the band occupation within a band in the limit of zero temperature. If a band is partly occupied, the crystal will behave as a metal, as electrons can fill states in the band with negligible energy cost. The Fermi energy lying between two bands means that at absolute zero, one of the bands is fully occupied whilst the other is empty. This defines a semiconductor or an insulator. A semiconductor or an insulator is defined by its band-gap energy E_g , i.e. the energy difference between the edge E_c of its lowest unoccupied band (the conduction band) and E_v that of its highest fully occupied band (the valence band), such that $E_g = E_c - E_v$. Conduction is then achieved by introducing

electrons into the conduction band (or holes to the valence band) and the band-gap energy represents the energy cost associated with this process. A photonic stimulation of energy $\hbar\omega \geq E_g$ results in the promotion of an electron to the conduction band and the creation of a hole in the valence band. These form a bound hydrogen-like system, the exciton, which, like hydrogen, can be characterised by a most probable distance between them, the exciton Bohr radius given by [81, 82]

$$a_B^* = 4\pi\epsilon_0 \frac{\epsilon\hbar^2}{\mu_{eh}e^2}, \quad (2.1)$$

where ϵ is the dielectric constant of the medium, $\mu_{eh} = [m_e^{*-1} + m_h^{*-1}]^{-1}$ is the reduced effective mass of the exciton and other symbols have their usual meaning. This quantity along with the effective masses and dielectric constants are characteristics of the lattice. The value of this band-gap energy determines whether the material is a semiconductor or an insulator; as a rule of thumb, a material would be a semiconductor if its band-gap energy is similar or below $50k_B T \sim 1.3 \text{ eV}$, where k_B is the Boltzmann constant, and T is room temperature. On the other hand, if the band-gap energy is significantly greater than this energy scale, the material is an insulator, where conduction and exciton formation demand a larger energy cost and do not occur in standard conditions.

However, this picture is somewhat complicated if the lattice is so small that it is comparable with, or smaller than, the length scales of electronic energy transfers [81, 82]. One such relevant energy scale is the de Broglie wavelength λ_e of electrons in the system. The thermal de Broglie wavelength in a crystal is given by [83]:

$$\lambda_e = \sqrt{\frac{2\pi\hbar^2}{m_e^*k_B T}}, \quad (2.2)$$

where m_e^* is the effective mass of an electron in the crystal. Applying this to a PbS lattice, where the electron's effective mass is $0.085m_e$ [84], yields $\lambda_e = 15 \text{ nm}$ at room temperature $k_B T = 25.26 \text{ meV}$, and $\lambda_e = 125 \text{ nm}$ at $T = 4.2 \text{ K}$ (Helium-4 boiling temperature at 1atm). One can note that this is two to three orders of magnitude higher than the lattice constant a_L of PbS at $T = 300 \text{ K}$ for which $a_L = 0.5936 \text{ nm}$ [85]. It is therefore possible to confine electrons similarly to an atom and its orbitals even within a polyatomic crystal. This confinement implies drastic changes in the electronic properties of such crystals. One can consider different regimes in this confinement determined with respect to the exciton Bohr radius. If a^* is the measure of this confinement, the case where $a^* < a_B^*$ is called strong confinement. In this configuration, an exciton is appropriately described in the crystal by a spherical potential well, and its energy spectrum is quantised. If $a^* > a_B^*$, one speaks of weak confinement, there is no bound exciton state; the electron and hole spectra are treated independently. In the

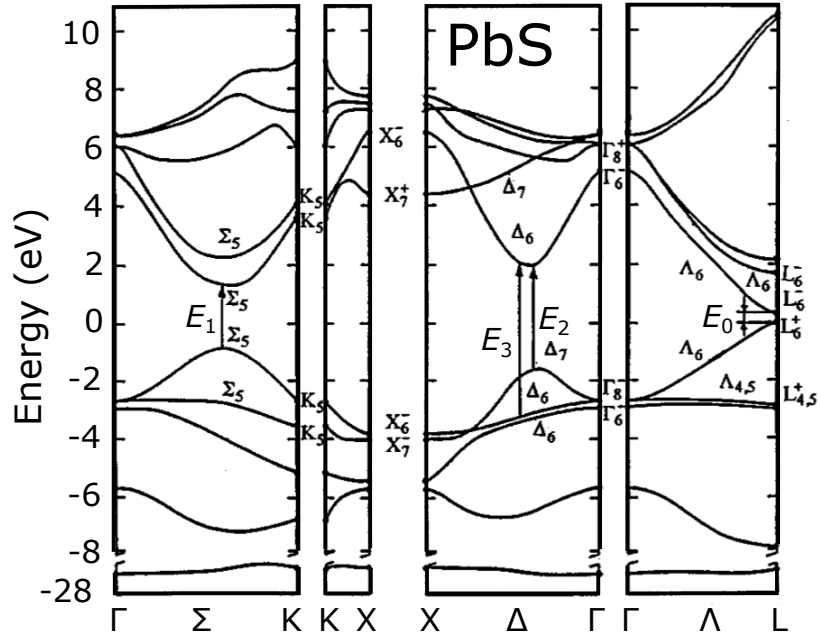


Fig. 2.1 Band structure of bulk lead sulphide, PbS, as calculated by S.E. Kohn *et al.* [1], adapted from Ref. [2]. E_i ($i = \{0, 1, 2, 3\}$) are the band gaps of the structure, E_0 being the primary and a direct band gap.

spherical well approximation, this spectrum is described as:

$$E_{nl}^e = E_g + \frac{\hbar^2 \chi_{nl}^2}{2m_e^* a^{*2}}, \quad (2.3)$$

$$E_{nl}^h = -\frac{\hbar^2 \chi_{nl}^2}{2m_h^* a^{*2}} \quad (2.4)$$

for electrons and holes respectively, taking E_v as the zero-point of this scale and where χ_{nl} is the n^{th} root of the spherical Bessel function of order l [82]. The electronic spectrum is then quantised as a result of this confinement; these discrete states liken nanocrystals to molecules. Importantly the extent of this confinement has a direct influence on the energy spectrum of the dot [81, 82]. Fig. 2.2 shows the size-dependence of the density of states in PbS clusters as well as the band-gap energy. One sees in the former that the fewer atoms there are, the sharper the energy density becomes with delta-like peaks. Each individual orbital level can then be occupied by up to two electrons or holes (accounting for spin degeneracy). In the case of PbS nanocrystals, further calculations and discussion can be found in Kang and Wise [86]. Importantly they find that the rocksalt crystal structure of PbS quantum dots

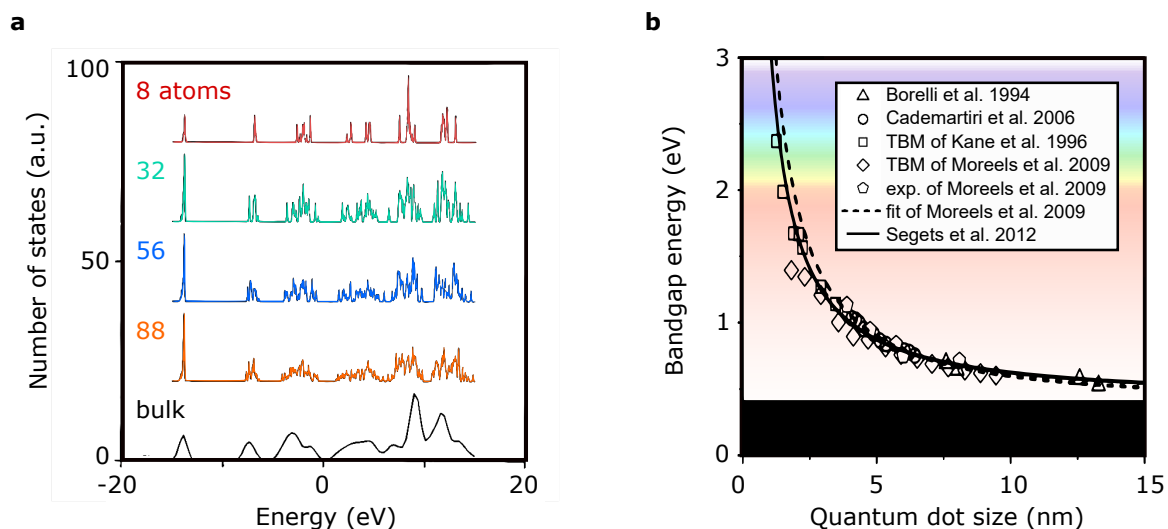


Fig. 2.2 Size-dependence of PbS electronic structure. **a**, calculated density of states at $T = 4.2K$ for PbS clusters of 8, 32, 56, 88 atoms, and bulk PbS; adapted from [3]. **b**, bandgap energy as a function of QD size, as obtained from various experimental measurements and theoretical models [4–8], adapted from [8].

has four equivalent L points in their Brillouin zone, resulting in the first excited levels $1S_e$ and $1S_h$ (which in molecular terms, correspond to the LUMO and the HOMO respectively) to be eightfold degenerate (with spin accounted for) [87]. The Zeeman splitting of energy levels under the influence of a magnetic field also exists in nanocrystals. This effect is also a function of confinement: the g factors which define the magnitude of the splitting depend on nanocrystal size [88]. Nanocrystal growth methods offer a tunability of the nanocrystal size and thus of their electronic and optical spectrum.

2.2.3 Single-electron tunnelling devices

It was realised as early as the late 1960s that confining electrons in small volumes at low temperature, such that the energy required to add an electron to the system is largely greater than the thermal energy of the system, would lead to a feedback effect where the Coulomb repulsion between the electrons confined would make the addition of each electron significant enough to control the number of electrons confined discretely [89–92]. These considerations were inspired by preceding experiments which involved small metallic grains, the first of which is commonly attributed to Gorter in 1951 [90, 76]. The study of single-electron phenomena became an active field of research that went in parallel with the development of nano-fabrication techniques to reduce the scale and increase the precision of devices.

In the mid-1980s, the availability of electron-beam lithography enabled the fabrication of well-defined features, dots and gaps down to the order of 20 nm [93], comparable to the de Broglie wavelength of conduction electrons in semiconducting media [94]. This has led research on single-electron transport and quantum-mechanical effects in the single-electron regime to gain exceptional momentum in the late 1980s and early 1990s with reviews by M.H. Devoret [95], U. Meirav and E.B. Foxman [94]. As efforts are being made to reach the limit of size reduction in electronics, this otherwise unavailable type of transport has been expected to deliver a new generation of devices with single-electron sensitivity for sensors, data storage, and logic operations [95]. However, the scalable and reliable device integration of this type of transport has proven challenging, to the extent that it is still mainly being investigated in laboratories and has not entered industrial applications.

2.3 Theory

2.3.1 Single-electron tunnelling

Classical Coulomb blockade

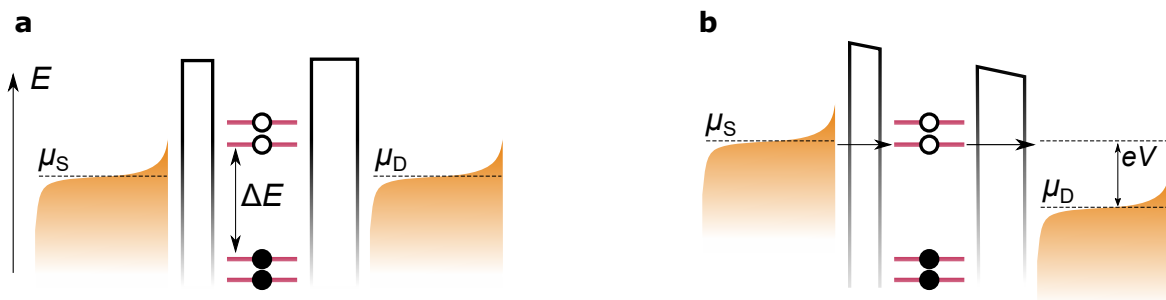


Fig. 2.3 Diagram of a Coulomb blockade configuration. The central island is a dot with a discrete energy spectrum. Two energy scales operate in parallel to determine the transport, i.e. the charging energy, and, in the quantum case, the discretised density of states in the dot. These determine an energy difference ΔE , which represents the energy needed to change the charge occupancy in the dot. **a**, system at zero bias. **b**, system at non-zero source-drain voltage, such that an energy level is available for tunnelling which results in a single-electron tunnelling current.

Single-charge tunnelling relies on a basic set-up which can be described as follows. One considers two metallic electrodes, a *source* and a *drain*, separated by an insulating gap in the middle of which is a third metallic electrode, the *island*. For completeness one can also consider the existence of a gate that one can charge to apply an adjustable electric field at the

island. Current can only flow between source and drain by going through the island. The current carriers can only travel into and out of the island by tunnelling.

Let $q = -Ne$ be the discrete charge on the island, where N is the number of electrons. On the other hand, the charge around the island, Q_G , is a continuous (non-discrete) quantity, as it corresponds to a rearrangement of the electron gas in a positive ion background [96]. It can be adjusted continuously through a gate voltage. Thus, a non-zero net charge Δq may arise in the system, which, in equilibrium, should be less than $e/2$ in magnitude. The energy cost of a transition to a state where the dot contains N electrons is given by

$$U(N) = \frac{\Delta q(N)^2}{2C}, \quad (2.5)$$

where $\Delta q(N) = Q_G - eN$. The charging energy for different N is illustrated in Fig. 2.4. If the thermal energy is significantly lower than this cost, i.e. $U(N) \gg k_B T$, tunnelling is prevented by Coulomb repulsion; one speaks of Coulomb blockade.

There are two ways to overcome this blockade. One way is to tune potentials at source or drain by the charging energy $(e^2 + 2e\Delta q)/2C$ so as to let electrons traverse the potential barriers. If an electron is thus allowed to tunnel into the dot from an electrode and out of the dot into the other electrode by a potential difference, this results in a finite current. This corresponds to a vertical displacement in the energy diagram of Fig. 2.4.a. The dependence of this current on the charge on the dot results in characteristic step-like current-to-voltage curves. A second way to allow tunnelling to occur is by the means of a gate to change the charge around the island so as to make this charging energy cancel, i.e. by having $\Delta q = \pm e/2$ which will change the equilibrium charge Ne on the dot by one elementary charge unit. In this case the surrounding charge can be tuned by applying a voltage V_G on the gate such that $Q_G = C_G V_G$, where C_G is the capacitance of the dot to the gate. Differential conductance as a function of this gate voltage will show periodic sharp peaks occurring whenever $\Delta q = \pm e/2$. This transition corresponds to a horizontal displacement in 2.4.a.

Interestingly the behaviour observed when applying a source-drain voltage is dependent on the symmetry of the system. If the tunnelling barriers on both sides of the dot have similar resistance (or tunnelling rate), charges will transit in and out of the dot in the timescale of this tunnelling rate. Coulomb blockade will be seen as the suppression of current for a voltage that does not match the dot's charging energy. However, if the two barriers are asymmetric, i.e. the tunnelling rate of one barrier is lower than that of the other, this more resistive barrier will provide a bottleneck for this charge transfer. This means that the average charge occupancy of the dot will be appropriately described by the multiple of the charging energy provided by the voltage bias. This results in a succession of plateaux and steps in the

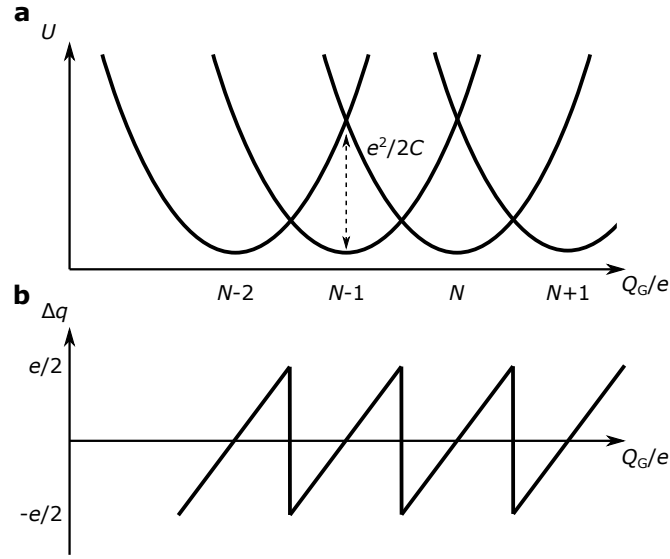


Fig. 2.4 Schematic of the charge occupancy of a quantum dot as a function of external charge. **a**, charging energy $U(N)$ for different values of N of the dot as a function of external charge Q_G . **b**, net charge q of a dot as a function of external charge. Adapted from [9].

I - V curves, a phenomenon often termed Coulomb staircase, after the staircase shape of the resulting I - V curve.

This system and single-electron transport are illustrated in Fig. 2.3. These diagrams of energy states as a function of position are commonly used to describe transport in systems such as this one. However in the case of SET, these can be particularly misleading as, because in this regime the location of single electrons affects the whole energy structure, these diagrams only represent snapshots in the cycle of transitions leading to current.

Quantum Coulomb blockade

If one replaces the metallic dot by a small semiconductor, the strong confinement leads the single energy spectrum to become quantised in states ϵ_i reminiscent of those that exist in molecules. These can no longer be neglected compared to the Coulomb energy. Such an island, now a quantum dot, containing N electrons has a total energy:

$$U(N) = \sum_{i=1}^N \epsilon_i + \frac{(-eN + C_G V_G)^2}{2C}. \quad (2.6)$$

The chemical potential in the dot is then:

$$\mu_{\text{dot}}(N) = U(N) - U(N-1) = \epsilon_N + \frac{(N-1/2)e^2}{C} - e \frac{C_G}{C} V_G. \quad (2.7)$$

When the dot gains an electron, for a constant gate voltage, this chemical potential changes by:

$$\mu_{\text{dot}}(N+1) - \mu_{\text{dot}}(N) = \epsilon_{N+1} - \epsilon_N + \frac{e^2}{C}. \quad (2.8)$$

One then notes that two energy scales contribute to transitions in the charge occupation state and one must distinguish the energy levels of the island (the excitation spectrum of the quantum dot) and the charge occupancy levels which, on top of the former, take the Coulomb energy into account and can be referred to as the addition spectrum [94]. The latter can be experimentally investigated with the two variable parameters at hand, voltage across the dot, source-drain voltage, $V_{\text{SD}} = V_{\text{source}} - V_{\text{drain}}$, and voltage applied to the gate, which tunes the equilibrium charge on the dot, V_G . Measuring current or conductance across the dot as a function of these gives characteristic patterns called Coulomb diamonds [9, 97] which are described in Fig. 2.5. As they give an insight into the energy levels of the semiconductor dot and its decoupling from the environment, this type of measurement can be regarded as electronic spectroscopy.

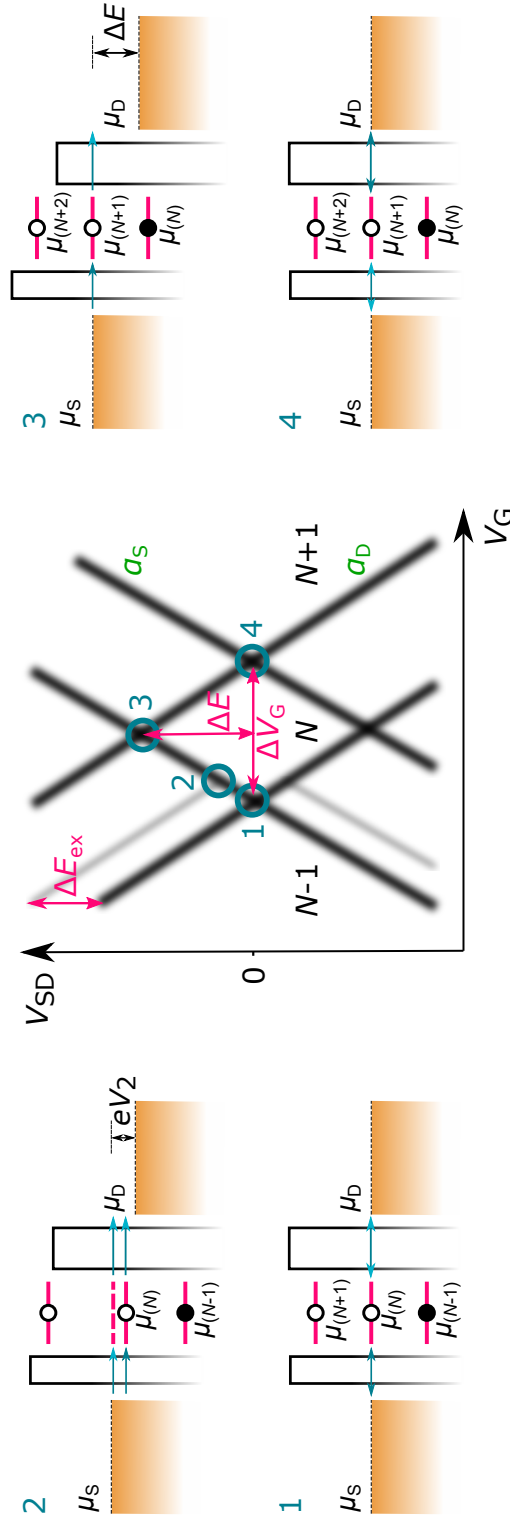


Fig. 2.5 Schematic of a Coulomb diamond. The central plot shows differential conductance as a function of source-drain voltage V_{SD} and gate voltage V_G , where the gate tunes the electrochemical potential inside the dot without affecting the leads. The peaks in conductance draw diamond-like structure in the V_{SD} - V_G space. Schematics 1-4 illustrate the transition points in the Coulomb diamond from an energy point of view, where the horizontal axis is position and vertical axis is energy. Cyan arrows show the allowed electron transfers. The distances between these peaks are revealing of the energy structure and capacitance of the dot. The annotated energy differences can be expressed as $\Delta E = \mu_d(N+1) - \mu_d(N) = \epsilon_{N+1} - \epsilon_N + e^2/C$, $\Delta E_{ex} = \epsilon_{N+1} - \epsilon_N$, whilst the gradients of the lines in the planes reveal the individual capacitances between the terminals, i.e. $\alpha_S = -C_G/C_D$, $\alpha_D = C_G/C_S$.

Sequential tunnelling model

Aside from experimental considerations, the non-linearity of the system has attracted the attention of theorists and been the focus of numerical studies since the 1970s. The establishment of such framework is generally attributed to Kulik and Shekhter in 1975 [92]. Their paper however makes the assumption that the energy level separation is negligible compared to the thermal energy of the system—while the latter is still much less than the charging energy necessary for the discretisation of current in the dot, i.e. $\epsilon_{i+1} - \epsilon_i \ll k_B T \ll e^2/C$, and the energy spectrum is treated as a continuum as is a valid approximation in metals. The Third International Conference on Superconducting Devices in 1985 saw two developments of this theory [96] by D.V. Averin and K.K. Likharev [98, 99] and Ben-Jacob *et al.* [100, 101] who considered single-charge tunnelling for Cooper pairs in superconducting media. G.-L. Ingold and Yu. V. Nazarov concerned themselves with the introduction of single-charge tunnelling in metallic dots into more complex electrical circuits [102] such as multijunctions and AC circuits. Subsequent theorists have worked for more refined predictions taking quantum-mechanical effects into account. C.W.J. Beenakker [103] goes beyond Kulik and Shekhter's approximation by considering a discrete spectrum of energy levels in a semiconductor island and treating electron transfer via these levels using rate equations. Bonet *et al.* [104] have also concerned themselves, using a similar master equation approach, with step characterisation under the influence of external magnetic field and different assumptions in relaxation in the dot. This chapter follows Bassett's derivation of the problem [97] to explain the rate-equation approach and derive the master equation. Conservation of energy in a transfer allows one to write the following equation describing a tunnelling event of an electron in state p in the quantum dot. The complete system can be described by a Hamiltonian of three terms

$$\hat{\mathcal{H}} = \hat{\mathcal{H}}_{\text{dot}} + \hat{\mathcal{H}}_{\text{res}} + \hat{\mathcal{H}}_{\text{tun}}, \quad (2.9)$$

which respectively represent the dot, the reservoirs and the tunnelling events that occur between the three. By defining states on the dot as $|s\rangle = |\{n_{l\sigma}\}\rangle$ which accounts for all electrons, indexed n in this notation, on the dot as well as their configuration within the energy levels of indices l, σ (respectively orbital and spin quantum numbers) of this dot, the first Hamiltonian can be written in second-quantised form as

$$\hat{\mathcal{H}}_{\text{dot}} = \sum_s E_s |s\rangle \langle s|, \quad (2.10)$$

where E_s is then the eigenenergy of the dot in state s , which as follows from Eq. 2.6 can be written as

$$E_s = \sum_{l\sigma} \epsilon_{l\sigma} n_{l\sigma} + \frac{(-eN + C_G V_G)^2}{2C}, \quad (2.11)$$

where we have now chosen to name the quantum numbers associated with the energy levels of the semiconductor nanostructure, l for the orbital quantum number and σ for the spin, and where $n_i = \{0, 1\}$ is the occupation number of energy level i .

The Hamiltonian describing the reservoirs is as follows:

$$\hat{\mathcal{H}}_{\text{res}} = \sum_{r=\{S,D\}} \hat{\mathcal{H}}_r = \sum_{r=\{S,D\}} \left[\sum_{k\sigma} \epsilon_{k\sigma r} \hat{a}_{k\sigma r}^\dagger \hat{a}_{k\sigma r} + \mu_r \hat{n}_r \right], \quad (2.12)$$

and the Hamiltonian that accounts for tunnelling between the leads and the dot is

$$\hat{\mathcal{H}}_{\text{tun}} = \sum_{r=\{S,D\}} \hat{\mathcal{H}}_r = \sum_{r=\{S,D\}} \left[\sum_{kl\sigma} T_{kl\sigma}^r \hat{a}_{k\sigma r}^\dagger \hat{a}_{l\sigma} + \text{H.c.} \right], \quad (2.13)$$

where $\hat{a}_{k\sigma r}$ is the annihilation operator for a particle in the lead state $|k\sigma\rangle_r$, $\hat{a}_{l\sigma}$ is the annihilation operator for a particle in the dot state $|l\sigma\rangle$, $\hat{n}_r = \sum_{k\sigma} \hat{a}_{k\sigma r}^\dagger \hat{a}_{k\sigma r}$ is the number operator of lead r , $\mu_r = -eV_r$ is the chemical potential in the lead. This last parameter is experimentally adjustable as the voltage bias across the island.

From these expressions, within the approximation of low quantum fluctuations, it is possible to apply Fermi's golden rule to describe tunnelling rate between the dot and the leads

$$W_{s'\chi' \rightarrow s\chi}^\pm \simeq \frac{2\pi}{\hbar} |\langle \chi s | \hat{\mathcal{H}}_{\text{tun}} | \chi' s' \rangle|^2 \delta(E_s - E_{s'} + E_\chi - E_{\chi'} \pm \mu_r). \quad (2.14)$$

Summing over contributions from all reservoir states can be shown to reduce to two tunnelling rates, one from reservoir r into the dot and the other into reservoir r out of the dot; respectively:

$$\gamma_{r,s' \rightarrow s}^+ = \sum_{l'\sigma} \Gamma_{l'\sigma}^r(E_s - E_{s'}) \langle s | \hat{a}_{l\sigma}^\dagger | s' \rangle \langle s' | \hat{a}_{l'\sigma} | s \rangle f_r(E_s - E_{s'}), \quad (2.15)$$

$$\gamma_{r,s' \rightarrow s}^- = \sum_{l'\sigma} \Gamma_{l'\sigma}^r(E_{s'} - E_s) \langle s | \hat{a}_{l\sigma} | s' \rangle \langle s' | \hat{a}_{l'\sigma}^\dagger | s \rangle [1 - f_r(E_{s'} - E_s)], \quad (2.16)$$

where $\hbar \Gamma_{l'\sigma}^r(E) = 2\pi \sum_k T_{kl\sigma}^r T_{kl'\sigma}^{r*} \delta(E - \epsilon_{k\sigma r})$ and $f_r(E) = 1/[1 + \exp((E - \mu_r)/k_B T)]$ is the Fermi distribution function. One can now write the total transition rate between two states of

the dot:

$$\gamma_{s's} = \sum_{r=\{S,D\}} (\gamma_{r,s' \rightarrow s}^+ + \gamma_{r,s' \rightarrow s}^-). \quad (2.17)$$

Considering the probability $P(s)$ of the system being in state s and two conditions for consistency allow one to write the problem as a master equation. Firstly, the transition rate into a state s_i must equal the transition rate out of it; in mathematical form:

$$\sum_{s'} [P(s')\gamma_{s's} - P(s)\gamma_{ss'}] = 0. \quad (2.18)$$

Secondly probabilities must be normalised, i.e. $\sum_s P(s) = 1$. Indexing these conditions in a matrix yields the master equation for state transitions in the dot:

$$\begin{pmatrix} \sum_i \gamma_{s_i s_1} & -\gamma_{s_1 s_2} & \cdots & -\gamma_{s_1 s_n} \\ -\gamma_{s_2 s_1} & \sum_i \gamma_{s_i s_2} & \cdots & -\gamma_{s_2 s_n} \\ \vdots & \vdots & \ddots & \vdots \\ -\gamma_{s_n s_1} & -\gamma_{s_n s_2} & \cdots & \sum_i \gamma_{s_i s_n} \\ 1 & 1 & \cdots & 1 \end{pmatrix} \begin{pmatrix} P(s_1) \\ P(s_2) \\ \vdots \\ P(s_n) \end{pmatrix} = \begin{pmatrix} 0 \\ 0 \\ \vdots \\ 0 \\ 1 \end{pmatrix} \quad (2.19)$$

This matrix equation makes it possible to find the occupancy probabilities. From these probabilities, one can finally deduce the current going through the leads as:

$$I_S = I_D \equiv I = -e \sum_{s_i s_j} [\gamma_{r,s_j \rightarrow s_i}^+ P(s_j) - \gamma_{r,s_i \rightarrow s_j}^- P(s_i)]. \quad (2.20)$$

This general approach serves as the basis for most theoretical simulations of Coulomb blockade transport. Approximations can be made to neglect matrix elements such as instant relaxation into the ground state. Extensions of the problem treating Zeeman splitting of the energy levels or heat-induced transfers are possible. It can be noted that this approach generally neglects some realities of experiments such as trapped charge in leads or surface states of the dots which effectively gate the island and are difficult to quantify. It is also generally assumed that electrostatically gating the dot displaces the chemical potentials inside it rather than a more realistic deformation of the potential well and barriers—and even the leads as in some experimental set-ups.

2.3.2 Negative differential resistance

Until now we have considered the two leads as metals, or well approximated as metals. In our system, where graphene is one of the electrodes, this approximation will only be valid in

particular conditions. Graphene is a semimetal, i.e. a material with a very small overlap or, in this case, no overlap but also no gap between its valence and conduction bands. Its density of states (DOS) follows the shape of Dirac cones. In its energy structure, graphene has a lower density of states around its Dirac cone than farther away from it, and depends linearly on this difference. This is schematically represented in Fig. 2.16, in the context of the system studied in the devices.

In an appropriate alignment of the Dirac cone with the dot in a source-dot-drain system, i.e. for an appropriate doping of the graphene, this arrangement can lead to negative differential resistance (NDR). NDR is a type of conduction where locally current decreases as the voltage bias is increased and is desirable for several applications. Components using NDR properties include diodes, such as impact ionization avalanche transit-time (IMPATT) diodes, or Gunn diodes. These diodes are commonly used in high-frequency oscillators, in the GHz range and beyond, where the NDR is used to cancel internal loss resistance in resonators, to limit damping of the oscillation [105]. Other applications of NDR devices include memory and logic devices, where NDR can enable the existence of several distinct states that can be used for memory and logic operations that go beyond binary systems [106, 107].

A SLG electrode can be simulated using the Landauer formalism, as described in Chapter 1, by making the tunnelling rate between the junction and the SLG lead a function of SLG's particular density of states. The rate can then be expressed as [61]:

$$\Gamma_D(E) = \Gamma_{D0} + \alpha |E - E_{\text{Dirac}}|, \quad (2.21)$$

assuming the SLG lead is the drain in the junction's disposition, and where Γ_{D0} is the tunnelling rate at the SLG electrode's Dirac point, and α is a coefficient of the linear increase in the SLG's DOS. The value of E_{Dirac} can then be given as

$$E_{\text{Dirac}} = E_{\text{Dirac}0} - \frac{q}{2} V_{\text{SD}}, \quad (2.22)$$

where γ_{SLG} is a coefficient that determines the effective SLG's doping applied by voltage on the drain. Introducing this energy-dependent rate into the transmission function in the Landauer formalism yields the transport that can be obtained using an SLG electrode. This is the basis of the simulations shown in Fig. 2.6.

Graphene as an electrode in such junctions then offers a possible route for obtaining NDR devices in nanoelectronic junctions, which may be useful considering the efforts to turn SLG into a viable constituent of electronic technology. Graphene however, due to its 2D nature, which makes it very sensitive to its environment and limits reproducibility, and the lack of an actual band-gap which would make the NDR mechanism more pronounced and demand

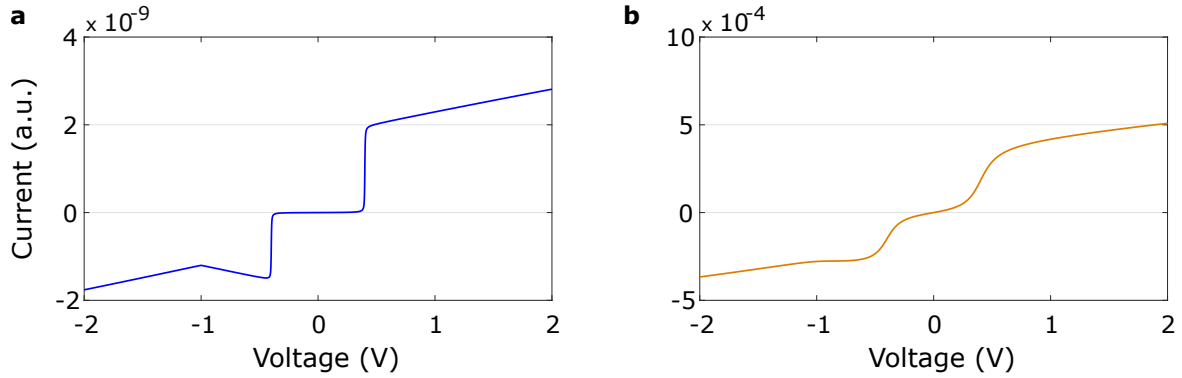


Fig. 2.6 Simulations of transport in metal-dot-graphene junctions. **a**, in a weakly coupled dot, the energy levels *scan* the graphene's DOS where, in an appropriate alignment of the levels with the Dirac cone leads to NDR. **b**, simulation in a similar system where the dot is more strongly coupled to the electrodes, leading to Lorentzian broadening, which effaces the current blockade and the minimum in the graphene's DOS.

Fig. 2.6	ϵ_0	temperature T	Dirac point	Γ_1	Γ_{r0}	α
a	-0.2 eV	4.2 K	300 meV	10^{-6} meV	10^{-7} meV	10^{-7}
b	-0.2 eV	4.2 K	300 meV	10^{-3} meV	10^{-3} meV	10^{-3}

Table 2.1 Parameters of Landauer model shown in Fig. 2.6. .

less critical conditions in terms of electrical coupling in the junction, may not be the best candidate compared to 2D semiconductors such as MoS₂, MoSe₂, WS₂, WSe₂, or indeed non-2D semiconductors.

Interestingly, narrowing the dimensions of graphene electrodes to constrained sizes can discretise its DOS itself and open gaps, such as to obtain interference-induced NDR as was recently shown by Caneva *et al.* [66].

2.4 Experimental procedures

2.4.1 Device design and fabrication

The device presented in this chapter consists of large-area two-terminal thin-film junctions. These junctions are a stacked structures where Au is used as a bottom electrode. These were made with optical lithography and have areas in the square-micron range. These are functionalised via a two-step SA process with a PbS QD SAM. A CVD-grown SLG sheet is deposited as a top electrode and patterned using OL and EBL leading to effective junction sizes ranging from the 100 nm² to the 10 μm² range.

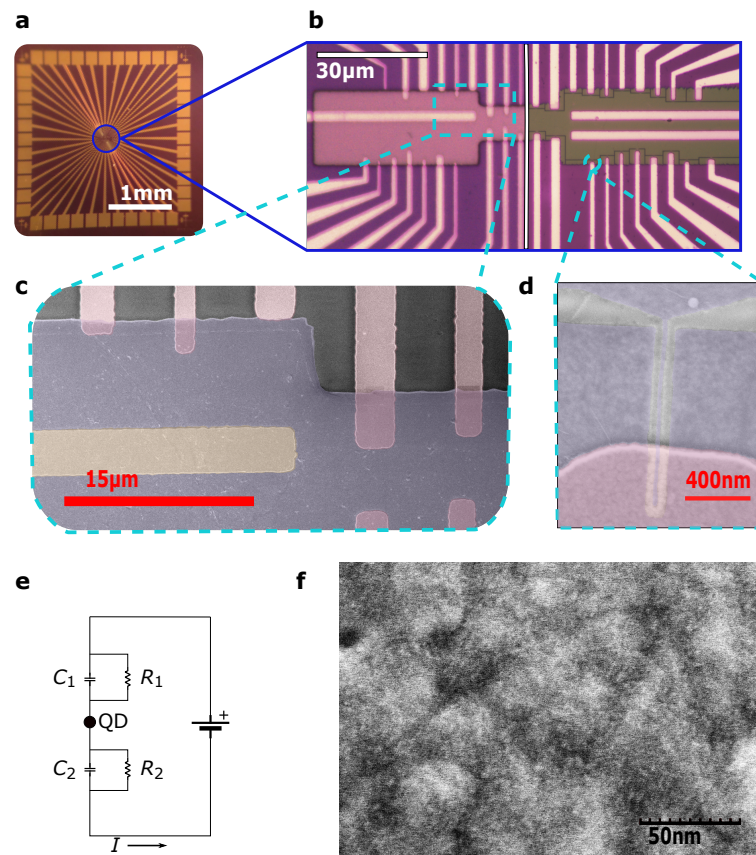


Fig. 2.7 Junction structure. **a**, photograph of a die. **b**, micrograph of junctions with left: OL device design, right: EBL device design. **c**, coloured SEM image of OL junctions where blue is SLG, pink is QD-coated Au, and yellow is bare Au. **d**, coloured SEM image of an EBL-design junction with similar colour code. **e**, electrical diagram of a junction as connected to a current source. The RC junctions represent the tunnelling barriers on each side of the QD. **f**, SEM image of a Au surface functionalised with the QD SAM.

Optical lithography

A mask for optical lithography (OL) was designed on AutoCAD by J.M. Fruhman. Details of this design are shown in Fig. 2.8. The quartz-based chrome mask was fabricated by JD Photo Data¹. On one device Au electrodes have the form of 42 fingers with horizontal thicknesses ranging from 0.8µm to 4µm and vertical thicknesses of 35nm. We showed that such horizontal resolution could be achieved, although at the limit of optical lithography, using LOR5B for an undercut and a Shipley 1805 optical resist and precise development time. 39 fingers, the vertical fingers on Fig. 2.8 bottom-left, support the junctions, whilst the

¹Photo Data Ltd, Photodata House, Knowl Piece, Hitchin, SG4 0TY, <http://jdphoto.co.uk/>

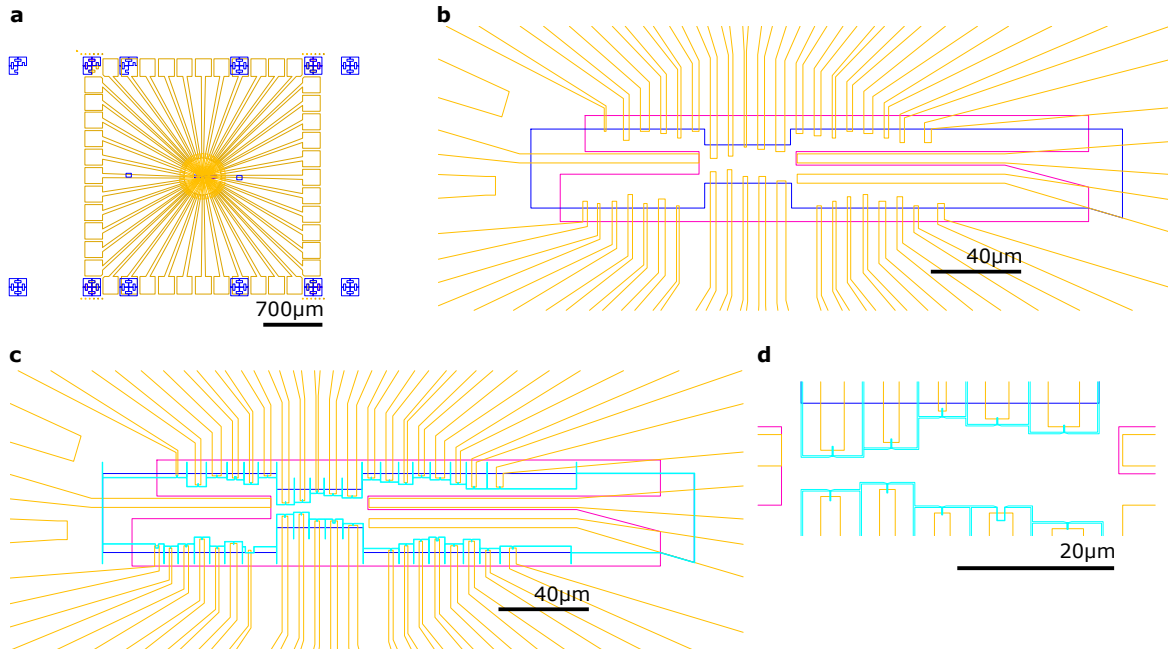


Fig. 2.8 Mask design for device fabrication. Orange/brown: pattern for evaporated Au, blue: OL pattern for SLG patterning, magenta: OL layer for selective SA, cyan: EBL pattern for SLG patterning. **a**, mask design for a single die of devices, including 39 junctions. One batch of such dice consists of an array of 6×6 dice. One die is approximately $3 \times 3 \text{ mm}^2$. At its edges, squares of thick Au are bonding pads connected to micron-sized junction in the central region of the die. **b**, detail of the die's central region. QD-decorated junctions appear as vertical Au fingers on the picture; the selective assembly determined by the OL layer (in magenta) exposes them the SA whilst protecting the fingers appearing horizontal here which are used for grounding. The SLG pattern coats the tips of all junctions, draping over the QD-decorated electrodes and in direct contact with the grounding electrodes. The overlap between the SLG layer and the QD-decorated electrodes determines the junction area. In this pattern variability in the junction size was deliberately introduced, and the junction size was of the order of the standard error on OL alignment, so as to obtain a statistical range of junction areas, including sub-micron features. **c-d**, detail of the design for EBL-defined junctions. The graphene is first etched according to the OL design, and a second step tailors trenches in the graphene to reduce the area of overlap between the graphene and the QD-decorated electrode down to areas of order $100\text{-}1000 \text{ nm}^2$. Design by JM Fruhman.

remaining three, horizontal on the figure, are directly contacted and will enable grounding of the device. These fingers show a range of lengths and widths for different active junction areas. These electrodes are evaporated onto the SiO₂/Si substrate via positive lithography [108]. A 10 nm layer of Ti is evaporated for better adhesion of Au, after which 25 nm of Au are evaporated, which is followed by a lift-off in SVC14. A similar process with a different part of the mask is used to create the Au electrodes linking the fingers to pads for electrical bonding. These arms are not as fine features, so do not require as much precision and can be thicker, i.e. typically 20 nm Ti, 50 nm Au.

Self-assembly

Once the electrodes have been evaporated, one proceeds to decorate the vertical fingers with a QD monolayer through self-assembly (SA). As this deposition needs to be selective, we again use mask OL. The design used for the deposition process is shown in Fig. 2.8. Shipley 1813 resist is spun, exposed through the mask and developed to only leave the vertical fingers exposed.

The deposition process is done in a N₂ glovebox, so as to avoid oxidation of the QDs as well as contamination. We used an N₂ glovebox in a cleanroom of the Electrical Engineering Division of the Engineering Department. Colloidal PbS quantum dots (QDs) capped with oleic acid (OA) are grown² in the OptoElectronics Group (M. Boehm, B. Ehrler) in the Cavendish Laboratory to a distribution of diameters of average 4.9 nm and standard deviation 0.8 nm (see Fig. 2.10). The devices are then immersed in solutions of 1,6-hexanedithiol (C6S2) dispersed in isopropyl alcohol (IPA) for roughly 24h³. The sulphur head-group is known to have a strong affinity with Au [37], these molecules attach in a dense monolayer on the exposed Au fingers. This is followed by an immersion in a PbS-in-octane dispersion for a further 24 h. A self-assembly process attaches the PbS QDs on to the exposed thiol head of the C6S2 to which they strongly adhere, by displacing the OA ligands from QDs, which are comparatively weakly-bonded. At the end of this immersion, a spinning process is realised to ensure only an attached monolayer of PbS QDs remains on the fingers. The resist can then be removed with acetone and IPA.

This SA process, and the characteristics of the resulting film, including its monolayer nature, has been characterised through quartz crystal microbalance (QCM) and atomic-force microscopy (AFM), as will be discussed in Sec. 2.5.1 and 2.5.1.

²See M.A. Hines and G.D. Scholes [109] for a widely cited colloidal PbS QD growth method.

³In subsequent devices, IPA has been replaced with toluene or alkane solvents. IPA was observed to partially dissolve photoresist, leaving, however, a residue, which can be seen through optical microscopy, and which should have prevented SA, and explain why this process still allowed for grounding contacts to behave as short circuits. Alkane solvents and toluene were seen to not affect photoresist.

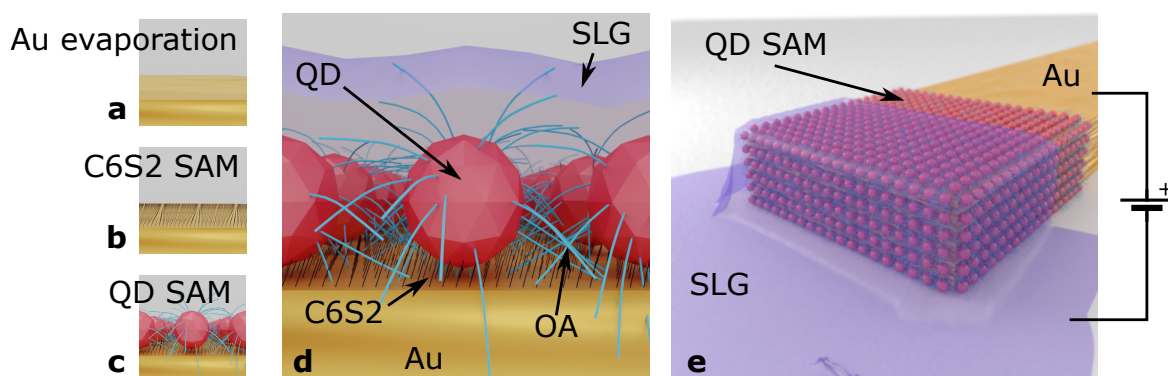


Fig. 2.9 Junction structure. **a-c**, SA steps. **d**, impression of the SA structure at the single-QD scale. ~ 5 nm-diameter QDs are attached to Au through the SAM of C6S2 linkers. The QDs have OA ligands. A sheet of CVD graphene is draped over the QD SAM. **e**, schematic of a junction. The Au finger is coated with the QD SAM and a layer of SLG coats their tips.

Graphene deposition and patterning

After the QD deposition process, the sample is taken out of the glovebox and the graphene deposition is done immediately. It is done via wet transfer. Single-layer CVD graphene is grown in the Cambridge Graphene Centre (formerly in the Electrical Engineering Division of the Engineering Department of Cambridge University), by U. Sassi, D. de Fazio, Z. Zhao, and A.C. Ferrari.

The CVD growth process is done on a copper foil; as a result of the growth, the foil is coated with SLG on both sides. Using adhesive tape, one sticks a piece of the SLG-coated copper foil (cut to the dimensions of the target chip) onto a piece of PET sheet. This allows one to spin Poly(methyl methacrylate) (PMMA) on the face of the copper foil which is not against the PET sheet. Using a spinner, a typical rate would be 4×10^3 rpm for 1 min. Using scissors, one can remove the copper foil from the PET sheet. The copper foil now has one side with exposed SLG and the other with SLG protected by a PMMA layer. The exposed SLG face is then etched away by oxygen plasma, in a reactive-ion etching system or an RF asher. For removal of SLG a typical recipe would be 20 W for 20 s in the RIE, or 10 W for 30 s in the RF asher. Following this process, the SLG is only on one side of the copper foil and protected by a PMMA layer. Following this the foil is dipped below the surface of an etchant with the PMMA facing up. The aqueous etchant, hydrochloric acid or ammonium persulfate (APS) will keep the structure at its surface due to the hydrophobicity of PMMA and will etch away the copper until there is only PMMA on SLG left at the surface. With APS a typical concentration is 2 g for 150 mL of DI water, which typically etches the copper foil in 12 to 24 h. Wet transfer consists in *fishing* the floating PMMA-coated graphene from

underneath with the device, graphene facing down. A successful transfer should cover a whole sample (6×6 devices) and avoid ripples on the graphene layer. Following this, a baking process can be realised to dry the samples.

The superficial PMMA layer is then dissolved in acetone, exposing the graphene. Patterning of this graphene layer is done by optical lithography. Shipley 1805 optical resist is spun on the sample and exposed through the appropriate mask feature (blue lines in Fig. 2.8), which allows us to remove the resist layer everywhere but above the electrode area. The etch is done by RIE, in which the samples are bombarded vertically with oxygen plasma in a vacuum chamber [110]. An exposure time was calibrated so as to etch the exposed graphene whilst keeping the resist-covered areas—20 s at 20 W. After the graphene is patterned, it is possible to develop the remaining resist, although results suggest that leaving it on increases their shelf life. At this point the basic device is made. The junctions and the graphene electrode have a range of overlap randomised by the error ($\pm 2 \mu\text{m}$) in optical lithography and the varying positions of the fingers. Overlaps can range, roughly, from $0.2 \mu\text{m}^2$ to $20 \mu\text{m}^2$, which corresponds to a number of contacted QDs ranging from 1,000 to 100,000, using the number density obtained in Section 2.5.1.

Electron-beam lithography

In order to reduce the contacted area in the junctions, an electron-beam lithography (EBL) pattern was designed by J.M. Fruhman. The idea is to refine the patterning of the graphene electrode layer by cutting thin fingers inside it with a range of widths down to the order of 20 nm. Combining deep ultra-violet (DUV) exposure and EBL and using PMMA as resist, it is possible to develop thin trenches inside the original pattern so as to cut away large areas only leaving small graphene fingers overlapping with the Au fingers (QD junctions) (see Fig. 2.7.d). DUV can expose PMMA in a similar way to EBL, but is compatible with OL masks—provided these are made of quartz and not of soda lime. This makes it possible to directly pattern the PMMA used for the SLG wet transfer, first with the OL mask, and then with EBL without changing resist, and thus leaving the SLG protected. The etch is then done by RIE as previously described. Figure 2.8 shows details of this approach. The electron-beam pattern is aligned to the Au fingers through alignment marks; this ensures an overlap with these fingers and overcomes the possible imprecision of optical lithography. This results in overlap areas of the order of 1000 nm^2 , which brings down the number of contacted QDs to two-digit numbers.

2.4.2 Electrical characterisation

I-V measurement in liquid He

A finished device is observed on a microscope where one looks at the overlap between the graphene electrode and the different NC-covered Au fingers. Either the fingers with smallest overlap, so as to minimise chances of short circuit, or a range of overlaps, as well as the bare Au electrodes (grounding contacts), are chosen and bonded to a leadless chip carrier (LCC) package. This package is connected to an electrical probe with 20 contacts. This probe is inserted into a liquid Helium-4 dewar at $T = 4.2$ K. A Keithley 236 Source Measure Unit (SMU) is connected to individual contacts on the probe, themselves connected to individual fingers of the device. All other contacts are grounded. The SMU allows one to apply a direct current (DC) voltage, and measure the resulting current. The current goes through one junction, into the graphene electrode and into low-resistance grounding contacts which are grounded, making the connected junction the most resistive and only non-Ohmic element, thus revealing its transport profile. The SMU is operated and values are recorded via C.J.B. Ford's LabView-based software CryoMeas.

In a typical measurement, current would be recorded while the DC voltage would be swept back and forth over a range of $[-1\text{ V}, 1\text{ V}]$ at a typical rate of 10 V/h . A current compliance limit is set to prevent high currents likely to damage the devices, and is typically gradually increased over successive measurements of the junction, as well as the measured voltage range, to observe higher-bias and higher-current behaviour. The resolution both in voltage and current can be adjusted to go to higher values or resolve smaller features depending on what is observed.

Measurement with temperature control

In order to check whether SET transport can be observed at higher temperatures, another measurement was conducted in an assessment cryostat which offers temperature control nominally over a range 1.5 K to room temperature, owing to a ^4He pumping system, and integrated heater and thermometer. A device already measured in liquid He was selected for its high number of junctions displaying Coulomb staircases in a prior measurement. This device was connected to a probe compatible with the system and cooled down to base temperature, 1.5 K. We measured the junctions' *I-V* profiles until we found a staircase to study as a function of temperature. The junction is then continually measured, with voltage swept back and forth, as the temperature was brought up. At the time of measurement the thermometer could only sustain the range $[1.5\text{ K}, 62\text{ K}]$ which set a limit on the temperature up to which we could confirm the effect.

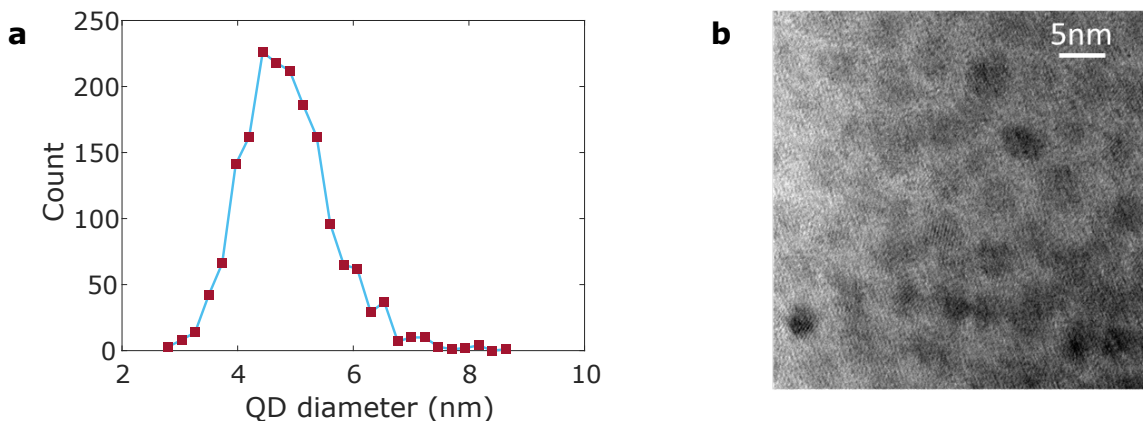


Fig. 2.10 QD size measurement from TEM imaging. **a**, QD diameter extracted from TEM imaging, binned. **b**, TEM image from dropcast QDs. Crystal facets can be seen on some of the QDs.

An integrated magnet offered the possibility to apply magnetic fields on a range $[-8\text{ T}, 8\text{ T}]$. As a quick test the devices were measured over this range, but no Zeeman splitting could be resolved.

2.4.3 Imaging

A range of methods was used to image various aspects of the device. Firstly, the QD sizes were assessed through transmission electron microscopy (TEM) by J.M. Fruhman and B. Ehrler. Secondly, atomic force microscopy (AFM) and AFM derivatives, such as ultrasonic force microscopy (UFM) were used for imaging different regions of the device. The AFM imaging was done both in the Cavendish Laboratory and at the University of Lancaster in B.J. Robinson's group: A. Robson, X. Wang. Some of the imaging was done by myself in Cambridge, under their supervision in Lancaster, and by the Lancaster group without me but under my instructions.

Transmission electron microscopy

The QDs were dropcast from the colloid on a TEM substrate and analysed through TEM. From this it was possible to count QDs and measure their diameter. One image obtained this way is shown in Fig. 2.10, as well as the extracted size distribution (which omits the OA ligands). We find the average diameter to be 4.9 nm with a standard deviation of 0.8 nm.

Atomic force microscopy

Atomic force microscopy (AFM) is a type of surface analysis tool which operates by dragging a tip of atomic size (only a few atoms wide) across the surface under study. In the course of this experiment several signals can be extracted. The standard analysis done by AFM is that of profilometry to assess the height variations across a surface [111]. Other signals can be extracted, e.g. by using conductive tips and extracting special electrical signals (DC or AC modes).

AFM systems were used in the Cavendish Laboratory and B.J. Robinson's laboratory at the University of Lancaster. A variety of set-ups and tests were made which are described in Section 2.5.1.

2.4.4 Quartz crystal microbalance

Quartz crystal microbalance (QCM) offers a way to monitor the assembly or deposition of nanoscale films on substrates. The method relies on the piezoelectric effect used on a quartz crystal made to oscillate at a frequency which depends on the mass attached to its surface. The QCM experiments were done in Lancaster by myself supervised by B.J. Robinson and X. Wang.

Concept

The method was formally introduced by Sauerbrey in 1959 [112]. It uses a thickness-shear-cut⁴ quartz crystal sandwiched between two electrodes, which will drive the piezoelectric oscillation. In this setup the driven acoustic wave has resonant frequency

$$f_0 = \frac{v_q}{\lambda_0} = \frac{\sqrt{\mu_q}}{2d_q}, \quad (2.23)$$

where v_q is the velocity of sound in quartz, λ_0 is the acoustic wave's wavelength, d_q is the quartz crystal thickness, μ_q is the shear modulus of quartz, and ρ_q its density. Depositing material on the QCM's surface will change the material thickness and mass, and, as a consequence, this resonant frequency. Sauerbrey introduces the assumption that material added onto a surface of the QCM affects this vibration mainly through its mass and not its elastic properties: "at the surface of the [quartz] plate there is a wave antinode. The layer on the surface of the quartz only affects the resonant frequency through its mass, not through

⁴The crystal cut axis is important for obtaining the piezoelectric effect. A discussion can be found in R. Mazzocco's PhD thesis [113].

its elastic properties. It follows that an added thin layer on the plate affects the frequency in exactly the same way an extra quartz thickness of the same mass would⁵ [112]. This approximation is widely used for small frequency changes, typically below 5% [114]. In this approximation, one can correlate the mass deposited in the active area Δm with Δf , the resulting shift in the resonant frequency of the oscillator using the so-called Sauerbrey Equation:

$$\Delta f = -2 \frac{f_0^2 \Delta m}{A \sqrt{\mu_q \rho_q}}, \quad (2.24)$$

where f_0 is the resonant frequency, A the area of the electrode on the QCM. By measuring the frequency shift, one can deduce the added mass on the crystal's surface and deduce the deposited thickness or packing density. Typical QCMs operate in the MHz range, and shifts of the order of 1 Hz can detect nanogrammes deposited on surfaces of a few square millimetres.

Measurement set-up

The experimental set-up used for the QCM measurement is shown in Fig. 2.11. A schematic of a QCM sample is shown in Fig. 2.11.a, where the active area (where the deposited material affects resonant frequency) is determined by the parallel-plate capacitor formed by the two electrodes sandwiching the quartz plate, i.e. the circular gold disks on either side of the sample. In our experiments we use QCM samples of frequency range 10 MHz with active area $2 \times \pi (0.25 \text{ cm})^2$ (counting the two faces of the sample). The electrical circuit driving the QCM is shown in Fig. 2.11.b; it shows the electrical representation of the QCM and its connection to a self-adjusting voltage-controlled AC source, or phase-locked oscillator (PLO). A voltage-controlled oscillator (VCO) drives the the QCM close to its resonant frequency; the phase between current and voltage across the QCM is measured by a phase detector. In a perfectly resonant system, this phase is 0. An integrator converts the dephasing between current and voltage into an output gain or loss. This gain or loss is converted into a frequency shift by the VCO until the phase is suppressed and the frequency is on resonance [115, 113]. The driving circuit locks itself onto the QCM's resonant frequency. This frequency can be precisely measured by attaching a frequency counter, which gives this frequency and thus allows for real-time monitoring of the mass deposition.

In our case, our QCM samples are bought commercially from ICM (International Crystal Manufacturing)⁶, while the PLO is a commercial system from Maxtek INFICON PLO 10i⁷.

⁵Translated from German by this dissertation's author.

⁶ICM, International Crystal Manufacturing, 10 N Lee Ave, Oklahoma City, OK 73102, USA. Now out of business.

⁷INFICON (Instruments For Intelligent Control), Hintergasse 15B, 7310 Bad Ragaz, Switzerland.

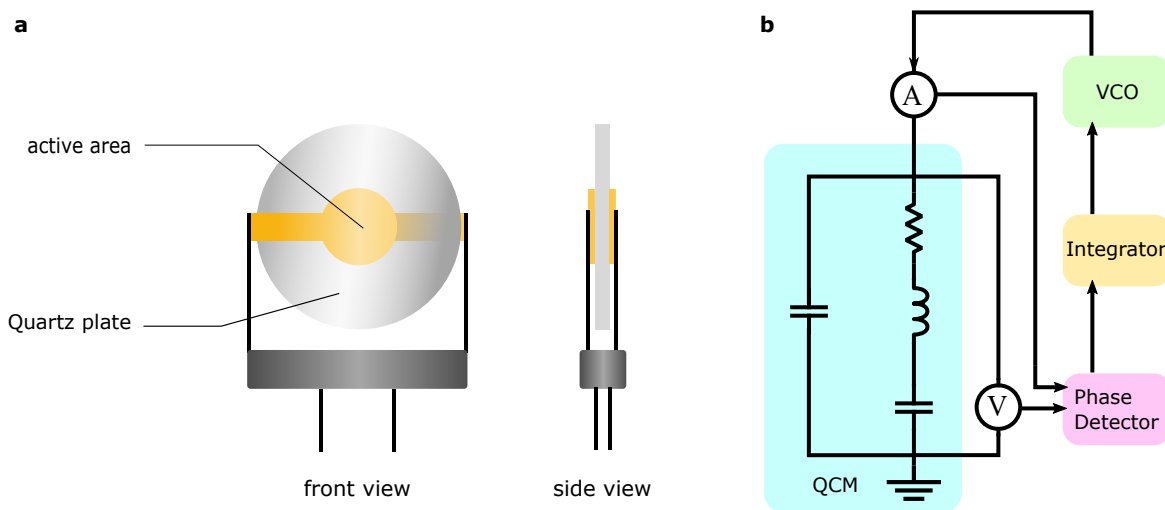


Fig. 2.11 Quartz crystal microbalance QCM set-up. **a**, schematic of a QCM sample with front and side views. **b**, electrical set-up driving the QCM. This includes the QCM's circuit which is connected to an ammeter and a voltmeter. The I - V phase is measured by a phase detector and rectified through frequency by an integrator connected to a voltage-controlled oscillator (VCO). The relevant quantity, the resonant frequency, can be extracted via a frequency counter.

2.5 Results

2.5.1 Verification of monolayer formation

Quartz crystal microbalance measurement

Several techniques were used to assess the successful assembly of a QD film. As explained in Section 2.4.4, QCM can be used to obtain information about the film's assembly. We repeat the self-assembly process described in Section 2.4.1 on the Au electrodes of both sides of a QCM sample and record the frequency shift after the deposition of C6S2 and the QDs⁸. In our system, with a 10 MHz QCM, we find the relation between the frequency shift and the mass per unit area deposited:

$$\Delta f = \left[-4.5 \times 10^{13} \text{ Hz}/(\text{ng}/\text{nm}^2) \right] \frac{\Delta m}{A}. \quad (2.25)$$

After the C6S2 assembly on the QCM's Au electrodes (a one-day immersion in a 1 mM solution of C6S2 in IPA), we dry the samples in vacuum to remove potential solvent contamination. We then observe a frequency shift of -58.3 Hz on the QCM system, which

⁸Due to availability, the solvent used for the PbS QDs was changed to a mixture of octane and hexane (1:25), which is unlikely to noticeably affect the deposition, being both alkane of similar length.

corresponds to a C6S2 packing density of 5.2 molecules/nm², slightly higher than a saturated SAM typically at 4.5 molecules/nm² for thiolates on Au [37], which may be due to residues or dithiol dimers, which are a common defect in dithiolate SAMs. For our purpose the existence of these potential residues is not critical for obtaining SET transport, as they are expected to be longer, hence less conductive than the rest of the structure, causing less conductive pathways for the current. The frequency shift we see after the QD assembly (a one-day immersion in a 1 mg/mL PbS QD solution in the alkane solvent), and subsequent vacuum drying, is found to be -135.6 Hz, or a mass-per-unit-area gain of 3.01×10^{-12} ng nm⁻². Using the size distribution obtained through TEM (Fig. 2.10), and assuming an OA ligand packing density of 3.5 nm⁻² on the QDs' surface as reported in M.A. Boles's thesis [116], we can estimate the average QD mass to be 6.4×10^{-10} ng. From this we deduce a QD coverage of 4.86×10^{-3} nm⁻² and, assuming an average QD diameter of 4.86 nm from the TEM measurement, an average QD neighbouring distance of 14.3 nm centre to centre, and 9.5 nm surface to surface, close to a value reported in the literature OA-capped QD superlattices of 9.7 nm [117]. The QCM samples were imaged through AFM so as to measure the substrate's roughness. The root-mean-square roughness was found to alter the effective surface negligibly compared to the approximation of an ideally smooth surface. However, AFM imaging is itself limited in this precision, and the roughness measurement would not have accounted for surface defects or irregularities of nanometre or subnanometre sizes.

Atomic force microscopy imaging

A first method was applied by A. Robson and B.J. Robinson at the University of Lancaster at my request and consists in using the AFM tip to mechanically scrape the surface and mechanically remove the QDs on its surface. This was done on devices used for measurements, and I extracted the cross-section profile shown in Fig. 2.12. The AFM was used with maximum force to sweep over a square-shaped region 16 times and mechanically remove the SAM from its surface. A control experiment was realised on the same device, following the same procedure, with 21 sweepings, in a region that was protected from self-assembly by photoresist.

Resolving the QDs attached on the Au surface is made difficult by the very nature of its oleic ligands, which smoothen the height profile and the roughness of its substrate. On the control imaging shown in Fig. 2.12, in the uncleaned region, the root-mean-square (RMS) roughness is measured to be 1.2 nm, and the average roughness 0.9 nm. To counter the averaging effect caused by ligands, only a contact mode can resolve the QD SAM profile. This was done by myself with X. Wang in Lancaster. On an Au substrate prepared with template stripping, with a roughness of 0.15 nm (RMS) and 0.12 nm (average), we replicate

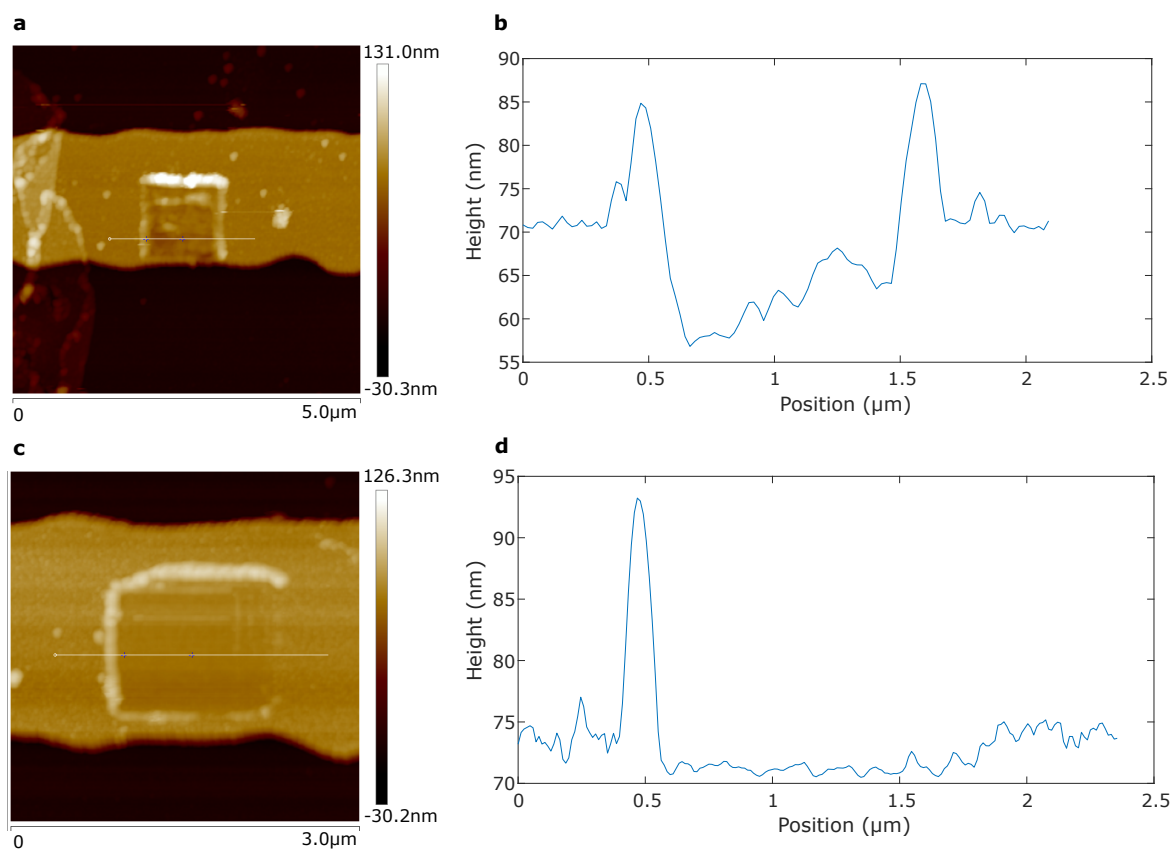


Fig. 2.12 SAM verification using mechanical cleaning. **a-b**, height profile cross-section of QD SAM. **a**, height profile, the line shows cross-section used for height profile analysis shown in **b**. **c-d**, height profile cross-section on control substrate without SAM, examined in a similar way.

the self-assembly recipe, to decorate it with QDs. The sample was imaged in the AFM using a force constant of 0.3 N m^{-1} and a loaded force from probe to sample around 2.3-2.9 nN. A stronger force was found to displace the QDs, which can be seen as defects in the scanning direction showing a constant height along a scanning line. This force range was found to be appropriate for measuring their height. The result is shown in Fig. 2.13. Interestingly, a reported artefact of this imaging approach is the horizontal spreading of features as the contact mode forces the tip, which has finite diameter, to elevate at the edges of the structure. This results in QDs appearing as 10-20 nm features on the image.

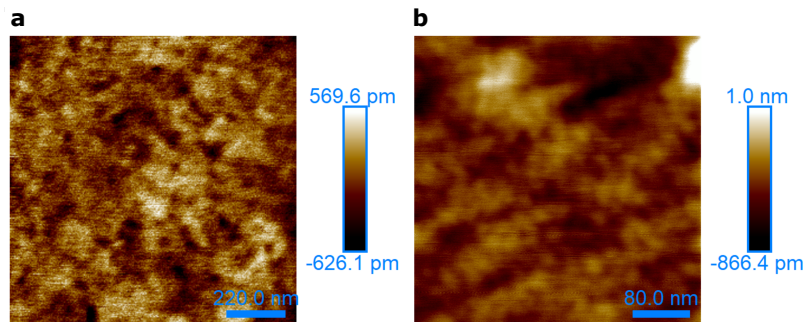


Fig. 2.13 AFM imaging of QD SAM formed on template-stripped Au. **a**, imaging of template-stripping-prepared Au substrate. **b**, imaging of the QD SAM.

2.5.2 I - V profiles

Single-electron tunnelling

Many junctions, about 42% of the total⁹, display, in their I - V curves, current blockade at low bias, and series of current plateaux, as can be seen in Fig. 2.14. These are a signature of Coulomb staircases and single-electron tunnelling. We use StC as a shorthand for the junctions displaying steps. These effects are usually stable in repeated measurements of the same junction. Thermally cycling, i.e. taking the device out of and placing it back into a He dewar for a second measurement, the junctions most often preserve these effects. The I - V profiles, however, vary noticeably from junction to junction, in the positions of the steps, and their regularity. It can be seen that the junction shown in Fig. 2.14.a has steps of similar height and plateaux of similar width. A typical charging energy can be extracted from the plateau width, which would be of $e\Delta V = 100$ meV. Neglecting the single-electron energy-level difference¹⁰ we can estimate the total capacitance of the system to be of order 10^{-18} F. These types of junctions appear in OL and EBL devices alike in similar proportion, with a yield around 42% in both populations.

This type of transport is typical of a QD junction, as illustrated in Fig. 2.16. The Au electrode constitutes the source, while SLG is the drain. The QD is placed between them. The tunnelling barriers are provided by the organic molecules in the system. Between the QD and the Au electrode the covalently bonded C6S2 anchor provides a tunnelling barrier with a length expected to be fixed by the tight packing of the SAM on the Au surface. Using the software Avogadro we estimate the fully extended sulphur-to-sulphur length of C6S2 to be

⁹The criteria used to determine this yield are discussed in detail in Sec. 2.5.3.

¹⁰As mentioned in Sec. 2.2.2, one should expect this difference between single-particle energy levels to be negligible in some transitions due to degenerate levels, including the spin degeneracy, but our measurements cannot give a formal proof of this.

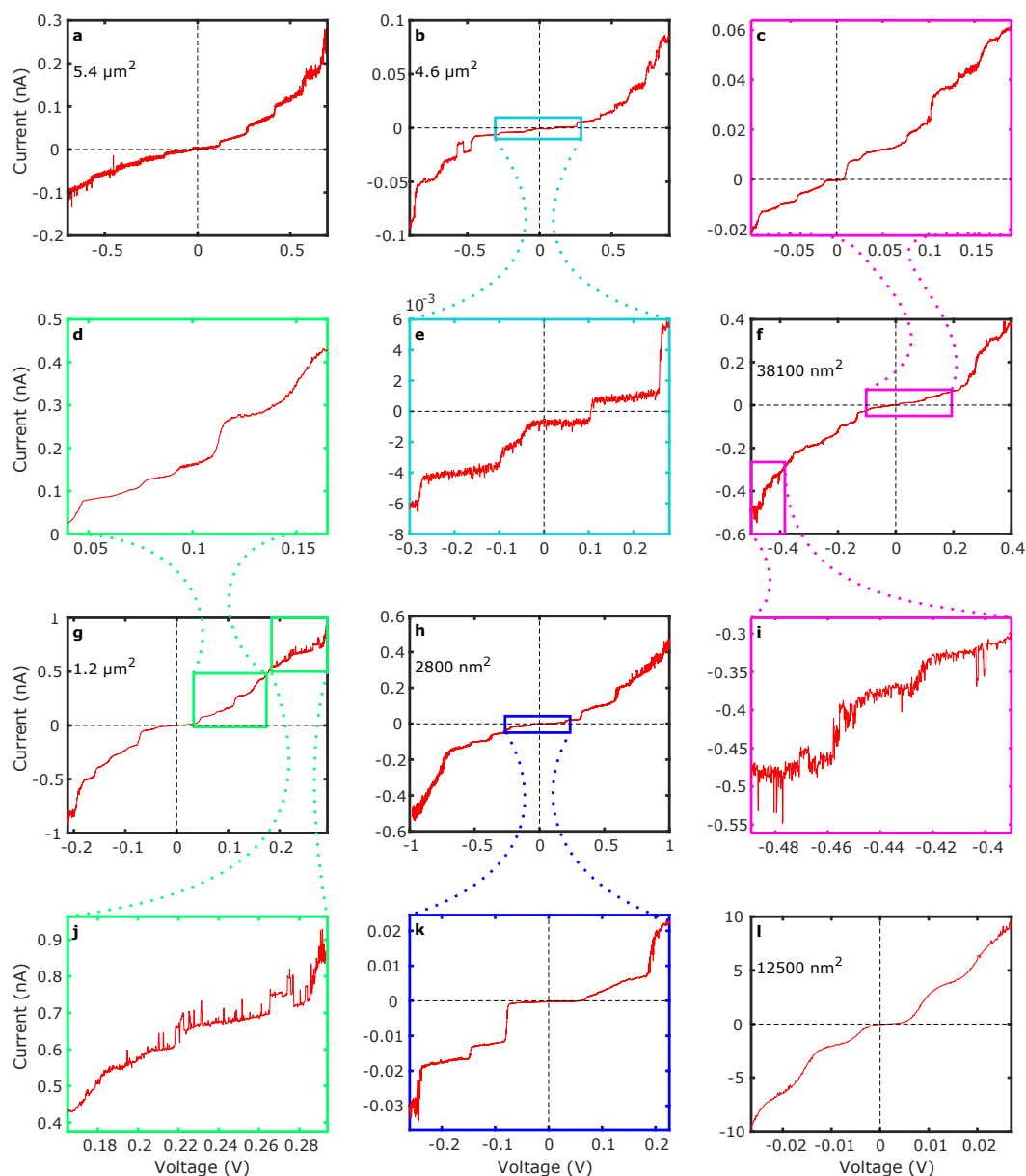


Fig. 2.14 I - V measurements displaying Coulomb staircases, from OL junctions (**a**, **e**, and details of these measurement) and EBL junctions (**f**, **h**, **i** and details); the areas are displayed in graphs. These measurements are selected representative measurements of each junction, their behaviour varying only in a minor way over successive measurements. Taken from [10].

0.94 nm. A typical reported tilt angle of alkanethiolate/alkanedithiolate SAMs on Au of 28° reduces the thickness of the SAM to 0.8 nm. These two values provide an upper and lower limits to the effective tunnelling length depending on the contribution of charges hopping from a C6S2 molecule to its neighbour (via through-space tunnelling); this contribution is

dependent on tilt angle and was found by Song *et al.* [118] to be negligible compared to tunnelling along molecular chains for the aforementioned standard tilt angle, which would make 0.9 nm a valid effective tunnelling-barrier width. The other tunnelling barrier, between the QD and the SLG drain, is provided by the OA ligands covalently bonded on the QD and stacked against the SLG by a van der Waals bond. The disposition of the OA molecules in this interstice is more challenging to predict. Their unfolded length can be estimated using Avogadro to be 2.2 nm. However, imaging done on PbSe QDs of similar diameter (6 nm) by Gunawan *et al.* [119] shows that the OA ligands wrap around their QDs, thus forming a shell of thickness varying around 1 nm. We can expect a similar arrangement in our very comparable system. These two tunnel barriers, by their effective width, their different coupling to the electrodes and their different lead densities of states provide an asymmetry in the source-dot-drain structure, i.e. the tunnelling rate between source and dot is different from that between drain and dot. The shorter length and stronger covalent bonds in the C6S2 barrier makes it likely that it is the barrier with higher tunnelling rate across it. This asymmetry makes the obtention of Coulomb staircases possible, i.e. the discretisation of charges travelling through the dot by Coulomb charging, manifested as successions of steps and plateaux in the I - V characteristics—different from mere Coulomb blockade which only corresponds to current blockade at low voltage bias.

The clarity of the SET features can seem surprising given that the QD number density measured in Section 2.5.1, i.e. $4.86 \times 10^3 \mu\text{m}^{-2}$, implies thousands of QDs are contacted in OL junctions, and few to hundreds in EBL junctions. However, a few elements appearing in the data inform us of why this is the case, as is discussed in Section 2.5.4.

A junction previously shown to exhibit Coulomb staircase was tested in the set-up with temperature control. It had retained its staircase behaviour after thermal cycling, and the I - V curve was recorded continuously as the temperature was increased from 1.5 K to 62 K. It was shown to preserve its characteristics and exhibit clear and unaltered staircases up to the maximum temperature allowed by the system at the time as shown in Fig. 2.15. Attempts to measure similar patterns at room temperature have remained elusive, although in principle this should be energetically possible. It is possible that fluctuations from the environment destabilise the system, aside from the thermal broadening.

Short circuits

The most common type of failure in the devices is short circuits (ShC). This type of failure is common in molecular devices built by layer stacking. We expect these to result from SLG penetrating through a pinhole in the C6S2:QD SAM and locally making direct contact to the Au. The resulting I - V measurements provide an Ohmic profile, with a high conductivity.

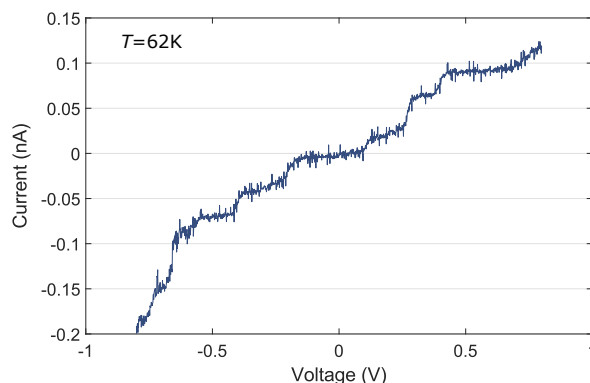


Fig. 2.15 I - V curve of junction exhibiting Coulomb staircase at 62 K.

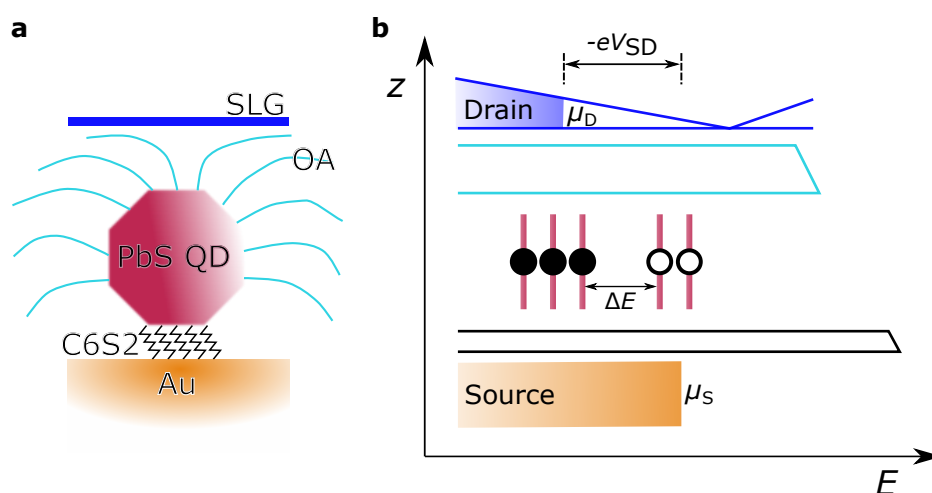


Fig. 2.16 Schematic of the system. **a**, schematic of a single-QD system as contacted in the junction. **b**, corresponding energy structure. The C6S2 SAM and the OA ligands form tunnelling barriers on each side of the junction. The two leads are Au and SLG.

As can be seen in Fig. 2.20, a typical conductance per unit area in for these junctions is $1 \times 10^{-5} \text{ S } \mu\text{m}^{-2}$ for OL junctions and $1 \times 10^{-3} \text{ S } \mu\text{m}^{-2}$ for EBL junctions.

The SLG only has to make direct contact with Au on one restricted region for this low-resistance path to electrically dominate the conduction and dominate the transport, thereby hiding signs of transport through the SAM in the rest of the junction's area. The occurrence of ShC in a junction is then related to the quality of the SAM, and in particular the density of pinholes too large in area for the SLG to be suspended over. If this density is fixed—as one may expect from a similar fabrication procedure, or indeed the same fabrication batch—the probability of a short circuit through a pinhole is expected to scale with junction area as will be discussed in Section 2.5.3.

Fig. 2.17 subplot	Junction ID	ϵ_0	G_0	Γ_l	Γ_r
a	220041	-0.63 eV	12 nS	0.10 eV	0.10 eV
b	340027	-0.67 eV	7 nS	0.017 eV	0.19 eV
c	310007	-0.44 eV	0.44 nS	0.20 eV	0.21 eV
d	370037	-0.82 eV	1.7 nS	0.046 eV	0.080 eV
e	420010	-0.61 eV	5.3 nS	0.092 eV	0.10 eV

Table 2.2 Parameters of Landauer model fits on non-Ohmic smooth curves displayed in Fig. 2.17.

Non-Ohmic smooth curves

Another type of I - V profiles commonly encountered is that of non-Ohmic smooth curves (SmCs). These typically have high differential conductance at 0 V, showing no blocked region. However, as opposed to ShCs, these deviate from a linear Ohmic curve. This behaviour suggests transport through nanostructures but bypassing the source-island-drain configuration. In most measurements a current compliance limit was set in the measurement to prevent high currents from damaging junctions or the SLG, thus limiting the voltage range over which most of these junctions were measured. A few however were measured over a voltage range spanning 2 V. One configuration that can deliver the observed I - V characteristics is that of SLG making direct contact to the C6S2 through a pinhole in the QD film. Transport through alkanethiol and alkanedithiol SAMs has been studied by other groups in nearly all SAM device or STM set-ups, as they offer a clear benchmark of successful electrical contact to the SAMs, owing to their smooth and stable I - V properties and the clear exponential dependence of conductance on molecular length, i.e. number of carbon atoms in the alkane chain. This has led to the publication of extensive information on these molecules' transport properties and the development of several models [33, 35, 120, 32, 30]. Transport in alkanethiols over a range of $[-1.5 \text{ V}, 1.5 \text{ V}]$ is appropriately described by HOMO-dominated transport, where the DOS can be approximated to a Lorentzian-broadened single energy level. In this assumption we can use the Landauer model to fit I - V measurements and find the junction's energy parameters as shown in Fig. 2.17.

The parameters obtained from the fits are displayed in Table 2.2. ϵ_0 represents the energy of the HOMO with respect to the Fermi energy at 0 V. Other values for comparison are lacking in the literature, as although the shape of the I - V characteristics of alkanethiol and

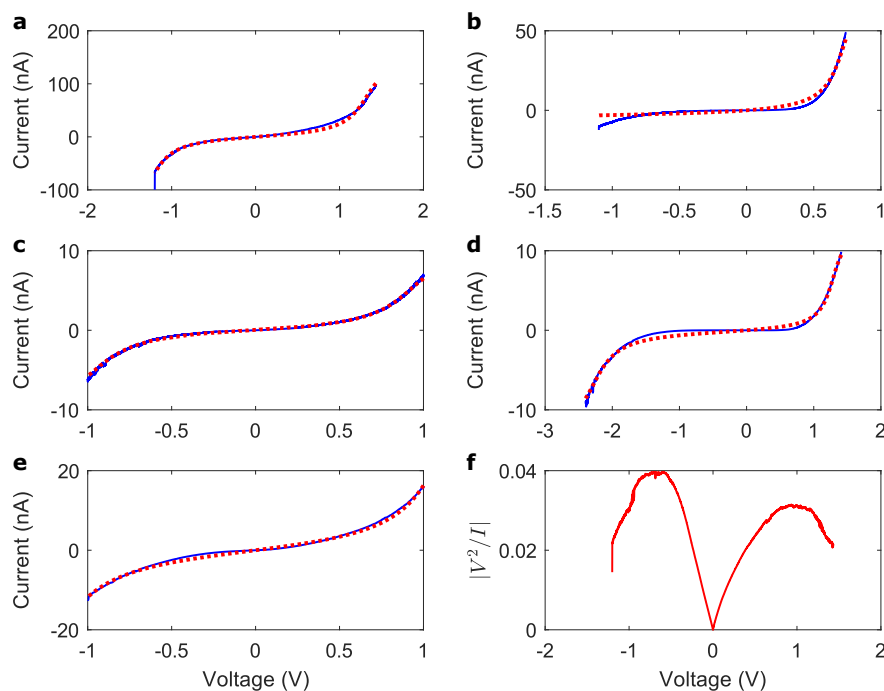


Fig. 2.17 Junctions exhibiting smooth non-Ohmic I - V profiles. **a-e**, I - V measurements and Landauer fits. Blue line: experimental data. Red dotted line: Landauer model fit. **f**, measurement shown in **a** in form $|V^2/I|$ versus voltage V .

alkanedithiol junctions are similar¹¹, the number of carbon atoms and chemical nature of the electrodes will affect all fitting parameters extracted from the fits.

We can look at the symmetry of the transport. Uneven coupling between the two leads can be modelled in the Landauer model using a parameter which divides the voltage drop across the junction. Asymmetry in the coupling with the leads leads to rectifying behaviour [14], as can be seen in the fits. We see that in the few junctions displaying rectifying properties, assuming HOMO-dominated transport, interestingly, the asymmetry is consistent with a junction coupled more strongly to the SLG lead. The coupling between Au and the C6S2 (rate Γ_1) is a covalent bond, whereas that between the C6S2 and the SLG (rate Γ_r) is a physisorption. This suggests that, in this particular junction, conduction may be mediated by a different system, some structure either coupled more strongly to the SLG electrode or LUMO dominated.

These fits are rough-and-ready descriptive fits of the transport, and further improvements could be made for a more rigorous study of the transport. For example, using a different set-up which records the differential conductance along with the current would enable fitting

¹¹An interesting discussion of the *universality* of alkanethiol/alkanedithiol junctions can be found in Xie *et al.* [30]. They show, experimentally and through calculations, that in C_nS_2 junctions and junctions where in C_nS_2 a C atom has been replaced by a heteroatom, the I - V curves can be rescaled into a universal curve.

the derivative of the current with respect to voltage, which could improve the quality of the fits. However, given the likely complexity of the junction in these special cases where the transport is not explained by QD transport and the fact that these could correspond to several scenarios (different coupling strength or inclusion of impurities) a more rigorous fit would hardly be more informative.

A model was developed by Ioan Bâldea [30], which is fast and suitable for assessment of experimental data. The position of this level can be read out by plotting $|V^2/I|$ against V , as in Fig. 2.17. In this approximation, a transition voltage V_t can be read as the maximum of this curve on either voltage polarity. This transition voltage can be shown to be related to the HOMO misalignment from the Fermi energy by:

$$E_{\text{HOMO}} - E_{\text{F}} = -\frac{\sqrt{3}}{2} e |V_t|. \quad (2.26)$$

This allows for classification of data, but it considers ideal systems where the two leads are identical and the coupling with the junction is equal on either side. This is a valid approximation only for a subset of the junctions in this system.

Open circuits

The other observed, although significantly less frequent, type of failure is open circuits. These are somewhat more difficult to explain. They are unlikely to result from properties of the junctions as they are made, as their nanometre thickness should in principle allow at least some tunnelling current. The possible explanations are either defects in the SLG, where the part contacting the junction may have been separated from the central SLG sheet by a tear, or else acute contamination by various impurities from solutions or resists in the junction could also prevent conduction. Other possible failures could arise from a disconnection of the bonding wires.

Random telegraph noise

The vast majority of the StCs display random telegraph noise (RTN) in their I - V characteristics. This is manifested as an oscillation of the current between two (or more values) at a given voltage. This can be most clearly seen in Fig. 2.14.i-j. A typical time frequency for this oscillation is of the order of 10 Hz making it resolvable with the rate at which the SMU collects data.

The existence of trapped charges is a widely reported phenomenon in colloidal quantum dots, where these can be observed in optical measurements and has implications in e.g. the

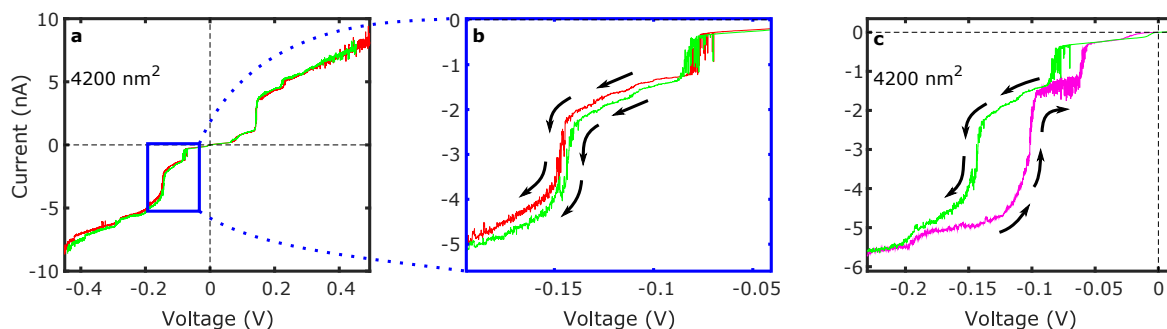


Fig. 2.18 Hysteresis in staircases in I - V characteristics. **a**, I - V curve of junction exhibiting Coulomb staircase. **b-c** details of subsequent measurements of the same junction. **b**, two measurements whilst varying the voltage in the same direction show similar characteristics with slightly shifted steps. **c**, voltage bias sweeps in opposite directions show displaced current steps and different transitions. Figure taken from [10].

efficiency of QD solar cells [121–127]. In an electronic junction set-up, as in an optoelectronic set-up, these trapped charges cause a local electrostatic gating of the QDs. It is often understood as deep potential wells that can typically exist at the surface of QDs. Several strategies exist to change affect and reduce the occurrence of trapped charges, namely through ligand exchanges, changing the organic molecules covering the QDs' surface, or growing a semiconductor outer shell during the QD growth to produce what is known as a core-shell structure.

These long-lived states existing at the surface of the QDs electrostatically locally gate the QDs and can change their conduction state; in the SET regime, this can result in significant changes in the current, changing the number of electrons energetically allowed to transit through the dot at one time by one. These oscillations between two states are often most present around a step in the I - V curve, as can be seen e.g. in Fig. 2.18.**b-c** suggesting that the trapped charges can help or hinder the transition to the next plateau energetically.

Hysteresis

When sweeping voltage back and forth on the same junction as we have done, some hysteresis effects are observed as a displacement of the steps after sweeps over large voltage ranges. Such a displacement can be seen in Fig. 2.18. This effect is commonly observed in single-electron transport and is attributed to trapped charges in or around the island and effectively gating the dot as previously discussed [94].

In this case keeping the voltage within a small range maintains reproducible transitions, while bringing the voltage to the negative and going back up changes the profile of this transition significantly. One first notes in this case that these are transitions between the same

channels as curves meet. In the hysteretic case, in the initial sweep down, the larger step has a finite width whilst it becomes much sharper when going up. The positions and sizes of the steps are also changed. This difference was observed over repeated measurements of the junction. There then exist several possible series of transitions between two same channels; the prevalence of a given transition can be sensitive to the electrostatic environment.

Break-down

A few junctions also exhibit an unstable behaviour that can be irreversibly changed by applying a critical voltage across the junction. These break-down profiles are characterised by jumps in current of no reproducible or obvious structure. These can result in quantitative changes in a similar profiles but also in an abrupt transition from a StC to a SmC or a ShC. This can be attributed to an instability of the graphene electrode, which under the capacitive force can be dragged into contact with the C6S2 or the Au, or permanently rearrange its shape and contact on the QDs.

Negative differential resistance

Several junctions exhibit NDR in their I - V curves. The NDR features are stable and reproducible over subsequent measurements. We have tagged seven junctions showing this behaviour, which comprise six EBL junctions and one OL junction. Three of the EBL curves are shown in Fig. 2.19. One notes that the NDR is observed locally, following a rapid increase in current, most likely a Coulomb step, but occur at different voltages from one junction to the next.

It was discussed in Section 2.3.2 that such features can be observed for a particular alignment of the first resonant conduction level and the minimum of the Dirac cone. The minimum of the Dirac cone is shifted by the doping of the graphene. Unfortunately graphene is extremely sensitive to its environment and its doping can be affected drastically on a very local scale, i.e. it may be different from one junction to the next, or indeed within a junction. Raman spectroscopy is a way to get a measurement of this doping and typically resolves areas of $1\ \mu\text{m}^2$. Some Raman spectroscopy has been done by D. De Fazio and results are being compared at the time of writing.

2.5.3 Statistical analysis

To study the junctions' behaviour statistically, using MATLAB we compile the recorded data into a hierarchical database consisting of four levels, which, listed in a downward order, are: chip (wafer), die, junction, measurement. This database makes it easy to extract data

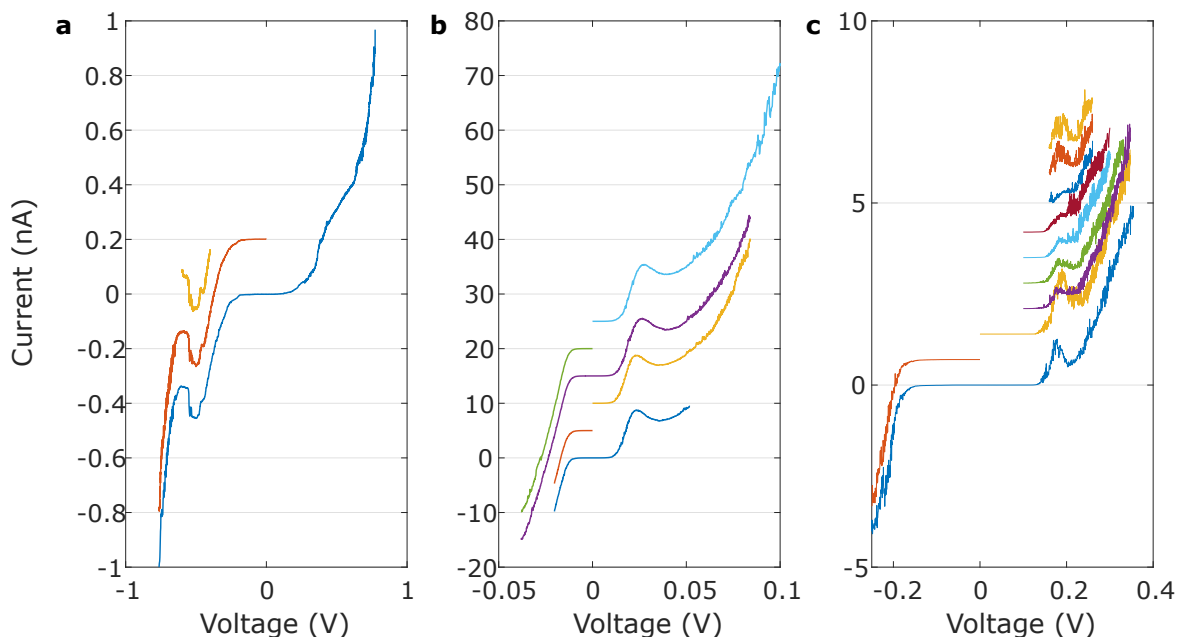


Fig. 2.19 Waterfall plots of I - V curves of junctions exhibiting NDR. Subsequent measurements of the same junction are shifted vertically for clarity. Junction IDs are as follows: **a**: 290014; **b**: 260030; **c**: 290033.

according to various parameters at the relevant level as shown in Table 2.3. This ability is interesting for three main aspects. Firstly, it helps distinguish populations corresponding to different transport mechanisms in the measurements. Secondly, it allows us to compare the yield to junction geometry and other fabrication parameters and so quantify the viability of the device and suggest routes to its improvement. Thirdly, we fit hyperbolic tangent functions onto steps in the I - V data; these can be correlated to other parameters of the junction.

Some of the parameters, namely the tags about the presence and coordinates of steps, the presence of random telegraph noise (RTN), representative measurements, and the classification are the result of an interactive review of the I - V profiles made possible by a MATLAB code.

In this classification, we scrutinised the I - V data for each junction and applied relevant labels to be recorded in the database. If a step could be seen within the resolution of the measurement (typically ~ 1 pA) and was discernible from the background conductance, the junction was labelled as having a step, or StC. If, on the other hand, the curve appeared Ohmic over the measurement range, it was labelled as a short circuit, or ShC. These junctions being typically more conductive, a current compliance was applied and limited the voltage range over which they were measured, so as to protect the device from high currents; this may have limited the characterisation. Finally, if the junctions exhibited non-Ohmic conductance,

but showed no apparent steps, these were labelled as non-Ohmic curves, or SmCs. For these too, a current compliance often restricted the voltage range used for the measurement. Other labels, namely open circuits, or break-down curves, were applied for the relevant junctions. The presence of RTN was also recorded, where junctions exhibiting the sharp oscillations were given a specific label.

To perform the fits of the step functions, we used the bespoke MATLAB code I wrote to interactively locate the step and improve fits until satisfactory. The fitting function used is:

$$I(V) = I_0 + \Theta(V_s - V)g_0V + I_h \tanh\left(\frac{V - V_s}{V_w}\right) + \Theta(V - V_s)g_1V, \quad (2.27)$$

where I_0 is the current at the centre of the riser, $\Theta(x)$ is the Heaviside step function, g_0 and g_1 are the gradient before and after the riser respectively, V_s is the voltage at the centre of the riser, I_h is the height (magnitude) of the riser, and V_w is the width of the riser. These parameters are then recorded in the database to offer a quantitative description of the steps. This gives an extensive register of all steps measured and allows for comparisons.

Information on the junctions' geometry was extracted from imaging of these junctions. In the case of OL devices, we take micrographs of the die, and measure the misalignment of the SLG layer compared to the mask design (on CAD file). In the case of EBL junctions we use SEM pictures of the junctions to assess the overlap of the QD SAM-coated Au electrode with the SLG top contact.

Statistical distinction of populations

As explained in Section 1.2.2, a statistical approach is the canonical method for distinguishing transport regimes in junctions. In our case, using the measured area and extracting the conductance per unit area at 0V, G_0/A , we can compare conductance between different families determined by the inspection of I - V profiles.

An example of this binning is shown in Fig. 2.20.c, where we compare the different populations as separated by their label, as a function of the current density.

It can be informative to compare populations. For example, the EBL and OL junctions show different conductance per unit area for the corresponding populations, higher for EBL junctions than for OL junctions. This might be explained by the fact that the EBL junctions have a slightly different geometry in that the SLG top electrode has three open edges, as opposed to one for OL junctions; this should make the SLG top electrode more flexible and freer to come in closer contact with the underlying junction. In addition, it may be indicative of a reduced effective contact area in OL junctions where only a fraction of the area is effectively contacted.

Level	Field
Chip (wafer)	Chip name
	Chip ID
	Chip ID number
	Lithography design for SLG electrode (e.g. OL or EBL)
	Type of SAM
	Presence of top gate
Die	Die ID
	Die ID number
	Number of thermal cycles
	Lab book entry
Junction	Junction ID number
	Contact number
	Measured misalignment in junction area
	Junction width
	Junction length
	Junction area A with error
	Lab book entry
	Presence/number of current plateaux
	Coordinates of current plateaux
	Step fit parameters $V_s, I_0, V_w, I_h, g_0, g_1$ (cf. Eq. 2.27)
	Presence of RTN
Classification (e.g. StC, SmC, ShC)	
Low-voltage conductance G_0	
Measurement	Measurement ID number
	Representative measurement tag

Table 2.3 Database structure. Four tables constitute the database compiling the data. These have database fields to enable a statistical analysis.

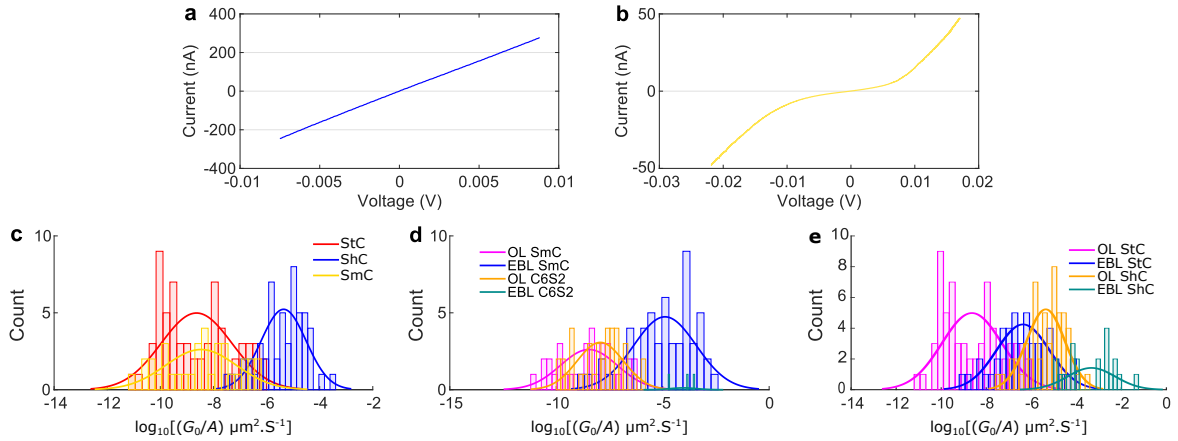


Fig. 2.20 Categories of junction characteristics and comparison of conductance. **a**, representative ShC. **b**, example of SmC. **c-e**, histograms displaying G_0/A , the conductance per unit area (whereby the area used is the junction's area), for different populations of junctions. **c**, comparison of the three main categories StC, ShC, and SmC in OL devices. **d**, comparison of SmC for OL and EBL devices with control C6S2 SAM devices made with OL and EBL. **e**, comparison between OL and EBL devices for StC and ShC junctions.

Yield regression

An interesting observation that can be made with statistics is the correlation of the yield, i.e. the likelihood of obtaining a StC, with the geometry of the junction. This is informative as to the conduction mechanism in the SAM, and gives clues as to the limitations of the device and possible improvements in future architectures.

Such a regression is shown in Fig. 2.21. It shows for OL devices the StC yield compared to the two dominant failure modes¹² as a function of junction area. We see a clear increase in yield as the junction area is reduced. If one considers a constant probability of a defect which could result in a ShC or SmC per unit area, as one can expect from a simultaneous SA, increasing the area should consequently increase the probability of failure. Interestingly doing the same regression on EBL junctions results in a similar pattern, as shown in Fig. 2.21.**b-c**, but the two curves do not join, and the larger-area EBL junctions show a lower yield than the smaller-area OL junctions. The SLG being more flexible in EBL junctions should make the SLG more flexible and freer to protrude inside the underlying SAM to produce either of the failure modes.

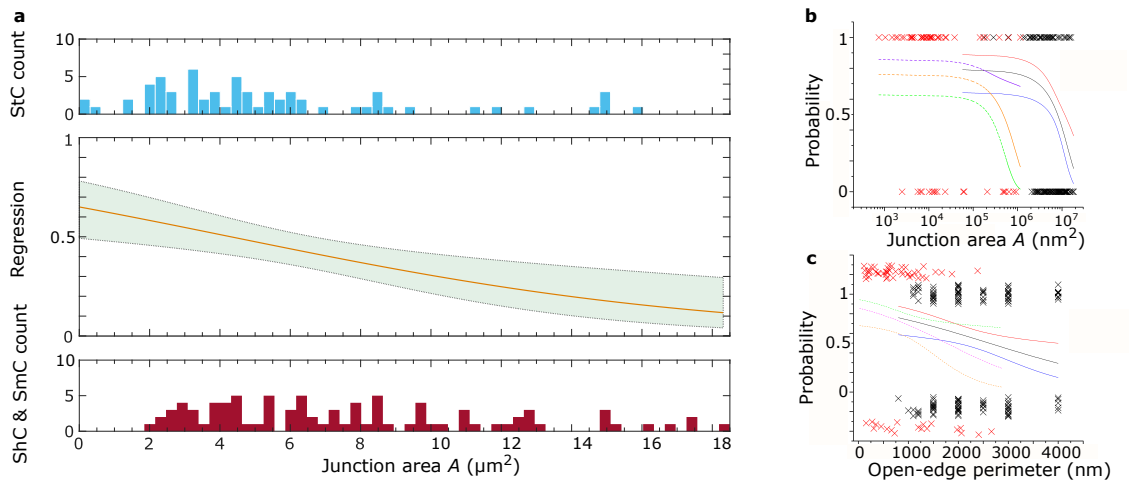


Fig. 2.21 Logistic regression of StC yield as a function of junction geometry. **a**, logistic regression against junction area for OL devices. Top (bottom): histograms of occurrence of StC (SmC and ShC) as a function of junction area. Centre: logistic regression. Orange line: regression, spring green region: confidence interval. Adapted from [10]. **b**, logistic regression for OL and EBL junctions against junction area, where solid (dashed) lines are the average and confidence interval of the regression for OL (EBL) junction. Crosses show individual events (1 for StC, 0 for SmC or ShC). **c**, logistic regression against perimeter of the SLG open edge; vertical noise has been added to crosses so as to make their densities more apparent.

Plateau characterisation

As the steps in the I - V curves were fitted with hyperbolic tangent functions, it is possible to extract the resulting fitting parameters and compare these with other parameters.

The resulting patterns are not straightforward to interpret. However, when comparing the height of the closest steps to 0 V in both polarities, one can distinguish two trends for each batch, i.e. a higher and a lower conduction trend. These are made explicit by a colour code in Fig. 2.22.

Interestingly, comparing the conductance at low voltage, the gradient at 0 V, with the height of the first step, a trend emerges, as can be seen in Fig. 2.22. This is informative as it shows that the *background* conduction, i.e. conduction outside of the steps, is correlated in magnitude with the increase in conduction produced by a step.

¹²Open circuits were omitted as they are deemed to not result from a junction's behaviour.

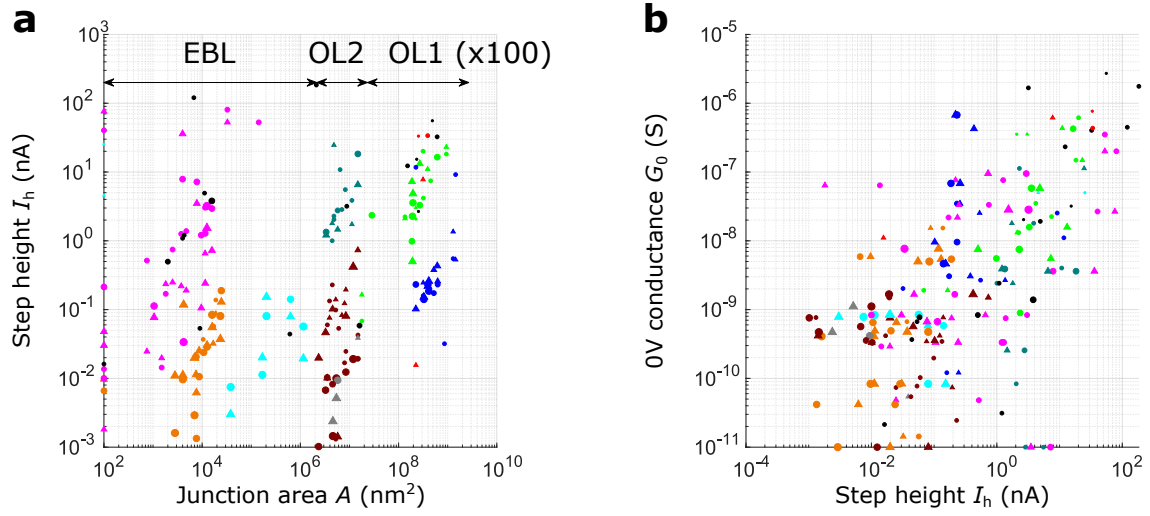


Fig. 2.22 Scatter plot of step fit parameters with junction geometry and I - V characteristics. **a**, Scatter plot of step height against junction area. The different populations are made explicit by a colour code and a shift separating the batches of OL devices. For all batches two populations have been distinguished with the colour code due to their different conductance regime (high and low) and apparent inclusion in different trends in the scatter plot. The EBL batch has a further division consisting of OL-sized junctions included in the EBL pattern. **b**, scatter plot of conductance at 0V, G_0 , against step height I_h extracted from the step fits. Circles (triangles): first steps occurring at positive (negative) voltage polarity. The size of the marker is proportional to our appreciation of the clarity of the step, i.e. presence of noise, or background conduction.

2.5.4 Discussion

Interpretation

An important question arises from the results of this project, namely how can we obtain such clear signatures of Coulomb blockade and staircases in a system supposed to contact tens to thousands of QDs? Several clues bring an explanation to this question.

Firstly, the presence of trapped charges, made evident by hysteresis and RTN, signifies a particular type of conduction. These trapped charges affect conduction to the extent that they can interfere with transitions in the discretised SET conduction state through RTN, or significantly shift the voltage needed for an SET transition as is seen through hysteresis in the I - V curve. Single trapped charges could not cause such noticeable shifts if a large number of QDs were effectively contributing to the current. It was measured through QCM that the average spacing between QDs is of 9.5 nm, a distance over which a single trapped charge is unlikely to electrostatically affect the chemical potential of the next QDs to an extent that

would be measurable. This points to a very local conduction which can be affected by surface states in QDs.

Secondly, the correlation of the first step's height with the 0V conduction rules out individual dots providing the steps whilst 0V conduction comes from the whole contacted area. It suggests that most of the conduction is due to a local conduction track going through a low number of QDs, which provide the current plateaux through SET, and the background conduction can be attributed to Lorentzian broadening of the QD's conduction levels through coupling to the electrodes.

Thirdly, a comparison to the literature in SAM devices would suggest that a small fraction of a contacted SAM being responsible for most of the conduction is actually a classic result in the field. Indeed, the literature on contacting molecular SAMs electrically reports a typical contacting efficiency of 10^{-4} of the area significantly contributing to the current [39], despite recent efforts where the contacting efficiency was increased to 10-100%, using conjugated molecules and SLG, in what is an exceptional result in the field [61]. In our system a reduction of 10^{-4} would allow for single or few QDs to dominate the transport.

Several physical factors can explain the reduction of the effective contacted area. Firstly the QDs contacted have a normal distribution of sizes as shown in Fig. 2.10, with average 4.9 nm and a standard deviation of 0.8 nm. These result in variations in the charging energy; the self-capacitance of a sphere is given by:

$$C_{\text{sphere}} = 4\pi\epsilon r, \quad (2.28)$$

where ϵ is the dielectric constant and r the sphere's radius. Secondly the OA tunnelling barrier offers a variety of configurations in its stacking to the SLG top electrode, with different conductivity. The presence of contaminants, impurities, between the SAM and the SLG cannot be excluded, and these would make the underlying structure electrically inactive. Finally the SLG top electrode is not flush against the SAM equally over the junction's area. This was imaged by B.J. Robinson and A. Robson by ultrasonic force microscopy (UFM). This method enables a combined measurement of a height profile and the rigidity of the underlying surface through high-frequency oscillations of the cantilever [128]. They found that the stiffness of the SLG on the junction, i.e. the rigidity of its contact, varied noticeably across the junction area (see Fig. 2.23).

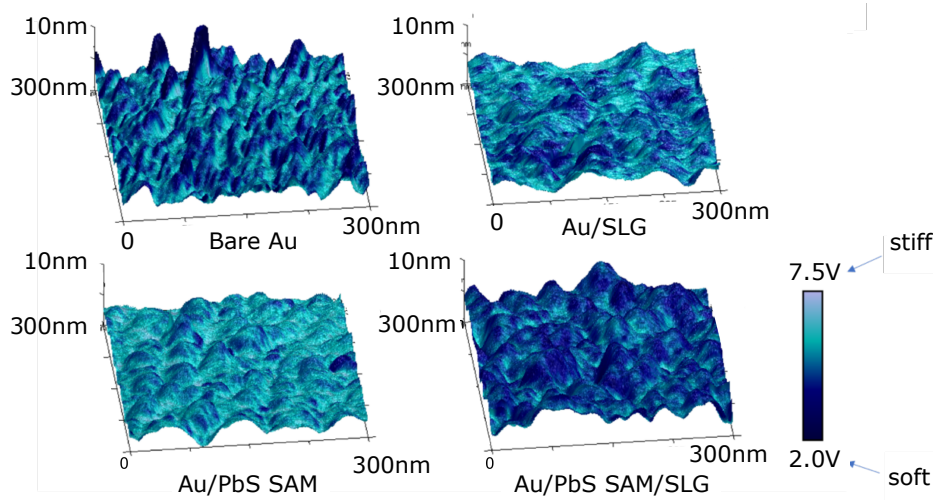


Fig. 2.23 AFM-UFM imaging of different regions of a device. The height profile for all surfaces is on the same scale for comparison. The colour shading gives a measure of the rigidity of the underlying surface.

2.6 Further devices

2.6.1 Self-assembly variations

Concept

The conduction properties of the junctions can be altered by changing parameters of the QD SAM through self-assembly. Firstly the charging energy of the QDs can be altered by changing the anchor group and the QD's size.

The capacitance of a sphere placed a distance d from a plate is the sum of the sphere's self-capacitance and the capacitance between the dot and the electrodes, which can be approximated to parallel plate systems for simplicity (further justified by the existence of flat facets in nanosize dots):

$$C_{\text{tot}} = C_{\text{dot}} + C_S + C_D = 4\pi\epsilon_{\text{dot}}r + \frac{\epsilon_S A_{\text{dot}}}{d_S} + \frac{\epsilon_D A_{\text{dot}}}{d_D}, \quad (2.29)$$

where d_D (d_S) is the distance between the QD's surface and the drain (source), A_{dot} is the effective area of the dot in the parallel-plate capacitor approximation, and the ϵ are the dielectric constants of the relevant media.

One sees that the total capacitance C_{tot} can be reduced by minimising the QD's radius r and the maximising the barrier widths d_D and d_S . Reducing the total capacitance is attractive as it implies an increase in the charging energy $E_C = e^2/C$. Maximising this charging energy, as well as reducing electrical coupling to the electrodes through wider

Device number	Anchor molecule	QD diameter	QD capping ligand
1	C6S2	5 nm	OA
2	C6S2	3 nm	OA
3	C2S2	5 nm	OA
4	C6S2	5 nm	C6S2*
5	C6S2	5 nm	C2S2*
6	Benzene-1,3-dithiol (CBnS2)	5 nm	OA

Table 2.4 Devices with SA variations. Capping ligands with asterisk (*) are obtained through ligand exchange following the SA on the anchor SAM; being dithiolates they are likely to cross-link QDs within the superlattice.

tunnelling barriers, gives prospect for higher-temperature Coulomb blockade by eliminating both thermal broadening (and preventing thermal fluctuations from overcoming the charging energy) and lifetime broadening.

Another parameter that can be adjusted in the SAM is the interdot coupling. The distance between QDs in the QD superlattice can be adjusted through the ligands decorating the QDs and separating them from one another. Weidman *et al.* list interdot distances obtained by ligand exchanges in PbS QD superlattices [129], and show a large degree of tuneability. The degree of interdot coupling can be interesting to observe new types of transport. Indeed, a high level of interdot coupling can lead to stable NDR [130].

Devices

To investigate differences induced by such variations in the superlattice parameters. One can resort to a statistical analysis of a large number of devices with distinguishable variations.

I made six batches of devices following a recipe similar to that described in Section 2.4.1 for OL junctions; these are listed in Table 2.4, with the respective changes in the SA.

For devices of types 4 and 5 which include a ligand exchange, the treatment was done as follows. After the QD SAM formation applying the recipe from Section 2.4.1, the target ligand was dropcast on the chips, using 10 mM solutions in octane. Following a 10s wait, the chips are spun and rinsed three times with IPA. This was done in the OptoElectronics Group's glovebox with J. Xiao's help. The graphene transfer was then done by myself and D. De Fazio.

The devices were fabricated, some of them are ready to be measured, whilst others require final fabrication steps. This was not done for lack of time, but is being planned with the rest of the research group.

2.6.2 Top-gated devices

Concept

We saw in 2.3.1 that adding a third terminal in a QD junction can lead to a pattern of transport known as Coulomb diamonds which give a reading of the junction's electronic structure and capacitances. The added level of control added by a third terminal, the gate, is desirable as it enables this electronic spectroscopy. Relevant research effort have studied this type of transport in QDs of various types [27, 131, 29, 132, 29, 133].

In the examples cited the junctions consist of single QDs and the structure is compatible with the addition of a gate. Typically a dot is introduced inside a nanogap in such a way that the QD can be gated by charging the Si substrate and using it as a back gate [27, 131, 29, 132, 29].

In our structure, a back gate would be ineffective as the electric field would be screened by the Au bottom electrode. A side gate would also be ineffective as the active QDs are enclosed within micrometre or 100-nanometre size junctions making them inaccessible to an electrostatic gate placed at a junction edge. The thinness of the junctions would also make the fabrication of such a gate without current leakage challenging.

An attractive property of SLG is its transparency. In effect, an SLG electrode is thin and transparent enough to not screen electric fields. This provides us with an alternative arrangement for the addition of a gate. We can a gate on top of the junction so as to electrostatically gate the QDs through the SLG. Gating nanostructures through SLG has been demonstrated recently by Bouvron *et al.* [63] in an STM set-up. Adapting this approach to gate SAL devices would be a very desirable step forward as it would give a level of electronic control thus far unavailable in SAM devices, which are typically thought to be more compatible with commercial technology.

Two attempts were made to construct this device, one by J.M. Fruhman and measured by me with J.M. Fruhman and L.F.L. Eyre, and another attempt with a different design fabricated and measured by myself.

First design

The mask includes features to add a top gate to the basic device; these are shown in the bottom-right of Fig. 2.24 where two gate designs (in red), a one-piece and a two-arm designs, are made possible by using a different alignment in exposure, and an insulating layer (in yellow) covers the active region.

The insulating layer between the graphene electrode and the gate is aluminium oxide Al_2O_3 deposited by Atomic Layer Deposition (ALD). An advantage of ALD is the possibility

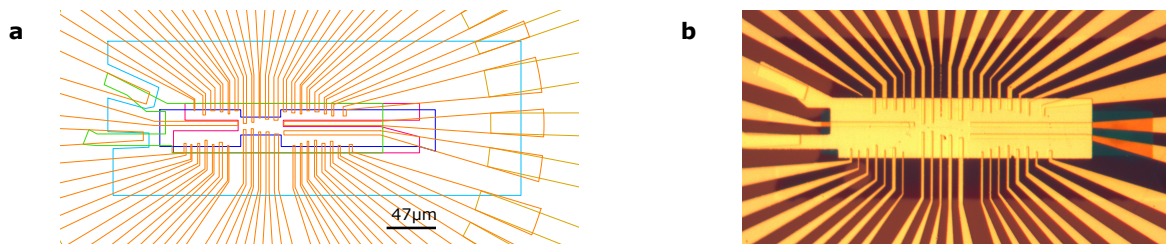


Fig. 2.24 Mask used for first design of device with top gate. **a**, mask design made by J.M. Fruhman including dielectric layer (light blue) and top Au gate (green). **b**, micrograph of a device.

to precisely control the thickness of the deposited layer. ALD is a self-limited CVD process in the sense that it works by cycles of successive reactions and consequently the thickness can be tuned very precisely. In the case of Al_2O_3 , deposition rates of 0.11 nm/cycle are reported [110]. After the evaporation of a thin adhesive layer of aluminium, roughly 10 nm of insulating Al_2O_3 is then deposited by ALD. An AZ Image Reversal resist, which allows to invert the photo-development pattern of the insulating mask feature, is then used to etch the Al_2O_3 around the active region using Decon 90 as the etchant.

After the insulating layer has been deposited, the gate electrode can be evaporated. Again, using standard optical lithography, with the mask feature for the gate, we evaporate 30 nm of Au. It has however been suggested that a prior Cr evaporation would result in better adhesion of this top gate [110].

The electrical set-up used is similar to that described in Section 2.4.2, with an additional voltage source to allow for measurements along both source-drain voltage and gate voltage axes. Firstly the top gate was tested, to make sure the Al_2O_3 dielectric does not leak if the junctions are grounded, following this junctions are measured individually. Unfortunately none of the measured devices exhibited the desired transport profile. Most of the top gates were found to short circuit to the junctions pointing to structural problems in the dielectric. Some devices had a working top gate but most of the junctions were then short circuits, suggesting that the fabrication steps to add the top gate damages the junctions underneath. One junction showed StC type conduction and a quick test showed successful gating of the conduction in it. Two limitations of this design were taken into account in the next attempt to produce a device with top gate. Namely, here there is only one top gate, and a local defect causing a short circuit to the graphene makes this top gate inefficient for the whole device. Secondly, while Al_2O_3 ALD can in principle deliver high-quality dielectric films which

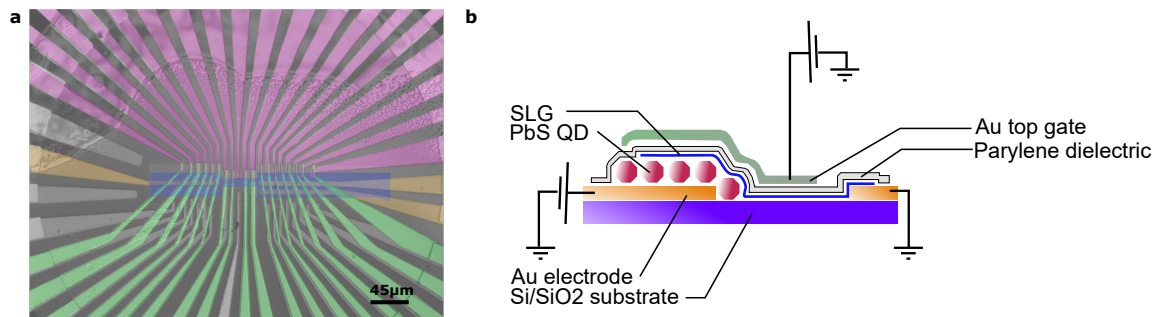


Fig. 2.25 Top-gated device. **a**, false-colour micrograph of a device, where pink is QD SAM-coated Au electrodes, gold is Au fingers, blue is SLG, and green is top gate contacts. **b**, schematic of the device's structure. On top of the standard device, a layer of parylene is deposited and serves as the dielectric. A layer of Au contacts is deposited on top of the parylene and is used as top gates.

conform to the surface topology, the deposition process used was in a chamber at 180°C. Such a temperature is very likely to damage the SAM¹³ and create pinholes in the junction.

Second design

In this second device I made new OL features on an OL mask to address the aforementioned problems. As opposed to the previous design, the top gates are independent contacts each aiming to gate a single contact.

The dielectric chosen is parylene C. Parylene C is a polymer-based insulator used in electronic technology. Its electrical properties make it a robust insulator able to withstand high voltages before leakage, and its pinhole-free and conformal deposition by CVD and impermeability make it a material of choice to protect objects from possible oxidation [134]. The CVD deposition process, unlike ALD, is done at room temperature and room pressure conditions, making it less likely to damage sensitive devices [134]. The thickness deposited can be adjusted through the quantity of precursor (in granular form) placed in the furnace, measured through ellipsometry or profilometry, and etched with O₂ plasma.

Finished devices were taken from batch 1 of Table 2.4. Parylene C was put deposited twice on the device by D. Kos. After a first deposition of thickness 16nm to encapsulate and protect the device, I used an OL process with the initial SLG OL design, deliberately shifted, to etch the SLG away from the contacts appearing lower in Fig. 2.25, making these open circuits. The etch was done using O₂ plasma in an RF asher. With a power of 100 W, a

¹³Alkanethiolate SAMs have been seen to be affected by temperatures above 50°C by our collaborators at the University of Lancaster.

typical etching rate for parylene was measured to be 25 nm/min with an ellipsometer, whilst showing apparent variations across samples surfaces. This is a similar rate to the etching rate of Shipley optical resists with similar parameters. Following this a further 38 nm parylene deposition was realised so as to make the total parylene thickness above the SLG of 54 nm, and 38 nm above the now inactive contacts. The parylene was patterned so as to cover the device's central region¹⁴ Following this a lift-off process was used to deposit the top gates onto the device. Parylene was found to be affected by SVC-14 used in the lift-off process such that it can be removed by it when the temperature is raised; keeping the temperature at room temperature and caution was shown to work. One can see however some bubbling forming in Fig. 2.25 which results from this process. Optical resist was then deposited on the device for protection—just dropped on the surface and heated on a hot plate. An OL process was used to open the bonding pads for electrical bonding, and the devices were diced using a wafer saw by D. Ellis.

A first device was measured in liquid He, in a set-up similar to that described in Section 2.4.2. This preliminary test showed half the contacted gates to work without leaking, the rest showing conduction, either Ohmic or non-Ohmic. However, none of the junctions exhibited the SET behaviour sought after, and were mainly ShCs. It is possible that the plasma etching processes heated the devices and damaged the SAMs thus causing pinholes and ShCs. It is also possible that the apparent instability of parylene in contact with SVC-14 has led to pinholes which short some of the gates with the SLG.

Conclusion

The attempts to obtain a three-terminal device have so far been unsuccessful. The second attempt brings improvements in the design, but the development of more delicate fabrication recipes to deposit and pattern the dielectric. A way to deposit a dielectric without extreme temperature conditions or to pattern parylene without heating the device or partially dissolving the dielectric in SVC-14. The dielectric layer should also be made thinner than 54 nm for effective gating.

Alternatively, different architectures could be found. Using SLG as a bottom electrode would make it possible to use the substrate as a back gate. The difficulty of removing PMMA from the surface of SLG¹⁵ may then prove problematic, or require alternative SLG transfer methods. Work on SA of molecules or QDs on graphene has been studied by various groups, which could inspire further work [45, 29, 135].

¹⁴The relevant OL mask layer needs to be shifted when patterning the SLG so as to allow good electrical contact between the top gates and the Au contacts linked to the bond pads.

¹⁵From experience a $\sim 5\text{-}20\text{nm}$ remains attached on SLG surface and is very difficult to remove using standard acetone baths.

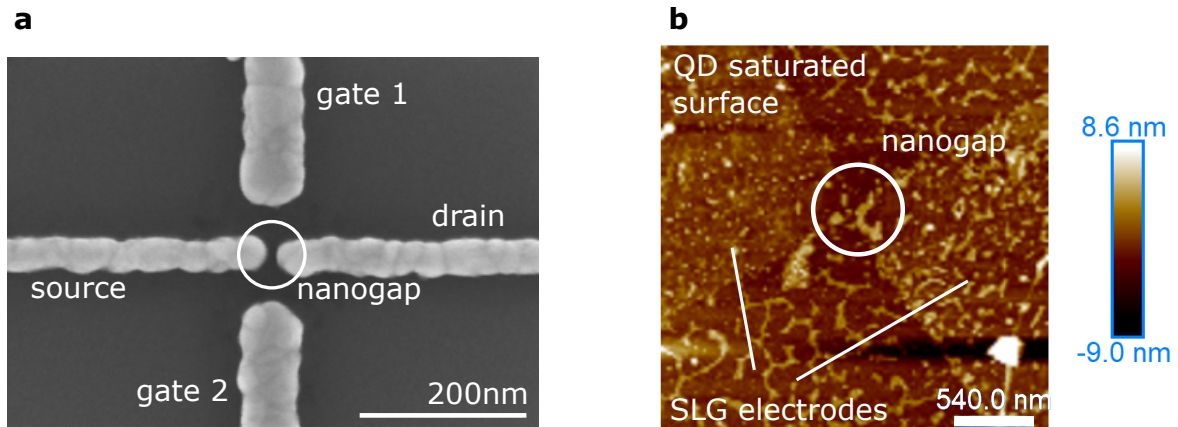


Fig. 2.26 Imaging of nanogap devices used for single-QD studies. **a**, SEM image of a metallic nanogap device taken by O. Chun. **b**, AFM image of a SLG nanogap device decorated with PbS QDs.

2.6.3 Single-quantum-dot junctions

In addition to this work, I initiated collaborations with researchers specialising in nanogap devices to investigate QD transport in a single-QD system.

Metallic nanogaps

The first collaboration is with Y. Majima's group at the Tokyo Institute of Technology. It specialises in QD transport in nanogap devices, where the nanogaps are formed by electroless plating in an Au iodine solution [27] to narrow down the separation between two metallic electrodes initially patterned by EBL. These can form nanogaps of the order of 3 nm. These devices have allowed them to investigate SET transport in single or few-QD arrangements using Au and Si QDs [27, 131, 136, 137].

I started a collaboration with them so as to study transport in PbS QDs in their nanogap devices. Devices of this type were prepared in their laboratory and shipped to us. An SEM image of one of the devices sent to us is shown in Fig. 2.26. I determined a SA process to decorate these devices with input from Y. Majima's group and help from J. Xiao. Such devices have been prepared and measured in our group by W. Guo, S. Ning and J. Girovsky at the time of writing.

The SA process aims to decorate the Au electrodes with QDs in such a way that they be sparsely distributed on the surface. This ensures that single or few QDs find themselves in the nanogap and the transport measured results from a single or few-QD system. This is achieved by using a mixed SAM as an anchor SAM. A first SA process decorates the metallic electrodes with a SAM 1-hexanethiol (C6S), typically through a 24 h immersion

in a 1 mM solution of C6S in octane or toluene. Following this a second SA process takes place whereby the sample is immersed in a solution of 1,8-octanedithiol (C8S2) for a further 24 h; this solution can be of a similar concentration of 1 mM. This second SA results in the formation of a mixed SAM, where most of the surface is covered in C6S, and C8S2 sparsely distributed in the SAM. The C8S2, thanks to its two thiolate ends, serves as the anchor, and its scattered presence in the SAM results in the sparse distribution of the QDs. Similarly the QDs can be deposited on the mixed SAM by an immersion in a 1 mg/mL solution for 24 h with a solvent compatible with the type of QD used (typically octane or toluene for PbS quantum dots). These devices can be measured in a cryogenic probe station owned by the Hitachi laboratory in the Cavendish Laboratory. The set-up allows for measurements down to ~ 30 K, and the control of four independent electrical contacts, which can be used for source, drain, and gate.

Graphene nanogaps

The second collaboration pertaining to nanogap devices is with J.A. Mol's group, formerly at the University of Oxford with G.A.D. Briggs, now at Queen Mary, University of London. They have developed a process to fabricate SLG nanogap devices through electroburning. A SLG layer is patterned in a bow-tie shape, such that there is a central constriction of typically 200 nm. Following this a high current is passed through this constriction; this results in increasing the temperature at the constriction and, in effect, burning the SLG at this constriction. The process can be repeated until the resistance at the constriction has stabilised into that of nanogap. Such gaps vary in size around 2 nm, they occasionally contain residual graphene QDs [29, 138].

I developed a recipe to decorate these devices with PbS QDs with help from X. Wang. Through repeated dropcasting solutions of 25 mg/mL PbS QD in octane. We found through AFM imaging that we could coat the whole device so that it be entirely coated with a QD film attached to the SLG through van der Waals stacking of the OA ligands (see Fig. 2.26).

At the time of writing, devices have been prepared and a measurement in the aforementioned cryogenic probe station is planned with J. Girovsky, and C. Evangeli.

2.6.4 Conclusion

In conclusion structures and strategies have been presented for the study of SET transport in scalable devices. We find that the high yield of the QD SAM devices makes the device concept a promising step forward towards the implementation of SET-based electronic technology. We have developed protocols to study the properties of the device through

measurement and characterisation methods, as well as statistical analysis. Various routes for improvement have been explored through these tools, or the refinement of the device design. We have also suggested ways to accompany the work on SAM devices with single-QD set-ups.

Chapter 3

Memristive switching devices for electrically controllable nano and micro actuation

3.1 Introduction

Although memristors were demonstrated as early as 1801 [139], and even occur in nature [140, 141], the formalism of memristors, as resistors of which the resistance keeps a memory of their operation history is recent, and their experimental realisation was only made official in 2008 [142]. Since then they have become a very active topic of research internationally, and several applications have been found. These rely on the inter-dependence of a memristor's resistance and its past operation, i.e. the existence of conductive and insulating—*on* and *off*—states in the two-terminal devices where the state can be electrically controlled. These two states arise from electrochemical reactions in the material, a change of the material's doping whilst in the circuit. In this chapter we explore the formalism of memristors, in electrical and chemical terms. We report an original memristive device where the chemical reaction causing the memristive behaviour causes electrically controllable mechanical actuation in the system in the form of bubbles of nanometre-to-micrometre sizes in the structure. We discuss the memristive reaction and resulting mechanical deformation and characterise the device both as a memristor and an actuator, and explain the differences from past and standard devices and the potential and novelty it brings in both applications.

Contributions

This chapter reports a project which is a collaboration between J.J. Baumberg's NanoPhotonics Group and the Semiconductor Group with C.J.B. Ford, both in the Cavendish Laboratory of Cambridge. J. Mertens and I initiated the project. I designed, fabricated the devices under C.J.B. Ford's supervision, and with input from D. Kos, J. Mertens and J.J. Baumberg, and assistance from collaborators in the Cambridge Graphene Centre, Z. Zhao and D. De Fazio supervised by AC Ferrari, for graphene growth and processing and operation of the ALD system. The devices were analysed in dark-field microscopy by D. Kos with my assistance. The electrical measurements of the memristive system was done by myself. The imaging and data analysis were done jointly by D. Kos and myself supervised by C.J.B. Ford and J.J. Baumberg. A scientific report was published in Wiley Small [12] where D. Kos and myself are listed as first and equal contributors. Further theoretical input was provided by G. Di Martino, A. Kuhn, and Raman characterisation was done by D. Yoon. The simulations presented in the chapter and the conversion efficiency calculated for all bubbles do not appear in the paper and are my own subsequent work.

3.1.1 History and development of memristivity

The electrodynamic duality principle is the physical principle whereby electric and magnetic fields behave analogously, in that an effect existing for an electric field has an equivalent effect relevant to magnetic fields and conversely. This is most easily seen in Maxwell's equations apparent symmetry. Applying the electrodynamic duality principle to the context of electrical circuitry, Leon Chua postulated in 1971 the existence of a fourth basic circuit element alongside resistors, inductors, and capacitors [143], which he termed memristor, a contraction of memory resistor. Four variables govern electrical systems: current i , voltage v , charge q , and magnetic flux ϕ . Basic circuit elements can be seen as two-terminal elements setting two of these variables in relation. In this picture, a memristor establishes a relation between flux and charge:

$$d\phi = M(q)dq, \quad (3.1)$$

where M is termed the memristance of the system. It should be noted that in a standard resistor M has no dependence on charge, and is equivalent to the component's resistance R . The voltage across a memristor is:

$$v(t) = M(q(t))i(t), \quad (3.2)$$

where t denotes time. Noting that $q(t) = \int_{-\infty}^t i(t') dt'$, one understands that the memristance depends on how much the current has passed through it over time. At any given point the memristor behaves as a resistor, but the value of the resistance is a function of its history, thus justifying the concept of memory resistor.

A seminal Nature paper by Strukov *et al.* [142] from HP indicates that according to this definition¹, memristors have been reported in the literature [145, 146], with their earliest example dating from 1962 [147], thus predating Chua's proposal. These experimental realisations consist of nanoscale oxide films sandwiched between two electrodes. This paper was the starting point of a new field of research motivating intense research efforts to develop memristive devices primarily, but not exclusively, in oxide films. These rely on the capacity for oxygen ions to move inside an oxide when subjected to a voltage, thereby changing the film's doping and conductivity. These experimental characterisations lead Chua to formally define the memristor as any two-terminal element that "exhibits a pinched hysteresis loop for all bipolar periodic input current signals (input voltage signals) which result in a periodic voltage (current) response of the same frequency, in the voltage–current (v – i) plane" in a 2014 review comparing recent memristor properties from an electrical point of view [148].

According to this definition, the first artificial memristor to be realised can be dated back to 1801; Humphry Davy's arc lamp has been shown through a replica [139] to exhibit a memristive behaviour. Interestingly some biological systems comply to this definition, as human skin has shown memristive hysteresis when being contacted [140]. This can be explained by the way fluids are transported with current through skin pores [149]. Experiments contacting plants, leaves of *Dionaea muscipula* (Venus flytrap) and *Mimosa pudica* (a.k.a. sensitive plant, shameplant, or touch-me-not) have shown similar memristive characteristics [141]. The research and development has, however, been most intense in platforms compatible with semiconductor technology. Books and reviews have been published reporting developments in the theory, experiments and applications [150, 148].

Titanium dioxide has been a material of choice in memristive devices, or related structures predating the formulation of the concept. Switching properties of TiO_2 were reported as early as 1968 [151], and around 300 papers were published on TiO_2 until 2008. Of particular interest to the electronic industry, structures similar to a memristive switch have been reported by IBM [152] and patented by Samsung [153]. The 2008 Nature paper explicitly states the potential of TiO_2 for memristors, and was accompanied by a patent application [154]. Electrolytic ion migration in Al_2O_3 was reported in memristive thin-film devices as early as

¹There is some controversy [144] as to whether this realisation of a memristor is indeed the prophetic fourth basic circuit element based on fundamental symmetry arguments. However, defining the memristor as a resistor whose resistance is history-dependent, the experimental realisation is established.

2006 [155, 156]. The electrolytic process has in fact been used since 1899 on much larger volumes as a way to obtain Al metal from its oxide ore in a process known as aluminium smelting [157]. Other architectures have utilised polymers as memristive media working according to a similar mechanism of ion migration [158–160]. A different system relying on a ferroelectric material as the memristive junction has been reported, where the polarisation of the ferroelectric can be switched through voltage and gradually change its resistance in the process [161]. Particularly relevant to CMOS technology, silicon oxide memristors have been developed where the memristive medium is a Si-rich silica film [162].

An alternative mechanism relies on spintronics, where spin polarisation is induced through changes in the magnetic domains, and creates memristive hysteresis [163, 164]. Several reports have demonstrated memristive devices using 2D materials as their active element. An interesting design uses graphene oxide as the memristive medium where a solution of graphene oxide is spun on electrodes, thus forming a film of multilayer graphene oxide [165]. HP also introduced a graphene-based memristive device where a gate facilitates the creation of ion conducting paths [166]. In the first example of a 2D memristor Sangwan *et al.* use single-layer MoS₂ as their memristive medium [167]. In this work, the memristive phenomenon is aided by grain boundaries in the 2D material. These grain boundaries can be seen as 1D channels of dopants in the material; when subjected to a bias these dopant lines can be caused to migrate over micrometre-size distances. Depending on the location and configuration of this grain boundary in the material, i.e. whether there are conduction paths circumventing the boundary or not, the conductivity is affected noticeably, thus creating reversible memristive off and on states respectively.

The use of memristors has been suggested for a range of technological applications. In 2015 the first commercial release of memristor-based technology was announced by American startup Knowm Inc., proposing a memristive component for machine learning applications [168]. It has also been suggested that replacing resistors by memristors in electronic oscillators leads to novel nonlinear oscillatory systems, as the resistance on which the working frequencies depends becomes a function of current and time [169–171]. Other proposed analogue applications include an adaptive filter [172], and a charge-pump phase-locked loop system (useful in communications system as a clock synchronisation mechanism) [173].

3.1.2 Memristive mechanism

Memristive switching relies on the change of conductance of a medium contacted by two terminals. As such, this requires the coupling of a chemical state (doping) with the voltage bias across the medium. Practically, this corresponds to an electrolytic process where a

voltage can drive the ions (cations or anions) across the material, thereby changing its chemical content, and, consequently, its conduction properties. A general review of this process was published by Yang *et al.* [11]. Oxide films, currently probably the most common memristive medium, whilst being stable insulators in bulk, can see their oxygen migrate as ions within it with sufficient energy. If the film is made thin enough, the voltage bias required to drive oxygen ion migration becomes attainable and one can controllably cause this reaction electrically. The ion migration is in itself a current following the direction of the voltage, and additionally results in the creation of reduced conductive filaments within the material. This phenomenon is called electroforming [174]. These conductive filaments are typically few and thin, around 1 nm in diameter. They have been observed in SiO₂-based memristors using transmission electron microscopy (TEM) [175]. A schematic representation is shown in Fig. 3.1. They create conductive paths within the material and short-circuit the initially insulating medium. If the device architecture allows it, the opposite reaction is possible whereby the conductive filaments can be partially re-oxidised (enough to prevent a continuous conductive channel across the material), turning the material back into an insulator. This process is described in the specific case of oxide-based memristors in Sawa's review [176].

An interesting question to ask is the fate of the oxygen that migrates out of the oxide film. A study by Chen *et al.* [177] shows it to depend on the nature of the electrode. They draw a comparison between chemically active and inert metals. In the former case, it is found that with reactive metals, such as Hf and Zr, a dense oxide layer forms at the electrolyte-electrode interface, which hinders the memristive switching. In the latter case, in this instance Ni and Co, but equally true for Au, where the oxygen is released from the material as a gas, and depending on the device geometry, can be trapped in a bubble or released as a gas, either case proving fatal for the device. Such bubbles have been noticed to form in junctions with Pt electrodes and a TiO₂ electrolyte [174]. Interestingly, these bubbles disappear when a voltage is not supplied, indicating that the oxygen spontaneously reintegrates the materials when no bias drives the forming. This is different from the device described in this chapter where using Au electrodes and Al₂O₃ as the electrolyte, bubbles were formed which were stable after removing the voltage.

3.1.3 Actuation at the nanoscale

As technology is reaching the nanoscale in many fields, it becomes important to harness mechanics at this scale. The development of mechanical tools is useful for a range of applications, such as imaging, nanoscale characterisation, sensing, and nanofluidics. Important applications, particularly relevant to this thesis, are atomic force microscopy (AFM) and scanning tunnelling microscopy (STM). As we have seen in Chapters 1 and 2, along with

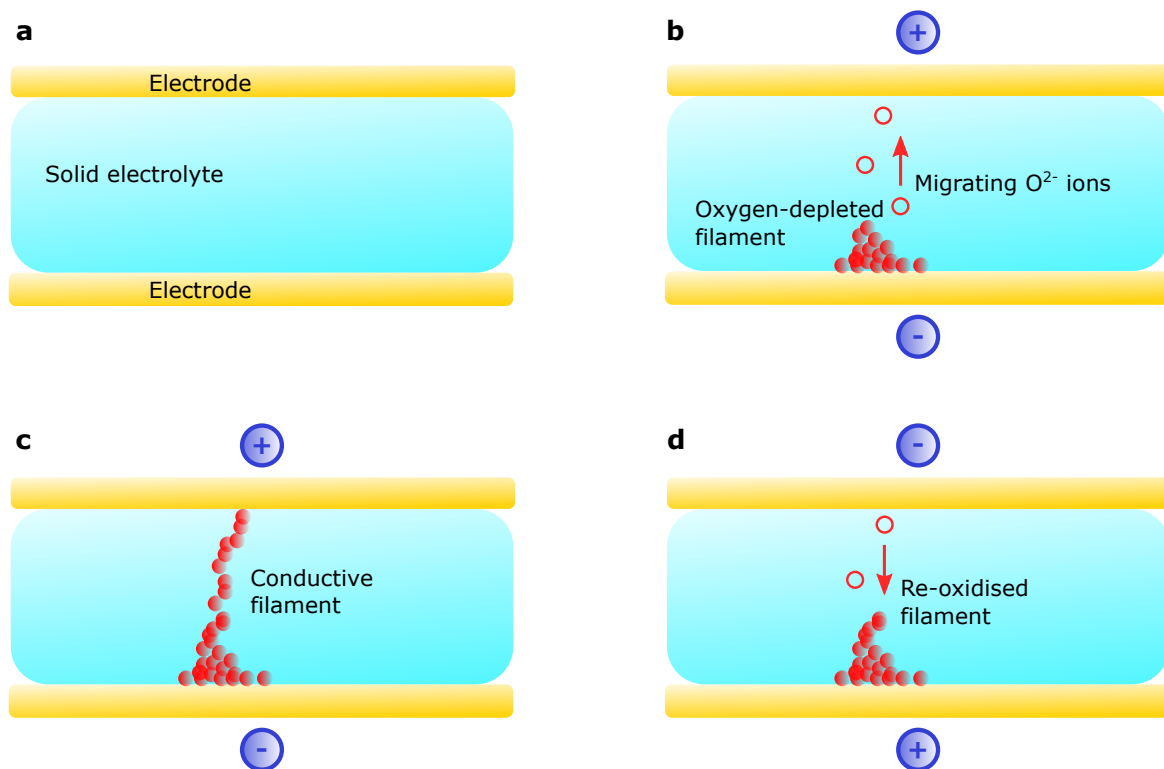


Fig. 3.1 Sketch of the memristive reaction in an oxide film. **a**, initial state of an oxide-based memristor: an insulating oxide film is placed between two electrodes. **b**, oxygen ion migration and oxygen-depleted filament formation as a voltage bias is applied across the film. **c**, memristor in *on* state, a conductive filament fully bridges across the film. **d**, reversal of the transition: a voltage bias in the opposite direction reintegrates oxygen into the reduced filaments, allowing a transition back into the insulating state. Adapted from Ref. [11].

other versions of high-precision actuated-tip-based imaging techniques, these enable extensive characterisation of nanostructures, electrically, energetically, and mechanically. A central part of an AFM is the actuating technology that determines its spatial resolution. This requires the ability to move the tip precisely and reversibly over nanoscale distances. Piezoelectric actuation has been a common mechanism for actuation in AFM set-ups since their creation [178]. A relevant system for this operation is that of bimorphs consisting in two stretchable units that can be alternatively expanded and retracted to operate an actuation by friction. Two types of systems have been the focus of recent research in nanomechanics; these are flexible polymers [179] and carbon-based nanomaterials [180, 181]. In the former case, it is possible to design polymers where the reactivity at the molecular scale can translate into deformation and mechanical forces. Polymer gels are stable through a balance between inter-molecular repulsive and attractive forces which determine a degree of expansion. In

this picture several factors are contributing to the mechanical state of the polymer: the polymer rubber's elasticity, the liquid viscous interaction in the polymer, inertial effects and electrophoretic interactions. These can be tuned in various ways: pH, ion concentration, electrical potential, temperature, solvent and gel composition [179]. Carbon-based materials are attractive in that their electronic properties make them compatible with electrical operation and their integration into CMOS electronic technology is more established. Carbon nanotubes (CNTs) have been discovered to be an appropriate material to constitute bimorphs [180] or nano-tweezers [182] as their morphology is found to be appreciably altered by current, yielding a powerful actuation force, which paved the way for subsequent active research in CNT-based actuation systems [183], CNT-based *artificial muscles* [184–186] and other CNT-based electromechanical devices [187].

3.2 Theory

3.2.1 Transport in memristors

In their seminal publication [142], Strukov *et al.* propose a simple model which assumes ohmic electronic conduction and a linear ionic drift in a uniform electric field with average ion mobility μ_i . In an electric field an ion is caused to drift with a velocity that is determined by its mobility as follows:

$$v_i = \mu_i E, \quad (3.3)$$

where v_i is the drift velocity and E is the electric field [188]. The ion mobility depends on the nature of the ion and that of the material; it has units of $\text{m}^2 \text{s}^{-1} \text{V}^{-1}$. In this picture, the voltage $v(t)$ will be related to the current $i(t)$ as a function of the film's conduction state $w(t)$ in the following way:

$$v(t) = \left[R_{\text{ON}} \frac{w(t)}{d} + R_{\text{OFF}} \left(1 - \frac{w(t)}{d} \right) \right] i(t), \quad (3.4)$$

where R_{ON} and R_{OFF} are the resistances of the conductive and insulating states respectively, and d is the thickness of the film. The state function $w(t)$ is here a distance and represents the penetration of the filament in the material (the length of the conductive filament), and can vary between 0 and d . In this approximation, the conductive state is obtained when a single filament bridge across the insulating material. In practice, this is most often the case as after this filament has formed it offers a conductive path for non-ionic charge carriers. This filament is also assumed to vary negligibly in resistance (which, equivalently, can be interpreted as the assumption that it varies little in its geometry), which is a valid assumption

in many cases reported in the literature [148]. The filament's length $w(t)$ is related to current, as its formation is done through ionic migration. In the approximation where $R_{\text{ON}} \ll R_{\text{OFF}}$, valid in most real systems, the filament length varies according to the equation:

$$\frac{dw(t)}{dt} = R_{\text{ON}} \frac{\mu_t}{d} i(t). \quad (3.5)$$

Integrating this, and defining the integrated current $\iota(t) \equiv \int_{t_0}^t i(t') dt'$, which is the amount of current that has passed through the system during a state transition (having started here at time t_0), we can find an expression for $w(t)$:

$$w(t) = R_{\text{ON}} \frac{\mu_t}{d} \iota(t). \quad (3.6)$$

$\iota(t)$ has dimension of charge, and is a measure of the material's doping. Using this, one can write the memristance of the system as a function of this doping:

$$M(\iota) = \left[R_{\text{ON}}^2 \frac{\mu_t}{d^2} \iota(t) + R_{\text{OFF}} \left(1 - R_{\text{ON}} \frac{\mu_t}{d^2} \iota(t) \right) \right]. \quad (3.7)$$

Simulations using this approach with realistic parameters are shown in Fig. 3.2. Equation 3.7 highlights the importance of miniaturisation for obtaining memristive transport. The d^{-2} dependence means that to operate a similar doping transition, a 1 μm -thick film will require 10,000 times more current than a 10 nm-thick film.

The cyclic aspect of a memristor makes an AC voltage appropriate for characterising it. If one applies an AC voltage of the form:

$$v(t) = v_0 \sin(\omega t), \quad (3.8)$$

where v_0 is the voltage amplitude and ω the driving frequency, it becomes informative to compare the two timescales in the problem, that of the memristive behaviour and that of the driving frequency. Indeed the state of the memristive material changes as a function of time and several cases can be identified depending on the driving frequency and whether it allows for full state transitions in the material. This is the case if

$$\Delta w = R_{\text{ON}} \frac{\mu_t}{d} \int_{t_0}^{\pi/\omega} i(t') dt' = d, \quad (3.9)$$

where at t_0 the material is in its insulating state and π/ω is half the AC period. Within half the period, enough current must flow to fully transition the material from its insulating state into its conductive state. Using this it is possible to extract an approximate expression for the maximum frequency ω_M at which this occurs, which we term the memristor's critical

frequency. Let us rewrite this expression:

$$R_{\text{ON}} \frac{\mu_t}{d} \int_{t_0}^{\pi/\omega_M} \frac{v(t')}{M(t')} dt' = d. \quad (3.10)$$

Assuming a high on-off ratio, for most of the time interval, $M(t)$ can be simplified to the term relevant to its insulating part, i.e. $M(t) \approx R_{\text{OFF}}(1 - (w(t)/d))$. Until the conductive filament is nearly fully formed, at which point the current shoots off over a very small time interval, we shall assume the memristance follows a near-linear decrease². For simplicity, we can approximate $M(t)$ to its average value over the range, i.e. $M(t) \approx R_{\text{OFF}}/2$. This is a valid approximation in the limiting case where the time interval is just enough for the state transition, and it simplifies the problem and resulting expression greatly. This gives us:

$$\frac{2R_{\text{ON}} \mu_t}{R_{\text{OFF}} d} v_0 \int_{t_0}^{\pi/\omega_M} \sin(\omega_M t') dt' = d. \quad (3.11)$$

Integrating and rearranging the factors, we obtain the critical frequency:

$$\omega_M = 4 \frac{R_{\text{ON}} \mu_t}{R_{\text{OFF}} d^2} v_0. \quad (3.12)$$

This equation relates different aspects of a memristor's performance. We notice the inverse dependence on $R_{\text{OFF}}/R_{\text{ON}}$, the maximum on-off resistance ratio; this means that a high on-off ratio, an important property for logic or information storage applications, is detrimental to high-frequency operation. The inverse-square dependence on material thickness d makes it a crucial parameter for the frequency range also.

Varying the AC frequency in the system, as shown in Fig. 3.2.f³, shows different operation regimes, labelled 1, 2, and 3 in the figure. In this example, the ω_M is found numerically to be 3.96 Hz, against 4 Hz as calculated with Eq. 3.12. Regime 1 is the low-frequency regime, where $\omega \ll \omega_M$. In this regime, the on-off resistance ratio observed is the highest obtainable, i.e. that between a fully insulating film and a fully formed conductive filament. An example of this is shown in Fig. 3.2.e. Interestingly, in this regime, the on-off transition is much faster to occur than its opposite, resulting in a rectifying behaviour, where the low resistance state is only seen in one voltage polarity. In the high-frequency regime, where $\omega \gg \omega_M$, the state transition cannot occur within the short period, and the material remains in its off state. An interesting regime is that where the frequency is close to the memristor's critical frequency,

²The variation of the voltage over this half-period being symmetric, i.e. having no net increase or decrease over the interval, justifies this approximation.

³The frequencies displayed in the x-axis are not angular frequencies.

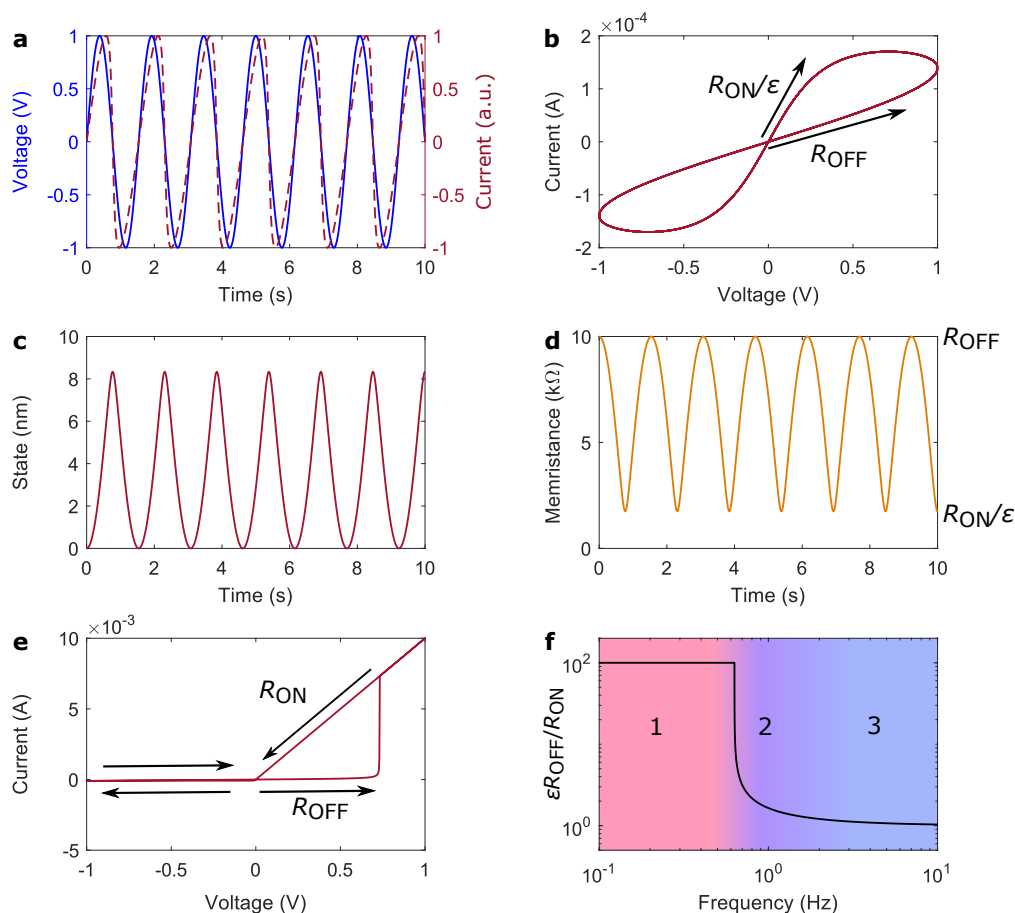


Fig. 3.2 My simulations of a memristive system. **a-d**, evolution of the system of several AC periods. These were produced using the following parameters: $R_{\text{OFF}}/R_{\text{ON}} = 100$, $\omega = 5.03$ Hz, $v_0 = 1$ V, $d = 10$ nm, $\mu_l = 10^4$ nm² s⁻¹ V⁻¹. **e-f**, frequency dependence of the system. Only changing the AC frequency, different regimes, labelled 1, 2, and 3, can be seen in relation to the critical frequency ω_M , found here to be 3.96 Hz—where Eq. 3.12 gives 4 Hz. **e** shows a low frequency regime, at $\omega = 628$ mHz, where the maximum on-off ratio $R_{\text{OFF}}/R_{\text{ON}}$ ratio is reached. **f**, effective on-off ratio $\epsilon R_{\text{OFF}}/R_{\text{ON}}$ as a function of frequency.

$\omega \sim \omega_M$, which we label Regime 2. In this regime, the state transition takes place partially within the half-period. Such a situation is shown in Fig. 3.2.a-c. The filament only forms to 8/10 of the film thickness, sufficient to change the resistance noticeably but not reach the full on-off resistance ratio $R_{\text{OFF}}/R_{\text{ON}}$ possible in the memristor. An attenuation factor ϵ can be introduced, such that the observed *on* state has resistance R_{ON}/ϵ . Unlike the low-frequency regime, the state transition takes place over similar timescales in both directions, resulting in a more symmetric conduction pattern.

3.2.2 Plasmonic detection with nanoparticles on a mirror

The discretisation of the electronic spectrum observed in semiconductor nanocrystals at small sizes was postulated to occur in metallic nanoparticles by H. Fröhlich in the 1930s [75]; whilst having a smaller energy separation between states (typically below 1 meV) than in semiconductors and only observed in extreme conditions [189]. The size dependence of their properties is less obvious than in semiconductor nanocrystals; instead one finds that optically, metal nanoparticles couple strongly with their environment and their spectrum is highly affected by their surroundings. In the long-wave approximation, the dipole moment of a nanoparticle in a medium will be given by

$$\mathbf{p} = \epsilon_0 \epsilon_h \alpha \mathbf{E}_0, \quad (3.13)$$

where ϵ_0 is permittivity in vacuum, ϵ_h is the dielectric constant of the host medium, \mathbf{E}_0 is an applied external electric field and

$$\alpha = 4\pi R^3 \frac{\epsilon_{np} - \epsilon_h}{\epsilon_{np} + 2\epsilon_h}, \quad (3.14)$$

is the polarisability of the nanoparticle with dielectric constant ϵ_{np} and radius R [81]. Two things can be noted in this relation; firstly the dependence on the dielectric properties of the host medium, secondly the divergence of the polarisability for certain values of ϵ_{np} . This dielectric constant can be described as a complex function of frequency, $\epsilon(\omega) = \epsilon'(\omega) + i\epsilon''(\omega)$. The condition for resonance becomes $[\epsilon'(\omega) + 2\epsilon_h]^2 + [\epsilon''(\omega)]^2$ being at a minimum. The solutions to these result in a luminescence spectrum with resonant features that depend on the nanoparticle's environment, and on its coupling to it and that can be used to probe it. It is also possible to selectively couple nanoparticles to more reactive elements in their environment. An interesting configuration separates gold nanoparticles from a bulk gold electrode using a spacer (molecule monolayers or other thin films) [190]; this system is often referred to as the nanoparticle on mirror (NPoM). The externally induced dipole in the nanoparticle is found to induce a mirror dipole in the bulk, affecting the luminescence spectrum [191]. One finds a strong dependence of the spectrum on this spacing; the resonant peaks are redshifted (blueshifted) as the nanoparticles are brought closer to (farther away from) the bulk. Through their luminescence these nanoparticles can be used as sensors of their environment. The analysis of such configurations with different and especially tunable spacings is of interest for probing interaction between these nanoparticles and the bulk.

3.3 Experimental procedures

3.3.1 Device design and fabrication

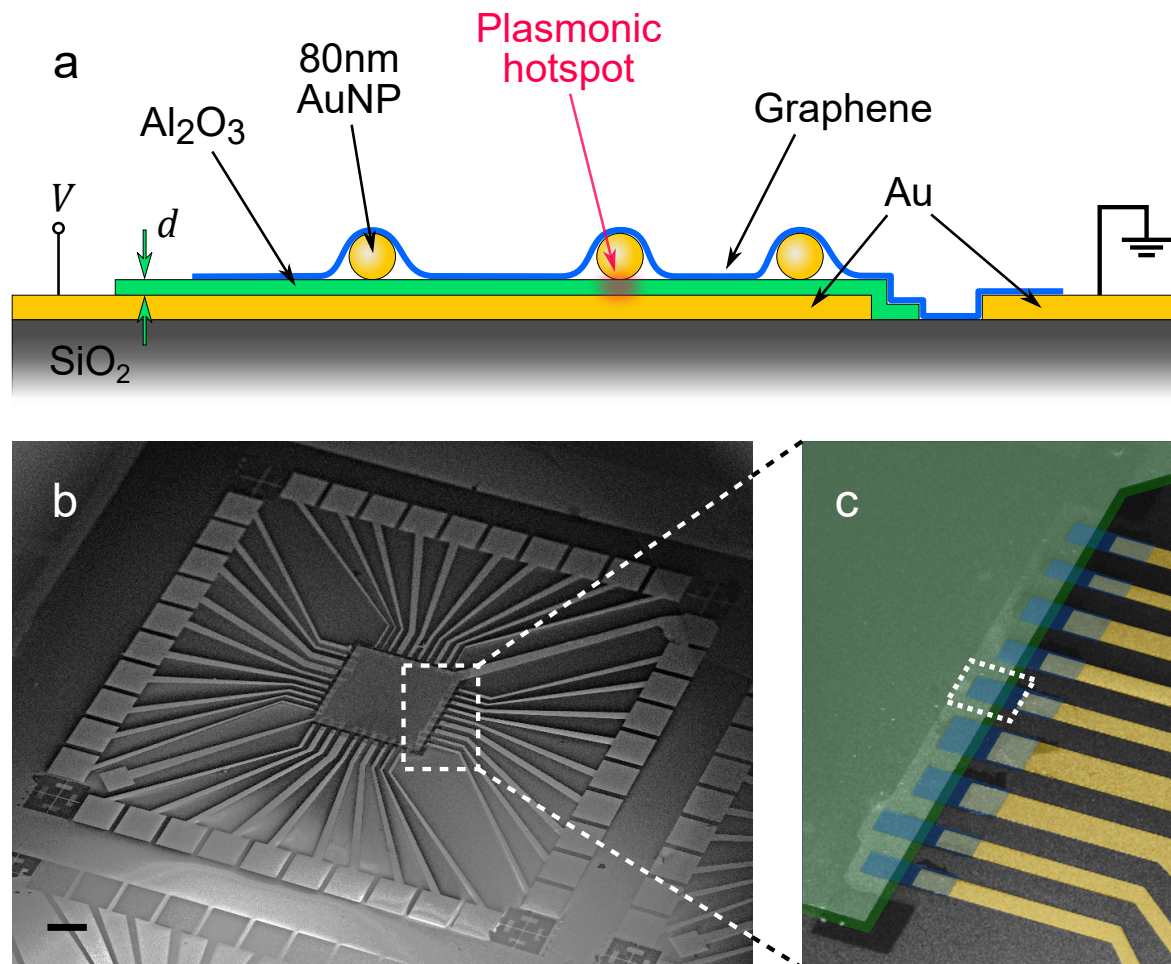


Fig. 3.3 Memristive device structure. **a**, sketch of the device structure. **b**, SEM image of the device; the scale bar is 200 μ m. **c**, false-colour detail of **b**, where yellow is Au, green is the Al₂O₃ film, and blue is SLG. Adapted from D. Kos and H.P.A.G. Astier *et al.* [12].

The device studied in this thesis combines the architecture of a memristor (metal-oxide-metal), with that of the NPoM system (NP-insulator-metal). Its fabrication involves a range of fabrication techniques common in semiconductor research and industry to scalably realise electronic junctions through vertical stacking of the materials on a SiO₂:Si substrate. A sketch and pictures of the device structure are shown in Fig. 3.3. Au is used as a bottom electrode, and constitutes the mirror of the NPoM system. The memristive medium, which provides the plasmonic gap between the NP and the mirror, is Al₂O₃, a standard dielectric in semiconductor devices. On this film Au NPs are dropcast sparsely onto the Al₂O₃ surface.

Finally the whole structure is covered by SLG as the top electrode of the memristor structure. SLG was chosen, as its transparency allows for optical detection of the NPs underneath, and its flexibility allows it to follow mechanical deformation of its substrate. Chemical vapour deposition (CVD) on a sacrificial Cu substrate allows the growth of wafer-scale areas of SLG sheets, which makes it compatible with parallel fabrication of many devices. Each layer is patterned using optical lithography according to an OL mask design made specifically for this study. This mask enables a large mirror in the centre of the device to be coated with Al_2O_3 . An SLG top electrode is patterned into stripes that cover and form junctions on the edges of this structure, and connect these to Au electrodes linked to contact pads appropriate for electrical characterisation. The fabrication aims to use only scalable processes and takes into account the electrical as well as optical aspects of the device.

Substrate

For compatibility with semiconductor industry standards, an SiO_2 :Si substrate was used. The SiO_2 layer is 285 nm thick, which optimises the contrast with SLG, making it visible with optical microscopy.

Au bottom electrode

The bottom Au electrode is deposited via thermal evaporation through a lift-off process done by optical lithography. The pattern consists of several chips to be realised in parallel (6×6). Each chip consists of a central $\sim 1 \text{ mm}^2$ Au mirror separated from electrodes connected to large contact pads appropriate for wire bonding or operation on a probe station. This Au layer, being the mirror of NPoM, needs to be relatively thick to accommodate for the vertical plasmonic modes, in this instance $\sim 100 \text{ nm}$. This thickness is also large enough to facilitate wire bonding for electrical measurements. In the same evaporation, prior to the Au, an interstitial $\sim 20 \text{ nm}$ -thick layer of Ti for better adhesion to the SiO_2 .

Al_2O_3 layer

The Al_2O_3 layer can be deposited by atomic layer deposition which enables the growth of high-quality smooth films of nanometre thickness. These can be pinhole-free over square-micron areas for few-nanometre thicknesses, and the cyclic layer-by-layer deposition ensures a subnanometre control over the obtained thickness. The process is done at 180° C , which ensure a solvent-free deposition. In some processes an adhesive layer of Al is evaporated onto the sample prior to the process, to prime it and ensure better adhesion; this was deliberately not done. Several chips were made with different numbers of deposition cycles, i.e. 30, 60,

90, 120. The thickness expected from a number of cycles varies from system to system and according to parameters of the process, but is usually around 0.12 nm/cycle. The chips with 30 and 120 cycles proved unfit for electrical operation (short-circuited and too resistive respectively), so only those with 60 and 90 cycles will be presented in this report. In an AFM measurement we found the Al₂O₃ thickness in these to be 8 nm and 12 nm respectively. After deposition, the Al₂O₃ is patterned via OL, by protecting a region with photoresist from a subsequent a chemical etch. This process results in removing the Al₂O₃ outside the mirror region. An appropriate etchant for nanometre thicknesses is MF-319 developer with a rule-of-thumb etching rate of 1.5 nm/min, which is what was used (whereas that of buffered hydrofluoric acid would be 1.5 nm/s).

Au NP decoration

An Au NP solution (bought from BBI Solutions) is dropcast on the whole sample, with a concentration calibrated to yield a deposition with a number density of $\sim 0.1 \mu\text{m}^{-2}$. This density needs to be sparse enough to allow for the luminescence measurement of single NPs, i.e. within the collection point of the microscope collecting the spectrum, which is $\sim 1 \mu\text{m}^2$, there needs to be only one NP. The NPs are then sparsely and randomly located over the whole sample including on the structure of interest.

SLG deposition

An SLG sheet the size of the sample was deposited onto it via wet transfer as described in Sec. 2.4.1. After the sample has dried, and PMMA washed away from its surface with acetone, an OL process is used to pattern the SLG into stripes covering areas of typically $500 \mu\text{m}^2$ (with variations to allow for later comparison) on the stacked structure and bridging these to the external Au electrodes. The SLG outside of these regions (protected by photoresist Shipley S1813) is removed by reactive ion etching (RIE). Finally the whole sample is washed in acetone and isopropyl alcohol.

3.3.2 Electrical characterisation

The junctions formed as described in the previous section are then characterised electrically through their I - V spectrum. Two set-ups are used to do this.

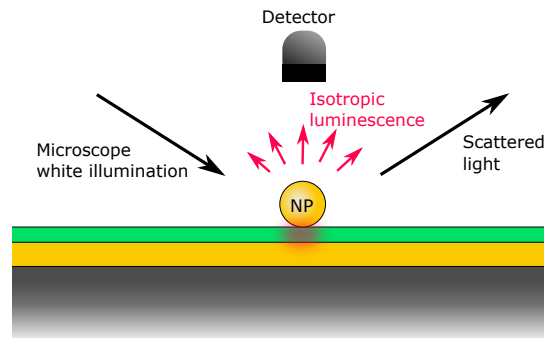


Fig. 3.4 Dark-field optical set-up. The illumination is deviated from the detector so as to collect isotropic luminescence from the NPs.

Cryogenic probe

For the electrical characterisation the chip is also cleaved into devices and the contact pads of the individual contact wire-bonded to a leadless chip carrier (LCC). This LCC is plugged into a cryogenic probe which connects the junctions and mirror to Bayonet Neill–Concelman (BNC) terminals. Connecting these successively to a Keithley 236 Source Measure Unit (SMU), the junctions can be individually measured. The voltage is linearly swept back and forth in the range $[-10\text{ V}; 10\text{ V}]$ at a typical rate of 10 mV s^{-1} whilst the current is recorded. A current compliance limit is applied to prevent currents too high (above $1\text{ }\mu\text{A}$) from running through the device and damaging it. The SMU operation is monitored using the Labview-based software CryoMeas written by C.J.B. Ford.

Probe station

A probe station with two conductive tips connected to a Keithley Series 2600B SMU and ground respectively is used to probe individual junctions. As shown in Fig. 3.3.a, a voltage is applied on the central mirror and each junction's contact pad is successively grounded to measure their I - V spectrum. The SMU is monitored here using a Python code. The set-up includes a microscope which helps to direct the probes, and allows for real-time monitoring of the plasmonic system in dark field (more details in 3.3.3).

3.3.3 Optical set-up

To observe the plasmonic modes of the NPs, the device is observed in dark field. Dark-field microscopy revolves around the separation of two light paths: that of the illumination light and the light collected for forming the image. A special objective unit is used which consists of two separate optical paths: the objective which is used for collecting the light and bringing

it into the detector or eye piece, and a peripheral hollow-cylinder path around the main objective which can direct light onto the sample plane with an incident angle. White light illumination from a halogen source is fed into the objective unit. An adjustable iris placed between the source and the objective unit gives control of which of these two paths the illumination takes to illuminate the sample space. If it directs the illumination through the main objective, one obtains standard bright-field microscopy where the illumination is parallel to the microscope axis, and the light directly scattered from the sample is collected in the objective. If, however, the iris makes the illumination go through the peripheral path, the angle of incidence with respect to the microscope axis being between 60.5° and 69° is not comprised in the collection angle of the objective which only extends to 58° . This means that directly scattered light from a horizontal surface does not enter the objective; thus flat substrates (whether they be metallic or insulating) appear dark, hence the name dark-field microscopy. On the other hand, surface irregularities, or edges can diffract or scatter the light into the objective and thus appear bright. In the case of NPs, these can absorb the incident light at their plasmonic resonance and re-radiate it isotropically, which is collected by the objective. A simplified schematic is shown in Fig. 3.4. In bright-field microscopy this luminescence would be covered and undetectable in the midst of the light directly scattered off the surface. The same image taken in bright and dark fields is shown in Fig. 3.5. In the dark-field image, horizontal surfaces appear dark, and the Au edges appear bright gold, the NPs appear green on SiO_2 and red on the stacked structure. Dark-field microscopy is then an ideal set-up to resolve these plasmonic structures.

In addition, beam splitters can be added between the objective and the detector to divert some of the image for analysis. In this case a 50:50 beam-splitter sends the image into an optical fibre leading it into a cooled spectrometer. The spectrometer has a spectral range of 400 nm to 1000 nm, adapted for our system. The optical fibre only collects light from a small central region from the image such that only a specific point is analysed by the spectrometer. A $50\ \mu\text{m}$ -diameter fibre coupled with a $100\times$ magnification lens results in an effective collection spot on the sample space of $1\ \mu\text{m}$ in diameter for spectroscopy. This allows for the spectroscopy of single NPs provided they are sparse enough on the sample to only find one within this area [192].

The microscope used is a customised Olympus BX51. The light is collected through a $100\times$ dark-field objective (Olympus LMPLFLN100xBD, NA 0.8), and analysed via a fibre-coupled cooled spectrometer (Ocean Optics QE65000). The typical integration time used for spectroscopy is 1 s.

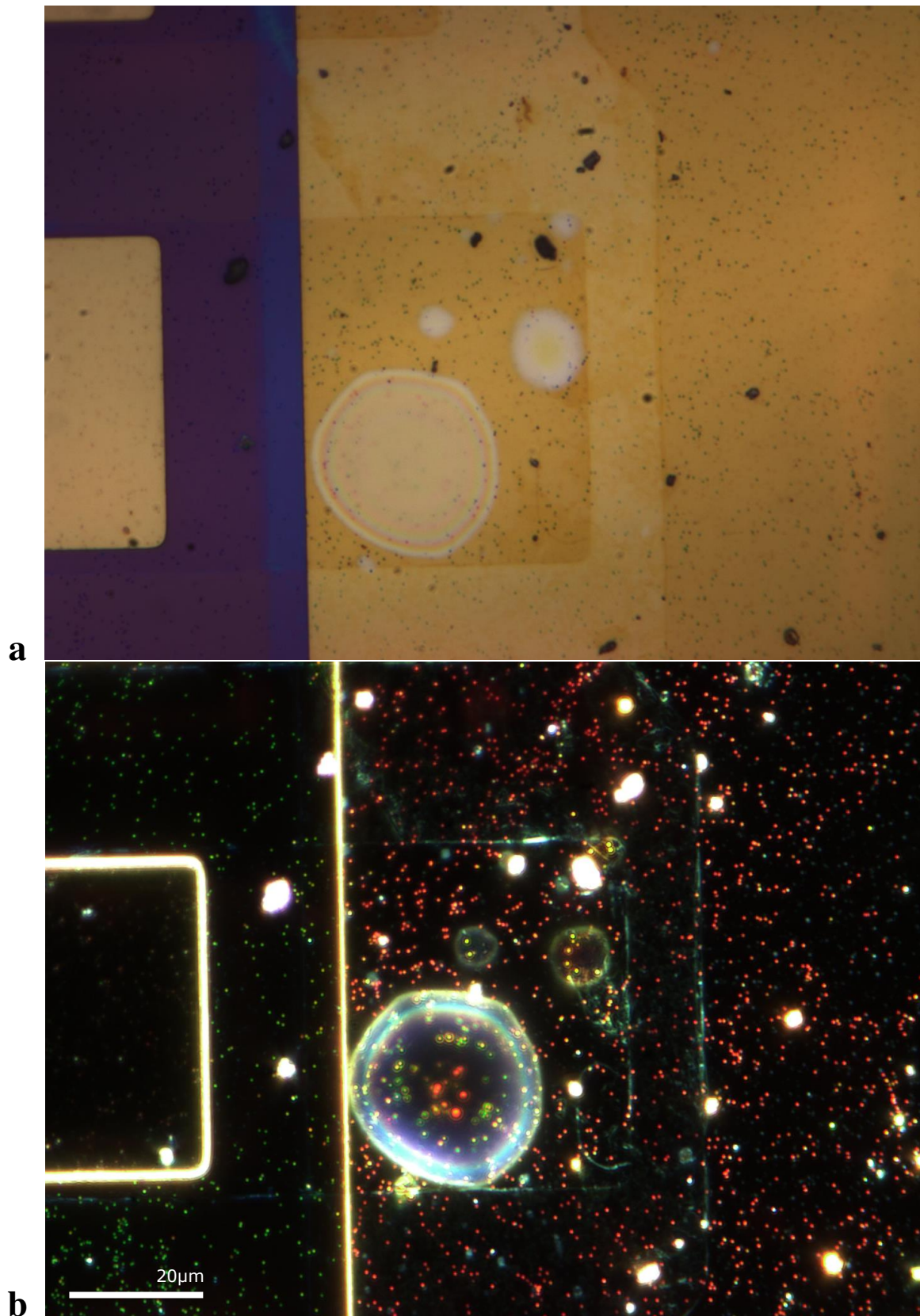


Fig. 3.5 Micrographs of a junction. **a**, bright-field micrograph. **b**, dark-field micrograph.

3.3.4 Imaging

Various forms of imaging are used to characterise the devices. Atomic force microscopy (AFM) in non-contact mode is used to measure the thickness of the Al_2O_3 films, and the inflation of the bubbles obtained after electroforming as described below. The system used is an Asylum Research MFP-3D, and the software used for analysis is the Asylum Research AFM Software.

We used scanning electron microscopy (SEM) and energy-dispersive X-ray spectroscopy (EDX) for high-resolution images and element content analysis of regions of the devices.

3.4 Results

3.4.1 Memristive behaviour

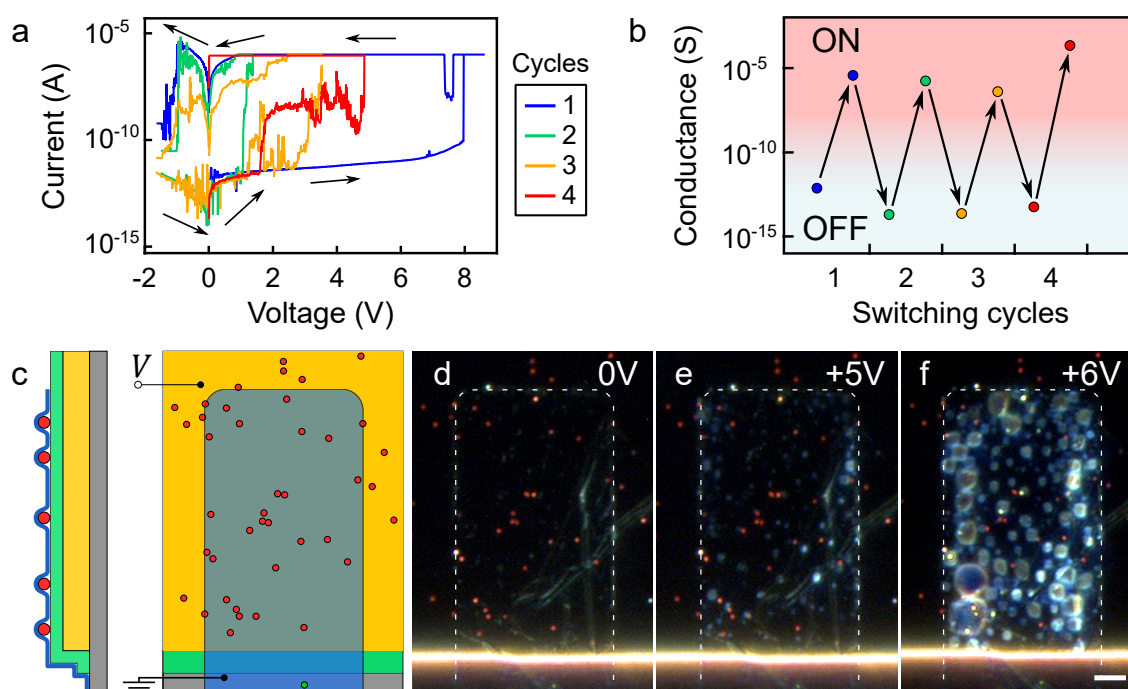


Fig. 3.6 Electrical measurement of the junctions. **a**, I - V cycles in a given junction. **b**, conductance cycles. **c**, sketch of device structure, side view (left) and top view (right). **d-f**, dark-field image of the junction as voltage is applied; scale bar: $5\ \mu\text{m}$. Adapted from Ref. [12].

The devices display memristive behaviour in nearly all junctions. The voltage is slowly increased across the initially insulating device; the resistance is measured to be $R_{\text{OFF}} =$

1–100 T Ω . In terms of conductance per unit area, assuming a typical junction area of $\sim 500 \mu\text{m}^2$, this amounts to $(G_0/A)_{\text{OFF}} = 0.1\text{--}10 \text{ nS mm}^{-2}$. This resistance is stable over a large voltage range. Bringing it to a critical voltage, $\sim 5 \text{ V}$ for a Al_2O_3 thickness of 8 nm and $\sim 7 \text{ V}$ for 12.5 nm, causes the current to jump to its compliance limit (typically 1 μA). The resistance observed then, R_{ON} , ranges from 10 k Ω to 1 M Ω , corresponding to conductance per unit area of $(G_0/A)_{\text{ON}} = 1\text{--}100 \mu\text{S mm}^{-2}$. Bringing the voltage back to the opposite sign leads to a return to the insulating state recovering the off-state resistance value. Several cycles can be produced in this way, although after ~ 5 cycles, the memristive behaviour becomes compromised and the device is *stuck* in its last state. After the initial cycle the voltage required to transition the device into its *on* state is found to be lower (around $\sim 5 \text{ V}$ rather than $\sim 7 \text{ V}$ for the thicker Al_2O_3 films). The resistance of the conductive state is found to vary over as much as two orders of magnitude within the same junction. Certain cycles have display on-off resistance ratios of 10^8 , which has been termed ‘ultrahigh’ in some of the literature

Interestingly, current plateaux can be seen in the conductive state, as apparent in Fig. 3.6.a, which suggests the existence of several conductive configurations and conductive filament arrangements, as does the variation of on-state conductance.

3.4.2 Actuation through bubble inflation

As can be seen in Fig. 3.6, morphological changes appear with increasing voltage and accompany the conductance increase. These can be seen in the form of bubbles gradually expanding, and merging, in dark field. Reversing the voltage to operate the opposite transition also leads to a deflation of these bubbles, which can be completely suppressed in this way. Setting the voltage to zero keeps the bubble stable in its latest stage of inflation for months. This offers a voltage-controlled height adjustment. Interestingly, the location and relative sizes of the bubbles is constant in a junction, and recovered even if they have been completely suppressed in a previous cycle. This allows for repeatable actuation, which can be calibrated. Further information can be drawn from topographic imaging with AFM and high-angle SEM. These confirm the appearance of bubbles which can be a few tens of micrometres in horizontal diameter, and as high as 1 μm in height, most bubbles reaching up to a few hundred nanometres before collapse. Comparing this height measurement with the electrical behaviour and the dark-field imaging reveals the physical mechanism behind this electrically driven actuation. Bulging of the Au as a result of electrostatic force is excluded as a hypothesis, as the inflation is only observed in one polarity, where electrostatic attraction is independent of voltage polarity. Another hypothesis is that the bubbles are contained between the graphene and the Al_2O_3 layer. Two arguments from the imaging contradict this. Firstly

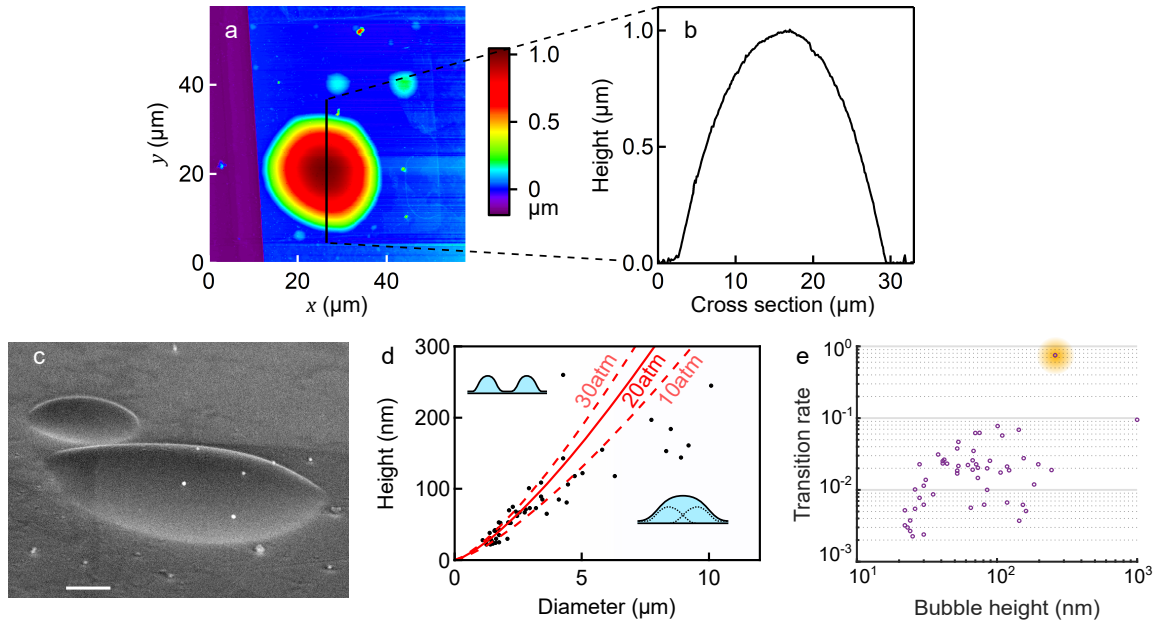


Fig. 3.7 Profile of bubbles. **a**, AFM image of a large bubble. **b**, height cross section of imaged bubble. **c**, high-angle SEM image of a bubble (scale bar 1 μm). **d**, pressure fits from AFM-imaged bubbles. Adapted from [12]. **e**, estimate of the degree of conversion of oxygen transfer from film to bubble for bubbles measured as a function of their height.

Layer	Thickness D	Young's modulus Y	Poisson's ratio ν
Al_2O_3	12.5 nm	170 GPa ([193])	0.24 ([194])
SLG	0.34 nm ([195])	1 TPa ([195])	0.13 ([196])

Table 3.1 Values used for pressure calculations.

the high-angle SEM reveals a highly opaque bubble surface which cannot be accounted for by SLG. Secondly, bubbles beyond a critical size scatter light in dark-field microscopy which cannot be explained by the corrugation of SLG alone. We conclude that the bubbles are related to changes in the Al_2O_3 film.

As mentioned in 3.1.1, ion migration is known to occur in Al_2O_3 , and memristive devices using it have been demonstrated. Our device's structure is expected to deliver this mechanism, and it is confirmed by the electrical behaviour. An electrolytic process occurs in our device's Al_2O_3 film. The voltage drives O^{2-} ions from the film towards one of the electrodes, leaving oxygen vacancies in the material. As explained still in 3.1.2, if this electrode is an inert material such as Au or Pt, which does not oxidise easily, the oxygen ions will not be absorbed into the material, and the following reaction will occur: $2\text{O}^{2-} \rightarrow 4\text{e}^- + \text{O}_{2(\text{g})}$, thus forming bubbles of oxygen gas.

It is possible to infer some properties of these bubbles from first-principle calculations. The pressure inside the reservoirs can be calculated from their geometry. In the case of a spherical-cap shape, the pressure P can be obtained from [197]:

$$P = \frac{Y}{1-\nu} \frac{8Dh^3}{3r^4}, \quad (3.15)$$

where Y is the Young modulus of the reservoir's wall material, ν its Poisson ratio, D its thickness, h the height of the bubble, and r its base radius. Here the wall consists of two layers, i.e. Al_2O_3 (with the analysis restricted to the thicker films on which we did the AFM imaging) and graphene, with properties listed in Table 3.1. Assuming there is little interaction between the two layers, one can add the two pressure contributions from the different layers, i.e.

$$P = \frac{8h^3}{3r^4} \sum_l \frac{D_l Y_l}{1-\nu_l} \approx (8.39 \times 10^4 \mu\text{m atm}) \frac{h^3}{r^4}, \quad (3.16)$$

where $l \in \{1, 2\}$ indexes the layers.

From the imaging done with AFM, we can extract the geometric dimensions and obtain typical pressure values of 20 ± 10 atm. These fits have been performed by D. Kos and are shown in Fig. 3.7.c as a function of the base diameter and height of the bubbles. Interestingly a deviation is seen when the bubbles go beyond $5 \mu\text{m}$ in base diameter. This is understood as the point when neighbouring bubbles typically merge, delaminating the film between them, resulting in a sudden drop in pressure. Calculating this for the large bubble shown in Fig. 3.7.b, with $h = 1.00 \mu\text{m}$ and $r = 13.5 \mu\text{m}$ we get a value of 2.5 atm.

This allows us to draw an estimate of the quantity n_{O_2} of O_2 contained in the bubbles. Using the ideal gas law,

$$n_{\text{O}_2} = \frac{PV}{RT}, \quad (3.17)$$

where, as per standard nomenclature, V is the volume of the contained gas, T the temperature, and $R = 8.3 \text{ J K}^{-1} \text{ mol}^{-1}$ the gas constant, we can find the number of O_2 molecules. The volume of a bubble, where the height is negligible compared to the base radius, is

$$V_{\text{bubble}} = \frac{\pi}{6} h(3r^2 + h^2) \approx \frac{\pi}{2} hr^2. \quad (3.18)$$

Hence for a typical bubble that was measured, with radius $r = 1.27 \mu\text{m}$ and height $h = 67 \text{ nm}$, we obtain a pressure of $P = 9.5$ atm, a volume of $V = 0.17 \mu\text{m}^3$, and an O_2 quantity of $n_{\text{O}_2} = 6.8 \times 10^{-17}$ mol. We can then estimate the fraction of oxygen conversion in the film,

$$f_{\text{O}} = \frac{n_{\text{O}}[\text{in bubble}]}{n_{\text{O}}[\text{in initial film}]} = \frac{2n_{\text{O}_2}}{3n_{\text{Al}_2\text{O}_3}}, \quad (3.19)$$

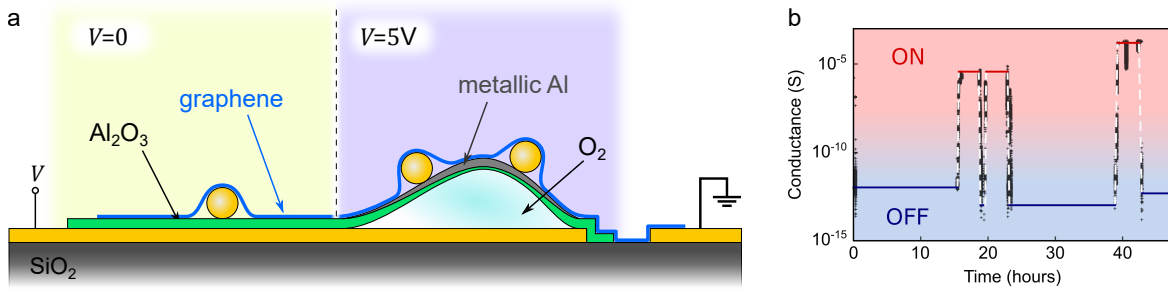


Fig. 3.8 Electroforming in the device structure. **a**, Schematic of the device topography in its inflated form. **b**, Conduction state stability as a function of time. Adapted from [12].

where the $2/3$ factor accounts for the number of oxygen atoms, and $n_{\text{Al}_2\text{O}_3}$ is the initial Al_2O_3 quantity over the area of the bubble. Using molar mass $M_{\text{Al}_2\text{O}_3} = 101.96 \text{ g mol}^{-1}$, density $\rho_{\text{Al}_2\text{O}_3} = 2.8 \text{ g cm}^{-3}$, as well as the volume of a cylinder, we can re-express the quantity

$$n_{\text{Al}_2\text{O}_3} = \frac{\pi r^2 D_{\text{Al}_2\text{O}_3} \rho_{\text{Al}_2\text{O}_3}}{M_{\text{Al}_2\text{O}_3}}. \quad (3.20)$$

Applying this to all bubbles measured with the AFM, we find various degrees of oxygen conversion, varying from 0.2% to 75% as shown in Fig. 3.7.e. The degree of conversion increases with bubble height and diameter, it does not stay constant as the bubble expands. The higher degrees of oxygen transfer correspond to a nearly complete reduction, or smelting, of the Al_2O_3 film and raises interesting questions about the filament topography.

3.4.3 Filament profile

As discussed in 3.1.1, in typical oxide-based memristors, conductive filaments giving rise to the component's *on* state are generally individual nanometre-thin filaments that form stable paths between the two electrodes. The fact that in our devices we see bubbles where the amount of oxygen expelled over square microns nears 10%, or indeed 75% in one bubble, suggests that their filament topography is atypical. If gas accumulates between the film and the electrode, and the bubble keeps expanding as current itself accumulates, what happens to the conductive filaments?

In our films, conduction starts at a site where the conductivity is highest in the junction. As the conduction is done through ion migration or hopping, very small variations in the conductivity, caused by atomic defects in the Al_2O_3 films or at the interfaces can lead to large differences in conductivity over the junction's area and determine a preferred path where the conduction will start. At the site of conduction, the film is reduced to Al (or AlO_{1-x} if

partially reduced), and O_2 is encapsulated between the film and the lower Au electrode. This gas physically separates the reduced film from the electrode, thus opening the contact. At the edges of the bubble, however, the Au bottom electrode is physically closer to reduced Al in the film, making these regions more conductive than in the rest of the film's area. This means that the conduction can then take place at these edges. The ion migration likely is aided by a higher temperature from Joule heating, leading to the expansion of an already existing bubble (rather than a general expansion of bubbles randomly general over the film's area). This is also consistent with the repeatability of bubble sizes and locations over several cycles.

Once the gas is enclosed in the micro-tank, the reduced Al_2O_3 film's lower surface is exposed to O_2 gas, which makes it possible for a native oxide layer to grow. The conversion of Al_2O_3 into Al to sufficiently high a degree will be observable in bright-field microscopy, as can be seen for a bubble converted to $\sim 10\%$ Al in Fig. 3.5. This can be used to obtain some more information about the composition of the protuberance. Bright-field spectroscopy was used by D. Kos and J.J. Baumberg to estimate with a transfer matrix method model an effective layer thickness of a bubble selected for its large size, which was found to have the highest degree of conversion among imaged bubbles. They found that a residual 4.5 nm layer of Al_2O_3 delivered the best fit; close to the 4 nm thickness expected for Al's native oxide in ambient conditions [198].

3.4.4 Plasmonics

NPs sitting on these bubbles have their luminescence spectrum affected by the inflation. An example is shown in Fig. 3.9.a-c, where the spectrum of an NP is compared between the initial (deflated) configuration, and after a bubble has been inflated. One sees that the overall dark-field intensity is higher on an inflated bubble, but also the resonant peak has blueshifted noticeably. Figure 3.9.d-e shows how the change in luminescence is correlated with the current and conductance in the system. The luminescence increase and blueshift follow an increase of the current in the system. In Fig. 3.9.f-g we show that the change monitored with the NP's luminescence spectrum is reversible and can be controlled in a stable manner by setting a voltage in the appropriate direction. Three scenarios can explain the blueshift observed, i.e.

1. a change in the refractive index in the medium surrounding the NP,
2. a change in the spacer's conductivity,
3. a variation in distance from the mirror, which is a nanometre-sensitive process.

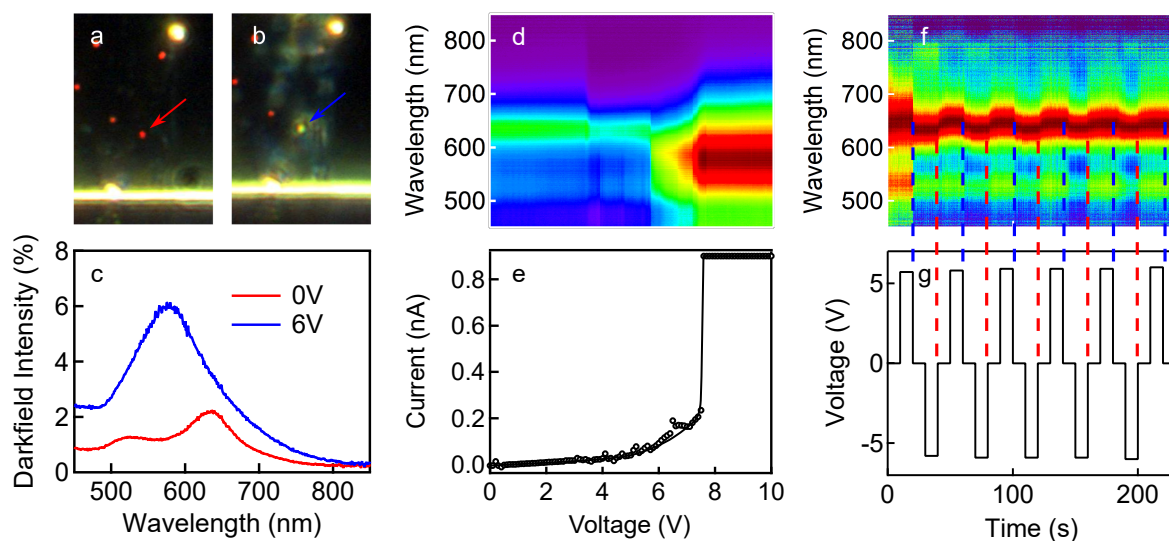


Fig. 3.9 Evolution of the NPs' luminescence spectra during actuation. **a-b**, dark-field micrograph of junction with NP colour switching. **c**, corresponding luminescence spectrum of indicated NPs. **d-e**, NP spectrum (**d**) and corresponding junction current (**e**) as voltage is increased. **f-g**, NP spectrum (**f**) as voltage is swept in cycles (**g**). Taken from [12].

According to the discussion of the electroforming in the film, the three scenarios are expected to occur in parallel in the film. Scenarios 1 and 2 can arise from the reduction, be it partial, of the Al_2O_3 , changing both its refractive index and conductivity. Scenario 3 can arise from two effects, firstly the elevation of the NP from the bottom Au mirror, which results in an increase of the effective mirror separation. Secondly, however, if the reduction of the film is comprehensive enough, the film having become metallic can screen the electric field and act as the mirror in the system. The combination of these two contributions yields a non-trivial correlation with the state of inflation. However, one finds that for an early stage of inflation, when the bubble is only tens of nanometres high, and if the reduction is partial (with a conversion rate sufficiently low) a calibration can be established to correlate within a small range the bubble inflation and the NP's luminescence spectrum. The spectrum displayed in Fig. 3.9.f as a function of voltage cycles in Fig. 3.9.g is estimated to correspond to inflations of the order of 20nm in height, after comparison with AFM. This confirms the NPs as appropriate sensors for the actuation for bubble sizes that are not resolvable optically. Furthermore, restraining the magnitude of the inflation was seen to allow for a higher number of cycles. An appropriate operation range may be one that is best characterised using this paradigm.

3.5 Discussion

3.5.1 Comparison of transport with standard memristor

The system in our devices deviates from the model described in Section 3.2.1 due to the particularity of its electroforming mechanism. Indeed, the theoretical model, which proves accurate for the majority of oxide-based memristors, relies on the assumption that a single or few filaments make a conductive bridge across the material, defining a single *on* state. In our devices, the conductive state can correspond to many different arrangements depending on the advancement of the reduction in the film. Indeed the reduction determines the inflation of the bubbles, and we established that the conduction is primarily at their edges. This could be modelled by adapting the state variable $w(t)$ defined in Section 3.2.1 to account for this. One can define a state variable which would have the dimension of area, as follows:

$$W(t) = w(t)p(t), \quad (3.21)$$

where $w(t)$ is the filament length as previously, and $p(t)$ would be the effective perimeter of all bubbles in a junction. It then describes the area of filaments across the materials (orthogonal to the film plane). This would require establishing an *on* conductance per unit length g_{ON} , such that a wall of filaments of area $dp(t)$, where d , as before, is the film's thickness, would have conductance $g_{ON}p(t)$.

Experimentally obtaining a reliable correlation between these is challenging as the junctions have been found to be too fragile to obtain more than ~ 6 cycles in a given junctions before the memristive behaviour is compromised. Additionally the devices were protected by a current compliance, as SLG is easily damaged by high currents. The SLG was inspected using Raman spectroscopy, performed by D. De Fazio, and was found to have been damaged during device operation, with apparent defects and tears, which can be attributed to the mechanical strain and/or the current. Optical accessibility of the NPs required SLG; however, if one omits these, it opens a range of possibilities for the choice of top electrode, which can be chosen to be more conductive, and more physically robust, with the remaining requirement that they be flexible enough to follow deformations. This would allow a more robust device, and a more complete study of the electrical aspect.

For this study, an AC/DC-mixed measurement set-up, such as the one described in 4.3.3 would be most appropriate, as it would allow a direct reading of the conductance with minimal voltage variation, and thus restrict the current. It would allow the critical frequency to be reliably obtained and the ion mobility in the material to be extracted. The fragility of the devices, rarely able to deliver more than a few cycles, justified our approach of using a DC

measurement giving us more control to monitor the applied voltage in real time. However, in a device optimised to be more stable, an AC method would deliver valuable information.

3.5.2 Bubble control

As discussed, the initial location of the bubbles is random in the junctions. In an industrial application, being able to determine the location of this inflation may be desirable. The conductivity's sensitivity to variations in the thickness/doping in the films gives scope for easily obtaining this control. One could locally dope the film using a focussed ion beam, or partially etch the film in a small area in the junction's film. The conduction will be initiated there and progress to the rest of the film.

Another adjustment that can be made is to further constrain the O₂ encapsulation so as to prevent the gas from escaping the tanks, which is often related to the memristive device's breakdown. The bubbles are expanded beyond the layer's boundary. A rupture in the Al₂O₃/SLG layers can also arise (which D. Kos investigated using an AFM tip with a large force). This could be optimised in a different device architecture by constraining all edges of the junction. For this purpose, defining a pore (not dissimilar to the pattern introduced in 4.3.2) where an *active* film is surrounded by a thicker insulator less likely to contribute to current. Here the junction and the surrounding insulator could be the same material with different thicknesses. Alternatively, other insulators unlikely to undergo ion migration can be used in addition; parylene could be one such candidate, as a robust insulator with limited electrical leakage.

Another possible limitation of the structure is the incomplete re-oxidation of the layer when deflating bubbles. The re-oxidation of the filaments may then be partial, and although the bubbles are deflated, their oxygen content may be reduced from the previous cycle. This would limit the number of cycles that can be operated in a device. In this respect, it is possible that a large degree of oxygen conversion would be unlikely to provide a device operable over many cycles. However, we have seen that limiting the inflation to nanometric sizes—to the point that they are best observed using the NPs' luminescence—can result in more successive cycles. Optimising an operation range which maximises reproducibility would be an interesting step forward in demonstrating a technologically relevant device.

3.6 Conclusion

I have presented a device that combines electrical and mechanical memories for electrically operated actuation. We analysed the two aspects and explained their correlation. The device

architecture has potential for precisely electrically controllable high-force actuation at the nano and micro scales. I characterised the memristive reaction electrically and discussed its deviation from standard memristive operation. The actuation was tracked and characterised by AFM and other imaging techniques. We explored how Au NPs deposited on the surface of the mechanically and chemically changing films had potential for detection through their plasmonic coupling with their environment in the device. The investigation of the electronic behaviour and device topography offer a deviation from standard memristive behaviour, in the electroforming pattern and resulting electronic behaviour; this has potential for a novel kind of such components both for high *on-off* resistance ratio memristive switches, and for applications in nano and micro-scale actuation.

Chapter 4

Thermoelectricity in molecular self-assembled monolayers

4.1 Introduction

In this chapter we report on a project aiming to develop thermoelectric devices based on molecular self-assembled monolayers (SAMs). Along with C.J.B. Ford and collaborators B.J. Robinson (University of Lancaster), C.J. Lambert (University of Lancaster), and M.R. Bryce (University of Durham), we wrote an application for a research council grant which was accepted and started in Oct. 2017. The role of my group in the Cavendish Laboratory as part of this collaborative grant is to develop thin-film devices which contact molecular SAMs and utilise them for enhanced thermoelectric conversion for energy harvesting. In the frame of this project I set out ways to get the project started through benchmarking devices and experiments. This chapter contains a discussion of relevant research fields, technological developments and theory. It presents device architectures and measurement protocols to develop the target device, which should eventually be applicable to a variety of molecules, in particular novel molecules developed as part of the research grant. The results presented in this chapter are preliminary in that more devices and experiments are being planned at the time of writing as well as parts of data analysis being on-going.

Contributions

In this project I contributed to design and write the vision for the grant along with the its other authors. As part of this grant, J. Girovsky was employed as a research assistant in our group. I proposed the protocol for thermoelectric measurement and together with J. Girovsky designed the *I-V* characterisation set-up. We established the relevant measurement set-ups

together. I proposed the project of developing devices contacting alkanethiols as a proof of concept experiment for effective electrical probing of molecular SAMs. In the first batches of devices, J. Girovsky was shadowing me and I trained him on the various fabrication processes. The devices according to the design with pores, as described in Sec. 4.3.2 was designed and calibrated by me and the devices also fabricated and analysed by me with J. Girovsky's help. Measurements of the devices were shared between J. Girovsky and me on a set-up we automated. The BOC8S structure and associated study described in Sec. 4.3.1 was proposed by me. For all devices listed in this chapter I performed all steps of fabrication; for batches consisting of many devices parts of the processes were done together with J. Girovsky. I set out the protocol for the statistical analysis of the devices, and the data extraction has been shared between J. Girovsky and me. The project was supervised by C.J.B. Ford.

4.2 Thermoelectricity

The thermoelectric effect is an effect whereby a temperature gradient is associated with an electric potential difference. It has attracted attention as a green method to extract energy from naturally generated heat (e.g. as a complement or an alternative to photovoltaics) and recover some of the thermal energy discarded in some exploited thermodynamic processes (e.g. turbines, steam engines). In low-temperature physics, it can be attractive to regulate temperature more locally than the cold bath of a cryostat and go beyond its temperature limitations. More recently it was realised that such effects were enhanced by, and could be intertwined with, quasiparticle transfers in low-dimensional nanostructures such as nanowires and quantum dots. This has led it to be a focus of theoretical and experimental condensed matter research.

4.2.1 First principles

Consider a conducting or semiconducting element placed between two heat baths of different temperatures, a hot reservoir at T_H and a cold reservoir at T_C . The temperature gradient will lead charge and heat carriers to diffuse from the hot reservoir to the colder one. An intuitive picture of the effect would consist in considering that the carriers travel faster at higher temperature and would be slower in a colder medium, this means that charge carriers are more localised in the cold part than they are in the hot one which they would leave more readily. This results in a net charge transfer from the hot end to the cold end. The first reported observation of this effect is attributed to Thomas Seebeck in the 1820s [199]. The quantity describing the amplitude of that effect is named after him; the Seebeck coefficient S

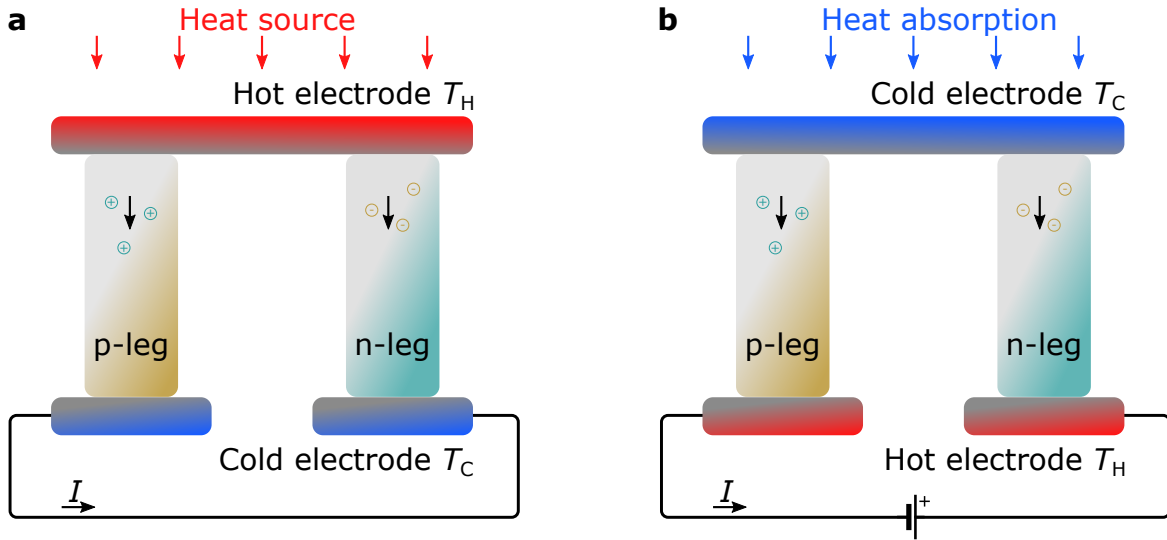


Fig. 4.1 Sketch of basic thermoelectric cells. **a**, Seebeck cell: heat supplied by the environment generates current in the circuit via the thermoelectric effect. **b**, Peltier cell: supplying current to the cell creates a temperature difference between the two surfaces.

of a system is expressed in its simplest form as:

$$S = \frac{V}{T_H - T_C}. \quad (4.1)$$

A more precise expression considers the generated electric field and the temperature gradient with respect to linear position,

$$S = \frac{-\left(\frac{\partial V}{\partial x}\right)}{\left(\frac{\partial T}{\partial x}\right)}. \quad (4.2)$$

This also implies that the resulting voltage depends on the nature of the charge carriers in the medium. For a *p*-type semiconductor where current is carried by positive holes, $S > 0$, whereas in a *n*-type semiconductor, $S < 0$. A basic thermoelectric generator would be constituted of two thermoelectric media, as described in Fig. 4.1. The voltage thus created will be given by

$$V_S = (S_p - S_n)(T_H - T_C). \quad (4.3)$$

The reverse effect whereby a current leads to a temperature difference was discovered by Jean C.A. Peltier in 1834 [200]. Peltier's law is as follows:

$$\Phi = \Pi J, \quad (4.4)$$

where Φ is the heat flux, Π is the Peltier coefficient of the medium, and J the current density. The Seebeck and Peltier effects are in essence the same physical phenomenon and both relevant constants are related through the relation: $\Phi = STJ$, where T is the temperature of evaluation¹. A Peltier cell is shown in Fig. 4.1.b.

Two equations describe the heat and charge transfer in the thermoelectric media:

$$J = \sigma E - S \sigma \frac{\partial T}{\partial x}, \quad (4.5)$$

$$\Phi = STJ - \kappa \frac{\partial T}{\partial x}, \quad (4.6)$$

where E is the applied electric field (not generated by the temperature gradient), κ is the thermal conductivity of the medium and σ is the electrical conductivity.

4.2.2 Thermoelectric efficiency

It is important to consider the efficiency of this conversion. Using Eq. 4.5 and 4.6 one can show the efficiency of the system to be given, in optimal load conditions, by:

$$\eta = \frac{T_H - T_C}{T_H} \frac{\sqrt{Z\bar{T}} + 1 - 1}{\sqrt{Z\bar{T}} + 1 + \frac{T_C}{T_H}}, \quad (4.7)$$

where

$$Z\bar{T} := \frac{S^2 \sigma \bar{T}}{\kappa}, \quad (4.8)$$

$\bar{T} := (T_H + T_C)/2$ being the average temperature. The dimensionless quantity $Z\bar{T}$, is known as the thermoelectric figure of merit of the system and is the most commonly quoted index of performance for thermoelectric devices, most commonly written ZT . One notes that the limit $\lim_{Z\bar{T} \rightarrow \infty} \eta = (T_H - T_C)/T_H$ is equal to the Carnot efficiency of a heat engine working at these temperatures and is the highest possible heat-energy conversion efficiency. The aim is then to maximise the figure of merit, as it corresponds to a higher conversion efficiency. As seen, for a given temperature this is achieved for low thermal conductivity κ , high electronic conductivity σ and high Seebeck coefficient S . Research has been conducted to find natural or synthetic bulk materials which optimise this [201]. From this view-point, graphene being an excellent heat and electric conductor would be a rather poor thermoelectric material with a Seebeck coefficient of order $10 - 100 \mu\text{VK}^{-1}$ in its pristine form compared to the most

¹Generally taken to be the average between the two reservoirs, i.e. $(T_H + T_C)/2$ in the Seebeck configuration.

commonly used thermoelectric material Bi_2Te_3 which has a coefficient of $0.1 - 0.25 \text{ mV/K}$ when evaluated around 300 K [202].

This poses to the question: "what optimises the thermoelectric performance of a material?" Looking at the figure of merit defined in Eq. 4.8, we can note various routes. Firstly, one notes that the thermal conductivity is the sum of two contributions, i.e.

$$\kappa = \kappa_e + \kappa_{\text{ph}}, \quad (4.9)$$

where κ_e is the electronic contribution to the thermal conductivity, and κ_{ph} is the phononic contribution to the thermal conductivity [203]. There exists an inherent conflict in trying to maximise the electrical conductivity σ whilst minimising the thermal conductivity, as the electrical conductivity and the electronic contribution to the thermal conductivity κ_e are related by the Wiedemann-Franz law [203]:

$$\frac{\kappa_e}{\sigma} = LT, \quad (4.10)$$

where $L = (\pi k_{\text{B}}/e)^2/3 = 2.4 \times 10^{-8} \text{ J}^{-2} \text{ K}^{-2} \text{ C}^{-2}$ is a constant called the Lorenz number. This relation strictly restricts the extent to which the thermoelectric effect can be optimised². For an efficient thermoelectric generator it is desirable to suppress the phononic contribution κ_{ph} , i.e. to have $\kappa_{\text{ph}} = 0$. This delivers, using Eq. 4.8 and 4.10, the expression for the figure of merit:

$$Z\bar{T} = \frac{S^2}{L}, \quad (4.11)$$

where we note that the temperature dependence has disappeared and that the performance depends then solely on the system's Seebeck coefficient. This regime is an attractive goal in the development of thermoelectric materials and explains the common use of granular or disordered structures such as powders and polymers [206, 203].

4.2.3 Thermoelectricity and density of states

The two equations describing charge and heat currents across a material with cross section A , sandwiched between two electrodes of different potential and temperature, as described in

²The failure of the Wiedemann-Franz law has been studied in recent years for exceptional systems. In mesoscopic systems, at finite temperature, particular geometries making use of quantum interference can cause deviations halving the κ_e/σ ratio [204]. In Fermi gases in the normal-to-superfluid transition, where heat and particle transport timescales are seen to diverge causing a breakdown of the Wiedemann-Franz law [205].

Eq. 4.5 and 4.6, can be written so as to make the density of states of a material explicit:

$$\begin{pmatrix} I \\ \dot{Q} \end{pmatrix} = \frac{2}{h} \begin{pmatrix} e^2 L_0 & \frac{e}{T} L_1 \\ e L_1 & \frac{1}{T} L_2 \end{pmatrix} \begin{pmatrix} \Delta V \\ \Delta T \end{pmatrix}, \quad (4.12)$$

where $I = JA$ is the electric current, $\dot{Q} = \Phi A$ is the heat current, ΔV and ΔT are respectively the differences in potential and temperature between the two electrodes, and where

$$L_n = \int_{-\infty}^{\infty} (E - E_F)^n \mathcal{T}(E) \left(-\frac{\partial f(E, T)}{\partial E} \right) dE. \quad (4.13)$$

In this expression, E_F is the system's Fermi energy, $\mathcal{T}(E)$ is the transmission coefficient for electrons of energy E passing through the system from one electrode to the other, and $f(E, T)$ is the Fermi-Dirac distribution function. Using this, in the $\Delta T = 0$ case, one can express the system's electrical conductance $G = \left(\frac{I}{\Delta V} \right)_{\Delta T=0}$ as

$$G = \frac{2e^2}{h} L_0, \quad (4.14)$$

and conversely, in the $I = 0$ case, the Seebeck coefficient, $S = -\left(\frac{\Delta V}{\Delta T} \right)_{I=0}$, as

$$S = \frac{-1}{eT} \frac{L_1}{L_0}. \quad (4.15)$$

A standard approximation assumes that $\mathcal{T}(E)$ varies slowly on the scale of $k_B T$ close to E_F . In this approximation, in

$$L_0 = \int_{-\infty}^{\infty} \mathcal{T}(E) \left(-\frac{\partial f(E, T)}{\partial E} \right) dE, \quad (4.16)$$

We can then use the first-order Taylor expansion around E_F :

$$\mathcal{T}(E) \approx \mathcal{T}(E_F) + \left. \frac{d\mathcal{T}(E)}{dE} \right|_{E=E_F} (E - E_F), \quad (4.17)$$

so as to obtain:

$$L_0 \approx \int_{-\infty}^{\infty} \left(\mathcal{T}(E_F) + \left. \frac{d\mathcal{T}(E)}{dE} \right|_{E=E_F} (E - E_F) \right) \left(-\frac{\partial f(E, T)}{\partial E} \right) dE. \quad (4.18)$$

Separating terms and removing constants from the integral yields:

$$L_0 \approx \mathcal{T}(E_F) \int_{-\infty}^{\infty} \left(-\frac{\partial f(E, T)}{\partial E} \right) dE + \left. \frac{d\mathcal{T}(E)}{dE} \right|_{E=E_F} \int_{-\infty}^{\infty} (E - E_F) \left(-\frac{\partial f(E, T)}{\partial E} \right) dE. \quad (4.19)$$

The integral in the first term is unity as $\frac{\partial f(E, T)}{\partial E}$ is a normalised function; that in the second term is easily seen to be zero from parity arguments. This yields:

$$L_0 \approx \mathcal{T}(E_F). \quad (4.20)$$

Using the same expansion in

$$L_1 = \int_{-\infty}^{\infty} (E - E_F) \mathcal{T}(E) \left(-\frac{\partial f(E, T)}{\partial E} \right) dE \quad (4.21)$$

gives

$$L_1 \approx \mathcal{T}(E_F) \int_{-\infty}^{\infty} (E - E_F) \left(-\frac{\partial f(E, T)}{\partial E} \right) dE + \left. \frac{d\mathcal{T}(E)}{dE} \right|_{E=E_F} \int_{-\infty}^{\infty} (E - E_F)^2 \left(-\frac{\partial f(E, T)}{\partial E} \right) dE. \quad (4.22)$$

We recognise the integral from the first term which is zero. Noting that the Lorenz number is $L = (1/eT)^2 \int_{-\infty}^{\infty} (E - E_F)^2 \left(-\frac{\partial f(E, T)}{\partial E} \right) dE$, we find the expression:

$$L_1 \approx (eT)^2 L \left. \frac{d\mathcal{T}(E)}{dE} \right|_{E=E_F}. \quad (4.23)$$

Using this approximate expression in Eq. 4.15, gives us:

$$S \approx -eTL \frac{\left. \frac{d\mathcal{T}(E)}{dE} \right|_{E=E_F}}{\mathcal{T}(E_F)}, \quad (4.24)$$

which, recognising a differential identity, delivers the expression:

$$S \approx -eTL \left. \frac{d \ln \mathcal{T}(E)}{dE} \right|_{E=E_F}. \quad (4.25)$$

This expression is one of importance: the Seebeck coefficient depends on the derivative of the logarithm of the transmission function of the system; it is enhanced by sharp variations in the system's density of states. These sharp features can be obtained by constraining the spatial dimensions of a material, such as nanowires (1D) or quantum dots (0D). Pioneering work on thermoelectricity in constrained structures, in particular by Hicks and Dresselhaus [207], was done in the 1990s, and has since become an active field of research in low-dimensional physics and molecular electronics [208–210]. The electronic spectrum of an ideal quantum dot, a potential well, is described by a series of δ -functions [9]. In a real system two main effects broaden these peaks: electron lifetime in QDs and coupling to the electrodes causing homogeneous broadening [13], and temperature causing inhomogeneous broadening [210]. In practice this implies several points where a trade-off needs to be reached. The broadening due to coupling to the electrodes is increased as the system is put in closer contact with the electrodes, which also increases the electrical conductance of the system. Secondly, although a very sharp variation due to a fast-varying DOS causes an increase in the Seebeck coefficient, this also restricts the energy window where the system can be used as a TEG; a DOS consisting of a series of δ -functions would be inoperable in practice as the TE efficiency would be infinitely high, but only in the infinitely narrow slopes on either side of the δ -functions.

4.2.4 Thermoelectricity in a weakly coupled junction

It was realised in the 1990s that beyond the properties of these bulk materials, the thermoelectric efficiency could be further improved by changing their electronic structure through dimensional constraints. The relevant quantities κ , σ and S are all functions of the electronic structure. We showed mathematically in Sec. 4.2.3 that sharp features in the electronic spectrum optimised the figure of merit. It is then interesting to consider the thermoelectric effect in the limit case of a discrete spectrum, that of a quantum dot.

Two-dimensional layer stacking of crystal lattices which effectively works as a succession of two-dimensional quantum wells was found to increase the efficiency and has been used to develop more efficient bulk thermoelectrics [207]; correlation of thermoelectrical efficiency and spatial confinement in 1D nanowires has been studied since [202]. The study of thermoelectricity in quantum dots has attracted some attention and various models of heat engines of Coulomb-blockaded systems have been studied experimentally and theoretically [211, 212, 208]. Theoretical work generally uses a master equation similar to that described in Sec. 2.3.1, and correlates heat current to electronic transfers [213].

A simplified model considers a dot with a single energy level ϵ_d —a valid approximation if $e^2/2C, \epsilon_{i+1} - \epsilon_i \gg k_B T$, and two reservoirs, source S and drain D, continuous in energy at

temperatures T_S and T_D respectively [214]. One can adjust the electrochemical potential of either reservoir r through voltage, $\mu_r = eV_r$, with a precision finer than the thermal energy.

If one considers two states of the dot, 0 (energy level unoccupied) and 1 (occupied), the master equation is then given by:

$$\begin{pmatrix} \sum_r \gamma_{r,1 \rightarrow 0}^- & -\sum_r \gamma_{r,0 \rightarrow 1}^+ \\ -\sum_r \gamma_{r,0 \rightarrow 1}^+ & \sum_r \gamma_{r,1 \rightarrow 0}^- \\ 1 & 1 \end{pmatrix} \begin{pmatrix} P(0) \\ P(1) \end{pmatrix} = \begin{pmatrix} 0 \\ 0 \\ 1 \end{pmatrix}, \quad (4.26)$$

where, for simplicity, we write the transition rates as

$$\gamma_{r,1 \rightarrow 0}^- = a_r f_r, \quad (4.27)$$

$$\gamma_{r,0 \rightarrow 1}^+ = a_r [1 - f_r] \quad (4.28)$$

where a_r is defined consistently with Eq. 2.15 and the Fermi-Dirac distribution function $f_r = 1/[1 + \exp((\epsilon_d - \mu_r)/k_B T_r)]$ now has a temperature specific to its reservoir r (source or drain). In this case, the current through a barrier between reservoir r and the dot is given by:

$$I_r = e [\gamma_{r,1 \rightarrow 0}^- P(0) - \gamma_{r,0 \rightarrow 1}^+ P(1)]. \quad (4.29)$$

This can be shown, using simple identities, to result in a total current

$$I = e \frac{a_S a_D}{a_S + a_D} (f_D - f_S). \quad (4.30)$$

From this, one can extract the heat extraction rate from the drain:

$$\dot{Q}_D = (\epsilon_d - \mu_D) \frac{I}{e}, \quad (4.31)$$

and the power produced by the system in the flow of electrons from drain to source:

$$P = (\mu_S - \mu_D) \frac{I}{e}. \quad (4.32)$$

This results in an efficiency

$$\eta = \frac{P}{\dot{Q}_D} = \frac{\mu_S - \mu_D}{\epsilon_d - \mu_D}. \quad (4.33)$$

This very simple model only considers heat transfer operated by electron displacement, but is useful to understand the phenomenon. It is the basis of theoretical predictions for the thermopower of molecular junctions which have allowed to confirm a maximum efficiency in

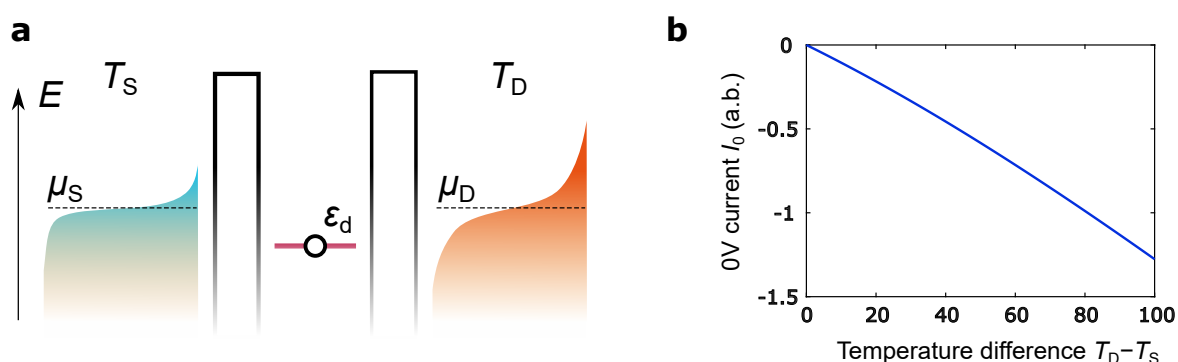


Fig. 4.2 Thermocurrent in a molecular junction. **a**, energy schematic of a single-level junction where the source and drain are at different temperatures, T_S and T_D respectively. The single level ϵ_d in the junction filters the conduction to a restricted energy interval. The finite temperature results in vacant states in the electrodes and a temperature difference can lead to transfer of electrons into the electrode having more vacant states in this interval. **b**, Landauer model simulation of the current at zero voltage resulting from a temperature difference; the energy level is set at -100 meV and temperature in the drain was varied from 293 K to 393 K while the source temperature was kept at 293 K.

configurations close to tunnelling resonance. It was predicted and observed experimentally that tuning an electrostatic gate resulted in sawtooth-like oscillations in the thermopower which revealed the electronic structure of a dot [215]. Related work was more recently applied to molecular junctions theoretically [216], relating fine structure of electrostatically gated thermopower to the electronic and phononic excitation spectrum, and experimentally [217, 218], which confirmed resonant features in thermopower in molecules and achieved large temperature gradients across junctions. Thermopower can provide a sensitive reading of the energy spectrum of a structure, whilst being less invasive than direct voltage bias, which capacitively applies strong forces between the leads and brings the system out of equilibrium by generating high charge transfer rates.

More complex configurations have introduced third terminals and second dots coupled to the first which enable detection of such heat transfers in the occupation statistics [209], but also bosonic transfer in the systems with phonon [219] and magnon baths [220]. Interestingly, the latter makes use of the Zeeman effect in quantum dots to generate a single-electron tunnelling spin current.

4.2.5 Thermoelectric materials

Several materials have been developed and utilised for use in thermoelectric generators (TEGs). Four main approaches are the focus of research and development for thermoelectric

generation. Several recent reviews cover materials developed in TEGs; a review by Twaha *et al.* is a good introduction to TEG devices [203]; Du *et al.* [206] and a recent book chapter by Prabhakar *et al.* [221] give an overview of recent development in polymer-based TEG devices, and applications in flexible and wearable energy harvesting.

Semiconductor alloys

Standard materials used for TEGs, known to have comparatively high Seebeck coefficients, are semiconductor alloys based on Bi, Te, Sb, Se, Ag. Intense research has been and is carried out to finely tune proportions of these elements to improve the figure of merit of such alloys. These can be integrated into devices in various forms: bulk, powder, paste, paint. In optimised alloys, ZT is typically around 1, going up to 1.3 [203].

Conductive polymers

Another attractive platform as a thermoelectric material is that of conductive polymers. These have low κ , are low-density, low-cost, and are easily synthesised. Poly(3,4-ethylenedioxythiophene) (PEDOT) and poly(3,4-ethylenedioxythiophene) polystyrene sulfonate (PEDOT:PSS) are standard base polymers for these studies as they have been extensively studied and can be tuned through doping, choice of solvent, crystallinity, and alignment control. Their flexibility makes them a viable platform for flexible TEGs. Using conductive polymers, values as high as ZT 0.4 have been obtained in p-type legs. n-type legs are more challenging for conductive polymers as most systems are not stable in air and more difficult to process [206].

Polymer-nanostructure composites

This approach aims to combine the low thermal conductivity and tuneability of conductive polymers with the high Seebeck coefficients of nanostructures. Such materials can be: Te nanorods, Bi-Te-, and Sn-Se-based alloys, carbon nanotubes, and graphene [206]. Research is in its infancy but some CNT-CP composites are predicted to show high ZT values. SnSe nanosheet/PEDOT:PSS composite films were experimentally demonstrated with room-temperature ZT of 0.32 [222].

Nanostructures

Nanostructures themselves have been studied as thermoelectric materials, mainly in academic research so far. These can be studied in single nanostructures, films, or monolayers of

them. Experimental and theoretical studies have focussed on quantum dots, namely in QD refrigeration [210], energy harvesting [208, 209]. Recent research has focused on molecular junctions developments of molecular junctions for thermoelectricity [223, 224, 29]. A particularly attractive concept in molecules is the possibility of engineering quantum interference to enhance the thermoelectric effect [225]. Metal-organic frameworks (MOFs) have been developed as thermoelectric materials [226]; these include nanostructures in an organic lattice structure, to deliver high thermal insulation.

4.2.6 Thermoelectric devices

Structure of a thermoelectric generator

The standard geometry of a TEG, is a succession of Seebeck units, such as the one shown in Fig. 4.1.a, each with a p-type leg and an n-type leg, connected in series, usually in a closely packed zig-zag geometry (common in thermal devices). This maximises the area of the hot electrode in contact with the environment and that of the cold electrode with a heat sink. In this set up, the voltage generated by a TEG of n units will be

$$V_{\text{TEG}} = nV_S = n(S_p - S_n)(T_H - T_C), \quad (4.34)$$

as outlined in Sec. 4.2.1. The resulting current produced is given by

$$I_{\text{TEG}} = \frac{nV_S}{nR_S} = \frac{V_S}{R_S}, \quad (4.35)$$

where R_S is the resistance of one Seebeck module. This resistance is an important consideration in TEG devices. Too high a resistance limits the energy that can be harvested. Another consideration in certain systems is the variability of this resistance which can be a limitation, as the legs are semiconductors whose resistance may depend on temperature. In flexible devices the contact efficiency between the legs and the electrodes may be altered by strain, making the thermoelectric efficiency unstable. In this device structure, the ratio of the cross-section of the p and n legs that optimises the thermoelectric efficiency can be shown to be [227]:

$$\frac{A_n}{A_p} = \sqrt{\frac{\sigma_p \kappa_p}{\sigma_n \kappa_n}}. \quad (4.36)$$

Alternative TEG device designs, such as folded and stacked arrangements, are suitable in particular contexts. These are particularly relevant to flexible TEGs, where all components need to comply to the strain, and this restricts the materials that can be used as substrate

(paper, fabric, PEDOT, polyimide) and the forms of the thermoelectric legs (powder, paste, paint, ink) [206].

Current technology

The commercial applications of TEGs are currently few, due to the inefficiency of the process and the relatively high cost of its introduction. Current applications can be separated between low-power and high-power regimes. The former regime includes portable devices, e.g. wristwatches with integrated TEG by Citizen and Seiko [206]. The latter includes space vehicles with high budget, and crucial autonomy. TEGs are increasingly found in individual vehicles; Volvo, Volkswagen, BMW and Ford are developing TEG systems with generated power of about 1 kW [203].

Future applications that have been suggested are the integration of TEGs into

1. solar cells, for complementing the photovoltaic effect [228],
2. fuel combustion systems which are very wasteful in heat energy (only 34% of the energy is typically used),
3. other industrial processes: a large amount of factory processes are thermal processes (e.g. 75% in the French industry sector [229]), e.g. furnaces, reactors, boilers, dryers; around 30% of the heat is estimated to be wasted in exhaust gases, cooling water and heated product,
4. electronics: this can be on the individual scale, making personal and/or portable devices (e.g. pacemakers, smartphones, personal computers) more energy-efficient and more autonomous, or on the large scale with the integration of TEGs in large data farms, mushrooming world-wide, factory-scale computer installations which currently require extensive refrigeration over large areas,
5. wearable devices: linked to the previous point as it aims to power portable electronic devices. However, as opposed to the recollecting waste heat from the electronics, various applications aim to collect heat from the human body making it complement a battery or be the sole source of energy.

Recent examples of wearable commercial applications include a TEG based on Bi_2Te_3 thermopiles collecting $100\mu\text{W}$ from a human wrist developed in 2004 by Holst Center. IMEC later adapted this approach to develop a wristwatch collecting $100\text{-}200\mu\text{W}$ at 23°C . The

same company also developed an electroencephalograph wearable on the forehead, collecting 2 mW at 23° C [221]. An early example of a flexible device is a 1997 Stordeur & Stark TEG, made by sputtering n and p-type Bi₂Te₃, collecting 20 μW for a 20 K temperature difference [221].

4.3 Experimental procedures

4.3.1 Molecules

Various molecules were used to benchmark the study of SAM junctions in devices to study their transport in the device and to produce a device with thermoelectric read-out. The molecular structures used in the project are shown in Table 1.1.

Alkanethiols

As a first population of molecules to benchmark the devices, we chose alkanethiols (*CnS*), and alkanedithiols (*CnS2*). As has been discussed in earlier chapters, this family of molecules is a *fruit fly* in the field of molecular electronics³, as it has been used extensively in STM-type experiments for fundamental studies of molecular transport [37, 30, 39, 32, 120, 230, 17, 67, 231–235], and as a canonical proof of concept for new architectures of devices contacting molecules⁴ [241, 33, 35, 36, 34, 231, 235]. It is the latter application we are interested in in this case. A discussion of transport in *CnS2* was had in Sec. 2.5.2. A property that makes *CnS* and *CnS2* molecules of choice for establishing the successful contacting of a device is the length dependence of their conductance. The conductance density of a SAM of *CnS* (in similar structures and with similar quality) should show an exponential dependence on the number of carbon atoms *n* in the alkane chain, i.e.

$$J_n(V) \propto \exp(-\beta n), \quad (4.37)$$

where β is the so-called attenuation factor or decay constant, which can be measured either per unit length or per number of carbon atoms in the chain [235, 234, 233, 232, 242, 231]. A similar length dependence exists for *CnS2*, with the coefficient factor measured to be similar [242], but the trend is shifted from that of *CnS*, owing to the extra sulphur atom. This

³Alkane-amines and alkane chains with other terminators are also common for similar effects on other substrates and with other nanomaterials, but are omitted in this chapter.

⁴It can also be pointed out that *CnS2* is used as anchors for attaching other elements through SA [137, 116, 236], and as we have seen in Chapter 2, or sub-elements of complex molecular structures in e.g. molecular diodes with head-tail molecular structures [237–240].

dependence was found to depend on the nature of the electrodes contacting the structures [17, 233]. A typical single-molecule conductance decay constant for C_nS_2 ranges from 0.8 to 1.0 per methane group in Au- C_nS_2 -Au systems [17, 243, 244], while it was measured to be 0.4 in Au- C_nS_2 -SLG systems [17], due to a different coupling to the electrodes. A review by Akkerman *et al.* [245] lists various measurements of this decay constant, and 0.8 to 1.0 per carbon atoms appear as a typical range for decay coefficients for alkyl-based junctions. In a system similar to ours, where the bottom electrode is Au, and the top electrode is multilayer graphene⁵ coated with Au, Wang *et al.* [35] report an attenuation factor for C_nS of 1.06 ± 0.14 per carbon atom ($0.85 \pm 0.11 \text{ \AA}^{-1}$). Interestingly, in experiments, this decay is mostly measured only for molecules of only an even number of carbon atoms, or exclusively molecules with an odd number, rarely a mix. It was shown that a shift in this decay existed between odd and even chains, which motivates the exclusion of this contribution [32]. Comparisons of this value are interesting for fundamental studies, but the very existence in the data of this decay already signifies the viability of an architecture to contact molecular SAMs. Indeed, junctions will most often display conduction, which may be due to conduction through the molecular SAM, or a short circuit. A large number of measurements is needed, and statistical analysis is needed to distinguish the two populations in the data [38], as indeed, in some devices, working junctions are vastly outnumbered by short circuits [231]. In individual junctions, a typical signature of transport through C_nS is an increase in conductance occurring around voltages of $\sim \pm 1.2 \text{ V}$ [30].

In order to verify that we are contacting desired molecules such that they determine the transport, we establish this benchmarking protocol. We ordered solutions of various C_nS and C_nS_2 commercially (from Sigma-Aldrich⁶) so as to gather a collection where the number of carbon atoms n of C_nS ranges from 6 to 14, while that for C_nS_2 ranges from 6 to 8. We fabricate devices with various populations in order to measure this decay coefficient, so as to confirm the viability of our architectures. A similar decay coefficient is expected to be seen in the thermoelectric efficiency, ZT , as a function of the alkanethiol length as has been predicted theoretically [246] and verified in single-molecule measurements [16]. Obtaining a measure of this decay in SAM devices would be a step forward towards technology-transferable molecular thermoelectric devices.

⁵N.B. We have used SLG which is expected to have a higher resistance, but possibly similar coupling to molecules.

⁶Sigma-Aldrich Corporation, St. Louis, Missouri, United States. www.sigmaaldrich.com/united-kingdom.html

Oligo(p-phenyleneethynylene)dithiols

A second population of molecules that we studied is that of Oligo(p-phenyleneethynylene)-dithiols (OPEs). OPEs are conjugated molecules that are common in the field of molecular electronics [230, 247–250]. They have been notably studied by other groups in mechanically controlled break junctions (MCBJs) [26, 248, 13]. An interesting result is that, in this set-up, the coupling to the electrodes can be tuned such that in the strong-coupling regime, the life-time broadening of the molecular orbitals leads to smooth conduction, while for weaker coupling, conduction closer to Coulomb blockade can be seen with apparent plateaux in the current profile [13, 251].

Moreover, OPE3 is often used as a base structure that can be functionalised, namely at its central benzene unit with molecular side groups [252, 234, 253, 250], or changed in conjugation between ortho, para, and meta [234, 254, 255]. These are found to noticeably affect their DOS and resulting electrical and thermal conduction properties.

The long-term goal of the project is to construct molecular structures that have enhanced thermoelectric effect through a tuning of their electrical and thermal conduction by tailoring of the chemical structure of the molecules. OPEs form an ideal candidate from a synthetic chemist's point of view for this work, making them an interesting molecule to verify our devices with.

Similarly to alkanethiols, OPEs exhibit a decrease in conduction as a function of their length. Carlotti *et al.* report literature values of the decay rate in single-molecule measurements and SAMs, where a typical decay coefficient ranges from 0.2 to 0.3 \AA^{-1} [256]. Interestingly, unlike C_nS , the Seebeck coefficient has been seen to increase as a function of chain length in single-molecule measurements [16].

Our OPEs are synthesised by collaborators L.J. O'Driscoll and M.R. Bryce at the University of Durham. They have synthesised and sent us OPE n of three lengths: 1, 2, 3. We have integrated them into devices as explained in this chapter.

BOC8S:C8S mixed SAMs

I proposed a third type of molecule for investigating the coupling strength between the SAM and an SLG top electrode depending on the molecule's interface with the SLG. The structure I suggested for synthesis is shown in Table 1.1 and was given the shorthand BOC n S. It consists of an alkanethiol on which a benzene arm is attached through an oxygen atom. The oxygen is thought to allow for an angle between the alkane chain and the benzene arm. The benzene arm is expected to couple more strongly to SLG through π -stacking, compared to a methane termination. In a dense SAM, the benzenes are expected to be tightly stacked

parallel to one another and perpendicularly to the SLG top electrode; the proposed protocol is to integrate them into a mixed SAM with C_nS of matching length, with various ratios of concentration. It is expected that as the BOC_nS is made more dilute among the C_nS , a transition will occur between a configuration where π -stacking is not permitted by the dense BOC_nS SAM to one where C_nS spacers enable this stronger coupling, and a second transition where C_nS dominates the transport and is less strongly coupled to the SLG. The principle can be applied to an arm with even stronger potential for coupling with SLG such as pyrene.

BOC_8S molecules were synthesised by L.J. O’Driscoll and M.R. Bryce, and sent to us and our collaborators in Lancaster. We have integrated them into devices varying the concentration ratio, as compared to C_8S in quantity, in the solutions used for SA. Our collaborators in Lancaster have been able to do local conductance measurements to quantify the differences in coupling, similarly as a function of concentration, and also between conductive tips of Au and of SLG. The results are being analysed at the time of writing. The pyrene variation of the BOC_nS structure has just been synthesised at the time of writing and will be integrated into devices by me and the rest of the group in the coming months.

4.3.2 Device design and fabrication

The devices for this project were built following two designs. The first design is similar to that described in Sec. 2.4.1, where the SA is adapted for the relevant molecules being studied.

Pore device design

I developed a second design, where the junctions are defined by pores. I designed the OL mask, which consists of several layers; it is shown in Fig. 4.3, and later calibrated the fabrication recipe. A first layer is that of the bottom electrode (brown in the figure), which can typically be made with Au through evaporation. A second layer is that of a dielectric (green), which is patterned so as to form pores (or valleys or crevasses) in the dielectric, thus exposing micron-size regions (with a range of geometries) of the bottom electrodes. These exposed regions are where the SA process is applied (blue) so as to coat them with a SAM of the desired molecule or structure, whilst keeping grounding contacts protected from the SA. Following the SA, a top electrode, typically graphene can be transferred and patterned (cyan) so as to cover the junctions and connect them to the four grounding contacts.

Further OL layers were prepared so as to allow for the integration of a top gate. Following the top contact deposition, another insulator can be put down on top of it and patterned (using

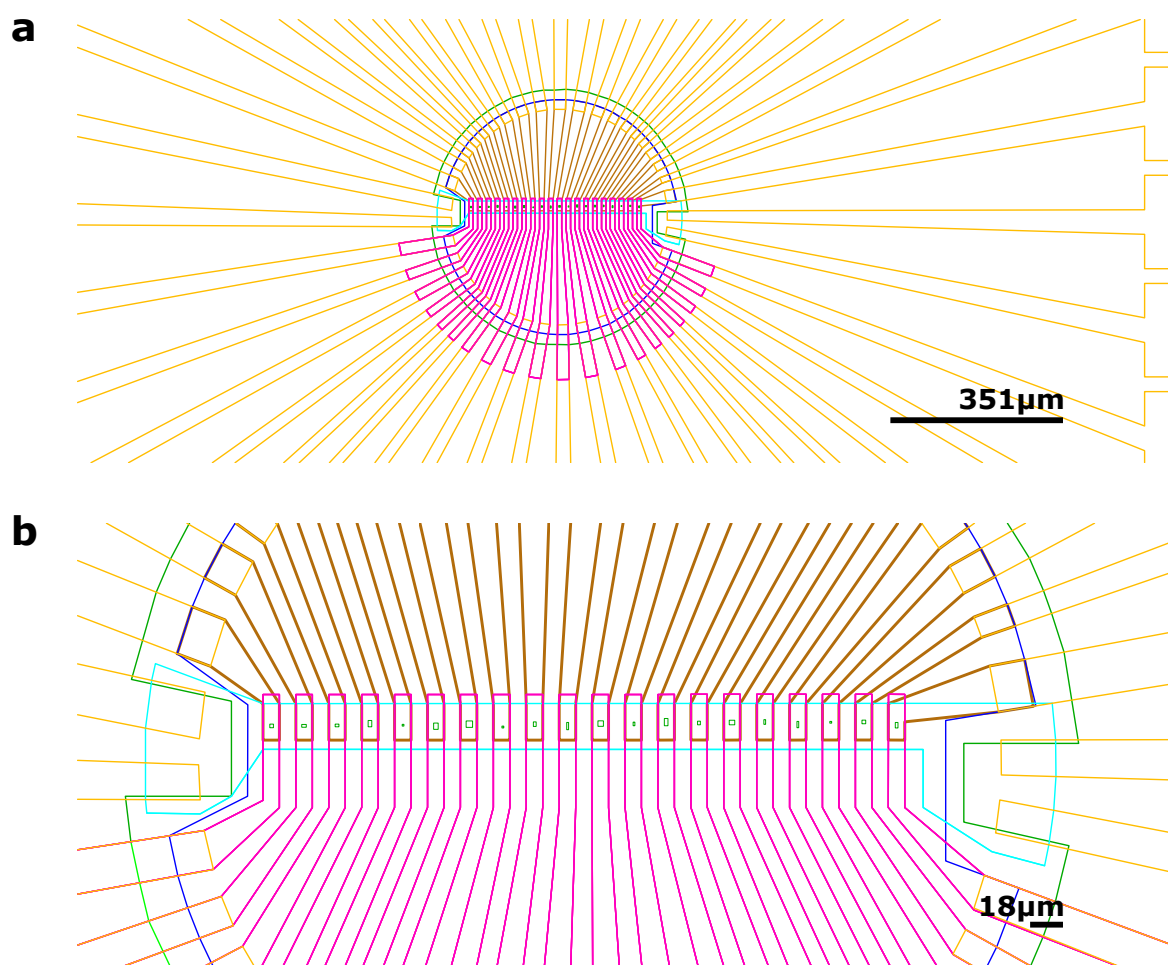


Fig. 4.3 Optical lithography mask design for device with pore/valley junctions. **a**, central region. **b**, detail of valleys. Brown: bottom electrodes, orange: connection to bonding pads, blue: self-assembly region, cyan: top electrode (graphene), green: insulator with pores, pink: top gate contacts.

an OL mask layer similar to that shown in green in the figure, but which does not contain the pores). When the second dielectric has been patterned, top gate electrodes can be deposited according to a pattern (shown in pink).

Alternatively, the OL layer for top contacts can be used in the same process as the bottom electrode. This would result in a junction being connected to two bonding pads and would enable four-terminal measurements of the junctions, with two terminals connected to the SLG, and two terminals connected to the bottom electrode. This set-up would eliminate contributions from resistance in the SLG and the bottom electrode and measure directly the voltage drop and the resulting current in the junction.

It aims to overcome several limitations of the former design as follows.

1. In the former design, the graphene top electrode is patterned on top of the SAM such that, at the edge of the graphene electrode the oxygen plasma that etches the graphene also damages the SAM, likely creating some risk of short circuit. In the new design, the edge of the graphene electrode is tens of microns away from the SAM junctions, resting on an insulator. This way the oxygen plasma etch does not come near the SAM junctions, and indeed, any etch, plasma-driven or chemical, for other types of top electrodes would not affect the SAM.
2. Related, but slightly different from the previous point, the open edge of the top electrode in the former design makes it possible for molecules to rearrange on the surface. If the Au surface at the edge of the junction is exposed by plasma having removed the SAM, the encapsulated SAM is suddenly offered more available surface which it can expand into, as is energetically possible, thus risking the creation of pinholes. In the new design, the molecules are encapsulated and protected in the valleys inside the insulator, which prevents such rearrangements.
3. The other edges of the junctions in the former design (i.e. the closed edges) which support the graphene are likely to have a different stress profile in the graphene as they elevate the latter away from the SiO₂ substrate on which it is strongly attached. In the new design, the edge of the junctions (of the valleys) may not be in as close a contact, but the profile can be expected to be more uniform over the area of the junction. The edges of the bottom electrodes are covered with an insulator which makes them electrically inactive.
4. The four grounding contacts, as opposed to three in the previous design, make it possible to do a 4-terminal measurement of SLG in a field-effect transistor (FET) set-up.
5. The design contains individual top gates for each of the junctions. This makes it more likely to obtain gated transport than a common top gate.
6. Particularly important in this project is thermal transfers within the device. To study the thermoelectric effect, we must ensure that a temperature gradient is created across the SAM junction. Thermal leaks from the contacts can hinder this, if the substrate and bottom electrodes are heated by these leaks. In the former design, thermal leaks into the substrate and indirectly into the bottom electrodes are possible. The new design with pores makes it so that the heat can be isolated from the substrate by the insulator, of which the thickness can be adjusted, and the thermal path across the junction can be made relatively shorter.

Fabrication recipe

The substrates used are cut from Si wafers with a 285 nm-thick SiO₂ layer which optimises the colour contrast of SLG making it visible with optical micrography. It can serve as a dielectric for a back gate. A batch would consist of an array of 6 × 6 dice.

In a typical device, the bottom electrodes and connections to bonding pads are of Au, evaporated by thermal evaporation in a lift-off process. The two layers can be developed simultaneously by exposing the bonding pads in the UV mask, and developing them partially (e.g. for 1 s) in MF-319 developer. This makes the features appear, including the alignment marks that can be used for the alignment of the bottom electrodes. The resist used is a bilayer of LOR5B and Shipley 1805. A standard evaporation rate for the Au is 0.1 nm/s; the thickness should be made sufficient for wire bonding the finished device, i.e. > 50 nm and an adhesion layer of Ti (~ 10 nm) should be evaporated onto the sample prior to the Au at a similar rate. The solvent used for lift-off is SVC-14.

Following this the dielectric layer can be deposited. We use Al₂O₃ deposited by ALD. For this deposition, we use the ALD system in the Semiconductor Physics Group's cleanroom at the Cavendish Laboratory, with A. Nasir and B. Ramsay. Prior to the deposition, the sample can be cleaned by ozone cleaning using an ozone cleaning system in the cleanroom. The thickness can be varied through the number of deposition cycles. It can be measured using ellipsometry. Typical thicknesses have ranged between 3 nm and 10 nm.

Following this, an OL step, using Shipley 1805 as a photoresist, is used to pattern the insulator so as to encapsulate the bottom electrodes apart from micron-size pores which will form the junctions. After the development of the photoresist, the Al₂O₃ is etched either in ammonium-fluoride-buffered hydrofluoric acid (BHF) or MF-319 developer. The rule-of-thumb etching rate of Al₂O₃ for these are 1.5 nm/s, and 1.5 nm/min respectively⁷. The success of the etch can be tested with AFM imaging.

A further OL step is done to define the regions in the device where the SA will be applied so as to include the pores and exclude the grounding contacts (see blue feature in Fig 4.3). The resist used is typically Shipley 1813.

Once this step of OL is done, the substrate can be diced into smaller samples (of 3 × 3, 2 × 3, or 2 × 6 devices) on which different SA processes will be applied. The devices can be cleaned with O₂ plasma in an RF asher for 1-2 min at 100 W, so as to remove potential organic contaminants on the pores' surface.

The devices can be taken into the N₂ glovebox in the Opto-Electronics Group's facilities in the Cavendish Department, where the SA is carried out. There, we use a SA process

⁷Using MF-319 to etch Al₂O₃ calls for caution as photoresist, even unexposed, can be dissolved after approximately 5 min.

previously calibrated by our collaborators X. Wang and B.J. Robinson at the University of Lancaster, with input from L.J. O’Driscoll and M.R. Bryce for molecules they have synthesised at the University of Durham. We tested solvents for compatibility with optical resists, so that they are not dissolved in the SA process; octane and toluene were found to be appropriate solvents for our molecules and stand this test. A typical concentration used was 1 mmol/L. The SA recipes usually consisted of repeated drop-casting and spinning iterations (30 s and 30 s), typically 5 times, followed by rinsing in the same solvents. Following the SA, the devices are dried using a N₂ gun. The devices are then sealed in bottles so as to keep them in N₂ gas while being moved, to minimise potential oxidation.

The devices are taken to a cleanroom for the SLG transfer, either that in The Cambridge Graphene Centre or the Semiconductor Physics Group’s cleanroom. We have used alternatively SLG grown by A.C. Ferrari’s group in the Cambridge Graphene Centre, and commercially bought SLG from ACS Material⁸ when the former was out of stock. We prepare the SLG in a similar way to that described in Sec. 2.4.1, a day early so that the etch of the Cu foil in APS (2 g in 150 mL of H₂O) is finished when the devices are brought to the cleanroom. The SLG is then coated with PMMA is floating on the surface. The devices are put in an acetone bath and rinsed with IPA to wash off the photoresist from the SA OL layer. The SLG:PMMA is transferred successively into two H₂O beakers to rinse off the etchant. Then the floating SLG layers are *fished* with the chips containing the devices so as to cover them completely. They are then allowed to dry in air overnight. In the more recent devices, they are dried in ultra-high vacuum in an evaporator overnight so as to remove possible solvent contaminants.

The PMMA can be washed off in acetone, to then coat the SLG with photoresist for the OL process to pattern the SLG⁹. Once the feature has been developed, the SLG can be etched using O₂ plasma in the RF asher. Typically a long etch of 1 min at 100 W would be applied, but to minimise heating of the devices, this was reduced in more recent devices to e.g. 30 s at 10 W.

The basic devices are ready at this stage to be bonded to an LCC package using a wedge bonder, so as to measure them electrically.

⁸ACS Material, LLC 959 E Walnut Street 100, Pasadena, CA 91106. <https://www.acsmaterial.com/>

⁹In more recent devices this step has been replaced by a direct OL patterning of the PMMA with a deep UV mask aligner, so as to save a spinning step, minimise exposure to developers, and avoid a baking step for the photoresist. However, this process has been seen to suffer from cracks in the PMMA, which leads to a partial etch of the underlying SLG. This was shown to be avoidable by baking the PMMA after its deposition onto the SLG:Cu foil at 150° C for 1 min.

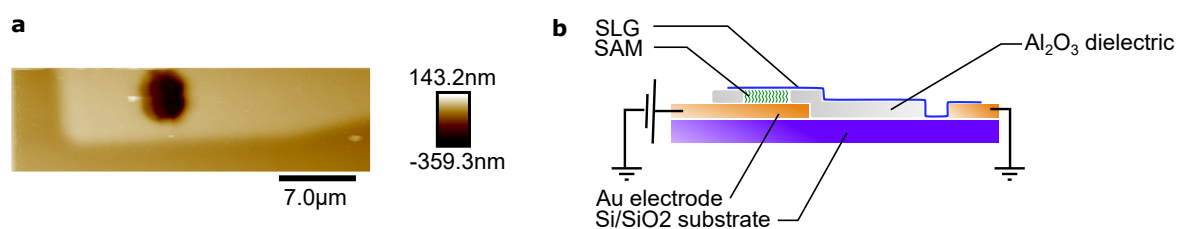


Fig. 4.4 Device design with pores. **a**, AFM image taken of etched pore with photoresist from OL. **b**, schematic of device with pore design.

Template stripping

In order to form high-quality molecular junctions, it is desirable to use a bottom electrode where the roughness is limited. Limiting the roughness improves a junction in two ways. Firstly, a smoother surface with fewer grain boundaries prevents impurities in the SAM which can arise in valleys between grains. Secondly, a smoother surface permits a more even contact of the junction as the top electrode can conform better to a surface with less height variation and will be able to contact inter-grain valleys more easily.

In order to obtain such smooth bottom electrodes several options exist. Firstly, Si wafer surfaces have low roughness, typically ~ 0.1 nm (RMS) [257], depending on the supplier, in comparison to evaporated Au, with e.g. 1.2 nm measured in Sec. 2.5.1. Using a bottom electrode that matches a wafer in roughness would be a step forward to improving the smoothness. Using SLG as a bottom electrode, for example, would offer an improvement in this respect. However, this would change the SA processes possible for forming a junction, imply changes in the conduction type for reasons discussed in Section 2.3.2. It is possible, however, to obtain Au of reduced roughness via a technique called template stripping, which consists in evaporating an Au (or another metal) layer onto a Si wafer and transferring this layer onto a second sample so that on the latter the face of the Au facing up is the one that was evaporated against the surface of the first wafer and has adopted its roughness—cf. 0.15 nm RMS roughness in the template-stripped sample in Sec. 2.5.1.

A proven recipe is as follows. We take an Si wafer and clean it thoroughly, with a Decon 90 and H_2O solution (with a volume ratio of 1:10), then rinse in acetone and IPA. We evaporate Au onto it, typically with a roughness above 70 nm. We then heat the wafer and an epoxy mixture to 60°C . We take the target samples to which we want to transfer the Au layer. We take $3\ \mu\text{L}$ of the epoxy preparation and use it to stick the sample onto the Au-coated wafer. We heat the structure to the curing temperature of the epoxy (in our case 150°C for 2 h) and then leave it to cool gradually, avoiding a sudden drop in temperature

Device number	Molecules	Variations	Design
1	C_nS	$n \in \{8, 10, 12\}$	Old
2	OPEn	$n \in \{1, 2, 3\}$	Old
3	BOC8S:C8S ($c\%$ BOC8S)	$c \in \{2, 9, 20, 100\}$	Old
4	C_nS	$n \in \{8, 10, 12, 14\}$	Old (some with Au top layer)
5	none		Pores
6	C_nS	$n \in \{8, 10, 12\}$	Pores

Table 4.1 Principal benchmarking devices fabricated and measured.

which may cause cracks in the Au¹⁰. After leaving the structure to rest for typically a day, we can use a scalpel to separate the two chips, peeling the Au off from the original surface. This results in a sample coated with smooth Au.

This technique is often used in STM or AFM-based experiments, as simple structures can easily be prepared in this way. Fabricating a device with a bottom electrode prepared in this way demands extra steps to pattern the electrodes. A test sample was prepared by template stripping where we etched the Au on the surface with a KI-based gold etchant. This resulted in clear OL patterns in smooth Au, but the remaining epoxy outside of the Au features may retain some of the Au and cause leakage. Further tests are needed to show whether this is a viable structure; these are being planned for future devices in the group. An attempt to use template stripping to transfer a structure of Au and ALD-deposited Al_2O_3 patterned by OL using a laser writer was used as a quick test. However, the strong adhesion of Al_2O_3 to the first Si wafer made it inconclusive. Parylene was found to be unsuitable for template stripping too as residual parylene was measured through ellipsometry on the first wafer.

4.3.3 Electrical characterisation

To measure the I - V characteristics of the junctions, we use a set-up mixing AC and DC voltages. This set-up is shown in Fig. 4.5.

The junctions are bonded and connected in a similar way to that explained in 2.4.2. Junctions and grounding contacts are bonded to an LCC package. This LCC package is connected to a wired probe with BNC connectors for connection to the electrical apparatus. In a typical measurement, we use a two-terminal arrangement, where to measure a junction, the chosen junction is connected to the voltage source, while one grounding contact is connected to the I - V converter.

¹⁰Other types of epoxy can be cured by UV radiation. If the target substrate is transparent, e.g. quartz, the curing can be done by using the UV radiation of the OL mask aligners. Preliminary tests have shown it to work on quartz substrate as the Au layer was successfully peeled off from the original substrate.

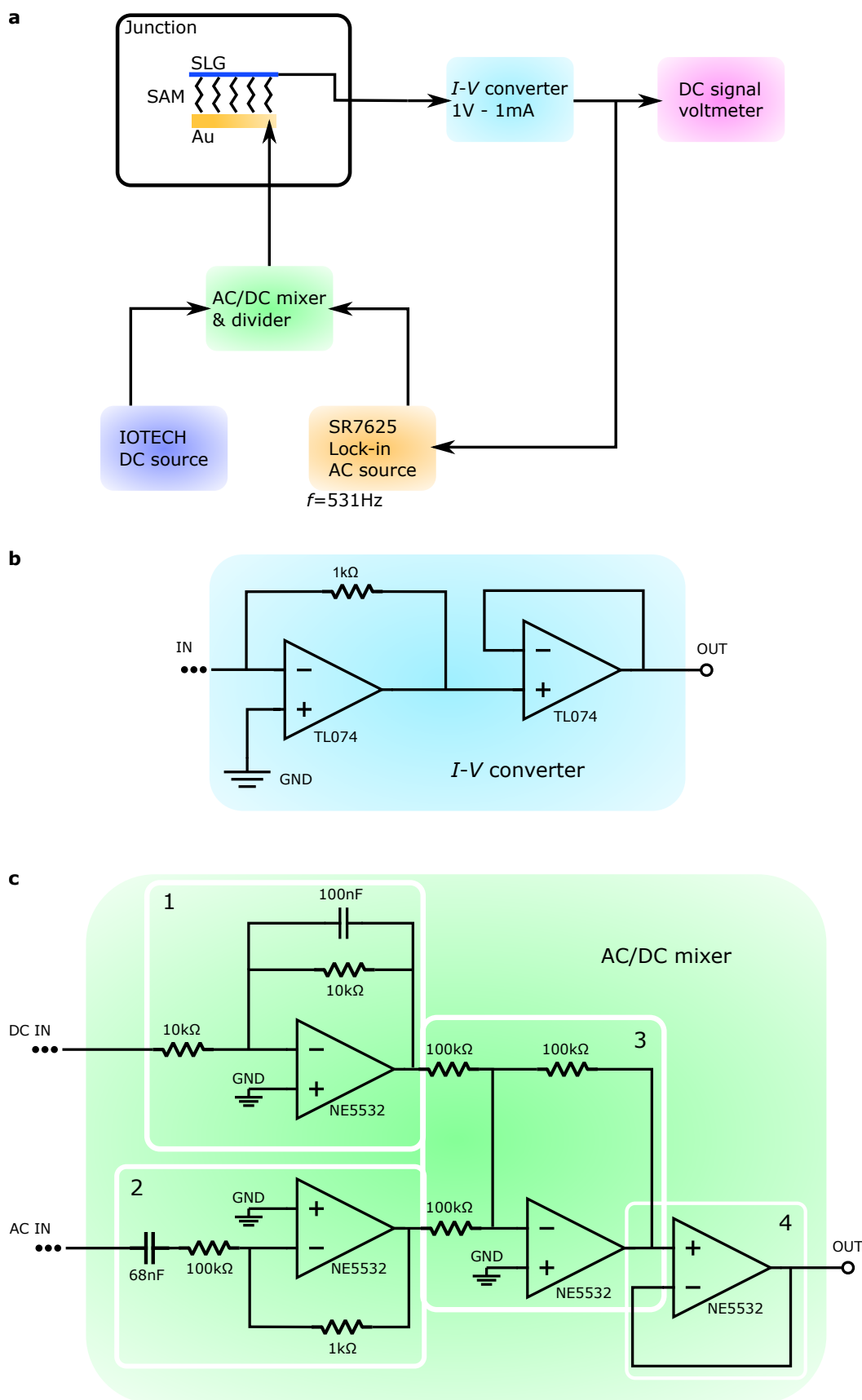


Fig. 4.5 Electrical characterisation set-up. **a**, schematic of the mixed AC/DC set-up. **b**, electrical diagram of the I - V converter. **c**, electrical diagram of the AC/DC mixer, described in Section 4.3.3.

The lock-in provides the AC voltage, and the IOTECH source provides the DC voltage. The DC voltage is thus modulated with AC voltage using an adder circuit. The AC/DC current passing through the junction is converted by the I - V converter into a voltage such that a current of 1 mA is converted to a voltage of 1 V as measured on the converter by a voltmeter.

The AC/DC mixer shown in Fig. 4.5.c consists of four units utilising operational amplifiers according to standard designs [258]:

1. inverting amplifier with low-pass filter (integrator amplifier),
2. inverting amplifier with high-pass filter (differentiator amplifier),
3. summing amplifier (voltage adder or summer),
4. buffer, or follower,

and works as follows.

An inverting amplifier (labelled 1) with low-pass filter, or integrator amplifier, collects the DC input and filters out any residual AC noise from the voltage. The voltage amplification ratio of an inverting amplifier is given by

$$A = -\frac{R_{\text{in}}}{R_{\text{fdbk}}} \quad (4.38)$$

where R_{in} is the resistance of the resistor placed before the operational amplifier connected in series to its negative input, and R_{fdbk} is the resistance of the resistor in the feedback loop (connected in parallel to the operational amplifier). In this component, the two resistors have the same resistance, making the amplification ratio -1. The capacitor, with capacitance C_{fdbk} , in the feedback loop (connected in parallel to the operational amplifier and the R_{fdbk} resistor turns the inverting amplifier into a low-pass filter with cut-off frequency

$$f_c = \frac{1}{2\pi R_{\text{fdbk}} C_{\text{fdbk}}}. \quad (4.39)$$

Here this cut-off frequency is 16 Hz.

The AC voltage, produced by the oscillator from the lock-in, is fed into the other branch of the AC/DC mixer. Before being added to the DC input, it goes through an inverting amplifier with high-pass filter, or differentiator amplifier, labelled 2 in Fig. 4.5. This inverting amplifier has amplification ratio $-R_{\text{in}}/R_{\text{fdbk}} = -0.01$, where R_{in} is the resistance of the resistor at the input, and R_{fdbk} is the resistance of the resistor in the feedback loop. This enables the voltage oscillation amplitude to be kept small in order to extract an accurate measure

of the differential conductance i.e. the AC amplitude should be small for the conductance to be approximately linear over the range of the oscillation. The voltage reduction through the inverting amplifier enables to have a small amplitude whilst reducing the sensitivity to noise in the AC source. The capacitor placed at the input of the inverting amplifier, with capacitance C_{in} , makes the unit a high-pass filter, where the cut-off frequency is

$$f_c = \frac{1}{2\pi R_{in} C_{in}}, \quad (4.40)$$

which here is 23 Hz. This eliminates possible residual DC biases in the AC signal.

The AC and DC branches meet in the summing amplifier unit (or voltage adder) labelled 3. The output current of the unit is a sum of the two signals, with the matched resistors making the amplification ratio -1:

$$I_{out} = -(I_{AC} + I_{DC}), \quad (4.41)$$

and

$$V_{out} = -(V_{AC} + V_{DC}). \quad (4.42)$$

This negative amplification ratio restores the current polarity to that fed into the AC/DC mixer.

Finally, the mixed current is fed into a buffer, or follower, labelled 4, which prevents feedback into the mixer, which could affect the current summing.

At the output of the AC/DC mixer, the voltage has the form:

$$V_{AC/DC} = V_{DC} + V_{AC} \sin \omega_{AC} t. \quad (4.43)$$

This is the voltage across the junction and the grounded SLG electrode. The current is fed into an I - V converter. The output of this I - V is at a potential which is related to the input current by a known fixed conversion rate. The AC/DC output of this converter is then fed into a DC voltmeter, which measures the DC voltage, and thus the DC current across the junction, and into the lock-in to measure the amplitude of the voltage oscillation at the source frequency, which corresponds to the amplitude of the current oscillation across the junction. We can extract the differential conductance from the latter. Indeed, the AC current amplitude extracted can be divided by the fixed AC voltage amplitude across the junction, so as to obtain, though a linear approximation, the differential conductance at a given DC voltage:

$$G = \frac{dI}{dV} \approx \frac{I_{AC}}{V_{AC}}. \quad (4.44)$$

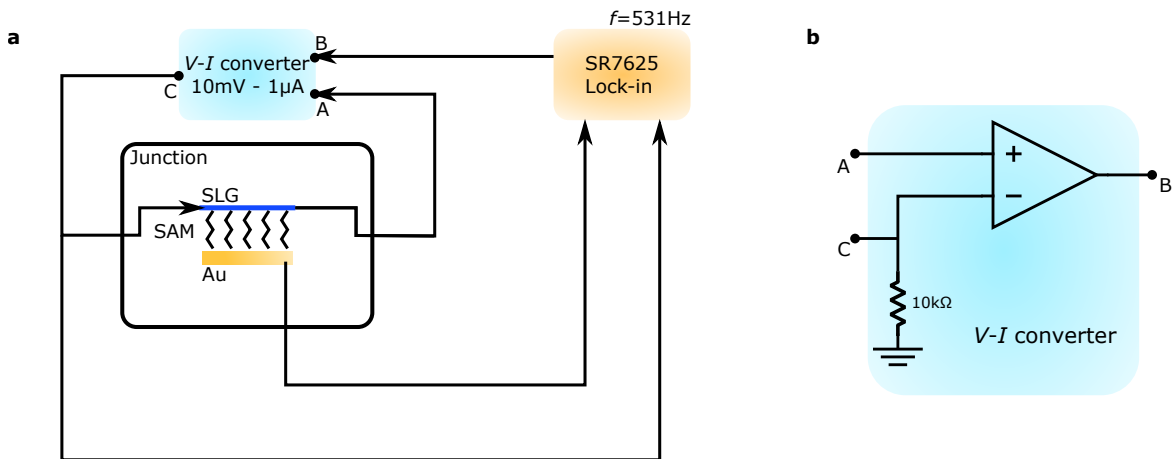


Fig. 4.6 Electrical set-up to measure the thermoelectric effect via the 2ω method. **a**, schematic of the whole set-up. **b**, electrical diagram of the $V-I$ converter.

A switch unit is used to automate the measurement so that a CryoMeas code can measure all bonded junctions successively. In a typical measurement, the voltage is swept over an interval which is gradually increased from $[-0.5\text{ V}, 0.5\text{ V}]$ to $[-1.5\text{ V}, 1.5\text{ V}]$, while the DC and AC parts of the current are recorded separately to deliver the $I-V$ curve and the differential conductance as a function of voltage simultaneously. The set-up is operated and the data collected via the LabView-based software CryoMeas.

4.3.4 Thermoelectric measurement

In order to measure the thermoelectric effect, we resort to the so-called 2ω method. This electrical set-up makes use of AC current to extract thermoelectric transport in a system. The very small thickness of the junctions in study makes heat leakage an important concern. Using ambient heating (e.g. through a Peltier unit) is likely to heat the whole structure evenly, and prevent the creation of a measurable temperature gradient across the junctions. An advantage of using AC methods is that these can provide a local heating by turning one of the electrodes as the heater, and thus creating this temperature gradient. The principle is simple: if an AC current of frequency ω , $I(t) = I_0 \sin(\omega t)$, passes through a medium, this medium will be heated by Joule heating. Joule heating is independent of the current direction, and given by

$$P(t) = RI(t)^2, \quad (4.45)$$

for an Ohmic conductor of resistance R , where $P(t)$ is the rate of conversion from electrical energy to thermal energy. As a result of this square dependence on current, the power is then

given by

$$P(t) = RI_0^2 \sin^2(\omega t) = RI_0^2 \frac{1 - \cos(2\omega t)}{2}, \quad (4.46)$$

i.e. the heating of the material oscillates at frequency 2ω . By looking at the second harmonic of the voltage frequency measured across the junction, we can single out contributions from thermal variations, without noise from the driving current at the base frequency.

In our system we wish to create a temperature gradient across the junction, i.e. heat one electrode whilst minimising heat leakage into the other. SLG being more resistive than Au electrodes makes it easier to heat up. The fact also that its resistance varies noticeably with temperature is attractive as it makes the measured resistance a real-time read-out of the effective temperature in the SLG if this dependence has been calibrated.

The electrical set-up used for this measurement is shown in Fig. 4.6. An AC voltage is set across the SLG using the SR7625 lock-in oscillator, which we set at a prime-number frequency, typically 531 Hz. This current going through the SLG at this frequency ω heats it at the second harmonic 2ω . The voltage across the SAM junction, i.e. between the Au and SLG electrodes, is connected to the lock-in set to pick out any voltage oscillation at frequency 2ω , which must be the thermovoltage. This frequency is that of the temperature oscillation in the heating electrode, and thus that of the oscillation in the temperature gradient across the junction. The voltage measured at the second harmonic then results from the creation of this gradient, without contributions from the voltage oscillation at the first harmonic. While it is possible that this reading may be in part affected by the resistance of the electrode or the junction varying as a function of this temperature oscillation, the resistance of the electrode is recorded, and tests can be carried out to establish the thermal origin of the measured voltage, as we will see in the following discussion.

Proposed protocol

In order to measure the thermoelectric performance of a device, a first step of calibration is needed, in which the temperature dependence of the SLG's resistance is measured against temperature.

A first proposed set-up would be to dip the device into a water bath, whilst protecting it with an insulator. Plugged to the measurement probe would be a commercial thermistor, which would give a real-time read-out of the heat bath's temperature. While the resistance of the SLG electrode is recorded, the temperature can be adjusted from an elevated temperature e.g. $\sim 50^\circ\text{C}$, whilst letting it cool down to room temperature. Recording the SLG's resistance as a function of temperature whilst keeping the voltage bias small so as to limit the Joule

heating, one can extract a calibration of the conductance against voltage. The calibration can then be used in thermoelectric measurements of the junctions.

Another set-up being developed at the time of writing involves a Peltier cooling module, which we bought commercially from Adaptive¹¹. The Peltier unit consists of a cold and a hot face; supplying current through it builds up a temperature difference between them, with a maximum of about 74 K. A stage can be built where the hot face of the Peltier unit is put in contact with a thermistor which records the temperature in real time, and the device being measured. This set-up allows for a controlled calibration of the temperature dependence of the SLG's resistance.

Following the calibration measurement, we know the relation between the graphene's resistance and the temperature difference (from base temperature), $R_{\text{SLG}}(\Delta T)$, which enables us to use it both as the heater and thermometer in the thermoelectric measurement. Whilst measuring a junction in the 2ω set-up, the voltage amplitude at the second harmonic, $V_{2\omega}$ is measured by the lock-in as well as the current through the graphene top electrode I_{in} from which the resistance and temperature are deduced. The relation between $V_{2\omega}$, ΔT , and I_{in} can then be compared. If both $V_{2\omega}$ and ΔT are found to scale linearly with I_{in}^2 , this suggests that most of the heating takes place in the top electrode and that the bottom electrode can be estimated to remain at substrate temperature with the temperature gradient across the junction approximately ΔT [259]. If this approximation can be made, the Seebeck coefficient is readily extracted as

$$S = -\frac{V_{2\omega}}{\Delta T}. \quad (4.47)$$

The Seebeck coefficient can be measured at different temperatures. If the heat transfer across the junction is significant to the extent that the bottom electrode's temperature is noticeably changed, a calculation of this transfer can be attempted from this deviation or simulated using a software e.g. COMSOL. It may be very desirable in this set-up to gain control of a top gate to make this measurement whilst being able to change the SLG's doping, and the molecular junction's DOS. In Mahapatra *et al.* [259] a similar set-up is used to measure the Seebeck coefficient in a bilayer graphene junction; their ability to tune the doping density in the graphene allows them to assess the phononic contribution to the thermoelectric coefficient. In this similar arrangement, temperature gradients of the order of 1–10 K were established across the junctions for heating currents of the order of 1–10 μA in the hot electrode. It is likely that in our systems similar gradients will be obtained for similar currents in our SLG top electrode. Heat leakage across the junction will depend on the nature of the SAM; although if in these conditions the bottom electrode can be approximated as being at the

¹¹ET-071-10-13 Peltier cooler module by Adaptive of European Thermodynamics Limited (www.etc.com).

substrate temperature in bilayer graphene junctions, SAM junctions may be expected to isolate even more strongly, thus keeping this approximation valid.

4.4 Preliminary results

4.4.1 *I-V* characterisation

The devices listed in Table 4.1 were measured in the automated set-up described in Sec. 4.3.3, and a large amount of data was collected. The data was extracted and normalised by area, as measured on micrographs, so as to find the current density. The measured current density at a set voltage was extracted for all junctions and averaged according to molecular population for comparison, in order to observe a molecular length dependence in the case of *CnS*, or study variations due to proportions in mixed SAMs.

CnS devices of batches 1 and 2

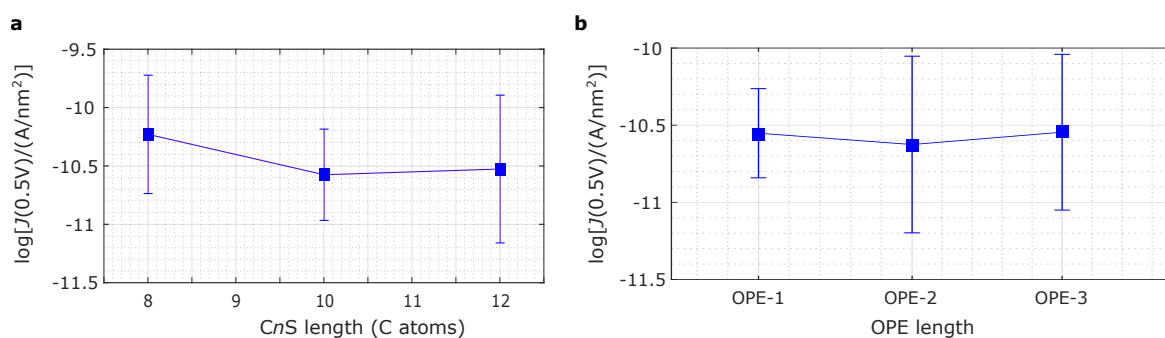


Fig. 4.7 Electrical characterisation of devices from batch 1. **a**, extraction of the decay coefficient for *CnS* from averaging measurements. **b**, extraction of the decay coefficient for OPEs.

The first batch of devices was inspired by the fabrication recipe developed and explained in Sec 2.4.1, shown to be effective for contacting QDs. As a first approach we applied a similar fabrication process to contact *CnS* of various lengths so as to verify a length dependence of the conductance. In the same fabrication batch we also contacted OPEs of various lengths using the same fabrication procedure.

The samples were characterised electrically as explained in Sec. 4.3.3. About 50 junctions were bonded and measured for each variation of the *CnS* length.

After the measurement, a value of current was extracted for a fixed voltage, 0.5 V, for each junction. We averaged this value of current according to the *CnS* length, so as to extract

an attenuation coefficient. Using micrographs of the devices, we can normalise this current per area, to obtain the current density. The resulting relation is shown in Fig. 4.7.a. The decay coefficient measured is approximately 0.2 per C atom, as opposed to a typical value of 0.8 to 1, as would be expected. The spread of values for the devices is large, such that the decay coefficient measured is not statistically substantial, as well as being 4 times smaller than expected, although C12S devices showed to be qualitatively different from C8S and C10S in the individual I - V profiles, as will be discussed below.

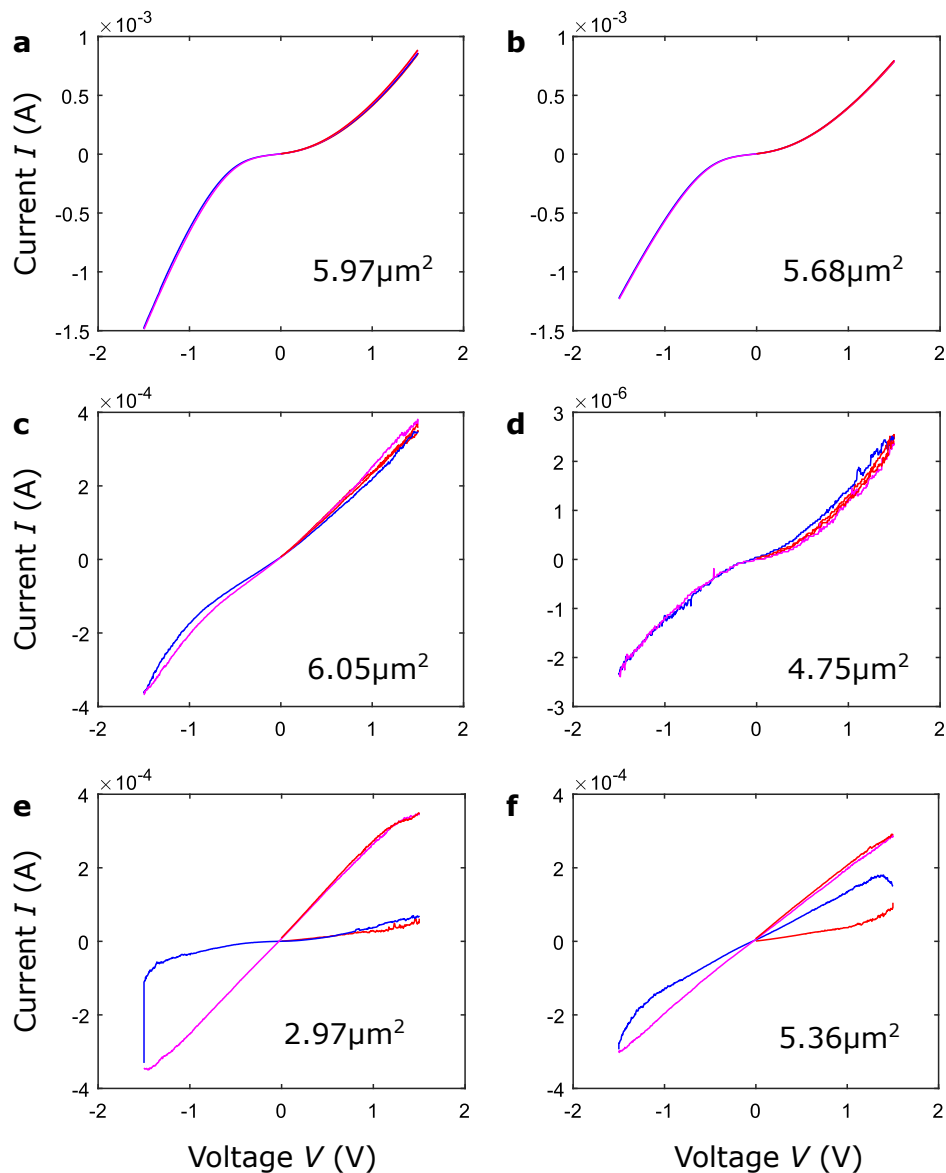


Fig. 4.8 I - V measurements of batch 1 devices contacting C12S. **a**, junctions exhibiting a non-Ohmic profile. **b**, junctions exhibiting a breakdown behaviour where the conductance undergoes an irreversible shift during a measurement.

Another matter of concern is that, in the C8S and C10S devices, the junctions measured showed no sign of a turn-on voltage at which conductance noticeably increases around 1.2 V, which is a common signature of transport in CnS , as discussed in Sec. 4.3.1 and 2.5.2. Indeed, most of them show highly linear behaviour over a range of -1.5V to 1.5V, as well as very high conductances, of the order of 1 k Ω , which is the same order of magnitude as the conductance measured on the grounding contacts across the SLG electrode. This suggests that the junctions are too conductive to be probed appropriately with SLG, which would constitute a more resistive part and constitutes most of the voltage drop in the structure. This would motivate a change to the contacting method. Comparison with literature values shows that indeed, C8S SAMs can lead to currents as high as $5 \times 10^5 \text{ A cm}^{-2}$ in Wang *et al.*'s Au-SAM-multilayer graphene-Au structure [35], whereas our range is limited to $1 \times 10^5 \text{ A cm}^{-2}$ by our SLG electrode.

The C12S devices, however, showed a range of interesting features. Some examples are shown in Fig. 4.8. Out of 68 junctions measured, 15 displayed an I - V profile that appears to be non-Ohmic, and is suggestive of transport through a nanostructure, excluding open circuits. This display a shift in conductance typically around $\pm 0.8 \text{ V}$. These profiles appear nearly symmetric, which suggests a strong electrical coupling of the SLG with the contacted structure. The turn-on voltage appears low compared to the literature value for CnS . This may be an indication of some contribution from impurities or capacitive effects in the junction. As current is passed through the junction, a capacitive force is expected to push the graphene closer to the underlying structure, thus increasing the conductance. This suggestion may be supported by the few junctions which display breakdown behaviour, with irreversible change in conductance during a measurement, as shown in Fig. 4.8. Several junctions were measured to be open circuits, about 30 open circuits were measured, which is much higher than in other devices. We attribute this to an issue with the graphene which may have been damaged during its processing, possibly partially etched during the process used to etch one of the two sides of the graphene on the Cu foil, or deposited in a way that hinders conduction. Micrographs of the devices show apparent wrinkles or cracks, which support this idea.

The measurements on OPEs displayed almost exclusively what appeared to be short circuits with no non-linearity. No attenuation factor was observed over our restricted statistical sample (see Fig. 4.7). The observations from the CnS devices led us to believe that the device structure and fabrication procedure, as they were, were unsuitable for electrically probing the OPE SAMs, and that more measurements should be made on a device shown to successfully contact SAMs through the length dependence of CnS .

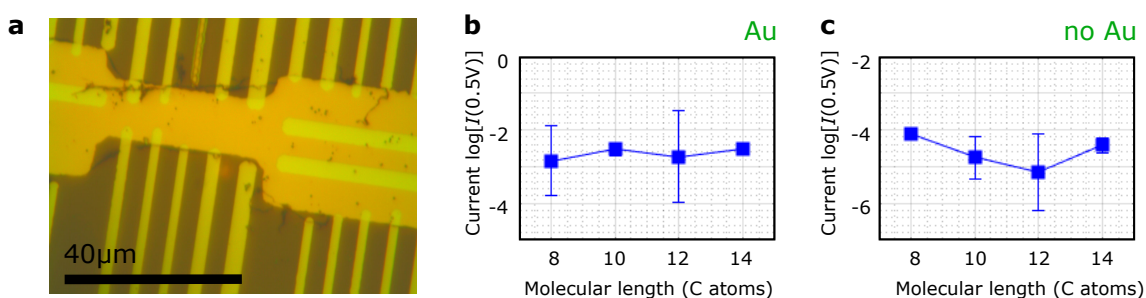


Fig. 4.9 Batch 4 C_nS devices. **a**, micrograph of a device with an SLG: Au top electrode. **b**, C_nS length dependence of current density for devices with an SLG: Au top electrode. **c**, C_nS length dependence of current density for devices with an SLG top electrode.

C_nS devices of batch 4

We made a second batch of devices to contact C_nS where we tried to address the low conductance of the top electrode.

We replaced the usual patterning process with the following. After SLG has been deposited on the device, we perform a lift-off process where, before etching the graphene, we evaporate Au in the desired area according to the SLG pattern's mask design—using a lift-off resist and negative photoresist bilayer to revert the pattern. We evaporate 20 nm of Au in a thermal evaporator, and perform the lift-off, so as to remove the Au outside of the top electrode pattern. The Au then serves as a mask during the oxygen plasma etch that follows. The SLG un-coated with Au is etched for ~ 1 min at 100 W in an RF asher. In the same fabrication run, devices similar to those of batch 1 were made simultaneously for comparison.

Following this, the devices were bonded and measured as previously. The junctions with an SLG: Au top electrode showed higher conductance than those with the SLG electrode. However, the junctions displayed Ohmic behaviour and the average conductance was not seen to depend significantly on C_nS length. The batch of devices where only an SLG top electrode was used showed a stronger dependence on C_nS length, apart from C14S which showed high conductance. Within the range from C8S to C12S, an average decrease in conductance could be seen (see Fig. 4.9). However, the sample is not statistically significant as the variations, a fortiori in the C12S population were large. Another batch of devices would be needed to increase the sample size. In this batch, a large number of junctions showed nonlinear behaviour. A condition was applied to filter these so as to only take them into account in the length dependence, such that only I - V deviating from a linear curve by a fixed margin were used. A combined regression with devices from batch 1 and batch 4 is being planned at the time of writing.

There are a number of limitations in this fabrication process. Firstly, the OL processes used to pattern the graphene top electrode required elevated temperatures, i.e. 120° C, which may have damaged the SAM and created pinholes. The etch of the SLG using oxygen plasma, may also have damaged the SAM at the edges of the junctions and permitting migration of the molecules out of the SLG-encapsulated area, as well as heating the region.

Devices of batches 5 and 6

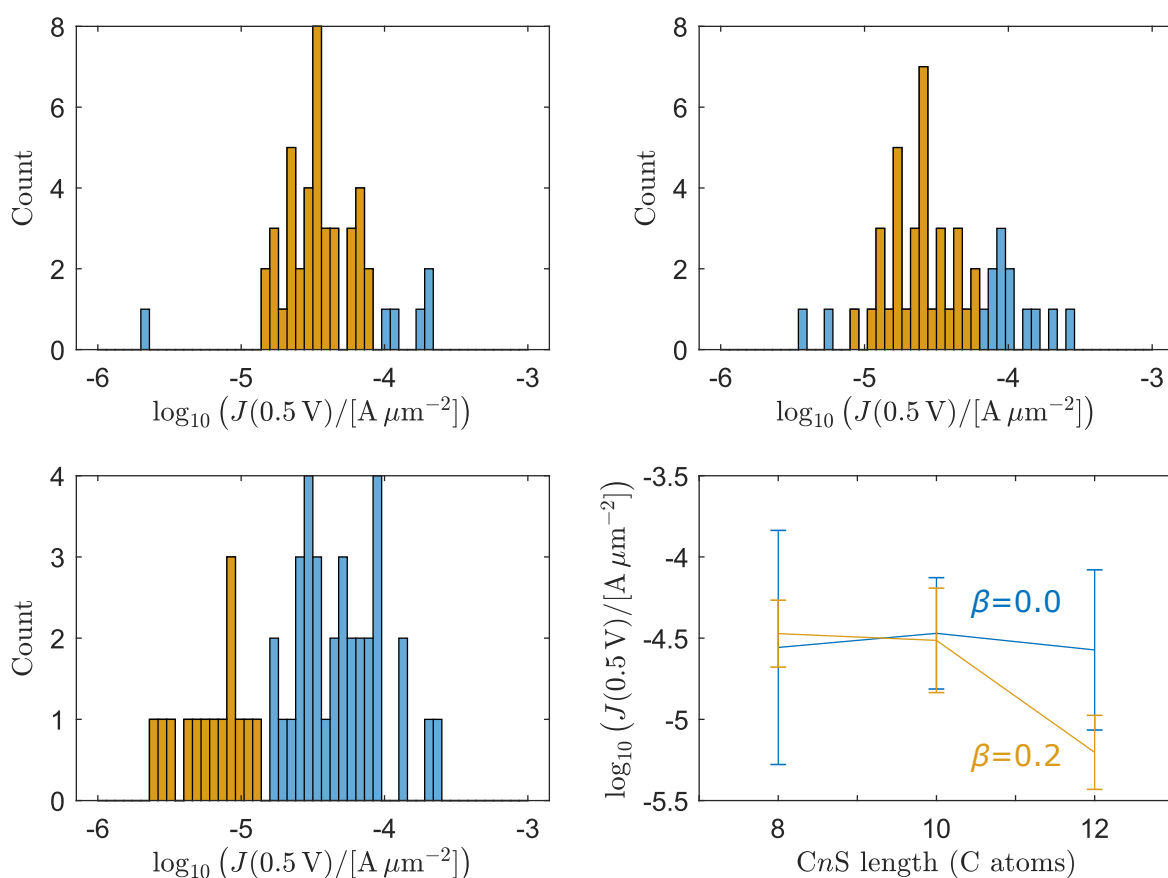


Fig. 4.10 Extraction of the decay factor for the devices of batch 5 as listed in Table 4.1, taken from 132 measured junctions. **a**, histograms of current at a fixed voltage for C8S junctions. **b**, similarly for C10S. **c**, similarly for C12S junctions. **d**, extraction of the decay coefficient as a function of CnS. The colour code in the histograms corresponds to the populations used to extract the average current for the junctions: combined blue and gold include the whole data, gold is a subset of the data used for the analysis omitting outliers in blue.

In parallel to the batches 1, 2, and 4, I developed another device architecture to contact molecular SAMs, encapsulating them in pores. The device design is described in Sec. 4.3.2.

Batch 5 was a test device to ensure the structure would effectively contact the bottom of the pores. In order to do this I fabricated a device without a SAM. At the time the device was made, due to no ALD system being available, I used an electron-beam evaporator to deposit Al_2O_3 as the insulator in which the pores would be etched. As opposed to ALD, which can form thin pinhole-free, evaporating the material requires a minimum thickness for the film to be continuous, although searches in the literature to find this minimum thickness proved unfruitful. I deposited a ~ 100 nm layer of Al_2O_3 using this system. I etched the pores using the OL pattern BHF I transferred SLG onto the samples via a standard wet transfer. Following a drying time of about a day, I patterned the graphene, according to the OL mask design, bonded and measured the device. Approximately half the junctions showed 1 k Ω resistance, whilst the other half were open circuits, which may be attributed to the high thickness of the insulator layer.

I then fabricated the next generation of $C_n\text{S}$ devices based on this design. An ALD system became available allowing me to deposit a film of thickness 3.6 nm as measured through ellipsometry. I used the relevant OL mask feature for SA and made devices with different lengths of $C_n\text{S}$.

We bonded and measured the junctions, 48 per $C_n\text{S}$ type, in the aforementioned set-up. I extracted the data and did the length regression, as shown in Fig. 4.10. The figure shows histograms of the junction current at a fixed voltage for the different $C_n\text{S}$ types. Looking at the histograms shown in Fig. 4.10.a-c, it is apparent that the spread of current values shows distinguishable population. As an example decay coefficients were extracted for different subsets of the data. In the population of C12S, a significant population appears in a lower-current region. One can infer that these junctions are ones where the transport is effectively through the molecular SAM, while the higher-current population corresponds to pinhole conduction. Such distinction is common in statistical analysis of large-area molecular junctions [38]. In the histograms for C8S and C10S, if this distinction exists between SAM and pinhole conduction, the overlap between the population appears more pronounced such that an objective criterion for separation is difficult to determine. These values of current are normalised by area using the dimensions of the OL mask design—deviations from this nominal value can be imaged by comparing it with actual AFM images of the pores. The apparent necessity to distinguish between subsets of the population is also a motivation for fabricating a larger number of devices. The fabrication procedure relies exclusively on processes that can be done in parallel for many devices. However, the electrical measurement of these devices would be a significant time constraint in gathering the data, as every device is independently bonded and measured successively, such that a measurement gathering substantial data can last a day for each device of 16 junctions.

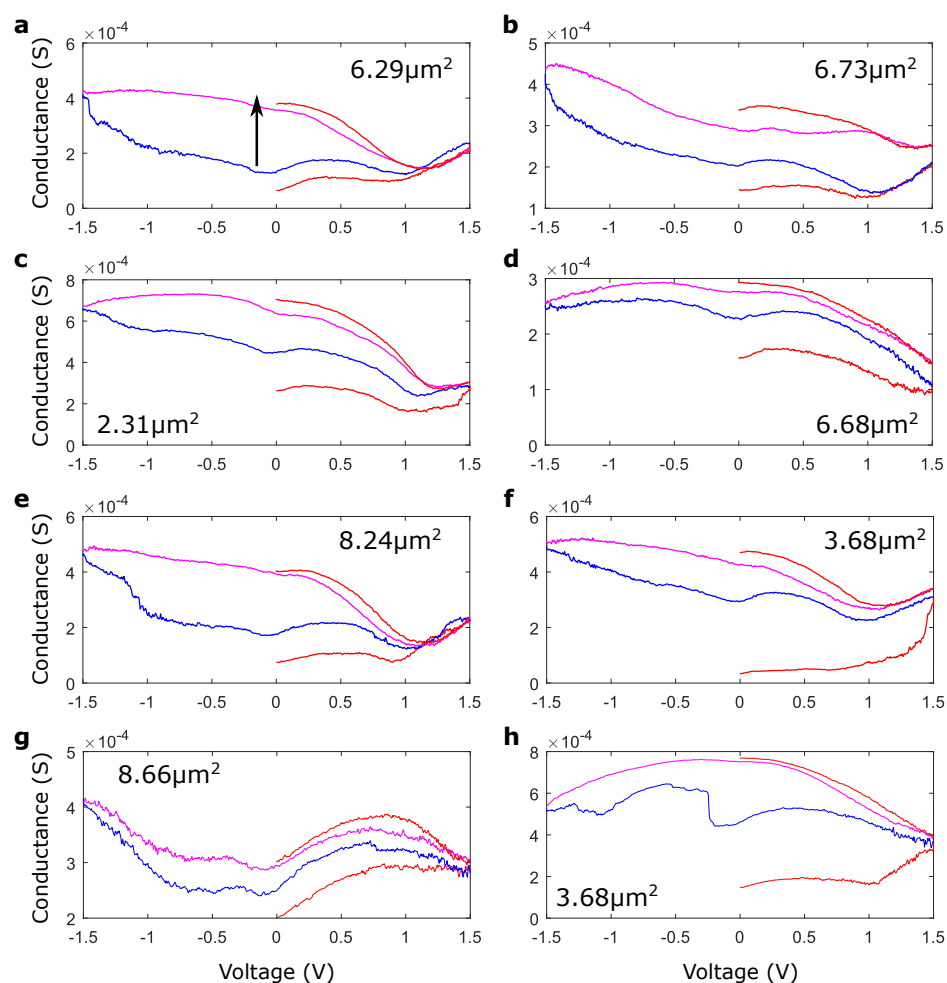


Fig. 4.11 Conductance data for BOC8S junctions. **a-f**, conductance data over successive measurements for junctions with 100% BOC8S. **g-h**, conductance data for junctions with 20% BOC8S. An arrow indicates the order of the measurements, in all the junctions displayed, the conductance increases over successive measurements.

BOC8S devices of batch 3

The measurements of the BOC8S-based SAM junctions, showed an interesting behaviour, which, however, made the planned observations difficult to extract. These were made using mixed SAMs of BOC8S and C8S with different proportions as listed in Table 4.1. In effect, a large number of devices showed hysteresis in their I - V characteristics. As the voltage was varied back and forth between -1.5 V and 1.5 V, the conductance of these junctions appeared to irreversibly increase, as shown in Fig. 4.11 and 4.13, where over successive measurements, the conductance is seen to increase by nearly an order of magnitude. Further measurements are needed to study the stabilisation in a high-conductance behaviour.

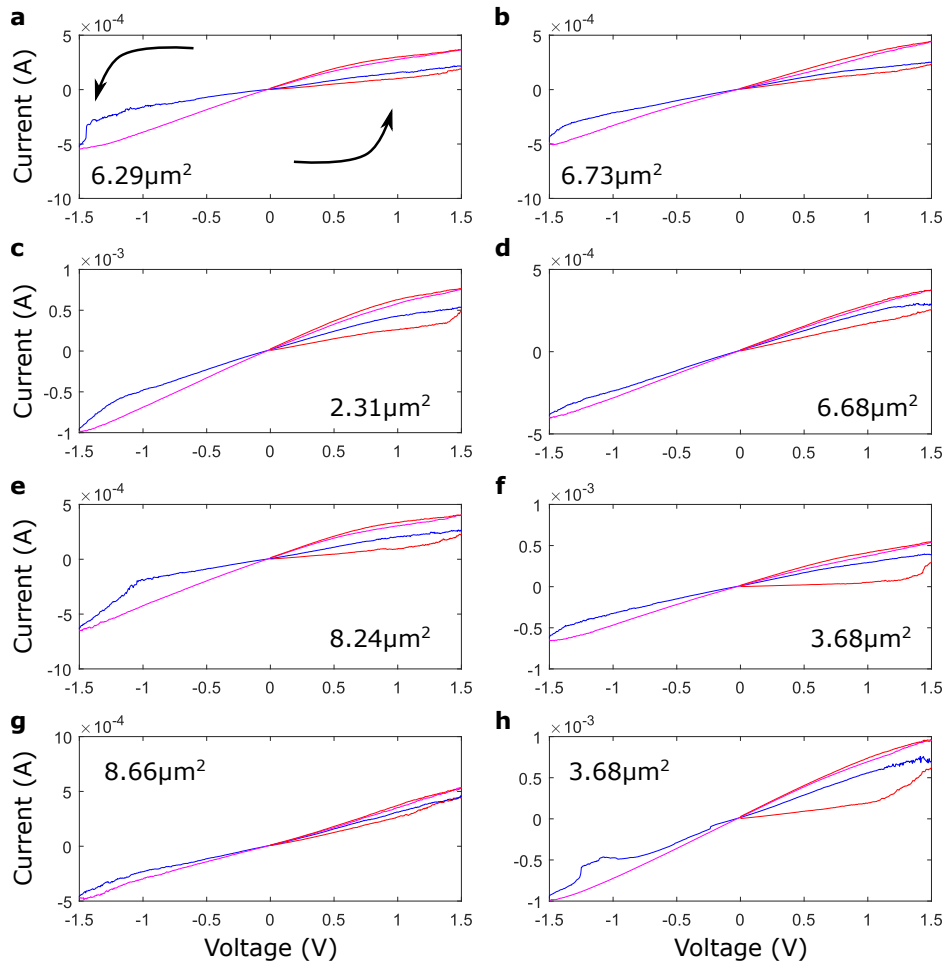


Fig. 4.12 I - V data for BOC8S junctions. The junctions, figure indices, and colours match those shown in Fig. 4.11. **a-f**, I - V data over successive measurements for junctions with 100% BOC8S. **g-h**, I - V data for junctions with 20% BOC8S. Arrows indicates the order of the measurements, in all the junctions displayed, the conductance increases over successive measurements.

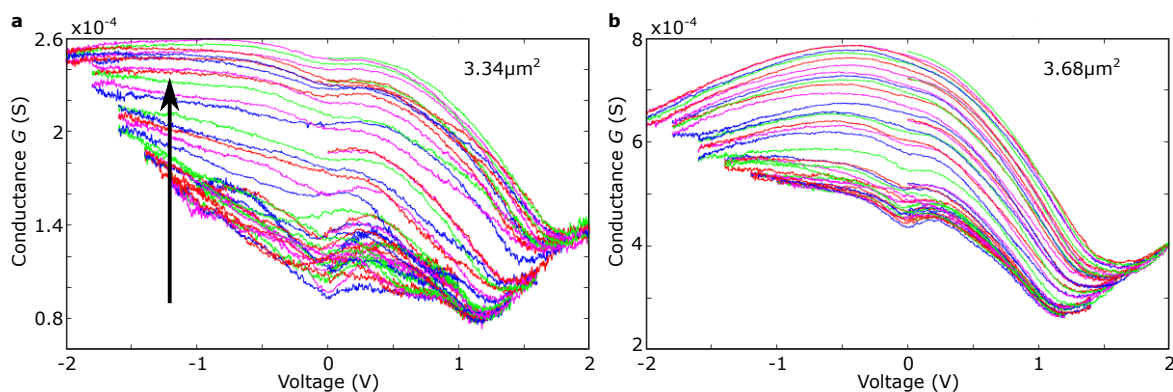


Fig. 4.13 Conductance profile of two (a, b) BOC8S junctions over many successive voltage cycles. A continuous conductance increase is seen over successive measurements.

The reason for this behaviour is difficult to probe. A likely scenario is an electrochemical reaction whereby the benzene arm is energetically permitted to detach from the BOC8S molecules to bind to the SLG. This process may be mediated by residual toluene solvents potentially present in the junction. However, the hypothesis of ion migration would seem to be contradicted by the fact that this increase occurs in both voltage polarities. Another possible scenario is that reducing BOC8S, i.e. detaching its oxygen terminated arm can be permitted by Joule heating. Another possibility is that the capacitive force across the graphene pushes it against the molecular structure and makes it form a π bond with the benzene ring.

Interestingly some asymmetry can be seen in the conductance profile of the junctions, where a polarity seems more conductive than the other. This may be expected from the asymmetric structure of the molecules, but is made difficult to probe by the continuous change over successive measurements.

The behaviour was best observed in junctions with 100% and 20% of BOC8S, where they accounted for 84% and 75% of measured junctions respectively, but was also present in samples of 9% BOC8S, where 39% exhibited this behaviour. This behaviour was not seen in 2% BOC8S junctions, where conduction was mostly Ohmic, apart from several open circuits, likely due to issues in the SLG transfer.

Interestingly, conductive-tip measurements carried out by our collaborators at the University of Lancaster on similar mixed SAMs did not produce this irreversible behaviour, and obtained data following the expectations laid out in Sec. 4.3.1. Analysis of these results is on-going and further devices are being planned for fabrication in the coming weeks, which will include the pyrene variations of the BOC n S structure.

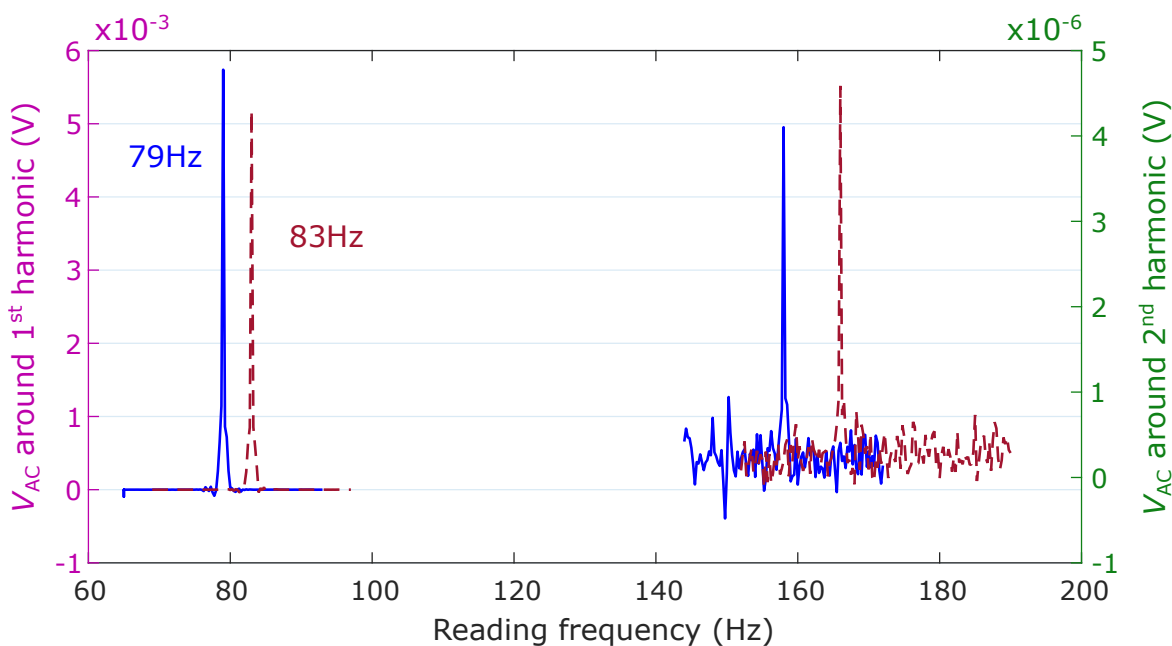


Fig. 4.14 Test of the 2ω measurement set-up. An AC voltage was set across the SLG electrode at two different frequencies, and the AC voltage across the junction was measured at the first and second harmonics.

4.4.2 Thermopower

As a test of the 2ω measurement method we connected one of the C12S junctions from batch 1 according to the arrangement described in Sec. 4.3.4. We set a driving AC voltage of 120 mV across the SLG top electrode and measured the AC voltage between the SLG and the junction's bottom electrode, for two different set frequencies, to verify a voltage could be seen at the second harmonic of the driving frequency. The results are shown in Fig. 4.14.

An AC voltage at the second harmonic was resolved for the two separate frequencies. The magnitude of the $V_{2\omega}$ is of the order of a few microvolts for a voltage across the SLG electrode of a few millivolts. The noise level at the second harmonic is of $\sim 0.5 \mu\text{V}$. First measurements of Seebeck coefficients in molecular junctions have reported values of the order of $10 \mu\text{V K}^{-1}$ in 1,4-benzenedithiol [260] and 1,1',4',1''-terphenyl-4-thiol molecules [261]. Assuming we create temperature gradients of the order of the order of 10 K or above, as discussed in Sec. 4.3.4, this would make it a suitable set-up for measuring thermovoltages in SAM junctions.

In order to relate this thermovoltage to a temperature gradient, a calibration measurement of the SLG's resistance as a function of temperature needs to be done.

The seemingly erroneous CnS length dependence observed thus far makes it uncertain that our devices effectively contact molecular SAMs. We are waiting for a confirmation of

a viable molecular device architecture to carry out the full protocol proposed in Sec. 4.3.4. However, the set-up seems to be adequate for the measurement of a thermovoltage at the second harmonic.

4.5 Discussion

Over the several iterations of devices to probe molecular SAMs electrically, several amendments were made to the fabrication procedure for future devices.

- Firstly, in the devices using the old design, the OL processes used to pattern the graphene top electrode required elevated temperatures, i.e. 120° C, which may have damaged the SAM and created pinholes. The etch of the SLG using oxygen plasma, may also have damaged the SAM at the edges of the junctions and permitting migration of the molecules out of the SLG-encapsulated area, as well as heating the region.
- In future devices, the patterning of the SLG is to be done directly on the PMMA used for transfer, so as to avoid a baking step. An OL process has been calibrated for patterning the PMMA using DUV to expose it through the OL mask. Preliminary tests have shown that cracks in the PMMA may become problematic at the stage of the plasma etch of the SLG, as the plasma can go through such cracks. To avoid these cracks baking the PMMA at the time it is deposited on the SLG:Cu foil structure has been shown to be effective by J. Girovsky.
- I developed an etch recipe on the RF asher, which would be more gentle on the device so as to limit the heating of the devices.
- Other steps involving temperature have been redesigned so as to avoid this heating, i.e. bonding the devices, which had typically been at 120° C has successfully been tested at 40° C. On a device of batch 4, bonding devices at 40° C as opposed to the typical 40° C has been shown to noticeably reduce the average conductance of measured junctions.
- A possible effect which may have been detrimental to our devices may be solvent contamination. Indeed the method of transferring graphene onto the samples is likely to encapsulate residual solvents from the SA, which have merely been dried at the stage of transfer. To remedy this, in recent devices, these were put in high vacuum, in an evaporator, for a few hours, so as to ensure the evaporation of residual solvents which may facilitate conduction bypassing the SAM.

Several other architectures are being planned at the time of writing. This includes one inspired by the aforementioned group, using multilayer graphene and evaporating Au on top. As a test (4 in Table 4.1), we fabricated devices using C_nS with an SLG top electrode, evaporated ~ 20 nm of Au onto the SLG through a lift-off process, and used the Au as a mask for the oxygen plasma etch. However, these exhibited only short circuits, possibly due to Au being evaporated through tears in the SLG. As a result we have bought multilayer graphene commercial to try this structure. Another interesting architecture is the one proposed by Puebla-Hellmann *et al.* [36], which self-assembles Au nanoparticles on top of the molecular SAM before coating them with a further layer of Au through evaporation; this has shown a high yield of functioning devices, around 95%, it demands, however, that the second head group be terminated with an appropriate head group for Au nanoparticles, such as a thiol termination. The OL design with pores is compatible with both architectures, so would require little adaptation in the fabrication procedure.

To complete and confirm a viable device architecture using the C_nS calibration, we are limited by the spread of current values for each of the population, their overlap with one another and with what may be short circuits in the junctions. This large overlap makes it difficult to identify working junctions from short circuits, and operate a regression of the length dependence. In order to counter this, in future devices we shall change the selected C_nS lengths used in the experiment from C8S, C10S, and C12S to C10S, C14S, and C18S. The C8S molecules are the most conductive ones with a resistance expected comparable to that of the SLG electrode, making the identification of short circuits particularly difficult with limited data; starting with a shortest length of 10 C atoms should help us go around this difficulty. Using a molecular-length step of four C atoms, as opposed to two, should result in larger differences in conductance of several orders of magnitude, and should make the length-dependence extraction less limited by the spread in each SAM type. Finally it can be expected that the probability of a short circuit is reduced the thicker the SAM is, which would also be beneficial.

Establishing an extra measurement set-up to speed up measurements would benefit the project greatly, as, especially in the extraction of the length dependence in C_nS junctions, we are limited by the amount of data which add to the uncertainty.

The 2ω measurement protocol is being developed at the time of writing, and is promising as a way to probe the thermoelectric performance of molecular structures, which to my knowledge has not been done in SAM devices.

4.6 Conclusion

In this chapter, we discussed the potential of molecular SAMs for thermoelectric devices. We saw that their transport properties are promising for enhanced thermoelectric performance, and the tunability offered by variations in the synthesis is a promising tool for obtaining high- ZT structures, as is the long term goal of the collaborative grant this project is associated with. Several strategies to integrate these molecular structures into devices have been proposed, fabricated and measured. To verify the suitability of a device architecture, we proposed the electrical probing of CnS SAMs to extract a molecular length dependence. We discussed improvements and limitations in the different iterations and scope for future improvements. More iterations and further data analysis is needed to obtain a definitive confirmation of working devices, which are currently in progress.

Chapter 5

Conclusion

In this thesis, we have covered several projects around thin-film devices to investigate functional types of transport.

In a first part, we showed that using graphene as a top electrode to contact quantum dot monolayers, or superlattices led to single-electron tunnelling with a high yield. We showed that it was possible to use arguments of statistical analysis to draw conclusions as to the topography of transport in the junctions. We discussed device architectures and characterised the quantum dot superlattice. We discussed ways to image the nanostructures in the devices. Further studies were proposed, i.e. the investigation of observed negative differential resistance in some of the junctions and ways to understand its occurrence. We proposed new devices to build a vertical single-electron transistor by gating through graphene. Further experiments are needed to develop a working architecture. Finally, routes to investigate quantum dot transport in a single-object approach, in nanogaps, were proposed with recipes developed. These are currently in progress.

In a second part, we demonstrated a thin-film device, which by contacting Al_2O_3 with graphene, operated both as a memristor and an actuator over the nanoscale up to microns. We studied the topography of the conduction in the film, which differentiates it from standard memristors. The particular filament formation, or electroforming, topography in the film is conducive to the actuation mechanism, and possibly the ultra-high on-off resistance ratios observed. Possible improvements to harness a better control of both of these properties were proposed through device designs.

Finally, in the third part, we proposed a vision for using molecular SAMs as thermoelectric materials, making use of the tailoring of their chemical structure to modulate electron and phonon transport in thermoelectric generators. We discussed strategies to develop the target device, and gather a confirmation of effective electrical contact of the molecular SAMs. We described several generations of devices for this effect. We introduced a new device design

offering advantages for the development of the target device. We presented characterisation set-ups to measure molecular junctions. We showed and discussed preliminary statistical analysis to understand transport in the several generations of devices. We proposed a protocol for the assessment of the thermoelectric efficiency of the devices, and did preliminary tests to verify its good functioning so it can be applied to certifiably working molecular devices. We proposed new molecular structures for investigating the contacting efficiency between graphene and different molecular structures, and showed results that will be compared with parallel characterisation by collaborators. We laid out plans, as the next steps in this project, both in terms of device fabrication, molecular structures, and data analysis.

References

- [1] S. E. Kohn, P. Y. Yu, Y. Petroff, Y. R. Shen, Y. Tsang, and M. L. Cohen, “Electronic band structure and optical properties of PbTe, PbSe, and PbS,” *Physical Review B*, vol. 8, no. 4, pp. 1477–1488, 1973.
- [2] H. Kanazawa and S. Adachi, “Optical properties of PbS,” *Journal of Applied Physics*, vol. 83, no. 11, pp. 5997–6001, 1998.
- [3] R. S. Kane, R. E. Cohen, and R. Silbey, “Theoretical study of the electronic structure of PbS nanoclusters,” *Journal of Physical Chemistry*, vol. 100, no. 19, pp. 7928–7932, 1996.
- [4] I. Moreels, K. Lambert, D. Smeets, D. De Muynck, T. Nollet, J. C. Martins, F. Vanhaecke, A. Vantomme, C. Delerue, G. Allan, and Z. Hens, “Size-Dependent Optical Properties of Colloidal PbS Quantum Dots,” *ACS Nano*, vol. 3, no. 10, pp. 3023–3030, 2009.
- [5] L. Cademartiri, E. Montanari, G. Calestani, A. Migliori, A. Guagliardi, and G. A. Ozin, “Size-dependent extinction coefficients of PbS quantum dots,” *Journal of the American Chemical Society*, vol. 128, no. 31, pp. 10337–10346, 2006.
- [6] N. F. Borrelli and D. W. Smith, “Quantum confinement of PbS microcrystals in glass,” *Journal of Non-Crystalline Solids*, vol. 180, no. 1, pp. 25–31, 1994.
- [7] R. S. Kane, R. E. Cohen, and R. Silbey, “Theoretical study of the electronic structure of PbS nanoclusters,” *Journal of Physical Chemistry*, vol. 100, no. 19, pp. 7928–7932, 1996.
- [8] D. Segets, J. M. Lucas, R. N. Klupp Taylor, M. Scheele, H. Zheng, A. P. Alivisatos, and W. Peukert, “Determination of the quantum dot band gap dependence on particle size from optical absorbance and transmission electron microscopy measurements,” *ACS Nano*, vol. 6, no. 10, pp. 9021–9032, 2012.
- [9] C. J. B. Ford, *The Physics of Nanoelectronic Systems, Part III course*. University of Cambridge, 2013.
- [10] J. M. Fruhman, H. P. A. G. Astier, B. Ehrler, M. Böhm, L. F. Eyre, P. R. Kidambi, U. Sassi, D. De Fazio, J. P. Griffiths, A. Robson, B. J. Robinson, S. Hofmann, A. C. Ferrari, and C. J. B. Ford, “High-yield parallel fabrication of quantum-dot monolayer single-electron devices displaying Coulomb staircase, contacted using graphene,” *in preparation*, 2019.

- [11] Y. Yang and W. Lu, “Nanoscale resistive switching devices: Mechanisms and modeling,” *Nanoscale*, vol. 5, no. 21, pp. 10076–10092, 2013.
- [12] D. Kos, H. P. A. G. Astier, G. D. Martino, J. Mertens, H. Ohadi, D. De Fazio, D. Yoon, Z. Zhao, A. Kuhn, A. C. Ferrari, C. J. B. Ford, and J. J. Baumberg, “Electrically Controlled Nano and Micro Actuation in Memristive Switching Devices with On-Chip Gas Encapsulation,” *Small*, p. 1801599, 2018.
- [13] R. Frisenda, *OPE3: a model system for single-molecule transport*. PhD thesis, TU Delft, 2015.
- [14] A. R. Garrigues, L. Yuan, L. Wang, E. R. Mucciolo, D. Thompon, E. Del Barco, and C. A. Nijhuis, “A Single-Level Tunnel Model to Account for Electrical Transport through Single Molecule-and Self-Assembled Monolayer-based Junctions,” *Scientific Reports*, vol. 6, no. 1, p. 26517, 2016.
- [15] C. Joachim, J. K. Gimzewski, R. R. Schlittler, and C. Chavy, “Electronic Transparency of a Single C60 Molecule,” *Physical Review Letters*, vol. 74, no. 11, pp. 2102–2105, 1995.
- [16] L. Rincón-García, C. Evangeli, G. Rubio-Bollinger, and N. Agrait, “Thermopower measurements in molecular junctions,” *Chemical Society Reviews*, vol. 45, no. 15, pp. 4285–4306, 2016.
- [17] Q. Zhang, L. Liu, S. Tao, C. Wang, C. Zhao, C. González, Y. J. Dappe, R. J. Nichols, and L. Yang, “Graphene as a Promising Electrode for Low-Current Attenuation in Nonsymmetric Molecular Junctions,” *Nano Letters*, vol. 16, no. 10, pp. 6534–6540, 2016.
- [18] C. He, Q. Zhang, S. Tao, C. Zhao, C. Zhao, W. Su, Y. J. Dappe, R. J. Nichols, and L. Yang, “Carbon-contacted single molecule electrical junctions,” *Physical Chemistry Chemical Physics*, vol. 20, no. 38, pp. 24553–24560, 2018.
- [19] L. E. Wilson, C. Hassenrück, R. F. Winter, A. J. White, T. Albrecht, and N. J. Long, “Ferrocene- and Biferrocene-Containing Macrocycles towards Single-Molecule Electronics,” *Angewandte Chemie - International Edition*, vol. 56, no. 24, pp. 6838–6842, 2017.
- [20] R. C. Temple, M. McLaren, R. M. D. Brydson, B. J. Hickey, and C. H. Marrows, “Long spin lifetime and large barrier polarisation in single electron transport through a CoFe nanoparticle,” *Scientific Reports*, vol. 6, no. 1, p. 28296, 2016.
- [21] C. Brun, K. H. Müller, I. P. Hong, F. Patthey, C. Flindt, and W. D. Schneider, “Dynamical coulomb blockade observed in nanosized electrical contacts,” *Physical Review Letters*, vol. 108, no. 12, p. 126802, 2012.
- [22] R. Wilkins, E. Ben-Jacob, and R. C. Jaklevic, “STM observations of Coulomb blockade and oxide polarization in small metal droplets,” *Physical Review Letters*, vol. 63, no. 7, p. 801, 1989.

- [23] W. Hong, H. Valkenier, G. Mészáros, D. Z. Manrique, A. Mishchenko, A. Putz, P. M. García, C. J. Lambert, J. C. Hummelen, and T. Wandlowski, “An MCBJ case study: The influence of π -conjugation on the single-molecule conductance at a solid/liquid interface,” *Beilstein Journal of Nanotechnology*, vol. 2, no. 1, pp. 699–713, 2011.
- [24] C. Zhou, C. J. Muller, M. R. Deshpande, J. W. Sleight, and M. A. Reed, “Microfabrication of a mechanically controllable break junction in silicon,” *Applied Physics Letters*, vol. 67, no. 8, p. 1160, 1995.
- [25] F. Schwarz and E. Lörtscher, “Break-junctions for investigating transport at the molecular scale,” *Journal of Physics Condensed Matter*, vol. 26, no. 47, p. 474201, 2014.
- [26] R. Frisenda, D. Stefani, and H. S. Van Der Zant, “Quantum Transport through a Single Conjugated Rigid Molecule, a Mechanical Break Junction Study,” *Accounts of Chemical Research*, vol. 51, no. 6, pp. 1359–1367, 2018.
- [27] Y. Azuma, Y. Onuma, M. Sakamoto, T. Teranishi, and Y. Majima, “Rhombic Coulomb diamonds in a single-electron transistor based on an Au nanoparticle chemically anchored at both ends,” *Nanoscale*, vol. 8, no. 8, pp. 4720–4726, 2016.
- [28] D. R. Strachan, D. E. Smith, D. E. Johnston, T. H. Park, M. J. Therien, D. A. Bonnell, and A. T. Johnson, “Controlled fabrication of nanogaps in ambient environment for molecular electronics,” *Applied Physics Letters*, vol. 86, no. 4, p. 043109, 2005.
- [29] P. Gehring, A. Harzheim, J. Spièce, Y. Sheng, G. Rogers, C. Evangeli, A. Mishra, B. J. Robinson, K. Porfyrakis, J. H. Warner, O. V. Kolosov, G. A. D. Briggs, and J. A. Mol, “Field-Effect Control of Graphene-Fullerene Thermoelectric Nanodevices,” *Nano Letters*, vol. 17, no. 11, pp. 7055–7061, 2017.
- [30] Z. Xie, I. Bâldea, S. Oram, C. E. Smith, and C. D. Frisbie, “Effect of Heteroatom Substitution on Transport in Alkanedithiol-Based Molecular Tunnel Junctions: Evidence for Universal Behavior,” *ACS Nano*, vol. 11, no. 1, pp. 569–578, 2017.
- [31] C. A. Nijhuis, W. F. Reus, J. R. Barber, and G. M. Whitesides, “Comparison of SAM-based junctions with Ga₂O₃/EGaIn top electrodes to other large-area tunneling junctions,” *Journal of Physical Chemistry C*, vol. 116, no. 26, pp. 14139–14150, 2012.
- [32] M. Baghbanzadeh, F. C. Simeone, C. M. Bowers, K. C. Liao, M. Thuo, M. Baghbanzadeh, M. S. Miller, T. B. Carmichael, and G. M. Whitesides, “Odd-even effects in charge transport across n-alkanethiolate-based SAMs,” *Journal of the American Chemical Society*, vol. 136, no. 48, pp. 16919–16925, 2014.
- [33] H. Jeong, D. Kim, D. Xiang, and T. Lee, “High-Yield Functional Molecular Electronic Devices,” *ACS Nano*, vol. 11, no. 7, pp. 6511–6548, 2017.
- [34] H. Jeong, D. Kim, P. Kim, M. R. Cho, W. T. Hwang, Y. Jang, K. Cho, M. Min, D. Xiang, Y. D. Park, H. Jeong, and T. Lee, “A new approach for high-yield metal-molecule-metal junctions by direct metal transfer method,” *Nanotechnology*, vol. 26, no. 2, p. 025601, 2015.

- [35] G. Wang, Y. Kim, M. Choe, T.-W. Kim, and T. Lee, "A New Approach for Molecular Electronic Junctions with a Multilayer Graphene Electrode," *Advanced Materials*, vol. 23, no. 6, pp. 755–760, 2011.
- [36] G. Puebla-Hellmann, K. Venkatesan, M. Mayor, and E. Lörtscher, "Metallic nanoparticle contacts for high-yield, ambient-stable molecular-monolayer devices," *Nature*, vol. 559, no. 7713, pp. 232–235, 2018.
- [37] J. C. Love, L. A. Estroff, J. K. Kriebel, R. G. Nuzzo, and G. M. Whitesides, "Self-assembled monolayers of thiolates on metals as a form of nanotechnology," *Chemical Reviews*, vol. 105, no. 4, pp. 1103–1169, 2005.
- [38] W. F. Reus, C. A. Nijhuis, J. R. Barber, M. M. Thuo, S. Tricard, and G. M. Whitesides, "Statistical tools for analyzing measurements of charge transport," *Journal of Physical Chemistry C*, vol. 116, no. 11, pp. 6714–6733, 2012.
- [39] A. Vilan, D. Aswal, and D. Cahen, "Large-Area, Ensemble Molecular Electronics: Motivation and Challenges," *Chemical Reviews*, vol. 117, no. 5, pp. 4248–4286, 2017.
- [40] K. S. Novoselov, A. K. Geim, S. V. Morozov, D. Jiang, Y. Zhang, S. V. Dubonos, I. V. Grigorieva, and A. A. Firsov, "Electric Field Effect in Atomically Thin Carbon Films," *Science*, vol. 306, no. 5696, pp. 666–669, 2004.
- [41] A. K. Geim, "Graphene: Status and Prospects," *Science*, vol. 324, no. 5934, pp. 1530–1534, 2009.
- [42] A. H. Castro Neto, F. Guinea, N. M. R. Peres, K. S. Novoselov, and A. K. Geim, "The electronic properties of graphene," *Reviews of Modern Physics*, vol. 81, no. 1, pp. 109–162, 2009.
- [43] C. Lee, X. Wei, J. W. Kysar, and J. Hone, "Measurement of the elastic properties and intrinsic strength of monolayer graphene," *Science*, vol. 321, no. 5887, pp. 385–8, 2008.
- [44] E. Pop, V. Varshney, and A. K. Roy, "Thermal properties of graphene: Fundamentals and applications," *MRS Bulletin*, vol. 37, no. 12, pp. 1273–1281, 2012.
- [45] G. Konstantatos, M. Badioli, L. Gaudreau, J. Osmond, M. Bernechea, F. P. G. de Arquer, F. Gatti, and F. H. L. Koppens, "Hybrid graphene–quantum dot phototransistors with ultrahigh gain," *Nature Nanotechnology*, vol. 7, no. 6, pp. 363–368, 2012.
- [46] J. T.-W. Wang, J. M. Ball, E. M. Barea, A. Abate, J. A. Alexander-Webber, J. Huang, M. Saliba, I. Mora-Sero, J. Bisquert, H. J. Snaith, and R. J. Nicholas, "Low-Temperature Processed Electron Collection Layers of Graphene/TiO₂ Nanocomposites in Thin Film Perovskite Solar Cells," *Nano Letters*, vol. 14, no. 2, pp. 724–730, 2014.
- [47] J. Liu, Z. Yin, X. Cao, F. Zhao, A. Lin, L. Xie, Q. Fan, F. Boey, H. Zhang, and W. Huang, "Bulk Heterojunction Polymer Memory Devices with Reduced Graphene Oxide as Electrodes," *ACS Nano*, vol. 4, no. 7, pp. 3987–3992, 2010.

- [48] C. Jeffrey, “First flexible graphene-based display created,” *New Atlas (news article)*, 2014.
- [49] X. Wang, L. Zhi, and K. Müllen, “Transparent, conductive graphene electrodes for dye-sensitized solar cells,” *Nano Letters*, vol. 8, no. 1, pp. 323–327, 2008.
- [50] G. Jo, M. Choe, C.-Y. Cho, J. H. Kim, W. Park, S. Lee, W.-K. Hong, T.-W. Kim, S.-J. Park, B. H. Hong, Y. H. Kahng, and T. Lee, “Large-scale patterned multi-layer graphene films as transparent conducting electrodes for GaN light-emitting diodes,” *Nanotechnology*, vol. 21, no. 17, p. 175201, 2010.
- [51] H. Haick, O. Niitsoo, J. Ghabboun, and D. Cahen, “Electrical contacts to organic molecular films by metal evaporation: Effect of contacting details,” *Journal of Physical Chemistry C*, vol. 111, no. 5, pp. 2318–2329, 2007.
- [52] B. Guo, L. Fang, B. Zhang, and J. R. Gong, “Graphene Doping: A Review,” *Insciences Journal*, pp. 80–89, 2011.
- [53] K. I. Bolotin, K. J. Sikes, Z. Jiang, M. Klima, G. Fudenberg, J. Hone, P. Kim, and H. L. Stormer, “Ultrahigh electron mobility in suspended graphene,” *Solid State Communications*, vol. 146, no. 9-10, pp. 351–355, 2008.
- [54] H. Hirai, H. Tsuchiya, Y. Kamakura, N. Mori, and M. Ogawa, “Electron mobility calculation for graphene on substrates,” *Journal of Applied Physics*, vol. 116, no. 8, p. 083703, 2014.
- [55] G. Konstantatos, I. Howard, A. Fischer, S. Hoogland, J. Clifford, E. Klem, L. Levina, and E. H. Sargent, “Ultrasensitive solution-cast quantum dot photodetectors,” *Nature*, vol. 442, no. 7099, pp. 180–183, 2006.
- [56] R. A. Barton, B. Ilic, A. M. van der Zande, W. S. Whitney, P. L. McEuen, J. M. Parpia, and H. G. Craighead, “High, Size-Dependent Quality Factor in an Array of Graphene Mechanical Resonators,” *Nano Letters*, vol. 11, no. 3, pp. 1232–1236, 2011.
- [57] J. S. Bunch, S. S. Verbridge, J. S. Alden, A. M. Van Der Zande, J. M. Parpia, H. G. Craighead, and P. L. McEuen, “Impermeable atomic membranes from graphene sheets,” *Nano Letters*, vol. 8, no. 8, pp. 2458–2462, 2008.
- [58] J. M. Yuk, K. Kim, B. Aleman, W. Regan, J. H. Ryu, J. Park, P. Ercius, H. M. Lee, A. P. Alivisatos, M. F. Crommie, J. Y. Lee, and A. Zettl, “Graphene Veils and Sandwiches,” *Nano Letters*, vol. 11, no. 8, pp. 3290–3294, 2011.
- [59] J. Vejpravova, B. Pacakova, J. Endres, A. Mantlikova, T. Verhagen, V. Vales, O. Frank, and M. Kalbac, “Graphene wrinkling induced by monodisperse nanoparticles: facile control and quantification,” *Scientific Reports*, vol. 5, no. 1, p. 15061, 2015.
- [60] Z. Osváth, A. Deák, K. Kertész, G. Molnár, G. Vértesy, D. Zámbo, C. Hwang, and L. P. Biró, “The structure and properties of graphene on gold nanoparticles,” *Nanoscale*, vol. 7, no. 12, pp. 5503–5509, 2015.

- [61] B. Li, M. Famili, E. Pensa, I. Grace, N. J. Long, C. Lambert, T. Albrecht, and L. F. Cohen, "Cross-plane conductance through a graphene/molecular monolayer/Au sandwich," *Nanoscale*, vol. 10, no. 42, pp. 19791–19798, 2018.
- [62] P. Song, C. S. S. Sangeeth, D. Thompson, W. Du, K. P. Loh, and C. A. Nijhuis, "Noncovalent Self-Assembled Monolayers on Graphene as a Highly Stable Platform for Molecular Tunnel Junctions," *Advanced Materials*, vol. 28, no. 4, pp. 631–639, 2016.
- [63] S. Bouvron, R. Maurand, A. Graf, P. Erler, L. Gragnaniello, M. Skripnik, D. Wiedmann, C. Engesser, C. Nef, W. Fu, C. Schönenberger, F. Pauly, and M. Fonin, "Charge transport in a single molecule transistor probed by scanning tunneling microscopy," *Nanoscale*, vol. 10, no. 3, pp. 1487–1493, 2018.
- [64] C. Lu, D. Zhang, A. Van Der Zande, P. Kim, and I. P. Herman, "Electronic transport in nanoparticle monolayers sandwiched between graphene electrodes," *Nanoscale*, vol. 6, no. 23, pp. 14158–14162, 2014.
- [65] C. S. Lau, J. A. Mol, J. H. Warner, and G. A. D. Briggs, "Nanoscale control of graphene electrodes," *Physical Chemistry Chemical Physics*, vol. 16, no. 38, pp. 20398–20401, 2014.
- [66] S. Caneva, P. Gehring, V. M. García-Suárez, A. García-Fuente, D. Stefani, I. J. Olavarria-Contreras, J. Ferrer, C. Dekker, and H. S. J. van der Zant, "Mechanically controlled quantum interference in graphene break junctions," *Nature Nanotechnology*, vol. 13, no. 12, pp. 1126–1131, 2018.
- [67] C. He, Q. Zhang, S. Tao, C. Zhao, C. Zhao, W. Su, Y. J. Dappe, R. J. Nichols, and L. Yang, "Carbon-contacted single molecule electrical junctions," *Physical Chemistry Chemical Physics*, vol. 20, no. 38, pp. 24553–24560, 2018.
- [68] C. N. R. Rao, P. J. Thomas, and G. U. Kulkarni, *Nanocrystals : synthesis, properties and applications*. Springer-Verlag Berlin Heidelberg, 2007.
- [69] D. J. Barber and I. C. Freestone, "An investigation of the origin of the colour of the Lycurgus cup by analytical transmission electron microscopy," *Archaeometry*, vol. 32, no. 1, pp. 33–45, 1990.
- [70] M. José-Yacaman, L. Rendon, J. Arenas, and M. C. Serra Puche, "Maya Blue Paint: An Ancient Nanostructured Material," *Science*, vol. 273, no. 5272, pp. 223–225, 1996.
- [71] M. Faraday, "The Bakerian Lecture: Experimental Relations of Gold (and Other Metals) to Light," *Philosophical Transactions of the Royal Society of London*, vol. 147, no. 0, pp. 145–181, 1857.
- [72] G. Mie, "Beiträge zur Optik trüber Medien, speziell kolloidaler Metallösungen," *Annalen der Physik*, vol. 330, no. 3, pp. 377–445, 1908.
- [73] R. Gans, "Über die Form ultramikroskopischer Goldteilchen," *Annalen der Physik*, vol. 342, no. 5, pp. 881–900, 1912.

- [74] R. Gans, "Über die Form ultramikroskopischer Silberteilchen," *Annalen der Physik*, vol. 352, no. 10, pp. 270–284, 1915.
- [75] H. Fröhlich, "Die spezifische Wärme der Elektronen kleiner Metallteilchen bei tiefen Temperaturen," *Physica*, vol. 4, no. 5, pp. 406–412, 1937.
- [76] C. Gorter, "A possible explanation of the increase of the electrical resistance of thin metal films at low temperatures and small field strengths," *Physica*, vol. 17, no. 8, pp. 777–780, 1951.
- [77] C. J. Stolle, T. B. Harvey, and B. A. Korgel, "Nanocrystal photovoltaics: a review of recent progress," *Current Opinion in Chemical Engineering*, vol. 2, no. 2, pp. 160–167, 2013.
- [78] V. L. Colvin, M. C. Schlamp, and A. P. Alivisatos, "Light-emitting diodes made from cadmium selenide nanocrystals and a semiconducting polymer," *Nature*, vol. 370, no. 6488, pp. 354–357, 1994.
- [79] P. Alivisatos, "The use of nanocrystals in biological detection," *Nature Biotechnology*, vol. 22, no. 1, pp. 47–52, 2004.
- [80] D. L. Klein, P. L. McEuen, J. E. Katari, R. Roth, and A. P. Alivisatos, "An approach to electrical studies of single nanocrystals," *Applied Physics Letters*, vol. 68, no. 18, pp. 2574–2576, 1996.
- [81] S. V. Gaponenko, *Introduction to nanophotonics*. Cambridge University Press, 2010.
- [82] S. V. Gaponenko, *Optical Properties of Semiconductor Nanocrystals*. Cambridge University Press, 1998.
- [83] A. Sacchetti, "Electrical current in nanoelectronic devices," *Physics Letters, Section A: General, Atomic and Solid State Physics*, vol. 374, no. 39, pp. 4057–4060, 2010.
- [84] Y. Wang, A. Suna, W. Mahler, and R. Kasowski, "PbS in polymers. From molecules to bulk solids," *The Journal of Chemical Physics*, vol. 87, no. 12, pp. 7315–7322, 1987.
- [85] O. Madelung, U. Rössler, and M. Schulz, eds., *Non-Tetrahedrally Bonded Elements and Binary Compounds I*, vol. 41C of *Landolt-Börnstein - Group III Condensed Matter*. Berlin/Heidelberg: Springer-Verlag, 1998.
- [86] I. Kang and F. W. Wise, "Electronic structure and optical properties of PbS and PbSe quantum dots," *Journal of the Optical Society of America B*, vol. 14, no. 7, p. 1632, 1997.
- [87] H. Wang, E. Lhuillier, Q. Yu, A. Mottaghizadeh, C. Ulysse, A. Zimmers, A. Descamps-Mandine, B. Dubertret, and H. Aubin, "Effects of electron-phonon interactions on the electron tunneling spectrum of PbS quantum dots," *Physical Review B - Condensed Matter and Materials Physics*, vol. 92, no. 4, p. 41403, 2015.
- [88] A. V. Rodina, L. Efros, M. Rosen, and B. K. Meyer, "Theory of the Zeeman effect in semiconductor nanocrystals," *Materials Science and Engineering C*, vol. 19, no. 1–2, pp. 435–438, 2002.

- [89] H. Grabert and M. H. Devoret, eds., *Single Charge Tunneling*, vol. 294 of *NATO ASI Series*. Boston, MA: Springer US, 1992.
- [90] J. Lambe and R. C. Jaklevic, “Charge-Quantization Studies Using a Tunnel Capacitor,” *Physical Review Letters*, vol. 22, no. 25, pp. 1371–1375, 1969.
- [91] R. I. Shekhter, “Zero anomalies in the resistance of a tunnel junction containing metallic inclusions in the oxide layer,” *Journal of Experimental and Theoretical Physics (Zhurnal Éksperimental’noĭ i Teoreticheskoi Fiziki)*, vol. 36, p. 747, 1973.
- [92] I. O. Kulik and I. Shekhter, “Kinetic Phenomena and Charge Discreteness Effects in Granulated Media,” *Journal of Experimental and Theoretical Physics (Zhurnal Éksperimental’noĭ i Teoreticheskoi Fiziki)*, vol. 41, no. 2, pp. 308–316, 1975.
- [93] G. Dolan and J. Dunsmuir, “Very small (20 nm) lithographic wires, dots, rings, and tunnel junctions,” *Physica B: Condensed Matter*, vol. 152, no. 1-2, pp. 7–13, 1988.
- [94] U. Meirav and E. B. Foxman, “Single-electron phenomena in semiconductors,” *Semiconductor Science and Technology*, vol. 11, pp. 255–284, 1996.
- [95] M. H. Devoret, D. Esteve, and C. Urbina, “Single-electron transfer in metallic nanostructures,” *Nature*, vol. 360, no. 6404, pp. 547–553, 1992.
- [96] D. K. Ferry, S. M. Goodnick, and J. Bird, “Transport in Nanostructures,” in *Transport in Nanostructures, Second Edition*, Cambridge University Press, 2009.
- [97] L. Bassett, *Probing Electron-Electron Interactions with a Quantum Antidot*. PhD thesis, University of Cambridge, 2009.
- [98] D. Averin and K. Likharev, “Probable coherent oscillations at single-electron tunneling,” in *SQUID ’85 Superconducting Quantum Interference Devices and their Applications*, Berlin, Boston: De Gruyter, 1985.
- [99] D. V. Averin and K. K. Likharev, “Coulomb blockade of single-electron tunneling, and coherent oscillations in small tunnel junctions,” *Journal of Low Temperature Physics*, vol. 62, no. 3-4, pp. 345–373, 1986.
- [100] E. Ben-Jacob, Y. Gefen, K. Mullen, and Z. Schuss, “Charge oscillations and Zener noise due to interband transitions in small junctions,” in *SQUID ’85 Superconducting Quantum Interference Devices and their Applications*, Berlin, Boston: De Gruyter, 1985.
- [101] E. Ben-Jacob, D. J. Bergman, B. J. Matkowsky, and Z. Schuss, “Master-equation approach to shot noise in Josephson junctions,” *Physical Review B*, vol. 34, no. 3, pp. 1572–1581, 1986.
- [102] G.-L. Ingold and Y. V. Nazarov, “Charge Tunneling Rates in Ultrasmall Junctions,” in *Single Charge Tunneling. NATO ASI Series (Series B: Physics)*, pp. 21–107, Springer, Boston, MA, 2005.
- [103] C. W. J. Beenakker, “Theory of Coulomb-blockade oscillations in the conductance of a quantum dot,” *Physical Review B*, vol. 44, no. 4, pp. 1646–1656, 1991.

- [104] E. Bonet, M. M. Deshmukh, and D. C. Ralph, “Solving rate equations for electron tunneling via discrete quantum states,” *Physical Review B*, vol. 65, no. 4, p. 045317, 2002.
- [105] D. Chattopadhyay and P. S. Rakshit, *Electronics: fundamentals and applications*. New Age Publishers, 2006.
- [106] H. Inokawa, A. Fujiwara, and Y. Takahashi, “Multipeak negative-differential-resistance device by combining single-electron and metal-oxide-semiconductor transistors,” *Applied Physics Letters*, vol. 79, no. 22, pp. 3618–3620, 2001.
- [107] A. C. Seabaugh, Y. C. Kao, and H. T. Yuan, “Nine-State Resonant Tunneling Diode Memory,” *IEEE Electron Device Letters*, vol. 13, no. 9, pp. 479–481, 1992.
- [108] G. S. May and S. M. Sze, *Fundamentals of semiconductor fabrication*. Wiley, 2004.
- [109] M. Hines and G. Scholes, “Colloidal PbS Nanocrystals with Size-Tunable Near-Infrared Emission: Observation of Post-Synthesis Self-Narrowing of the Particle Size Distribution,” *Advanced Materials*, vol. 15, no. 21, pp. 1844–1849, 2003.
- [110] S. Franssila, *Introduction to Microfabrication*. Chichester, UK: John Wiley & Sons, Ltd, 2010.
- [111] S. Hercules and D. M. Hercules, “Surface analysis,” *Encyclopaedia Britannica*, 2018.
- [112] G. Sauerbrey, “Verwendung von Schwingquarzen zur Wägung dünner Schichten und zur Mikrowägung,” *Zeitschrift für Physik*, vol. 155, pp. 206–222, 1959.
- [113] R. Mazzocco, *Measurements of Graphene-Environment Interactions on the Nanometre Length Scale*. PhD thesis, University of Lancaster, 2015.
- [114] A. K. Srivastava and P. Sakthivel, “Quartz-crystal microbalance study for characterizing atomic oxygen in plasma ash tools,” *Journal of Vacuum Science & Technology A: Vacuum, Surfaces, and Films*, vol. 19, no. 1, pp. 97–100, 2001.
- [115] “PLO-10 Series Phase Lock Oscillator, Operation and Service Manual, IPN 605800 Rev. G, Inficon,” tech. rep., 2007.
- [116] M. A. Boles, *Self-Assembly of Colloidal Nanocrystals: Surface Ligands Promote the Formation of Unexpected Superlattices*. PhD thesis, University of Chicago, 2016.
- [117] B. W. Goodfellow, Y. Yu, C. A. Bosoy, D. M. Smilgies, and B. A. Korgel, “The Role of Ligand Packing Frustration in Body-Centered Cubic (bcc) Superlattices of Colloidal Nanocrystals,” *Journal of Physical Chemistry Letters*, vol. 6, no. 13, pp. 2406–2412, 2015.
- [118] H. Song, H. Lee, and T. Lee, “Intermolecular chain-to-chain tunneling in metal-alkanethiol-metal junctions,” *Journal of the American Chemical Society*, vol. 129, no. 13, pp. 3806–3807, 2007.
- [119] A. A. Gunawan, B. Chernomordik, D. Plemmons, D. Deng, E. S. Aydil, and K. A. Mkhoyan, “Ligands in PbSe Nanocrystals: Characterizations and Plasmonic Interactions,” *Microscopy and Microanalysis*, vol. 19, no. S2, pp. 1506–1507, 2013.

- [120] W. Wang, "Electronic transport in self-assembled alkanethiol monolayers," *Physica E: Low-dimensional Systems and Nanostructures*, vol. 19, no. 1-2, pp. 117–125, 2003.
- [121] Z. Ning, M. Molnár, Y. Chen, P. Friberg, L. Gan, H. Agren, and Y. Fu, "Role of surface ligands in optical properties of colloidal CdSe/CdS quantum dots," *Physical Chemistry Chemical Physics*, vol. 13, no. 13, p. 5848, 2011.
- [122] F. Xu, L. F. Gerlein, X. Ma, C. R. Haughn, M. F. Doty, and S. G. Cloutier, "Impact of different surface ligands on the optical properties of PbS quantum dot solids," *Materials*, vol. 8, no. 4, pp. 1858–1870, 2015.
- [123] A. A. Bakulin, S. Neutzner, H. J. Bakker, L. Ottaviani, D. Barakel, and Z. Chen, "Charge trapping dynamics in pbs colloidal quantum dot photovoltaic devices," *ACS Nano*, vol. 7, no. 10, pp. 8771–8779, 2013.
- [124] M. Malicki, K. E. Knowles, and E. A. Weiss, "Gating of hole transfer from photoexcited PbS quantum dots to aminoferrocene by the ligand shell of the dots," *Chem. Commun.*, vol. 49, no. 39, pp. 4400–4402, 2013.
- [125] K. Szendrei, W. Gomulya, M. Yarema, W. Heiss, and M. A. Loi, "PbS nanocrystal solar cells with high efficiency and fill factor," *Applied Physics Letters*, vol. 97, no. 20, p. 203501, 2010.
- [126] K. S. Jeong, J. Tang, H. Liu, J. Kim, A. W. Schaefer, K. Kemp, L. Levina, X. Wang, S. Hoogland, R. Debnath, L. Brzozowski, E. H. Sargent, and J. B. Asbury, "Enhanced Mobility-Lifetime Products in PbS Colloidal Quantum Dot Photovoltaics," *ACS Nano*, vol. 6, no. 1, pp. 89–99, 2012.
- [127] A. H. Ip, S. M. Thon, S. Hoogland, O. Voznyy, D. Zhitomirsky, R. Debnath, L. Levina, L. R. Rollny, G. H. Carey, A. Fischer, K. W. Kemp, I. J. Kramer, Z. Ning, A. J. Labelle, K. W. Chou, A. Amassian, and E. H. Sargent, "Hybrid passivated colloidal quantum dot solids," *Nature Nanotechnology*, vol. 7, no. 9, pp. 577–582, 2012.
- [128] B. J. Robinson and O. V. Kolosov, "Probing nanoscale graphene-liquid interfacial interactions via ultrasonic force spectroscopy," *Nanoscale*, vol. 6, no. 18, pp. 10806–10816, 2014.
- [129] M. C. Weidman, K. G. Yager, and W. A. Tisdale, "Interparticle spacing and structural ordering in superlattice pbs nanocrystal solids undergoing ligand exchange," *Chemistry of Materials*, vol. 27, no. 2, pp. 474–482, 2015.
- [130] R. Pozner, E. Lifshitz, and U. Peskin, "Negative differential resistance probe for interdot interactions in a double quantum dot array," *Journal of Physical Chemistry Letters*, vol. 6, no. 9, pp. 1521–1528, 2015.
- [131] Y. Higashikawa, Y. Azuma, Y. Majima, S. Kano, and M. Fujii, "Integration of colloidal silicon nanocrystals on metal electrodes in single-electron transistor," *Applied Physics Letters*, vol. 109, no. 21, p. 213104, 2016.
- [132] M. Eich, R. Pisoni, A. Pally, H. Overweg, A. Kurzmann, Y. Lee, P. Rickhaus, K. Watanabe, T. Taniguchi, K. Ensslin, and T. Ihn, "Coupled Quantum Dots in Bilayer Graphene," *Nano Letters*, vol. 18, no. 8, pp. 5042–5048, 2018.

- [133] L. P. Kouwenhoven, T. H. Oosterkamp, M. W. S. Danoesastro, M. Eto, D. G. Austing, T. Honda, and S. Tarucha, "Excitation spectra of circular, few-electron quantum dots," *Science*, vol. 278, no. 5344, pp. 1788–92, 1997.
- [134] "SCS Parylene Properties, high-performance conformal coatings," tech. rep., Specialty Coating Systems, Indianapolis, IN 46278, United States, 2016.
- [135] P. Song, C. S. S. Sangeeth, D. Thompson, W. Du, K. P. Loh, and C. A. Nijhuis, "Noncovalent Self-Assembled Monolayers on Graphene as a Highly Stable Platform for Molecular Tunnel Junctions," *Advanced Materials*, vol. 28, no. 4, pp. 631–639, 2016.
- [136] P. U. Vivitasari, Y. Azuma, M. Sakamoto, T. Teranishi, and Y. Majima, "Coulomb blockade and Coulomb staircase behavior observed at room temperature," *Materials Research Express*, vol. 4, no. 2, p. 024004, 2017.
- [137] Y. Azuma, M. Sakamoto, T. Teranishi, and Y. Majima, "Memory operations in Au nanoparticle single-electron transistors with floating gate electrodes," *Applied Physics Letters*, vol. 109, no. 22, p. 223106, 2016.
- [138] P. Gehring, J. K. Sowa, J. Cremers, Q. Wu, H. Sadeghi, Y. Sheng, J. H. Warner, C. J. Lambert, G. A. D. Briggs, and J. A. Mol, "Distinguishing Lead and Molecule States in Graphene-Based Single-Electron Transistors," *ACS Nano*, vol. 11, no. 6, pp. 5325–5331, 2017.
- [139] D. Lin, S. Y. R. Hui, and L. O. Chua, "Gas Discharge Lamps Are Volatile Memristors," *IEEE Transactions on Circuits and Systems I: Regular Papers*, vol. 61, no. 7, pp. 2066–2073, 2014.
- [140] Ø. G. Martinsen, S. Grimnes, C. A. Lütken, and G. K. Johnsen, "Memristance in human skin," *Journal of Physics: Conference Series*, vol. 224, no. 1, p. 012071, 2010.
- [141] A. G. Volkov, C. Tucket, J. Reedus, M. I. Volkova, V. S. Markin, and L. Chua, "Memristors in plants.," *Plant signaling & behavior*, vol. 9, no. 3, p. e28152, 2014.
- [142] D. B. Strukov, G. S. Snider, D. R. Stewart, and R. S. Williams, "The missing memristor found," *Nature*, vol. 453, no. 7191, pp. 80–83, 2008.
- [143] L. Chua, "Memristor-The missing circuit element," *IEEE Transactions on Circuit Theory*, vol. 18, no. 5, pp. 507–519, 1971.
- [144] S. Vongehr and X. Meng, "The Missing Memristor has Not been Found," *Scientific Reports*, vol. 5, no. 1, p. 11657, 2015.
- [145] G. Dearnaley, A. M. Stoneham, and D. V. Morgan, "Electrical phenomena in amorphous oxide films," *Reports on Progress in Physics*, vol. 33, no. 3, p. 306, 1970.
- [146] R. Waser and M. Aono, "Nanoionics-based resistive switching memories," *Nature Materials*, vol. 6, no. 11, pp. 833–840, 2007.
- [147] T. W. Hickmott, "Low-Frequency Negative Resistance in Thin Anodic Oxide Films," *Journal of Applied Physics*, vol. 33, no. 9, pp. 2669–2682, 1962.

- [148] L. Chua, "If it's pinched it's a memristor," *Semiconductor Science and Technology*, vol. 29, no. 10, p. 104001, 2014.
- [149] G. K. Johnsen, C. A. Lütken, Ø. G. Martinsen, and S. Grimnes, "Memristive model of electro-osmosis in skin," *Physical Review E*, vol. 83, no. 3, p. 031916, 2011.
- [150] A. G. Radwan and M. E. Fouda, "Memristor: Models, Types, and Applications," in *On the Mathematical Modeling of Memristor, Memcapacitor, and Meminductor*, pp. 13–49, Springer International Publishing, 2015.
- [151] F. Argall, "Switching phenomena in titanium oxide thin films," *Solid-State Electronics*, vol. 11, no. 5, pp. 535–541, 1968.
- [152] A. Beck, J. G. Bednorz, C. Gerber, C. Rossel, and D. Widmer, "Reproducible switching effect in thin oxide films for memory applications," *Applied Physics Letters*, vol. 77, no. 1, p. 139, 2000.
- [153] S. Genrikh, C.-r. Cho, I.-k. Yoo, E.-h. Lee, S.-i. Cho, and C.-w. Moon, "Electrode structure having at least two oxide layers and non-volatile memory device having the same," *US Patent*, 2007.
- [154] R. S. Willaims, "Electrically actuated switch," *US Patent*, 2007.
- [155] K. M. Kim, B. J. Choi, B. W. Koo, S. Choi, D. S. Jeong, and C. S. Hwang, "Resistive Switching in PtAl₂O₃TiO₂Ru Stacked Structures," *Electrochemical and Solid-State Letters*, vol. 9, no. 12, p. G343, 2006.
- [156] C.-Y. Lin, C.-Y. Wu, C.-Y. Wu, C. Hu, and T.-Y. Tseng, "Bistable Resistive Switching in Al₂O₃ Memory Thin Films," *Journal of The Electrochemical Society*, vol. 154, no. 9, p. G189, 2007.
- [157] K. R. Van Horn, J. T. Staley, and P. R. Bridenbaugh, "Aluminum processing," *Encyclopaedia Britannica*, 2018.
- [158] T. Berzina, A. Smerieri, M. Bernabò, A. Pucci, G. Ruggeri, V. Erokhin, and M. P. Fontana, "Optimization of an organic memristor as an adaptive memory element," *Journal of Applied Physics*, vol. 105, no. 12, p. 124515, 2009.
- [159] A. Smerieri, V. Erokhin, and M. P. Fontana, "Origin of current oscillations in a polymeric electrochemically controlled element," *Journal of Applied Physics*, vol. 103, no. 9, p. 094517, 2008.
- [160] J. Kriegerand and S. Spitzer, "Non-traditional, non-volatile memory based on switching and retention phenomena in polymeric thin films," in *Proceedings. 2004 IEEE Computational Systems Bioinformatics Conference*, pp. 121–124, IEEE, 2004.
- [161] A. Chanthbouala, V. Garcia, R. O. Cherifi, K. Bouzehouane, S. Fusil, X. Moya, S. Xavier, H. Yamada, C. Deranlot, N. D. Mathur, M. Bibes, A. Barthélémy, and J. Grollier, "A ferroelectric memristor," *Nature Materials*, vol. 11, no. 10, pp. 860–864, 2012.

- [162] A. Mehonic, S. Cueff, M. Wojdak, S. Hudziak, O. Jambois, C. Labbé, B. Garrido, R. Rizk, and A. J. Kenyon, “Resistive switching in silicon suboxide films,” *Journal of Applied Physics*, vol. 111, no. 7, p. 074507, 2012.
- [163] Xiaobin Wang, Yiran Chen, Haiwen Xi, Hai Li, and D. Dimitrov, “Spintronic Memristor Through Spin-Torque-Induced Magnetization Motion,” *IEEE Electron Device Letters*, vol. 30, no. 3, pp. 294–297, 2009.
- [164] P. J. Metaxas, J. Sampaio, A. Chanthbouala, R. Matsumoto, A. Anane, A. Fert, K. A. Zvezdin, K. Yakushiji, H. Kubota, A. Fukushima, S. Yuasa, K. Nishimura, Y. Nagamine, H. Maehara, K. Tsunekawa, V. Cros, and J. Grollier, “High domain wall velocities via spin transfer torque using vertical current injection,” *Scientific Reports*, vol. 3, no. 1, p. 1829, 2013.
- [165] H. Y. Jeong, J. Y. Kim, J. W. Kim, J. O. Hwang, J.-E. Kim, J. Y. Lee, T. H. Yoon, B. J. Cho, S. O. Kim, R. S. Ruoff, and S.-Y. Choi, “Graphene Oxide Thin Films for Flexible Nonvolatile Memory Applications,” *Nano Letters*, vol. 10, no. 11, pp. 4381–4386, 2010.
- [166] J. Yang, F. Miao, W. Wu, S.-Y. Wang, and R. S. Williams, “Defective graphene-based memristor,” *US Patent Application*, 2010.
- [167] V. K. Sangwan, D. Jariwala, I. S. Kim, K.-S. Chen, T. J. Marks, L. J. Lauhon, and M. C. Hersam, “Gate-tunable memristive phenomena mediated by grain boundaries in single-layer MoS₂,” *Nature Nanotechnology*, vol. 10, no. 5, pp. 403–406, 2015.
- [168] R. C. Johnson, “Startup Beats HP, Hynix to Memristor Learning,” *EE Times (news article)*, 2015.
- [169] A. Talukdar, A. Radwan, and K. Salama, “Non linear dynamics of memristor based 3rd order oscillatory system,” *Microelectronics Journal*, vol. 43, no. 3, pp. 169–175, 2012.
- [170] A. Talukdar, A. Radwan, and K. Salama, “Generalized model for Memristor-based Wien family oscillators,” *Microelectronics Journal*, vol. 42, no. 9, pp. 1032–1038, 2011.
- [171] A. Talukdar, A. G. Radwan, and K. N. Salama, “Time domain oscillating poles: Stability redefined in Memristor based Wien-oscillators,” in *2010 International Conference on Microelectronics*, pp. 288–291, IEEE, 2010.
- [172] T. Driscoll, J. Quinn, S. Klein, H. T. Kim, B. J. Kim, Y. V. Pershin, M. Di Ventra, and D. N. Basov, “Memristive adaptive filters,” *Applied Physics Letters*, vol. 97, no. 9, p. 093502, 2010.
- [173] Y.-B. Zhao, C.-K. Tse, J.-C. Feng, and Y.-C. Guo, “Application of Memristor-Based Controller for Loop Filter Design in Charge-Pump Phase-Locked Loops,” *Circuits, Systems, and Signal Processing*, vol. 32, no. 3, pp. 1013–1023, 2013.
- [174] J. Joshua Yang, F. Miao, M. D. Pickett, D. A. Ohlberg, D. R. Stewart, C. N. Lau, and R. S. Williams, “The mechanism of electroforming of metal oxide memristive switches,” *Nanotechnology*, vol. 20, no. 21, p. 215201, 2009.

- [175] Y. Yang, P. Gao, S. Gaba, T. Chang, X. Pan, and W. Lu, "Observation of conducting filament growth in nanoscale resistive memories," *Nature Communications*, vol. 3, no. 1, p. 732, 2012.
- [176] A. Sawa, "Resistive switching in transition metal oxides," *Materials Today*, vol. 11, no. 6, pp. 28–36, 2008.
- [177] C. Chen, S. Gao, F. Zeng, G. S. Tang, S. Z. Li, C. Song, H. D. Fu, and F. Pan, "Migration of interfacial oxygen ions modulated resistive switching in oxide-based memory devices," *Journal of Applied Physics*, vol. 114, no. 1, p. 014502, 2013.
- [178] G. C. Binnig G., Quate C.F., "Atomic Force Microscope," *Physical Review Letters*, vol. 56, no. 9, pp. 930–933, 1986.
- [179] W. T. Huck, "Responsive polymers for nanoscale actuation," *Materials Today*, vol. 11, no. 7-8, pp. 24–32, 2008.
- [180] R. H. Baughman, C. Cui, A. A. Zakhidov, Z. Iqbal, J. N. Barisci, G. M. Spinks, G. G. Wallace, A. Mazzoldi, D. De Rossi, A. G. Rinzler, O. Jaschinski, S. Roth, and M. Kertesz, "Carbon nanotube actuators," *Science*, vol. 284, no. 5418, pp. 1340–1344, 1999.
- [181] Y. Huang, J. Liang, and Y. Chen, "The application of graphene based materials for actuators," *Journal of Materials Chemistry*, vol. 22, no. 9, pp. 3671–3679, 2012.
- [182] P. Kim and C. M. Lieber, "Nanotube nanotweezers," *Science*, vol. 286, no. 5447, pp. 2148–2150, 1999.
- [183] H.-C. Hung, "Actuator with carbon nanotube yarns," *US Patent*, 2009.
- [184] A. E. Aliev, O. Jiyoung, K. Mikhail, A. A. K. S. Fang, A. F. Fonseca, R. Ovalle, M. D. Lima, M. H. Haque, Y. N. Gartstein, M. Zhang, A. A. Zakhidov, and R. H. Baughman, "Giant-Stroke, Superelastic Carbon Nanotube Aerogel Muscles," *Science*, vol. 323, no. 5103, pp. 1575–1578, 2009.
- [185] U. Vohrer, I. Kolaric, M. H. Haque, S. Roth, and U. Detlaff-Weglikowska, "Carbon nanotube sheets for the use as artificial muscles," in *Carbon*, vol. 42, pp. 1159–1164, Pergamon, 2004.
- [186] H. G. Craighead, "Nanoelectromechanical systems," *Science*, vol. 290, no. 5496, pp. 1532–1535, 2000.
- [187] E. A. Laird, F. Pei, W. Tang, G. A. Steele, and L. P. Kouwenhoven, "A high quality factor carbon nanotube mechanical resonator at 39 GHz," *Nano Letters*, vol. 12, no. 1, pp. 193–197, 2012.
- [188] K. Gupta and W. L. Hosch, "Mobility," *Encyclopaedia Britannica*, 2007.
- [189] S. Kano, Y. Azuma, K. Maeda, D. Tanaka, M. Sakamoto, T. Teranishi, L. W. Smith, C. G. Smith, and Y. Majima, "Ideal discrete energy levels in synthesized au nanoparticles for chemically assembled single-electron transistors," *ACS Nano*, vol. 6, no. 11, pp. 9972–9977, 2012.

- [190] C. Ciraci, R. T. Hill, J. J. Mock, Y. Urzhumov, A. I. Fernandez-Dominguez, S. A. Maier, J. B. Pendry, A. Chilkoti, and D. R. Smith, “Probing the Ultimate Limits of Plasmonic Enhancement,” *Science*, vol. 337, no. 6098, pp. 1072–1074, 2012.
- [191] J. Mertens, A. L. Eiden, D. O. Sigle, F. Huang, A. Lombardo, Z. Sun, R. S. Sundaram, A. Colli, C. Tserkezis, J. Aizpurua, S. Milana, A. C. Ferrari, and J. J. Baumberg, “Controlling Subnanometer Gaps in Plasmonic Dimers Using Graphene,” *Nano Letters*, vol. 13, no. 11, pp. 5033–5038, 2013.
- [192] J. Mertens, *Plasmonic Cavities*. PhD thesis, University of Cambridge, 2015.
- [193] G. Simmons and H. Wang, *Single Crystal Elastic Constants and Calculated Elastic Properties: A Handbook*. Cambridge, Mass.: Cambridge, Mass., M.I.T. Press, 1971.
- [194] M. K. Tripp, C. Stampfer, D. C. Miller, T. Helbling, C. F. Herrmann, C. Hierold, K. Gall, S. M. George, and V. M. Bright, “The mechanical properties of atomic layer deposited alumina for use in micro- and nano-electromechanical systems,” *Sensors and Actuators A*, vol. 130, no. 131, pp. 419–429, 2006.
- [195] C. Lee, X. Wei, J. W. Kysar, and J. Hone, “Measurement of the elastic properties and intrinsic strength of monolayer graphene,” *Science*, vol. 321, no. 5887, pp. 385–388, 2008.
- [196] T. M. Mohiuddin, A. Lombardo, R. R. Nair, A. Bonetti, G. Savini, R. Jalil, N. Bonini, D. M. Basko, C. Galiotis, N. Marzari, K. S. Novoselov, A. K. Geim, and A. C. Ferrari, “Uniaxial strain in graphene by Raman spectroscopy: G peak splitting, Grüneisen parameters, and sample orientation,” *Physical Review B - Condensed Matter and Materials Physics*, vol. 79, no. 20, p. 205433, 2009.
- [197] M. K. Small and W. D. Nix, “Analysis of the accuracy of the bulge test in determining the mechanical properties of thin films,” *Journal of Materials Research*, vol. 7, no. 6, pp. 1553–1563, 1992.
- [198] T. J. Campbell, R. K. Kalia, A. Nakano, P. Vashishta, S. Ogata, and S. Rodgers, “Dynamics of oxidation of aluminum nanoclusters using variable charge molecular-dynamics simulations on parallel computers,” *Physical Review Letters*, vol. 82, no. 24, pp. 4866–4869, 1999.
- [199] T. J. Seebeck, “Über die magnetische Polarisation der Metalle und Erze durch Temperatur-Differenz,” *Annalen der Physik*, vol. 82, no. 2, pp. 133–160, 1826.
- [200] The Editors of Encyclopaedia Britannica, “Peltier effect,” *Encyclopaedia Britannica*, 2018.
- [201] T. M. Tritt and M. A. Subramanian, “Thermoelectric Materials, Phenomena, and Applications: A Bird’s Eye View,” *MRS Bulletin*, vol. 31, no. 03, pp. 188–198, 2006.
- [202] G. Pennelli, “Review of nanostructured devices for thermoelectric applications,” *Beilstein Journal of Nanotechnology*, vol. 5, no. 1, pp. 1268–1284, 2014.

- [203] S. Twaha, J. Zhu, Y. Yan, and B. Li, “A comprehensive review of thermoelectric technology: Materials, applications, modelling and performance improvement,” *Renewable and Sustainable Energy Reviews*, vol. 65, pp. 698–726, 2016.
- [204] M. G. Vavilov and A. D. Stone, “Failure of the Wiedemann-Franz law in mesoscopic conductors,” *Physical Review B - Condensed Matter and Materials Physics*, vol. 72, no. 20, 2005.
- [205] D. Husmann, M. Lebrat, S. Häusler, J.-P. Brantut, L. Corman, and T. Esslinger, “Breakdown of the Wiedemann-Franz law in a unitary Fermi gas,” *PNAS*, vol. 115, no. 34, pp. 8563–8568, 2018.
- [206] Y. Du, J. Xu, B. Paul, and P. Eklund, “Flexible thermoelectric materials and devices,” *Applied Materials Today*, vol. 12, pp. 366–388, 2018.
- [207] L. D. Hicks and M. S. Dresselhaus, “Effect of quantum-well structures on the thermomagnetic figure of merit,” *Physical Review B*, vol. 47, no. 19, pp. 727–731, 1993.
- [208] B. Sothmann, R. Sánchez, and A. N. Jordan, “Thermoelectric energy harvesting with quantum dots,” *Nanotechnology*, vol. 26, no. 3, p. 32001, 2015.
- [209] R. Sánchez and M. Büttiker, “Detection of single-electron heat transfer statistics,” *EPL*, vol. 100, no. 4, p. 47008, 2012.
- [210] J. R. Prance, C. G. Smith, J. P. Griffiths, S. J. Chorley, D. Anderson, G. A. Jones, I. Farrer, and D. A. Ritchie, “Electronic refrigeration of a two-dimensional electron gas,” *Physical Review Letters*, vol. 102, no. 14, pp. 1–4, 2009.
- [211] H. L. Edwards, Q. Niu, and A. L. De Lozanne, “A quantum-dot refrigerator,” *Applied Physics Letters*, vol. 63, no. 13, pp. 1815–1817, 1993.
- [212] J. P. Pekola, J. V. Koski, and D. V. Averin, “Refrigerator based on the Coulomb barrier for single-electron tunneling,” *Physical Review B - Condensed Matter and Materials Physics*, vol. 89, no. 8, pp. 2–5, 2014.
- [213] R. Sánchez, B. Sothmann, A. N. Jordan, and M. Büttiker, “Correlations of heat and charge currents in quantum-dot thermoelectric engines,” *New Journal of Physics*, vol. 15, no. 12, p. 125001, 2013.
- [214] M. Esposito, K. Lindenberg, and C. Van Den Broeck, “Thermoelectric efficiency at maximum power in a quantum dot,” *EPL*, vol. 85, no. 6, 2009.
- [215] A. Dzurak, C. Smith, C. Barnes, M. Pepper, L. Martín-Moreno, C. Liang, D. Ritchie, and G. Jones, “Thermoelectric signature of the excitation spectrum of a quantum dot,” *Physical Review B - Condensed Matter and Materials Physics*, vol. 55, no. 16, pp. R10197–R10200, 1997.
- [216] J. Koch, F. Von Oppen, Y. Oreg, and E. Sela, “Thermopower of single-molecule devices,” *Physical Review B - Condensed Matter and Materials Physics*, vol. 70, no. 19, pp. 1–12, 2004.

- [217] Y. Kim, W. Jeong, K. Kim, W. Lee, and P. Reddy, “Electrostatic control of thermoelectricity in molecular junctions,” *Nature Nanotechnology*, vol. 9, no. 11, pp. 881–885, 2014.
- [218] P. Reddy, S. Y. Jang, R. A. Segalman, and A. Majumdar, “Thermoelectricity in molecular junctions,” *Science*, vol. 315, no. 5818, pp. 1568–1571, 2007.
- [219] O. Entin-Wohlman, Y. Imry, and A. Aharony, “Three-terminal thermoelectric transport through a molecular junction,” *Physical Review B - Condensed Matter and Materials Physics*, vol. 82, no. 11, pp. 1–9, 2010.
- [220] B. Sothmann and M. Büttiker, “Magnon-driven quantum-dot heat engine,” *EPL*, vol. 99, no. 2, p. 27001, 2012.
- [221] R. Prabhakar, Y. Zhang, and J.-H. Bahk, “Flexible Thermoelectric Materials and Devices,” in *Flexible Energy Conversion and Storage Devices*, pp. 425–457, Weinheim, Germany: Wiley-VCH Verlag GmbH & Co. KGaA, 2018.
- [222] H. Ju and J. Kim, “Chemically Exfoliated SnSe Nanosheets and Their SnSe/Poly(3,4-ethylenedioxythiophene):Poly(styrenesulfonate) Composite Films for Polymer Based Thermoelectric Applications,” *ACS Nano*, vol. 10, no. 6, pp. 5730–5739, 2016.
- [223] C. Evangeli, M. Matt, L. Rincón-García, F. Pauly, P. Nielaba, G. Rubio-Bollinger, J. C. Cuevas, and N. Agraït, “Quantum thermopower of metallic atomic-size contacts at room temperature,” *Nano Letters*, vol. 15, no. 2, pp. 1006–1011, 2015.
- [224] C. Evangeli, K. Gillemot, E. Leary, M. T. González, G. Rubio-Bollinger, C. J. Lambert, and N. Agraït, “Engineering the thermopower of C60 molecular junctions,” *Nano Letters*, vol. 13, no. 5, pp. 2141–2145, 2013.
- [225] C. J. Lambert, H. Sadeghi, and Q. H. Al-Galiby, “Quantum-interference-enhanced thermoelectricity in single molecules and molecular films,” *Comptes Rendus Physique*, vol. 17, no. 10, pp. 1084–1095, 2016.
- [226] L. Sun, B. Liao, D. Sheberla, D. Kraemer, J. Zhou, E. A. Stach, D. Zakharov, V. Stavila, A. A. Talin, Y. Ge, M. D. Allendorf, G. Chen, F. Léonard, and M. Dincă, “A Microporous and Naturally Nanostructured Thermoelectric Metal-Organic Framework with Ultralow Thermal Conductivity,” *Joule*, vol. 1, no. 1, pp. 168–177, 2017.
- [227] L. Francioso, C. De Pascali, I. Farella, C. Martucci, P. Cretì, P. Siciliano, and A. Perrone, “Flexible thermoelectric generator for ambient assisted living wearable biometric sensors,” *Journal of Power Sources*, vol. 196, no. 6, pp. 3239–3243, 2011.
- [228] M. Benganem, A. A. Al-Mashraqi, and K. O. Daffallah, “Performance of solar cells using thermoelectric module in hot sites,” *Renewable Energy*, vol. 89, pp. 51–59, 2016.
- [229] C. Haddad, C. Périlhon, A. Danlos, M.-X. François, and G. Descombes, “Some Efficient Solutions to Recover Low and Medium Waste Heat: Competitiveness of the Thermoacoustic Technology,” *Energy Procedia*, vol. 50, pp. 1056–1069, 2014.

- [230] A. Salomon, D. Cahen, S. Lindsay, J. Tomfohr, V. Engelkes, and C. Frisbie, "Comparison of Electronic Transport Measurements on Organic Molecules," *Advanced Materials*, vol. 15, no. 22, pp. 1881–1890, 2003.
- [231] T. W. Kim, G. Wang, H. Lee, and T. Lee, "Statistical analysis of electronic properties of alkanethiols in metal-molecule-metal junctions," *Nanotechnology*, vol. 18, no. 31, p. 315204, 2007.
- [232] V. B. Engelkes, J. M. Beebe, and C. D. Frisbie, "Length-dependent transport in molecular junctions based on SAMs of alkanethiols and alkanedithiols: Effect of metal work function and applied bias on tunneling efficiency and contact resistance," *Journal of the American Chemical Society*, vol. 126, no. 43, pp. 14287–14296, 2004.
- [233] G. Wang, T. W. Kim, H. Lee, and T. Lee, "Influence of metal-molecule contacts on decay coefficients and specific contact resistances in molecular junctions," *Physical Review B - Condensed Matter and Materials Physics*, vol. 76, no. 20, 2007.
- [234] A. Salomon, D. Cahen, S. Lindsay, J. Tomfohr, V. B. Engelkes, and C. D. Frisbie, "Comparison of Electronic Transport Measurements on Organic Molecules," *Advanced Materials*, vol. 15, no. 22, pp. 1881–1890, 2003.
- [235] G. Wang, T. W. Kim, Y. H. Jang, and T. Lee, "Effects of metal-molecule contact and molecular structure on molecular electronic conduction in nonresonant tunneling regime: Alkyl versus conjugated molecules," *Journal of Physical Chemistry C*, vol. 112, no. 33, pp. 13010–13016, 2008.
- [236] E. Marx, D. S. Ginger, K. Walzer, K. Stokbro, and N. C. Greenham, "Self-Assembled Monolayers of CdSe Nanocrystals on Doped GaAs Substrates," *Nano Letters*, vol. 2, no. 8, pp. 911–914, 2002.
- [237] C. A. Nijhuis, W. F. Reus, and G. M. Whitesides, "Mechanism of Rectification in Tunneling Junctions Based on Molecules with Asymmetric Potential Drops," *Journal of the American Chemical Society*, vol. 132, no. 51, pp. 18386–18401, 2010.
- [238] J. Trasobares, D. Vuillaume, D. Théron, and N. Clément, "A 17 GHz molecular rectifier," *Nature Communications*, vol. 7, p. 12850, 2016.
- [239] X. Chen, M. Roemer, L. Yuan, W. Du, D. Thompson, E. Del Barco, and C. A. Nijhuis, "Molecular diodes with rectification ratios exceeding 10^5 driven by electrostatic interactions," *Nature Nanotechnology*, vol. 12, no. 8, pp. 797–803, 2017.
- [240] J. Yuan and J. Lou, "Memristor goes two-dimensional," *Nature Nanotechnology*, vol. 10, no. 5, pp. 389–390, 2015.
- [241] H. B. Akkerman, R. C. G. Naber, B. Jongbloed, P. A. van Hal, P. W. M. Blom, D. M. de Leeuw, and B. de Boer, "Electron tunneling through alkanedithiol self-assembled monolayers in large-area molecular junctions.," *Proceedings of the National Academy of Sciences of the United States of America*, vol. 104, no. 27, pp. 11161–6, 2007.

- [242] A. J. Kronemeijer, E. H. Huisman, H. B. Akkerman, A. M. Goossens, I. Katsouras, P. A. Van Hal, T. C. Geuns, S. J. Van Der Molen, P. W. Blom, and D. M. De Leeuw, "Electrical characteristics of conjugated self-assembled monolayers in large-area molecular junctions," *Applied Physics Letters*, vol. 97, no. 17, p. 173302, 2010.
- [243] T. Morita and S. Lindsay, "Determination of single molecule conductances of alkanedithiols by conducting-atomic force microscopy with large gold nanoparticles," *Journal of the American Chemical Society*, vol. 129, no. 23, pp. 7262–7263, 2007.
- [244] S. Y. Jang, P. Reddy, A. Majumdar, and R. A. Segalman, "Interpretation of stochastic events in single molecule conductance measurements," *Nano Letters*, vol. 6, no. 10, pp. 2362–2367, 2006.
- [245] H. B. Akkerman and B. De Boer, "Electrical conduction through single molecules and self-assembled monolayers," *Journal of Physics Condensed Matter*, vol. 20, no. 1, p. 013001, 2008.
- [246] Y. S. Liu, Y. R. Chen, and Y. C. Chen, "Thermoelectric efficiency in nanojunctions: A comparison between atomic junctions and molecular junctions," *ACS Nano*, vol. 3, no. 11, pp. 3497–3504, 2009.
- [247] G. P. Tang, Z. Q. Fan, X. J. Zhang, Y. Ren, and K. Q. Chen, "Negative differential resistance behaviour in OPE molecular devices with semiconductor electrodes," *Journal of Physics D: Applied Physics*, vol. 42, no. 17, p. 175104, 2009.
- [248] R. Frisenda, S. Tarkuç, E. Galán, M. L. Perrin, R. Eelkema, F. C. Grozema, and H. S. van der Zant, "Electrical properties and mechanical stability of anchoring groups for single-molecule electronics," *Beilstein Journal of Nanotechnology*, vol. 6, no. 1, pp. 1558–1567, 2015.
- [249] J. Liang, R. E. Smith, A. Vezzoli, L. Xie, D. C. Milan, R. Davidson, A. Beeby, P. J. Low, S. J. Higgins, B. Mao, and R. J. Nichols, "Electrochemically grafted single molecule junctions exploiting a chemical protection strategy," *Electrochimica Acta*, vol. 220, pp. 436–443, 2016.
- [250] J. J. Stapleton, P. Harder, T. A. Daniel, M. D. Reinard, Y. Yao, D. W. Price, J. M. Tour, and D. L. Allara, "Self-assembled oligo(phenylene-ethynylene) molecular electronic switch monolayers on gold: Structures and chemical stability," *Langmuir*, vol. 19, no. 20, pp. 8245–8255, 2003.
- [251] R. Frisenda and H. S. Van Der Zant, "Transition from Strong to Weak Electronic Coupling in a Single-Molecule Junction," *Physical Review Letters*, vol. 117, no. 12, 2016.
- [252] Z. Wei, T. Li, K. Jennum, M. Santella, N. Bovet, W. Hu, M. B. Nielsen, T. Bjørnholm, G. C. Solomon, B. W. Laursen, and K. Nørsgaard, "Molecular junctions based on SAMs of cruciform oligo(phenylene ethynylene)s," *Langmuir*, vol. 28, no. 8, pp. 4016–4023, 2012.

- [253] V. Kaliginedi, P. Moreno-García, H. Valkenier, W. Hong, V. M. García-Suárez, P. Buitter, J. L. Otten, J. C. Hummelen, C. J. Lambert, and T. Wandlowski, “Correlations between molecular structure and single-junction conductance: A case study with oligo(phenylene-ethynylene)-type wires,” *Journal of the American Chemical Society*, vol. 134, no. 11, pp. 5262–5275, 2012.
- [254] M. T. González, X. Zhao, D. Z. Manrique, D. Miguel, E. Leary, M. Gulcur, A. S. Batsanov, G. Rubio-Bollinger, C. J. Lambert, M. R. Bryce, and N. Agrait, “Structural versus electrical functionalization of oligo(phenylene ethynylene) diamine molecular junctions,” *Journal of Physical Chemistry C*, vol. 118, no. 37, pp. 21655–21662, 2014.
- [255] R. Miao, H. Xu, M. Skripnik, L. Cui, K. Wang, K. G. Pedersen, M. Leijnse, F. Pauly, K. Wärnmark, E. Meyhofer, P. Reddy, and H. Linke, “Influence of Quantum Interference on the Thermoelectric Properties of Molecular Junctions,” *Nano Letters*, vol. 18, no. 9, pp. 5666–5672, 2018.
- [256] M. Carloti, A. Kovalchuk, T. Wächter, X. Qiu, M. Zharnikov, and R. C. Chiechi, “Conformation-driven quantum interference effects mediated by through-space conjugation in self-assembled monolayers,” *Nature Communications*, vol. 7, 2016.
- [257] C. Teichert, J. F. MacKay, D. E. Savage, M. G. Lagally, M. Brohl, and P. Wagner, “Comparison of surface roughness of polished silicon wafers measured by light scattering topography, soft-x-ray scattering, and atomic-force microscopy,” *Applied Physics Letters*, vol. 66, no. 18, pp. 2346–2348, 1995.
- [258] P. Horowitz and W. Hill, “The Art of Electronics,” *Cambridge University Press*, 1992.
- [259] P. S. Mahapatra, K. Sarkar, H. R. Krishnamurthy, S. Mukerjee, and A. Ghosh, “Seebeck Coefficient of a Single van der Waals Junction in Twisted Bilayer Graphene,” *Nano Letters*, vol. 17, no. 11, pp. 6822–6827, 2017.
- [260] M. Tsutsui, T. Morikawa, Y. He, A. Arima, and M. Taniguchi, “High thermopower of mechanically stretched single-molecule junctions,” *Scientific Reports*, vol. 5, no. 1, p. 11519, 2015.
- [261] A. Tan, S. Sadat, and P. Reddy, “Measurement of thermopower and current-voltage characteristics of molecular junctions to identify orbital alignment,” *Applied Physics Letters*, vol. 96, no. 1, p. 013110, 2010.